NTech
Lehrstuhl für
Nukleartechnik

Technische Universität München

TECHNISCHE UNIVERSITÄT MÜNCHEN
Fakultät für Maschinenwesen

ANALYSIS AND EVALUATION OF THE DUAL FLUID REACTOR CONCEPT

XIANG WANG

Vollständiger Abdruck der von der Fakultät für Maschinenwesen der Technischen Universität München zur Erlangung des akademischen Grades eines

Doktor-Ingenieurs (Dr. -Ing.)

genehmigten Dissertation.

Vorsitzender: Prof. Dr.-Ing. Thomas Sattelmayer

Prüfer der Dissertation: 1. Prof. Rafael Macián-Juan, Ph.D.
2. Prof. Dr. hab. Mariusz Dabrowski
University of Szczecin/Polen

Die Dissertation wurde am 20.01.2017 bei der Technischen Universität München eingereicht und durch die Fakultät für Maschinenwesen am 27.06.2017 angenommen.

Statement of Originality

The work contained in this thesis has not been previously submitted for a degree or diploma at any other higher education institution. To the best of my knowledge and belief, the thesis contains no material previously published or written by another person except where due references are made.

Location Date Sign

Acknowledgment

At this moment, on the only page in this work belonging to me and where “I” is allowed to show up, I would like to give my most sincere thanks to my families, my friends, my colleges, my classmates as well as any one who has helped me with my work.

After all I would like to give my love to my parents. They have poured everything in my education and have given everything what I need for my study and for my living. Just till four years ago, the most part of my financial support came form them. As parents, what they have done has exceeded far more the word itself. Their meticulous care and kind considerations company me, though they are ten thousand miles away from me.

Especially I would like to give my most sincere respect to Prof. Dr. Macian who has given me such a good opportunity to study in one of the most famous universities in the world, Technical University of Munich. Also, in the last years, he has given to me uncountable helps and advises on my study, from the study on the basic theories, the choose of the theme, to the contact for the internship and the correction of my thesis, even when he was very busy. Without his generosity in knowledge and experience there is not any chance that I could go so far.

Secondly I would like to thank Dr. Seidl. Though we didn’t talk much, he has shown his extraordinary energy and experience gathered from his career. He is the most appropriate person who should discuss academic topic with, especially in the field of the nuclear reactor. His energetic figure and accurate conversational style have inspired me and has given me great courages from time to time.

I would also like to thank IFK, the institute of solid physics in Berlin. On the subject DFR we have talked a lot and have discussed on the very details. It is their creativity and brilliant idea that leads to the born of this thesis.

My college, Xun He, which was one of my best friends, is the person I must mention and give my thanks. We have together spent the Master study and Promotion in the same department. The conversation with him is always inspirational, joyful and helpful. I was so glad to have such a friend in Germany.

At last I would leave this place to give my thanks and love to my girl friend S. Gao, who encourages me when I feel depressed and supports me when I feel disappointed in the last two years.

Trademarks

ANSYS, ANSYS Workbench, CFX, FLUENT and any and all ANSYS, Inc. brand, product, service and feature names, logos and slogans are registered trademarks or trademarks of ANSYS, Inc.

COMSOL Multiphysics is a registered trademark of COMSOL AB.

MATLAB, SIMULINK are registered trademarks of The MathWorks Inc.

SCALE, KENO, NEWT, TRITON, TSUNAMI are products of Oak Ridge National Laboratory.

UNIX is a registered trademark of The Open Group.

Windows and Windows NT are either trademarks or registered trademarks of Microsoft Corporation.

All other registered and unregistered trademarks are properties of their respective owners.

Contents

Statement of Originality iii

Acknowledgment v

Trademarks vii

Table of Contents xiii

List of Figures xvii

List of Tables xx

Abbreviation xxi

Nomenclature xxiii

I Introduction 1

1 Present Situation Of Nuclear Energy 3
- 1.1 Generation IV 4
- 1.2 Objective and Outline 6

2 A Brief History of the MSR 9
- 2.1 Early stage 9
- 2.2 Renaissance 12
  - 2.2.1 Europe 12
  - 2.2.2 North America 13
  - 2.2.3 Asia 15

3 The Dual Fluid Reactor 19
- 3.1 Concept Overview 19
- 3.2 System Description 19
  - 3.2.1 Core 21
  - 3.2.2 Fuel Salt 21

3.2.3 In-/Outlet Plenums 22
3.2.4 Reflector 22
3.2.5 Fertile Blanket 23
3.3 Data Used for the Simulation 23
3.3.1 Geometric Data 23
3.3.2 Structural Materials 23
3.3.3 Temperatures 24
3.3.4 Physico-chemical Properties 24

4 Calculation Tools 27
4.1 Introduction 27
4.2 SCALE 27
4.3 SERPENT 28
4.4 SIMULINK 28
4.5 Fluent 28
4.6 COMSOL 28

II Neutronic Calculation 29

5 Neutronic Modelling of the DFR 31
5.1 Geometry 31
5.2 Fuel Salt Composition 33
5.3 Breeder Blanket Composition 33
5.4 Calculations Performed 34

6 Static Calculation 35
6.1 Introduction 35
6.2 Criticality 35
6.2.1 Theoretical Analysis 35
6.2.2 General Assessment 38
6.2.3 Group Constants 41
6.3 Delayed Neutron Data 44
6.4 Generation Time 44
6.4.1 Introduction 44
6.5 The In-hour Equation 46
6.6 Neutron Spectrum 47
6.6.1 Introduction 47
6.6.2 Neutron Energy Distribution 48
6.6.2.1 Evaluation of different Codes and Versions 48
6.6.2.2 Different Energy Group Structures 50
6.6.2.3 Different Nuclear Data Libraries 51

6.6.2.4 Neutron Energy Shift 52
6.6.2.5 Different Materials 58
6.6.2.6 Nuclear Reactions 59
6.6.3 Spatial Distribution of the Neutron Flux 60
6.7 Reaction Rates 62
6.8 Power Distribution 65
6.9 Conclusions 67

7 Sensitivity Analysis 69
7.1 Nuclide Importance 69
7.2 Geometry Feedback Coefficient 71
7.2.1 Description 71
7.2.2 Results 72
7.3 Thermal Feedback Coefficient 74
7.3.1 Description 74
7.3.2 Results 74
7.4 Conclusions 77

III Burnup Calculation 79

8 Introduction 81
8.1 Calculation options 82
8.1.1 Parameters 82
8.1.2 Results 83
8.1.2.1 Balance of Time and Memory 84
8.1.2.2 Evolution of k_{eff} 86
8.1.2.3 Material Inventory 86
8.2 Initial Load of Fuel Salt 88

9 Depletion without online-Processing 89
9.1 Single Fuel Tube Approach 89
9.1.1 Burnup Chain 89
9.1.2 Results 92
9.2 Full Core Approach 94
9.2.1 Description 94
9.2.2 Evolution of k_{eff} 94
9.2.3 Evolution of Inventory 94
9.2.4 Breeding Ratio 96
9.3 Conclusion 97

10 Depletion with Online-Processing 99

10.1 Description 99
 10.1.1 Reprocessing Techniques 99
 10.1.2 Fuel Reprocessing of the DFR 101
  10.1.2.1 Scenario I 103
  10.1.2.2 Scenario II 103
10.2 Results 106
 10.2.1 Results Of Scenario I 106
  10.2.1.1 Evolution of k_{eff} 106
  10.2.1.2 Evolution of the Core Inventory 106
  10.2.1.3 Breeding Ratio 106
 10.2.2 Results Of Scenario II 108
  10.2.2.1 Evolution of k_{eff} 109
  10.2.2.2 Evolution of the Core Inventory 110
  10.2.2.3 Breeding Ratio 111
10.3 Conclusions 113

IV Thermal-Hydraulic Calculation 115

11 System Analysis 117
11.1 Introduction 117
11.2 Modeling Approaches 118
 11.2.1 Zero-Dimensional Model 118
  11.2.1.1 Point Kinetics Model 118
  11.2.1.2 Thermal-Hydraulic Model 120
  11.2.1.3 System Description 122
  11.2.1.4 Parameters 123
 11.2.2 One-Dimensional Model 124
  11.2.2.1 One-dimensional Thermal-Hydraulic Model 124
  11.2.2.2 Power Profile 126
11.3 Results of the Simulations 128
 11.3.1 Steady-State Results 128
 11.3.2 Transient Results 129
  11.3.2.1 Response to a small Step Reactivity Change 129
  11.3.2.2 Response To large Step Reactivity Changes 130
  11.3.2.3 Response to a Ramp Reactivity Change 131
11.4 Conclusions 132

12 Single Cell Analysis 137
12.1 Introduction 137
12.2 Model Development 139

12.2.1 Two-Dimensional Model 139
12.2.1.1 Geometry 139
12.2.1.2 Materials 140
12.2.1.3 Mesh 140
12.2.1.4 Turbulence Models 140
12.2.1.5 Velocity Profile 142
12.2.1.6 Pressure Drop 144
12.2.1.7 Heat Transfer 146
12.2.1.8 Wall Function 150
12.2.2 Three-Dimensional Model 153
12.2.2.1 Geometry 154
12.2.2.2 Mesh 154
12.2.2.3 Power Profile 154
12.2.2.4 Velocity Profile 155
12.2.2.5 Boundary Conditions 155
12.3 Results 156
12.3.1 Steady State 156
12.3.2 Sensitivity 161
12.3.2.1 Velocity Profile 161
12.3.2.2 Wall Function and y^+ 165
12.3.2.3 Mesh Sensitivity 170
12.3.2.4 Sensitivity to Fuel Salt Properties 172
12.3.2.5 Sensitivity to Wall Properties 174
12.4 Conclusion 175

V Discussions **179**

13 Summary **181**

14 Outlook **183**
14.1 Longitudinal Study 183
14.1.1 Coupling 183
14.1.2 Other Fuel Types 183
14.2 Cross-Sectional Study 184
14.2.1 On Reactor Control 184
14.2.2 On Drain Tank 184
14.2.3 On Flow Direction 185
14.2.4 On Inlet/Outlet Distribution Zone 185
14.2.5 On Further Heating 185

Bibliography **200**

List of Figures

1.1 Nuclear energy development before and after Fukushima Accident . . 4
1.2 Molten Salt Reactor in Gen IV [gen02, pp.39] 5

2.1 System structure of ARE [BCM$^+$57] 10
2.2 Flow diagram of two fluids molten salt reactor concepts (left: 1950s, right: 1960s) [LeB10b, Rob65] 11
2.3 Flow diagram of MSRE [KB66] 12
2.4 Flow diagram of MSBR [Ros72] 13
2.5 MSFR and MOSART concepts 14
2.6 IMSR, FHR and SmAHTR concepts 15
2.7 TMSR and FUJI concepts 16

3.1 Working principal of the DFR 20
3.2 Demonstration of the inlet plenum [HRW$^+$15] 22

5.1 Horizontal section 32
5.2 Longitudinal section 32
5.3 Hexagonal array and fuel tube 32

6.1 Graphic demonstration of the multiplication factor k_{eff} 36
6.2 Assessment of U-Pu fuel salt k_{eff} 39
6.3 Comparison of $\bar{\nu}$ between SCALE CE and MG 40
6.4 Fission-capture ratio of U-Pu fuel 42
6.5 Graphical solution of the In-hour equation of the DFR (U-Pu fuel salt) 47
6.6 Various interactions of neutrons at different energy ranges [LB01] . . 48
6.7 Total neutron spectrum of U-Pu fuel 49
6.8 Neutron spectrum in different energy groups 51
6.9 Difference of neutron spectrum in libraries 52
6.10 Neutron spectrum in U-Pu fuel salt vs. theoretical spectra 53
6.11 Effect of the materials on the spectrum in the fuel salt 54
6.12 Dependency of neutron spectrum on neutron data libraries 55
6.13 Neutron spectra in materials 58
6.14 Characteristic peaks 60

6.15 Spatial neutron flux distribution for U-Pu fuel in the reactor 61
6.16 Reaction rate density 63
6.17 Visualization of fission reaction rate 65
6.18 Fission power distribution 66

7.1 Sensitivity of k_{eff} with regard to the most important nuclides in U-Pu fuel 70
7.2 Macroscopic cross section of fissionable nuclides in U-Pu salt fuel . . 71
7.3 Geometry coefficients (top: a, b; middle: c, d; bottom: e,f) 73
7.4 Temperature coefficient of the different DFR zones 76
7.5 Joint Temperature coefficient of Coolant/Reflector 77

8.1 Optimization mode 82
8.2 Time comparison between parameters 84
8.3 Memory comparison between parameters 85
8.4 k_{eff} comparison between parameters 86
8.5 Inventory comparison between parameters 87

9.1 Burnup chain of the fuel salts (modified and reproduced from [wim16]) 90
9.2 k_{eff} of the single fuel tube burnup 92
9.3 Interested nuclide inventories of the fuel in single fuel tube burnup . 93
9.4 Evolution of k_{eff} in depletion of U-Pu fuel 94
9.5 Evolution of selected inventories in the depletion of U-Pu fuel 95

10.1 Standard PUREX flowsheet [NEA67] 100
10.2 Capture-to-fission ratio of actinides for U-Pu fuel salt composition (reproduced with data from JANIS 4.0 [SBD14]) 102
10.3 Scheme for the on-line processing Scenario I 104
10.4 Scheme for the online processing in scenario II 105
10.5 Schematic representation of the investigated feed options 105
10.6 Change of k_{eff} in burnup with 28d-cycle fuel reprocessing 106
10.7 Change of fuel composition in burnup with 28d-cycle fuel reprocessing 107
10.8 Change of breeding ratio of scenario I 108
10.9 Change of k_{eff} in scenario II 109
10.10 Development of fissile nuclides in fuel salt in scenario II 110
10.11 Development of ^{238}U in scenario II 110
10.12 Development of other actinides in scenario II 111
10.13 Gain of fissile nuclides per week in scenario II 112
10.14 Change of breeding ratio of scenario II 113

11.1 Layout of the DFR-0D system with subsystems 122
11.2 Layout of the node in the DFR-1D system 125

11.3 Axial power distribution of the DFR in the simulation 127
11.4 System Steady-state Results 128
11.5 Transient results on small insert reactivities in step form 134
11.6 Power transient on insert reactivities in step form 135
11.7 Transient results on insert reactivities in ramp form 136

12.1 Evolution of the Geometry of the DFR 138
12.2 2D model and meshes of the fuel salt tube (FLUENT(m), COMSOL(r)) 140
12.3 Development of the velocity boundary layer 143
12.4 Radial initial velocity profile 144
12.5 Theoretical pressure drop 146
12.6 Temperature dependent *Nu* number of both liquids 150
12.7 Comparison of wall functions 152
12.8 Force balance of a fluid control element in the duct with constant cross-sectional flow area 153
12.9 Layout of the three-dimensional model 155
12.10 Steady state model performance (axial) 158
12.11 Steady state model performance (radial) 159
12.12 Steady state model performance (rainbow) 160
12.13 Sensitivity to velocity profile. Comparisons (axial) 163
12.14 Sensitivity to velocity profile. Comparisons (radial) 164
12.15 Selected y^+ results on axial distribution of flow properties 166
12.16 Completed y^+ results on axial properties 167
12.17 Relative differences of y^+ results in axial distribution of properties . 168
12.18 Layout of mesh size 170
12.19 Mesh Sensitivity. Comparison (axial) 171
12.20 Sensitivity to the heat capacity of the fuel salt. Comparison (axial) . 173
12.21 Sensitivity to the fuel salt thermal conductivity. Comparison (axial) 174
12.22 Sensitivity to wall thermal conductivity. Comparison (axial) 176
12.23 Comparison of axial temperature profile from 1D, 2D and 3D 177

List of Tables

3.1 Geometry parameter of DFR (Unit: m) 23
3.2 Proportions of nuclides in the structural material 24
3.3 Temperature parameter of DFR (Unit: K) 24
3.4 Physico-chemical properties used for the U-Pu fuel 25
3.5 Physico-chemical properties used for the coolant lead 25
3.6 Physico-chemical properties used for SiC 25

5.1 Proportions of U-Pu fuel 33
5.2 Breeder fertile material configuration 33
5.3 Correspondence of Codes to Calculations 34

6.1 Assessment of U-Pu fuel salt k_{eff} 39
6.2 Evolution of one-group constants with U-Pu fuel 43
6.3 Two group constants of the whole reactor with U-Pu fuel 43
6.4 Constants of DNPs of U-Pu fuel 44
6.5 Generation time of U-Pu fuel (10^{-6} s) 46
6.6 Generation time of U-Pu fuel in two energy groups (10^{-6} s) 46
6.7 Different energy group structures 50
6.8 Reaction rates (1/s) of selected nuclides of U-Pu fuel 64

7.1 Calculation design for temperature effect of U-Pu fuel 75
7.2 Independent temperature effect results (pcm /ΔK) 75
7.3 Joint temperature effect results (pcm /ΔK) 77

8.1 Optimization Options 83
8.2 Initial loading of the fuel salt (kg) 88

10.1 Brief information of the investigated feed options 105
10.2 Detailed information of the investigated feed options 109

11.1 Hydraulic parameters related to flow properties 123
11.2 Ramped insertions of reactivity 131

12.1 Values and relative differences of the characteristic ratios 138

12.2 $f - Re$ dependent pressure drop (Pa) 147
12.3 Assessment of Nu number correlations for fuel salt 148
12.4 Assessment of Nu number correlations for liquid lead 150
12.5 Extra model parameters related to flow properties 151
12.6 Extra model parameters related to flow properties 156
12.7 Cases in the steady state analysis 157
12.8 Cases in the sensitivity to the velocity profile analysis 162
12.9 Simulation design for y^+ investigation 165
12.10Cases in the mesh sensitivity study 170
12.11Cases in the sensitivity of the fuel salt properties 172
12.12Cases in the sensitivity of the wall property 175

0

Abbreviation

ARE	**A**ircraft **R**eactor **E**xperiment
DFR	**D**ual **F**luid **R**eactor
DNP	**D**elayed **N**eutron **P**recursor
GFR	**G**as-cooled **F**ast **R**eactor
GIF	**G**eneration IV **I**nternational **F**orum
LFR	**L**ead-cooled **F**ast **R**eactor
MSBR	**M**olten **S**alt **B**reeding **R**eactor
MSFR	**M**olten **S**alt **F**ast **R**eactor
MSR	**M**olten **S**alt **R**eactor
MSRE	**M**olten **S**alt **R**eactor **E**xperiment
PKM	**P**oint **K**inetics **M**odel
PUREX	**P**lutonium and **U**ranium **R**ecovery by **EX**traction
SCWR	**S**uper **C**ritical **W**ater **R**eactor (SCWR)
SFR	**S**odium-cooled **F**ast **R**eactor
VHTR	**V**ery **H**igh **T**emperature **R**eactor

Nomenclature

Upper-Case Letters

Symbol	Meaning	Unit	Appearance
A	Area	m^2	
C	DNP precursor concentration		
D	Diffusion coefficient	cm	
D_h	Hydraulic diameter	m	
E	Energy	MeV	
G	Mass flow density	$kg/(m^2s)$	
H	Height	m	
L	Length	m	
M	Mass	kg	
N	Number		
P	Power	W	
Q	Heat	J	
T	Temperature	K	
V	Volume	m^3	

Lower-Case Letters

Symbol	Meaning	Unit	Appearance
c_p	Specific heat	$J/(kg \cdot K)$	
d	diameter	m	
d$_r$	Relative difference		
h	Heat transfer coefficient	$W/(m^2K)$	
k	Multiplication factor		Part II, III
$\dot{m}$	Mass flow rate	kg/s	
p_w	Wet perimeter	m	
r	Radius	m	
t	Time	s	
v	Velocity	m/s	

Greek symbols

Symbol	Meaning	Unit	Appearance
β	DNP fracion		
κ	Thermal conductivity	$W/(m \cdot K)$	Part I, IV
Λ	Neutron generation time	s	
λ	DNP Decay constants	$1/s$	
ν	Neutron per fission		
ρ	Reactivity	pcm	Part II
ρ	Density	kg/m^3	
Σ	Macroscopic cross section	m^{-1}	
σ	Microscopic cross section	ba	
ϕ	Neutron flux	$1/cm^2s$	

Superscripts/subscripts

Symbol	Meaning	Appearance
core	Properties of core	
coolant, c	Properties of coolant	
fuel, f	Properties of fuel	
in	Inlet properties	
out	Outlet properties	

Part I

Introduction

Chapter 1

Present Situation Of Nuclear Energy

The Fukushima accident which happened in Japan on the 11th of March 2011 was a tragedy not only for the people affected, but also for the development of nuclear technology, especially its application to nuclear power generation. After the accident many countries utilizing nuclear power began to reconsider their nuclear policies under the pressure of public opinion and political concerns. Some of these countries decided to stop using nuclear power and, one of them, Germany, made this policy into law.

Nevertheless, according to Fig. 1.1 regenerated with data from **I**nternational **E**nergy **A**gency (IEA) [kwe08, kwe09, kwe10, kwe11, kwe12, kwe13, kwe14, kwe15] and the **I**nternational **A**tomic **E**nergy **A**gency (IAEA) [nts07,nts08,nts09,nts10,nts11,nts12, nts13, nts14] reports in the time frame 2006∼2014 from a worldwide point of view and taking into account the situation before the Fukushima accident, the descent of the nuclear energy share in the total electricity production has been apparent even from 2006. This is attributed to a stagnant development of the total capacity of nuclear power and to the increase of total electricity production in the same period. A precipitous decrease of the nuclear electricity share, as well as, of the new starts of nuclear power plant construction was encountered in 2011 in the aftermath of the accident. The countries, which examined the safety of their installations and faced the conflict between the increasing need of electric power and the potential lack of the capacity of the power generation, decided not to give up nuclear power. New nuclear power plants began to be built in 2012 and the total capacity of the nuclear power and share tended to recover and further rise.

At the same time, the pressure to significantly reduce the emission of greenhouse gases to the atmosphere, mainly CO_2, in order to prevent the onset of a potentially catastrophic global climate change, continues to be strong in most countries. The consideration of the available solutions for such a serious problem, factoring in the risks and benefits of the technologies mature enough to contribute effectively to a solution, has resulted in the fact that the reliance of many governments on nuclear electricity production remains strong. For this reason, up to 01 Nov. 2015 [wna08]

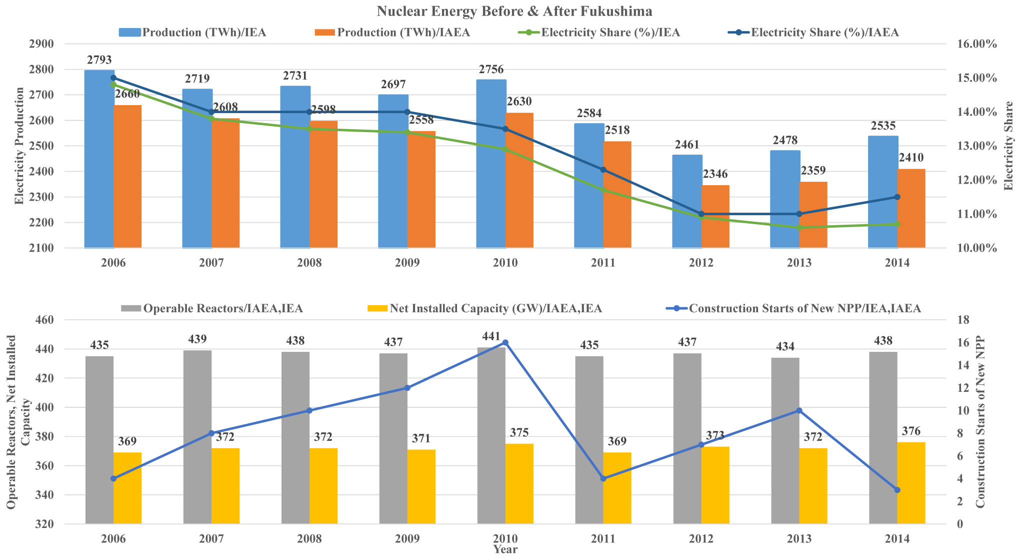

Figure 1.1: Nuclear energy development before and after Fukushima Accident

Based on IEA data from references mentioned in the text © OECD/IEA, IEA Publishing

modified by Xiang Wang. Licence: http://www.iea.org/t&c/termsandconditions/

there are 65 reactors with a total of $68GW_e$ under construction, 165 reactors with $185GW_e$ on order or planned, and even 324 reactors with $367GW_e$ proposed. It is predictable that, under actual technology standards, nuclear energy is playing and will go on playing an important role in the world electricity generation structure for years to come.

1.1 Generation IV

The **G**eneration IV **I**nternational **F**orum (GIF) was established in 2000 and obtained its formal charter in 2001. Six new reactor concepts were proposed in the following years to be considered as a technology road map for future nuclear energy system. The Gen-IV reactor types are expected to fulfill the goals of sustainability, economics, safety and reliability, as well as, proliferation resistance and physical protection. [gen14]

Of the six Gen-IV nuclear reactor types, four designs are fast neutron reactors: (**G**as-cooled **F**ast **R**eactor (GFR), **S**odium-cooled **F**ast **R**eactor (SFR), **M**olten **S**alt **R**eactor (MSR) and **L**ead-cooled **F**ast **R**eactor (LFR)) and three designs are thermal neutron reactors (**V**ery **H**igh **T**emperature **R**eactor (VHTR), **S**uper **C**ritical **W**ater **R**eactor (SCWR) and **M**olten **S**alt **R**eactor (MSR)) [gen02, pp.20], where the MSR is operated with thermal, epithermal or fast neutrons. Sustainability is an important characteristic of all these reactor types, since their main tasks may not only be electricity generation, but also the substantial reduction of the amount minor actinides contained in the spent fuel produced by the older and newer thermal reactors [gen02, pp.19]. Breeding of nuclear fuel from the large reserves of Th-232 and U-238 will also be a primary use of these reactors, thus extending the availability

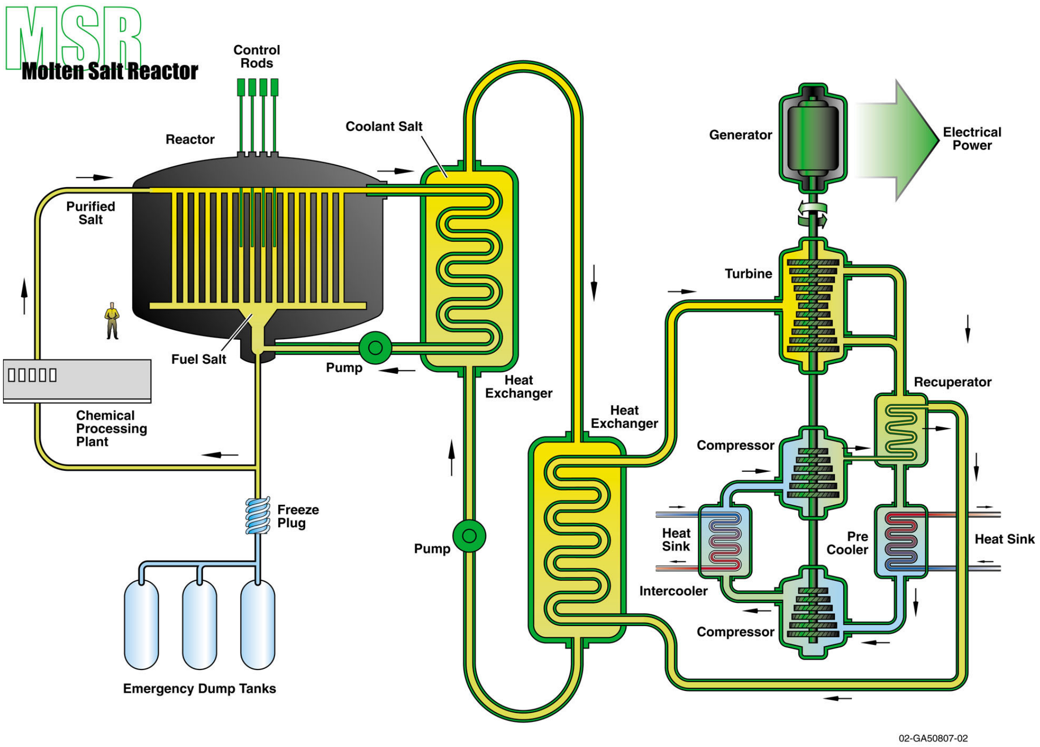
MSR
Molten Salt Reactor
Control Rods
Reactor
Coolant Salt
Purified Salt
Fuel Salt
Pump
Chemical Processing Plant
Freeze Plug
Emergency Dump Tanks
Heat Exchanger
Pump
Heat Exchanger
Generator
Electrical Power
Turbine
Recuperator
Compressor
Heat Sink
Pre Cooler
Heat Sink
Intercooler
Compressor
02-GA50807-02

Figure 1.2: Molten Salt Reactor in Gen IV [gen02, pp.39]

of nuclear fuel for many centuries. These two last goals are specially important for all the fast and epithermal reactor types. Of these reactors, the MSR can be considered as a ”revolutionary” type as it abandons conventional solid fuel desing based on fuel pellets, rods and assemblies, and makes the core a flowing molten mixture of Uranium, Plutonium or Thorium salts.

The importance of this feature is self-evident when the details and consequences of the Three Mile Island nuclear accident [nrc13] in 1979 and of the Fukushima nuclear accident [Kuc11] in 2011 are considered. Both of them suffered massive fuel rod damage and core melting caused by an uncontrollable temperature increase. The fuel pellets melted destroying the rod clads and released to the coolant a large amount of highly radioactive fission products. A considerable amount of them was then released to the environment in the case of Fukushima reactors, and in both cases seriously contaminated the reactor building.

In the MSR using liquid molten salts, the fuel is already molten and, therefore, the destruction of the fuel and melting of the core is not contemplated as an accident, while the reactor design takes already into consideration the protection against the released of any radioactive product outside the confined flowing paths of the molten core. The MSR has also a temperature-dependent passive safety system, which precludes large uncontrolled increases of reactor power and the molten core can be securely drained to holding tanks by gravity, which is clearly demonstrated in Fig. 1.2. In addition to this unique passive-safety feature the MSR provides many other benefits compared to more conventional reactor types [LeB10a] [Els13]. Thus, the MSR can fulfill the goals set by the Gen-IV Forum regarding the priorities of nuclear reactor designs [moi15]:

- to reduce weapons usable material in storage,
- to reduce need for high level waste repository space,
- to increase the proliferation resistance of nuclear energy,
- to make beneficial used of spent fuel from LWRs,
- to increase the fuel resource utilization,
- to extend the limit and range of non-carbon based technology for electricity and hydrogen production comparable with other alternatives economically.

From this unique feature start this work discusses the history and the nowadays of the MSR, and presents a preliminary analysis of one of the new variants of the MSR.

1.2 Objective and Outline

This thesis deals with the dual fluid reactor (DFR) concept and aims to analyzing its features under different circumstances. With this purpose, the steady-state characteristics of the reactor, the depletion of the fuel salt, and the dynamics of the reactor are investigated.

The thesis consists of five parts including 14 chapters. Part I focuses on the introductory facts, of which the first chapter is an introduction to the current general situation of nuclear energy. This chapter is followed by a brief history of the MSR. After that the basic description and parameters of the DFR concept are introduced in Chapter 3. The methods and codes used for calculations are presented in Chapter 4. These chapters provide the basic background and supplemental information to the thesis so that the calculations and analyses in subsequent chapters can be better understood.

Neutron and reactor physics for the DFR are presented in Part II, in which a model used for the criticality calculation is established and introduced in Chapter 5. With this model, a series of calculations to obtain important reactor parameters are carried out, including k_{eff}, delayed neutron information, neutron spectrum, etc. Results from different codes and code versions are produced. Sensitivity analysis for three important DFR design parameters, namely the nuclide composition, the geometry and the temperature conclude the analysis in this part.

In the Part III the depletion behavior of the DFR concept is examined. Initially burn-up related variables are studied so that a basis for subsequent burn-up calculations regarding computation time, memory usage and precision of the results can be established. Based on these results the depletion without and with online processing is calculated. The results are compared between simplified scenarios.

Thanks to the understanding of the DFR concept in gained the previous chapters, a series of thermal-hydraulic analysis are performed in the Part IV. The analysis makes use of a zero-dimensional model with point kinetics of the reactor core, one-dimensional coupled model with heat transfer, two-dimensional coupled model with fluid dynamics.

Finally, the conclusion chapter summarizes the most important results and conclusions are provided. An outlook for future research completes the content of the thesis.

Chapter 2

A Brief History of the MSR

2.1 Early stage

The molten salt reactor has gotten increased interest in the last few years, especially thanks to the inclusion of this concept with other advanced nuclear power system together in the Gen-IV forum, which it has expatiated in the last chapter. However the idea, the concept and even the design is never new in the scientific community.

The earliest investigation of molten salt reactors can be traced back to the late 1940's in a project aimed to develop a nuclear powered airplane in the United States. In the end this project did not result in the team developing an actual nuclear powered bomber, but the accumulated knowledge and experience produced an energy generation system for civil utilization. Due to several advantages identified for a liquid fuel, the experiments on molten salt fuels began in 1947 and became the "Aircraft Nuclear Propulsion Program" or "**A**ir **R**eactor **E**xperiment"(ARE) in the **O**ak **R**idge **N**ational **L**aboratory (ORNL). A small reactor (Fig. 2.1) was subsequently built and, in 1954, was successfully operated for 9 days at a steady-state outlet temperature of $1133K$, with a power output of $2.5MW_{th}$. The salt used at that time was the mixture of NaF-ZrF_4 as the carrier salt and the highly enriched ^{235}U. The most astonishing find was that the reactor coul run without mechanical or chemical problems, and the reactor was even self-regulating [BCM+57, pp.841-pp.853].

Based on the studies on the diverse features of the molten salt reactor, MacPherson's group at ORNL proposed two types of graphite-moderated reactors: single-fluid reactors in which the fuel salt contains both thorium and uranium, and two-fluid reactors (Fig. 2.2 left) in which the fertile salt containing thorium and fissile salt containing uranium are separated. It has to be mentioned that at this time the "two-fluid" concept was limited to the "two salts", as demonstrated in the figure: the blanket salt containing ThF_4 flows outside of the fuel salt with a Th-^{233}U mixture and, therefore, this kind of reactor can be operated as a breeder. The main superiority of a two-fluid system is the enormously simplified fuel processing with the method known as "vacuum distillation" [Sco66].

Later on in the 1960s another design of the two-fluid system [Rob65] appeared, as

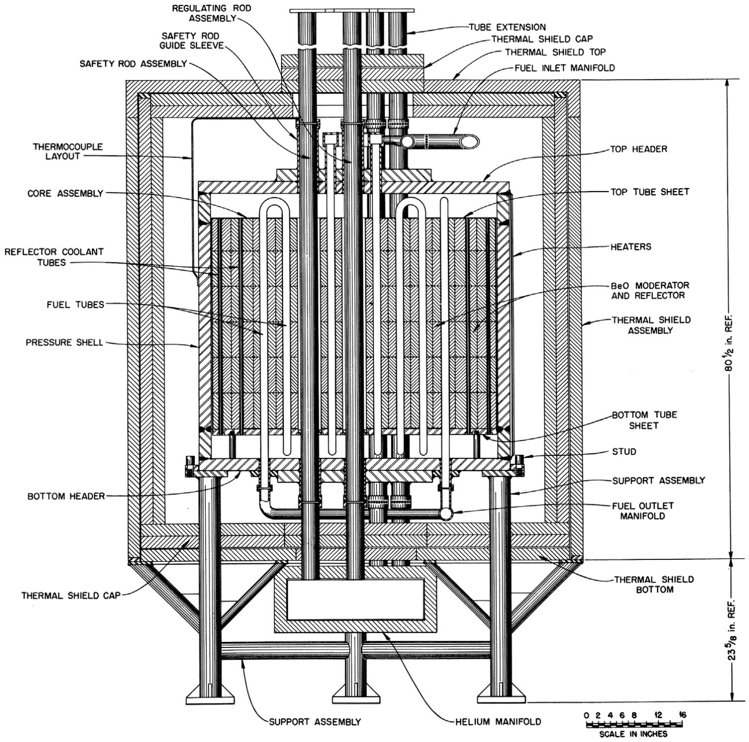
REGULATING ROD ASSEMBLY
SAFETY ROD GUIDE SLEEVE
SAFETY ROD ASSEMBLY
TUBE EXTENSION
THERMAL SHIELD CAP
THERMAL SHIELD TOP
FUEL INLET MANIFOLD
THERMOCOUPLE LAYOUT
CORE ASSEMBLY
REFLECTOR COOLANT TUBES
FUEL TUBES
PRESSURE SHELL
TOP HEADER
TOP TUBE SHEET
HEATERS
BeO MODERATOR AND REFLECTOR
THERMAL SHIELD ASSEMBLY
80 1/2 in. REF.
BOTTOM TUBE SHEET
STUD
SUPPORT ASSEMBLY
FUEL OUTLET MANIFOLD
BOTTOM HEADER
THERMAL SHIELD CAP
THERMAL SHIELD BOTTOM
23 5/8 in. REF.
SUPPORT ASSEMBLY
HELIUM MANIFOLD
0 2 4 6 8 12 16
SCALE IN INCHES

Figure 2.1: System structure of ARE [BCM+57]

demonstrated on the right side of Fig. 2.2. The structure of the reactor has introduced shell-pipes, by which hundreds of graphite fuel tubes separate the fuel salt and the blanket salt. This design improved the heat transfer between the fuel salt and the blanket salt, which also served as the coolant in the primary loop. However the large number of tubes also increased the possibility of cracking in the tubes caused by neutron radiation damage. Under these conditions, the replacement of the core or the vessel as a consequence of the complexity of the structure led the project to a standstill until late 1960s.

At the same time, since many features of a civilian reactor would vary from those of the ARE, a new "**M**olten-**S**alt **R**eactor **E**xperiments" (MSRE) project was then launched in 1960. A single-fluid reactor with graphite moderator was finally selected for the civil version of the MSR, but the fuel salt did not contain thorium and, thus, it was similar to the fertile fuel of the two-fluid reactor.

The MSRE with $8MW_{th}$ began in 1962 and the reactor was operated at full power from 1966 to 1968 as the first phase. The results were satisfactory, despite the problems identified with corrosion and the chemical stability of the fuel. In a second phase of the project, numerous additional investigations were carried out on the basic chemistry of molten fluoride salts and even on the breeding features of the two-fluid systems. In this second phase, from 1968, it became the first reactor to operate on ^{233}U .

After the abandonment of the two-fluid molten salt breeder reactor concept at the

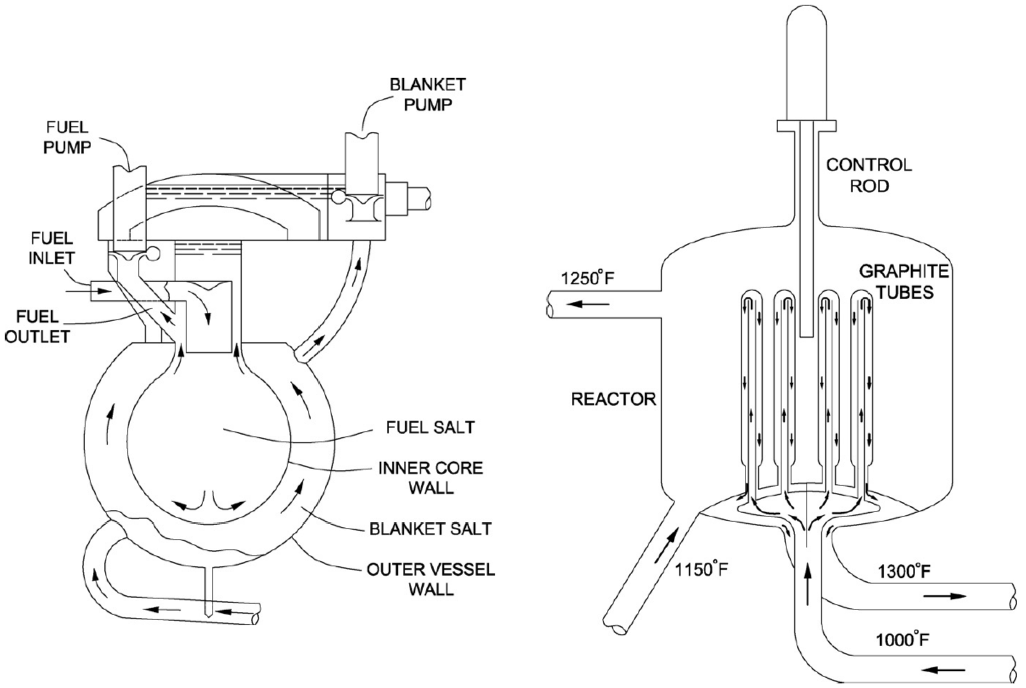

Figure 2.2: Flow diagram of two fluids molten salt reactor concepts (left: 1950s, right: 1960s) [LeB10b, Rob65]

end of 1960s, the final design in the “Golden Era” of the molten salt reactor was proposed as the “**M**olten-**S**alt **B**reeder **R**eactor” (MSBR) [Rob65], which maintained its basic design characteristics for decades and now appears also as one of the Gen-IV reactor concepts. The MSBR is designed with an electrical power of $1000MW_e$ with proposals from M. Taube et al. for a molten plutonium chloride fast breeder reactor cooled by molten uranium chloride [TL74, pp.277-pp.281], for example.

The MSBR program was finally terminated by the Atomic Energy Commission, for mainly political rather than technical reasons, at the time in the early 1970s. At the same time a molten salt reactor program in Britain, which was based on a $2.5GW_e$ “**M**olten **S**alt **F**ast **R**eactor” (MSFR) [mar14, SSA+74, MS76] concept using a plutonium-chloride mixture as the fuel salt and Helium gas as the coolant, developed by **A**tomic **E**nergy **R**esearch **E**stablishment (AERE) from 1964, ended in 1974 due to the lack of founding.

The research and studies about the molten salt reactor concepts were driven into a state of stagnation, with little progresses made by few researchers over the world [For06, Fur90, FAE+08, Gea92, Gea97]. During this period the researchers in the US brought about a new conceptual design of a “**D**enatured **M**olten-**S**alt **R**eactor” (DMSR) [EGB+80] with Once-Through Fueling and discussed the possibility of using denatured ^{235}U as the fuel salt. In Russia a molten-salt reactor program [Nov94] was started in the late 1970s concluding various theoretical and experimental investigations on the topic and verifying the feasibility of the MSRs, and was finally terminated in the wake of the Chernobyl Nuclear Accident in 1986.

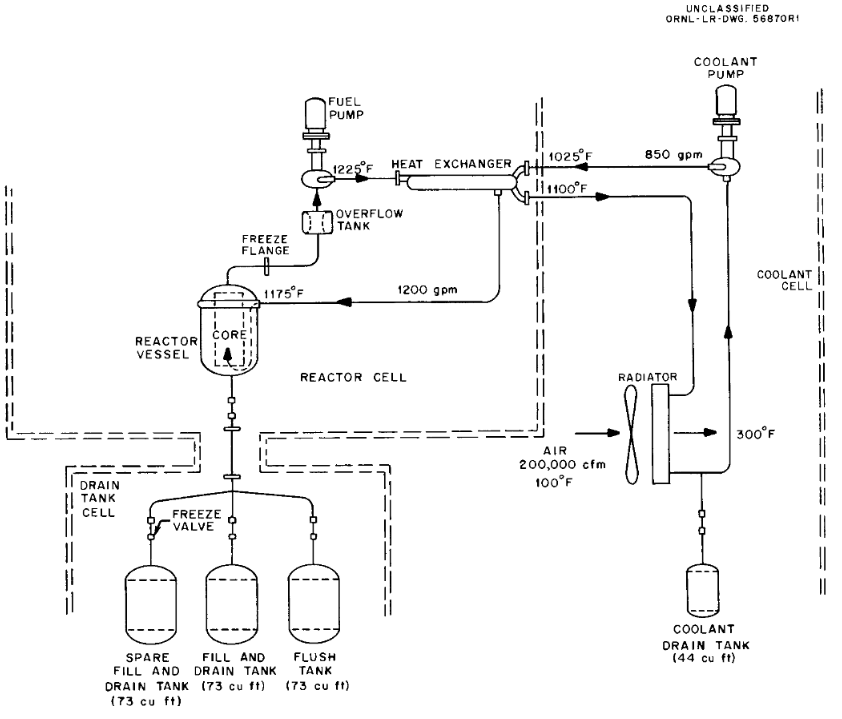
UNCLASSIFIED
ORNL-LR-DWG. 56870R1
COOLANT PUMP
FUEL PUMP
1225°F
HEAT EXCHANGER
1025°F
850 gpm
1100°F
OVERFLOW TANK
FREEZE FLANGE
1175°F
1200 gpm
COOLANT CELL
REACTOR VESSEL
CORE
REACTOR CELL
RADIATOR
AIR
200,000 cfm
100°F
300°F
DRAIN TANK CELL
FREEZE VALVE
SPARE FILL AND DRAIN TANK (73 cu ft)
FILL AND DRAIN TANK (73 cu ft)
FLUSH TANK (73 cu ft)
COOLANT DRAIN TANK (44 cu ft)

Figure 2.3: Flow diagram of MSRE [KB66]

A so called “resurgence of interest” [LeB10b] highlighted by the selection of this concept as one of the Gen-IV reactor types has once again raised interest in MSR research worldwide.

2.2 Renaissance

The reactor concepts proposed in the Gen-IV (Sec. 1.1) fostered other nuclear reactor types by pointing out new guidelines or road-maps for their developments and ultimate deployments, and helped significantly to bring back the molten salt reactor concept. With this call researchers swarmed around the concept of the molten salt reactors and found the forgotten reactor designs and ideas in the archives covered with dust for decades. Because of the high interest in its advantages and flexibility, the study of molten salt reactors is currently very active, and some representative examples are introduced here.

2.2.1 Europe

The **M**olten **S**alt **F**ast **R**eactor (MSFR, see Fig. 2.5 (a) concept is a $3GW_{th}$ fast-spectrum reactor using the Thorium fuel cycle. The concept was proposed [NH05, MHea06, MMLea09, For07, MLH08, MLHea09] based on the investigations of the MSBR at ORNL. The fuel salt used by the MSFR can be of various compositions according to the characteristics of its online fuel reprocessing unit. Compared to

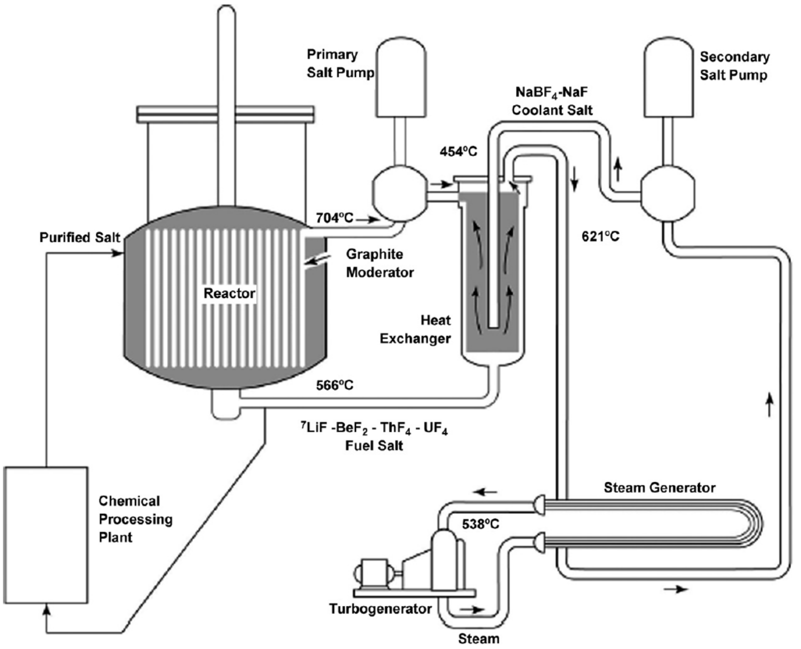
Primary Salt Pump
Secondary Salt Pump
NaBF$_4$-NaF Coolant Salt
454°C
704°C
Purified Salt
Graphite Moderator
Reactor
621°C
Heat Exchanger
566°C
^{7}LiF -BeF$_2$ - ThF$_4$ - UF$_4$ Fuel Salt
Chemical Processing Plant
Steam Generator
538°C
Turbogenerator
Steam

Figure 2.4: Flow diagram of MSBR [Ros72]

previous MSR designs the MSFR abandons the graphite moderator so that a fast neutron spectrum can be utilized for breeding.

The fuel salt flows inside of a central cavity, where the nuclear fission reactions take place. The compact design of the heat exchangers as well as other components ensures a small reactor size and a high efficiency of the heat transfer. Due to its unique potential in several fields, such as excellent safety neutronic coefficients, smaller fission inventories and others, the MSFR has been recognized as a long term alternative to the conventional solid fuel reactors and, therefore, has been officially evaluated by the Gen-IV as worthy of being further investigated since 2008 [BMLR$^+$13].

Based on the research performed in Russia in the 1970s, the intermediate/fast spectrum reactor design MOSART (**Mo**lten **S**alt **A**ctinide **R**ecycler and **T**ransmuter, see Fig. 2.5(b) [IF12] was given most of the resources in the last decade. From its name it is expected to be capable of fissioning the transuranium elements (TRU) from LWR spent fuel. Like the MSFR, the MOSART with a thermal power of $2400MW$ has a homogeneous cylindrical core in its center, but with the important difference that the MOSART still contains graphite blocks for the reflector [Iea05].

2.2.2 North America

After the research pioneered by the ORNL and its decades-long stagnation, the new concepts must always go straight back to the original ORNL investigations of the 60s and 70s. Thus, from the very basic definitions of the MSR, the molten salt can be used either as the fuel, which leads to the salt-fueled reactors, or as the coolant, which leads to the salt-cooled reactors.

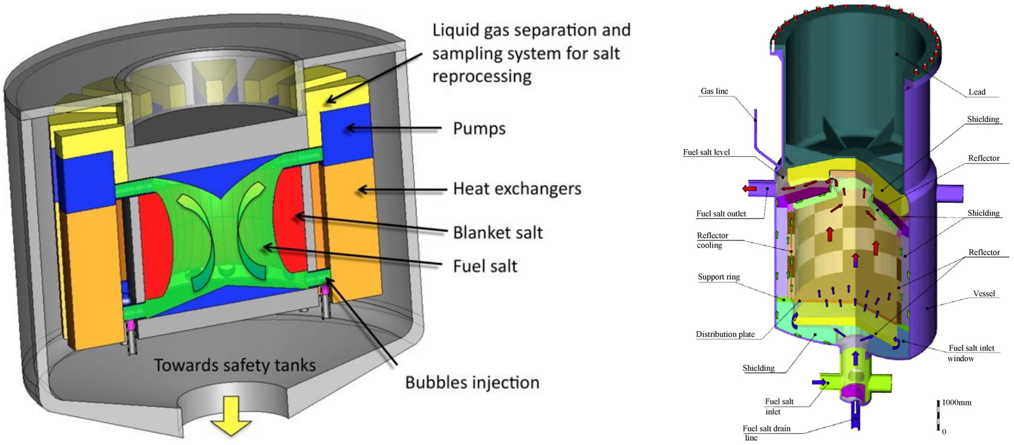
Liquid gas separation and sampling system for salt reprocessing
Pumps
Heat exchangers
Blanket salt
Fuel salt
Towards safety tanks
Bubbles injection
Gas line
Fuel salt level
Fuel salt outlet
Reflector cooling
Support ring
Distribution plate
Shielding
Fuel salt inlet
Fuel salt drain line
Lead
Shielding
Reflector
Shielding
Reflector
Vessel
Fuel salt inlet window
1000mm
0

(a MSFR [BMLR$^+$13, pp.5]

(b MOSART [ZQS09, pp.2780]

Figure 2.5: MSFR and MOSART concepts

In the following, the Canadian IMSR (**I**ntegral **M**olten **S**alt **R**eactor, see Fig. 2.6 (a) concept is a salt-fueled reactor while the American FHR (**F**luoride Salt-Cooled **H**igh-Temperature **R**eactor, see Fig. 2.6 (b), which absorbs the concept of SmAHTR(**S**mall **M**odular **A**dvanced **H**igh-**T**emperature **R**eactor, see Fig. 2.6 (c), is a salt-cooled reactor.

By combining the advantages from the molten salt reactor concept and the small modular reactor concept, the IMSR was born in 2013 [LI14] but its design is based on the DMSR [EGB$^+$80] design mentioned in the last section and the small modular reactor, SmAHTR [GGH$^+$10], both developed at the ORNL. Because of its relation to the DMSR, it is expected to utilize low-enriched uranium (LEU) with diverse options of carrier salts. The single control rod insertion is designed in the primary loop with a passive buoyancy driven system and in the secondary loop a passive temperature-induced negative reactivity injection is used. Thanks to an integrated primary heat exchanger, a replaceable low-maintenance core unit with high power density and a 7-year old operating cycle, the IMSR can be deployed in three different sizes to satisfy various electricity demands: IMSR80 for $32.5MW_e$, IMSR300 for $141MW_e$ and IMSR600 for $291MW_e$. By the early 2020s the IMSR is supposed to be licensed and ready for commercial construction.

The concept of the SmAHTR started in 2004 [IFO$^+$04] and inherit directly from AHTR (**A**dvanced **H**igh-**T**emperature **R**eactor) [For04]. As a thermal-spectrum nuclear reactor with use of liquid-fluoride-salt coolants. The tri-isotropic (TRISO)-coated particle fuel was selected for the fuel in the original design of the SmAHTR design [Gre10a], which was a quite unique combination at the time. However, after 3 months the fuel was changed to cylindrical annular compact fuel assemblies with three variations under consideration [Gre10b]. Graphite was chosen as moderator, similar to other gas-cooled high temperature reactors. The thermal output is expected to reach $125MW_{th}$. Like the IMSR, the main advantages of the SmAHTR are its small size and its flexible deployment. The FHR inherits the reactor design, the TRISO fuel type, and is rescaled to $100MW_{th}$. From 2004 to 2016 plenty of

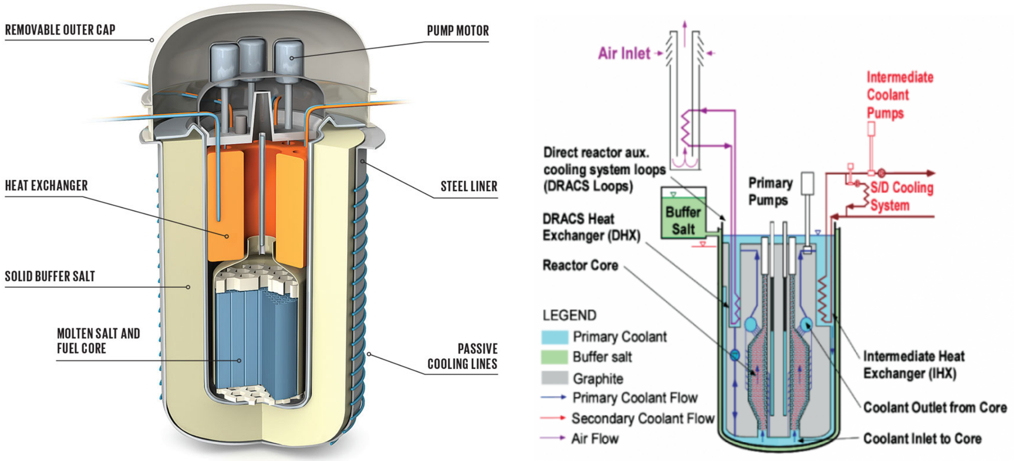
REMOVABLE OUTER CAP
PUMP MOTOR
HEAT EXCHANGER
STEEL LINER
SOLID BUFFER SALT
MOLTEN SALT AND FUEL CORE
PASSIVE COOLING LINES
Air Inlet
Intermediate Coolant Pumps
Direct reactor aux. cooling system loops (DRACS Loops)
Primary Pumps
S/D Cooling System
Buffer Salt
DRACS Heat Exchanger (DHX)
Reactor Core
LEGEND
Primary Coolant
Buffer salt
Graphite
Primary Coolant Flow
Secondary Coolant Flow
Air Flow
Intermediate Heat Exchanger (IHX)
Coolant Outlet from Core
Coolant Inlet to Core

(a IMSR [IMS]

(d FHR [FHRb]

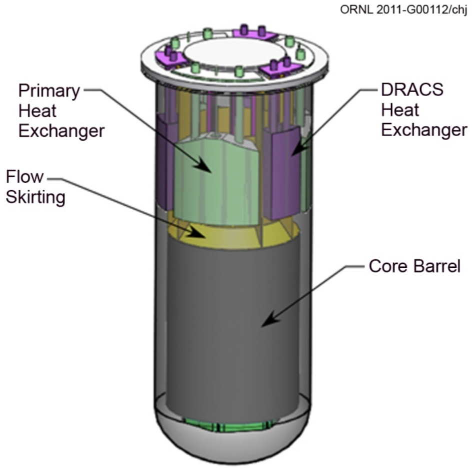
ORNL 2011-G00112/chj
Primary Heat Exchanger
DRACS Heat Exchanger
Flow Skirting
Core Barrel

(c SmAHTR [GGH+10, pp.XV]

Figure 2.6: IMSR, FHR and SmAHTR concepts

efforts have been directed to this subject, which can be found in the following references, especially some works have summarized the diverse research done on the FHR [SAB+14]. A list of the original ORNL reports about the development of the FHR can also be found in [FHRa].

2.2.3 Asia

The molten salt reactor concept proposed in China dates from 2011. Since the main purpose of the development of the nuclear energy generation system in China is to satisfy an enormous expected demand of the electricity, all established reactor types, and amongst them the molten salt reactor, are being investigated.

The interest in the molten salt reactor was raised by the Chinese Academy of Science in order to find a replacement for the current uranium-based nuclear reactors due to

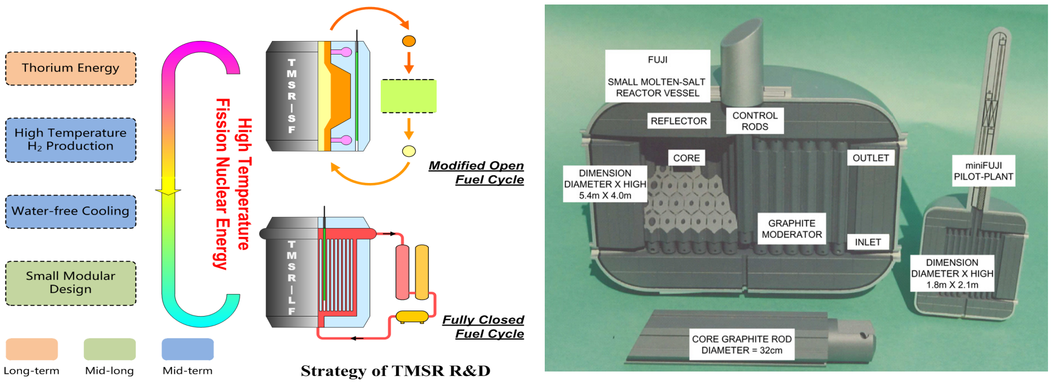
Thorium Energy
High Temperature H_2 Production
Water-free Cooling
Small Modular Design
Long-term
Mid-long
Mid-term
High Temperature Fission Nuclear Energy
TMSR-SF
Modified Open Fuel Cycle
TMSR-LF
Fully Closed Fuel Cycle
Strategy of TMSR R&D
FUJI SMALL MOLTEN-SALT REACTOR VESSEL
REFLECTOR
CONTROL RODS
CORE
DIMENSION DIAMETER X HIGH 5.4m X 4.0m
OUTLET
GRAPHITE MODERATOR
INLET
miniFUJI PILOT-PLANT
DIMENSION DIAMETER X HIGH 1.8m X 2.1m
CORE GRAPHITE ROD DIAMETER = 32cm

(a TMSR [Xu15]

(b FUJI [FAE+08, pp.1837]

Figure 2.7: TMSR and FUJI concepts

concerns about the shortage of the economically fabricated uranium based fuel, and the realization of the sustainable development of the nuclear energy by introducing breeder reactors. The production of the hydrogen as an important future energy carriers utilization is also being considered in the context of the MSR because of its very large outlet temperature. Therefore the "**T**horium **M**olten **S**alt **R**eactor Nuclear Energy System (TMSR, see Fig. 2.7 (a)" [JXD12] has been proposed. The detailed design of the TMSR system is, however, still unknown at the time of this thesis.

The project has been upgraded to one of the major national energy application-technology R&D projects of the Chinese Energy Administration and been further split into two sub-projects, namely the TMSR-LF and the TMSR-SF with solid and liquid fuel, respectively. The test reactors of 2MW_e to these two sub-projects are believed to start construction in 2017 and the 10MW_e version will be start construction in 2025 [TMS14].

In Asia Japan has also conducted the research and development of the molten salt reactor over 30 years after ORNL has stopped its project in 1970s. In this period Furukawa and his group started the conceptual design of the FUJI reactor series in the late 1980s based on their former project "**Thori**um **M**olten **S**alt **N**uclear **E**nergy **S**ynergetic **S**ystem (THORIMS-NES)" and on the ORNL achievements in the late 1980s.

The FUJI reactor (see Fig. 2.7(b) is not only one reactor, but a conceptual series of reactors belonging to THORIMS-NES, a expected global Thorium breeding fuel-cycle system, that the reactor can be flexible in the size and in the power from 150MW_e (for FUJI-II [FMO+87]) to 200MW_e (for FUJI-U3 [MYY05]) to satisfy different local demands. The design of the FUJI reactor is based on the design of the MSBR, where the fuel salt flows through the duct formed by the graphite block inside of a simple tank. Its graphite block however doesn't need to be changed during its lifetime like MSBR for its lower neutron flux and a higher graphite volume ratio, which is almost 90%. The analysis for the FUJI has proven the conversion ratio is very high [FAE+08, pp.1836], and because of the Fukushima nuclear accident, the safety issue is proven secured that the severe accidents are essentially impossible [VHP+12].

The complete FUJI project is expected to have three stages. Firstly the pilot-plant will be built as the “miniFUJI” with a power output from 7 to $10 MW_e$. After that a larger version called “FUJI-Pu” will be built as the small power reactor in the commercial power plants with a power output from 100 to $300 MW_e$. Finally the AMSB (**A**ccelerator **M**olten-**S**alt **R**eactor) will be developed as a fissile isotope producer to provide fuel to other project reactors until the final stage the THORIMS-NES network is completed [FAE+08, pp.1833].

Chapter 3

The Dual Fluid Reactor

3.1 Concept Overview

The design of the **D**ual **F**luid **R**eactor (DFR) combines the molten salt reactor concept with that of a liquid-metal cooled reactor (SFR, LFR [Fan07]). In comparison to the molten salt reactor concept (MSR [Hro06, pp.270-286]) of the Gen-IV [gen02] reactors the molten fuel salt of the DFR is cooled with a separated liquid lead loop, which, in principle, allows for higher power densities and better breeding performance. It is also different from the MacPherson's or the Robertson's two-fluid reactor designs, which separate the salt into fissile (fuel salt) and fertile (blanket salt) separated flows. The DFR and Taube's concept [TL74] both use a chloride based molten fuel salt in order to harden the neutron spectrum. Yet, the DFR does not combine heat removal and breeding into one single circuit, but separates the two functions into two independent circuits. Using lead as the primary means of heat removal has the advantage that the fuel and breeding inventory can be kept to a minimum.

3.2 System Description

The DFR is a $3000 MW_{th}$ reactor working on the fast neutron spectrum and based on the diverse fuel cycles. The liquid fuel processing is an important part in the DFR energy system, where a small amount of fuel is processed for the fission product removal, while the other fuel flows back with the processed fuel together back to the reactor core. Because of this real-time fuel online-processing feature and flexible fuel processing schedule, the DFR can be operated with a wide variety of fuel compositions.

In the DFR concept the nuclear fission reactions take place within the numerous fuel salt tubes, through which the molten fuel salts flow with a sufficient amount of fission material and, therefore, a critical mass in the core region is attained. The heat generated by the reactions is transferred to the coolant lead, which, thanks to its large thermal conductivity, removes the heat very rapidly and efficiently. Also the

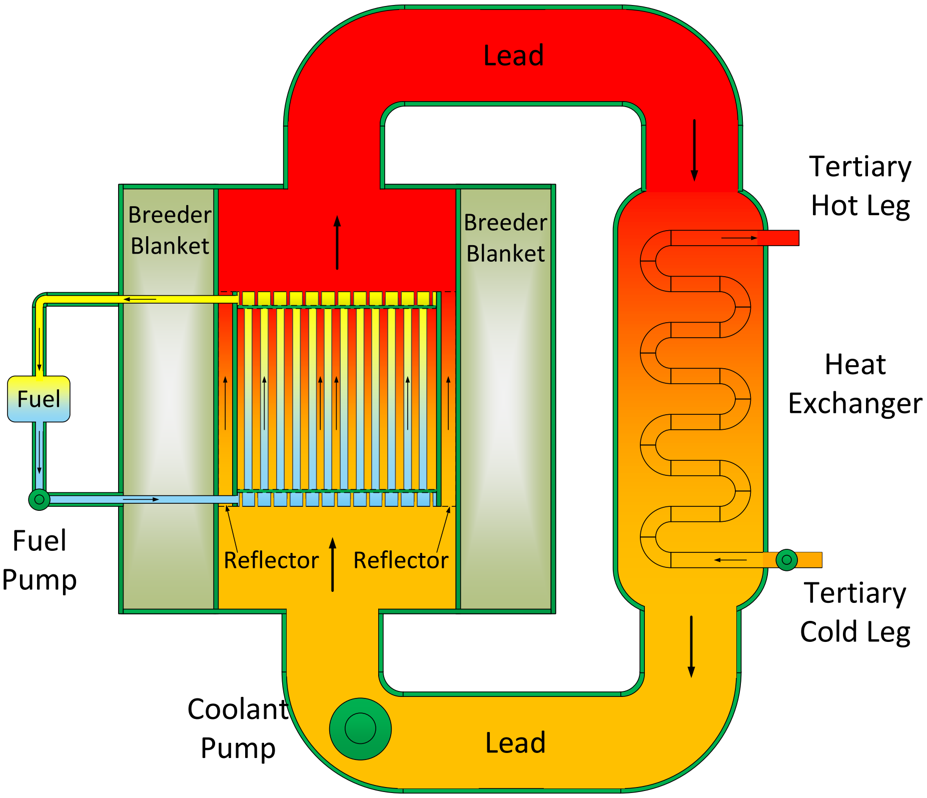

Figure 3.1: Working principal of the DFR

coolant lead serves as a reflector, which hardens the neutron spectrum and prevents a large quantity of neutrons from escaping.

For the purpose of initiating the thesis work and the analysis of the reactor, some fundamental drawings of the reactor are developed from a preliminary conceptual design. One of the possible configurations is depicted in Fig. 3.1.

The working principle of the fluids related to the nuclear reactor during the normal operation consists of two loops. In the primary loop, the fuel salt flows from across the outer surface of the core region through several cold legs meeting in the inlet plenum (Sec. 3.2.3). In the inlet plenum the fuel salt is distributed in the fuel channels of the core region (Sec. 3.2.1) opening at the top of the inlet plenum. Through the fuel tubes the fuel salt flows upwards reaching the top of the core region into the outlet plenum (Sec. 3.2.3). Again the fuel salt is re-distributed again flowing into the several hot legs. Through the primary pipes the fuel salt can be sent to processing units or to eventual storage tanks is needed. When the processed fuel salt satisfies the composition requirements, it will be pumped again into the cold legs to continue its way to the core region.

The loop containing coolant, considered as the secondary loop, flows in another separate circuit. The cold coolant enters the bottom of the reactor through the inlet legs of the coolant. The stream is distributed through the coolant tubes located in the inlet plenum and flow through the core region. The liquid lead flows upwards between the fuel tube arrays and takes the fission energy within it. At the top of the core region, the coolant is distributed once more and flows through the coolant tubes into the outlet plenum. Finally, the coolant reaches the coolant outlet nozzles and is directed to the heat exchange equipment, e.g. steam generator, cooling down in the process by transferring energy to the tertiary working medium. The cold coolant flows then back through the cold leg into the core region.

The circulation times of the fuel salt and the coolant depend mainly on the length of the external pipelines to the online-processing unit or to the heat exchanger. In addition to the mentioned components, the other important systems, which have a significant impact on the reactor performance, are discussed in the following pages.

3.2.1 Core

The core of the DFR is an active region inside cylindrical container located in the center of the reactor. It contains almost all the fission materials in the fuel salt tubes. The core is mainly composed with more than 13000 fuel salt tubes, which connect the outlet plenum over the top of the core and the inlet plenum under the bottom of the core.

3.2.2 Fuel Salt

The final choice of fuel composition is based on the results of parametric studies including neutronic and physical reactor features. Two basic fuel salt compositions are based on chloride or fluoride salts with several possible fissile and fissionable nuclides. They maintain the DFR reactor criticality during operation and ensure a neutron flux spectrum in the fast neutron region. In the design of the DFR a chloride U-Pu mixture is adopted for the fuel salt. The physico-chemical properties of the fuel are introduced later in Sec. 3.3.4 and the most appropriate composition is determined in Sec. 5.2.

The fuel salt flows from the inlet pipe and is distributed in the inlet plenum. It enters into the fuel salt tubes in the core region with the fuel salt inlet temperature and leaves the core into the outlet plenum with a higher outlet temperature. Fissions as well as other kinds of nuclear reactions take place in the core releasing energy and yielding fission products. They must be removed from the fuel salt in order to maintain the criticality of the reactor and the physico-chemical properties of the fuel salt itself in the processing units outside the reactor.

The control of the fission reaction in fuel salt is basically realized by the large negative temperature feedback of the fuel salt under operation conditions. The drain of the core in a specially prepared tank under the reactor is also used for emergency control of the reactivity. The temperature of the fuel salt depends also strongly on the pumpÂťs power and on the cooling capability of the heat exchanger. This topic, however, lays beyond the scope of this thesis. Further control measurements of the DFR energy system are left as a topic of future research.

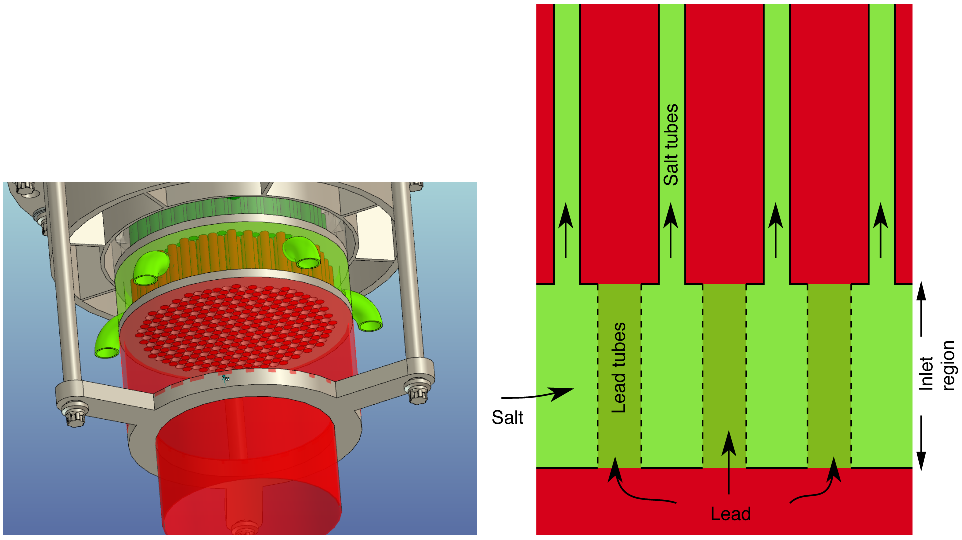

Figure 3.2: Demonstration of the inlet plenum [HRW+15]

3.2.3 In-/Outlet Plenums

The in-/outlet plena are regions adjoin to both axial ends of the core. The inlet plenum (Fig. 3.2) is under the bottom of the core and the outlet plenum is over the top of it. The in-/outlet plena are so constructed that the tubes in these two regions are arranged interlaced compared to the tubes in the core. The axis of a tube in the two plena is located on the middle point of a triangular area constructed by the projections of the centers of three neighboring fuel tubes. In this way the fuel salt and the coolant both can be equally distributed.

The fuel salt flows into the inlet plenum through entrances equally located on the outer cylindrical boundary of the reactor into the gap between hexagonally arranged coolant tubes containing the liquid lead. On a plate with holes between the inlet plenum and the core, the fuel salt flows through these holes into the fuel salt tubes of the core. In contrast the coolant lead flows inside of the tubes in the inlet plenum, and through holes on the interval plate into the gap between the fuel salt tubes in the core region. This flow pattern is reversed in the outlet plenum [HRW+15].

3.2.4 Reflector

The reflector is an annular, columnar-form container sharing the same axis with the core which encloses the core. The reflector of the DFR uses liquid lead as material, which serves not only as reflector, but also as the shield of the radiation. The reflector and the coolant have the same source of liquid lead in order to simplify the overall structure and to make sure that all the important materials in the reactor are liquid. Inside of the reactor the separating wall between the coolant and the reflector is designed to enable a *material exchange* between these two fluids. In this manner the temperature of the reflector is expected to rise faster than with a normal, separated heat transfer process. The details of such an arrangement is out of the scope of this

Parameter	Value	Parameter	Value
L_{tube}	2.4	Reflector thickness	0.15
$d_{tube,inner}$	0.0145	$H_{in/outletplenum}$	0.2
$d_{tube,outer}$	0.019	Fission zone wall thickness	0.01
Fuel tube distance	0.003	Fission zone outer wall thickness	0.01
Pin pitch	0.022	Reactor outer wall thickness	0.04
d_{core}	3.0	$d_{reactor}$	5.5

Table 3.1: Geometry parameter of DFR (Unit: m)

thesis and will be not discussed further. A simplified model for this configuration is, nevertheless, simulated in Sec. 7.3.

3.2.5 Fertile Blanket

The fertile blanket is a larger annular, columnar-form container sharing the same axis with the core and encloses the reflector. This structure is not part of the standard structure of the reactor, but it can be adopted depending on the actual needs.

The breeder materials depend on the specific fuel salt option utilized. Thus, for the U-Pu fuel salt $^{238}\mathrm{U\,Cl_3}$ is used for the fertile material. The detailed composition will be introduced in Sec. 5.3.

3.3 Data Used for the Simulation

3.3.1 Geometric Data

The geometric data of the DFR is listed in the following Table 3.1. The term “tube” in the subscripts refers to the fuel salt tube in the core. The fuel tube distance means the distance between the *outer walls* of neighboring fuel tubes. The wall thicknesses are only assumed values needed to complete the model, but not obtained from detailed mechanical calculations. In a future refinement of the structural model of the reactor (not included in this thesis), such thicknesses will be established more accurately.

3.3.2 Structural Materials

Fuel tubes have direct contact to the fuel salt and are located in the center of the reactor. For these reasons the material of the fuel tube must meet the most strict criteria on several aspects: (i) the resistance against corrosion by the fuel salt and the corrosion caused by the cooling lead on the other side; (ii) extremely high does radiation effect due to high neutron flux; (iii) mechanical strength for the momentum impacts due to the large amount of circulating mass and the pressure. The fuel tubes have to withstand these effects for a long time while keeping their mechanical and

Isotope	Fe	C	^{55}Mn	^{31}P	S	Si	Ni	Mo
Weight%	97.150	0.250	1.500	0.035	0.035	0.030	0.500	0.500

Table 3.2: Proportions of nuclides in the structural material

$T_{in,f}$	$T_{mean,f}$	$T_{out,f}$	$T_{in,c}$	$T_{mean,c}$	$T_{out,c}$	$T_{mean,b}$	$T_{mean,s}$
1200	1300	1400	977	1088	1200	1050	1250

Table 3.3: Temperature parameter of DFR (Unit: K)

material stability during operation. Moreover, such a material has to be reasonably easy to manufacture industrially with an acceptable price.

In the DFR design the fuel tube material is a ceramic fabricated with SiC suitable for its low neutron capture cross section [HRW$^+$15]. Based on the current experimental data SiC is very resistant against molten lead caused corrosion at more than 1200K [PMT05]. Especially the chemically vapor-infiltrated SiC matrix (CVI SiC/SiC) is recommended as the primary alternative for the high temperature, high neutron flux environment expected in the fuel container structure among various industrially available forms of SiC. The thermal properties of SiC, however, can be vary much due to difference crystal structure and to the process of fabrication [Mun97], e.g. thermal conductivity in SiC is a non-anisotropic property depending strongly on material structure [KWF07]. In this thesis the default value of the thermal conductivity from the original design [HRW$^+$15] is used for general calculations. Nonetheless, the influence of some other values is also evaluated and compared with the default value.

Structural components of the reactor such as outer shells and walls are assumed to be made of SA 533 Gr. B nickel alloy steel with the compositions shown in Table 3.2 [HRW$^+$15]. Depending on the radiation and corrosion damage expected, other high-performance alloys are also possible alternatives, i.e. Hastelloy N [Kog72] or Hastelloy X, etc.

3.3.3 Temperatures

The desing temperatures are listed in Table 3.3. The subscripts “in” and “out” stand for inlet and outlet, “f” for fuel salt, “c” for coolant, “b” for breeder blanket and “s” for structure. The temperatures at the inlet and outlet mean averaged values on the surface. The temperatures with subscripts are considered from the middle point of the flow channel between inlet and outlet.

3.3.4 Physico-chemical Properties

The properties of the U-Pu fuel salt: the density ρ, the kinetic viscosity ν, the dynamic viscosity μ, the thermal conductivity λ and the heat capacity at constant pressure C_p are listed in the Table 3.4. Since there is no current research data for the fuel salt composition, the formula of the density is approximated based on the

	Formula	Value at T_{mean}	Validity Range (K)
$\rho(g/cm^3)$	14.493-7.943E-3×T	3.5316	[1219-1303]*
$\nu(m^2/s)$	μ/ρ	1.27E-7	
$\mu(Pa \cdot s)$		4.50E-4	
$k(W/(m \cdot K))$		2	
$C_p(J/(kg \cdot K))$		400	

Table 3.4: Physico-chemical properties used for the U-Pu fuel

density function proposed for UCl_3 by [Jan75, pp.896]:

$$\rho = 13.652 - 7.943 \times 10^{-3} \times T(g/cm^3)$$

by assuming a linear function through a reference point $\rho(1380) = 3.5g/cm^3$, the density formula for the fuel salt can be achieved. Furthermore T_{mean} of the U-Pu fuel salt is also set to 1380K. The validity range of the fuel density is take from the validity range of UCl_3 since the expression of the density is derived from that of UCl_3 [Jan75, pp.896].

For the lead coolant, the properties are listed in Table 3.5 based on the existed experimental values [Sob11]. The T_{mean} is set to $1200K$.

	Formula	Value at T_{mean}	Validity Range (K)
$\rho(g/cm^3)$	11.441-1.2795E-3×T	9.860	[600-2000]
$\nu(m^2/s)$	μ/ρ	1.32E-4	[600-1470]
$\mu(Pa \cdot s)$	4.55E-4×$e^{1069/T}$	0.0013	[600-1470]
$k(W/(m \cdot K))$	9.2+0.011×T	22.4	[600-1300]
$C_p(J/(kg \cdot K))$	176.2-4.923E-2×T+1.544E-5×T^2 -1.524E6×T^{-2}	138	[600-1500]

Table 3.5: Physico-chemical properties used for the coolant lead

Finally, the properties of the fuel tube wall with the material SiC are listed in Table 3.6 from the existed researches [NMH+97]. T_{mean} is set to $1250K$.

	Formula	Value at T_{mean}	Validity Range (K)
$\rho(g/cm^3)$		3.210	
$k(W/(m \cdot K))$	6.11E4/(T-115)	53.8	[100-2300]
$C_p(J/(kg \cdot K))$		690	

Table 3.6: Physico-chemical properties used for SiC

Chapter 4

Calculation Tools

4.1 Introduction

Since the DFR system is a relative new concept, diverse calculations and analyses need to be carried out to verify the validity of the system. Also, because of the originality of the work, the results between different codes have to be compared to make the conclusion reliable. For this purpose, based on the available resources and computer capabilities, two kinds of calculation tools have been selected for the work and for utilized various purpose. The first kind is the neutronic or reactor physics related codes, namely SCALE and SERPENT. They are both Monte-Carlo codes for neutron physics problems. The second kind consists of the general simulation tool SIMULINK®, the multi-physics package COMSOL®, and multi-physics and thermal-hydraulic software FLUENT®.

4.2 SCALE

SCALE (Standardized Computer Analyses for Licensing Evaluation) developed at Oak Ridge National Laboratory [Bow11] is a set of nuclear safety analysis codes. In this work the version SCALE 6.1.3 is used. The module KENO-VI, one of the components of SCALE, is a further improved version of a previous Monte-Carlo criticality program used in the SCALE system, which carries forward all the features in its ancestors and contains a more flexible geometry package. Its capability for both a continuous neutron energy mode and a multi-group approach enables the assessment of its criticality results with other codes [Oak11, pp.2018-pp.2548]. For the sensitivity analysis of the nuclides in the fuel composition during reactor operation, the module TSUNAMI has been used [Oak11, pp.4249-pp.4354]. Finally, the module TRITON is utilized for the burn-up calculations.

4.3 SERPENT

SERPENT is a 3D continuous-energy Monte-Carlo code specialized in reactor physics and burn-up calculations, which is currently developed by the VTT Technical Research Center of Finland since 2004 [Lep12]. In this thesis the calculations are carried out with two versions: 1.1.19 of SERPENT 1 and 2.1.23 of SERPENT 2.

4.4 SIMULINK

SIMULINK® is a common used module of the integrated calculation software Matlab®. This software provides different models and computational blocks for real-time comprehensive simulations of complex systems. Compare to the typical m-files used by Matlab for modelling and calculation purposes, SIMULINK is capable to deal with more sophisticated problems, such as the mathematical modelling of the DFR system.

For more accurate simulation results a Realtime® Desktop Kernel is linked to the model in order to provide real clock signals and ensure the timing of the model is the same as the one expected during actual reactor operations.

4.5 Fluent

Fluent® is a calculation module of the ANSYS® Workbench® which specializes in the fluid flow simulations, including laminar and turbulence conditions, heat transfer and chemical reactions. Fluent is used in this work to perform thermal-hydraulic calculation in 2D and 3D configurations. In oreder to model the turbulent flow of the desired fluids, user defined functions (UDF) are implemented for the velocity profile and the heat source distribution.

4.6 COMSOL

COMSOL® Multi-physics is a comprehensive physical calculation package. It was originally named FEMLAB®, a simulation module of MATLAB®. After further development, COMSOL is capable of carrying out diverse analyses based on multi-physics coupling. The “Heat Transfer” and “Turbulence Flow” modules are used in this work to perform thermal-hydraulic calculation in 2D and 3D geometries, similar to those done with Fluent, and the results of both codes are then compared for reliability check.

Part II

Neutronic Calculation

Chapter 5

Neutronic Modelling of the DFR

This chapter presents the neutronic analysis of the DFR reactor concept. The DFR simplified model developed for the calculations is introduced and used with SERPENT, SCALE and other codes.

The analysis of the reactor is carried out at the full core scale. The DFR reactor core contains a large amount of fuel salt tubes, in which fission occurs. In the analysis the fuel tubes are not distinguished. First, the state of the reactor under stationary conditions is investigated with the calculation of several important parameters, such as the effective neutron multiplication factor, the delayed neutron data, including the delayed neutron fraction and the delay constants, the generation time of the neutrons, the in-hour equation of the system, the neutron spectra, the reaction rate density for various reactions in the fuel salt and other materials, and the power distribution in the core. Different codes and versions of codes, as well as different nuclear data libraries are used for this purpose, so that a cross-comparison for consistency can be made.

The general information of the single fuel salt tube including reaction rates, power generation and neutron flux are approximately obtained by the average of the whole core results.

5.1 Geometry

According to the basic information of the DFR discussed in previous chapters, a computational model used for the neutronic analysis is developed in this section.

Generally, the DFR model consists of several concentric cylindrical zones, namely the fission zone, the reflector, and the breeder blanket. Figure 5.1 [WSM15] shows this arrangement from the center to the periphery of the core region, for one quarter of the DFR core taking advantage of its symmetry. Based on the result of a sensitivity calculation done with coolant tubes in the breeding blanket, this component is ignored in the calculations, because of its irrelevant effect on the stationary calculation of the DFR reactor. This sensitivity calculation can be found later in Sec. 7.

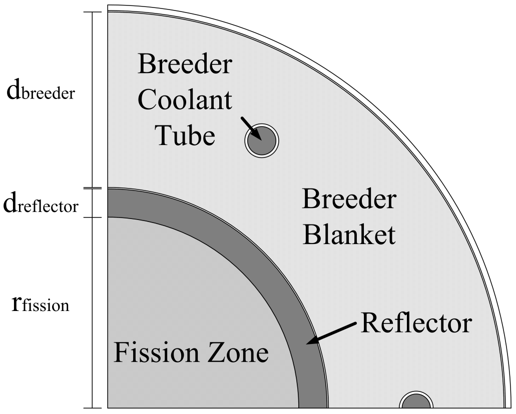
$d_{breeder}$
$d_{reflector}$
$r_{fission}$
Breeder Coolant Tube
Breeder Blanket
Reflector
Fission Zone

Figure 5.1: Horizontal section

The radius of the fission zone $r_{fission}$ is set to $135cm$, the thickness of the reflector $d_{reflector}$ is set to $20cm$, and the thickness of the breeder blanket $d_{breeder}$ is set to $125cm$. The breeder blanket's coolant tubes have a radius of $6cm$ for the outer surface of the tube wall and a radius of $5cm$ for the inner surface.

In the axial direction, the fission zone is located in the central region of the DFR core and its lower and upper parts are limited by the inlet and outlet plena respectively. The radial reflector surrounds the fission zone and spans between the top of the outlet plenum and the bottom of the inlet plenum. Beyond these two surfaces are the flow channels of the coolant, which act as axial top and bottom reflectors. The breeder blanket surrounds radially all of the internal cylindrical structures as the outermost core region.

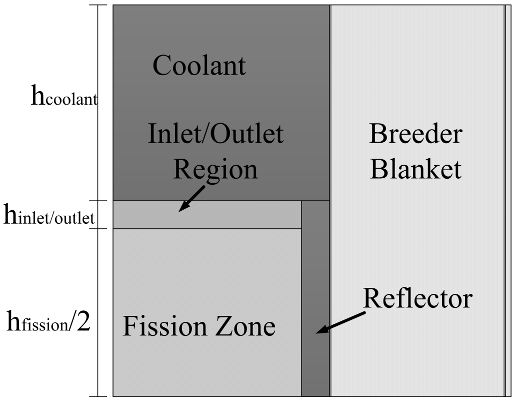
$h_{coolant}$
$h_{inlet/outlet}$
$h_{fission}/2$
Coolant
Inlet/Outlet Region
Breeder Blanket
Reflector
Fission Zone

Figure 5.2: Longitudinal section

The total height of the fission zone $h_{fission}$ is equal to $240cm$ and the inlet and outlet plena have each a height $h_{inlet/outlet}$ of $20cm$. The part of the coolant flow channels located inside the reactor (above and below the fission zone) each has a height $h_{coolant}$ of $140cm$, and the breeder blanket has a total height $h_{breeder}$ (or h_{core}) of $560cm$. The longitudinal view of the reactor in Fig. 5.2 shows also only one quarter of the reactor due to the symmetry along the central symmetry axis overlapped with the axis of the cylinder and the symmetry axis at half height.

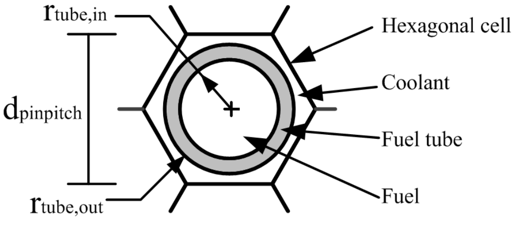
$r_{tube,in}$
$d_{pinpitch}$
$r_{tube,out}$
Hexagonal cell
Coolant
Fuel tube
Fuel

Figure 5.3: Hexagonal array and fuel tube

In the center of the model, inside of the fission zone, the treatment is slightly different depends on the different codes. The main idea aim is to generate a hexagonal array of the fuel salt tubes. The inner radius of the fuel salt tube $r_{tube,in}$ is set as $0.725cm$ and the outer radius $r_{tube,out}$ $0.95cm$. Each fuel tube can be considered in its own hexagonal cell as shown in Fig. 5.3. The pin pitch between the fuel tubes from center to center, which is also the size of the cell, is $2.2cm$. Between the outer wall of the fuel

Isotope	Mole% in the fuel	Atomic density($10^{24}/cm^3$)
^{37}Cl	75.000	1.820E-02
^{238}U	19.586	4.734E-03
^{238}Pu	0.113	2.749E-05
^{239}Pu	3.154	7.664E-04
^{240}Pu	1.346	3.271E-04
^{241}Pu	0.467	1.629E-04
^{242}Pu	0.334	8.109E-05

Table 5.1: Proportions of U-Pu fuel

U-Pu fuel	Mole%
^{37}Cl	75.0
^{238}U	25.0

Table 5.2: Breeder fertile material configuration

tube and the boundary of the lattice the coolant flows. The fuel salt flows inside of the inner wall and the wall material between the inner and the outer wall holds the flow.

The total number of the fuel salt tubes has been calculated by dividing the horizontal cross section of the fission zone by the horizontal cross section of a hexagonal cell. A theoretical total number of 13659 fuel tubes for the model is, thus, obtained. The total number of ***complete*** fuel tubes is 13406, obtained considering only the complete fuel tubes (but the hexagonal cell might not be complete).

5.2 Fuel Salt Composition

As mentioned in the previous chapters, the original design of the DFR reactor concept has selected a mixture of UCl_3 and $PuCl_3$ as the fuel salt (U-Pu fuel). From the chemical formula ^{37}Cl takes 75 mole% and the rest of heavy nuclides share 25 mole%. The detailed composition of the heavy nuclides mixture in both mole percentage and atomic density (at $1380K$) is listed in Tab. 5.1:

5.3 Breeder Blanket Composition

The composition of the breeder blanket is shown below in Tab. 5.2:

Code/Version/ Calculations	SCALE 6.1.3	SCALE 6.2b4	SERPENT 1.1.19	SERPENT 2.1.x
Single Fuel Tube				
-Reaction rates	○	○	○	○
-Power distribution			○	○
-Neutron distribution			○	○
Static Calculation				
-k_{eff}	○	○	○	○
-Delayed neutron data			○	○
-Generation time			○	○
-Neutron spectrum	○	○	○	○
-Reaction rates	○	○	○	○
-Power distribution			○	○
Sensitivity Analysis				
-Nuclide importance	○	○		
-Thermal feedback	○	○	○	○
-Geometry feedback	○	○	○	○

Table 5.3: Correspondence of Codes to Calculations

5.4 Calculations Performed

In order to get a more complete basis for comparison, several codes and versions have been employed. Because of the variety of the codes used in this work, not all the codes are used for every calculation. The following Tab. 5.3 clarifies this approach.

In the following sections, SERPENT 1 is specified for SERPENT 1.1.19 and SERPENT 2 is for SERPENT 2.1.23. Other versions for the occasional situation will be individual remarked.

Chapter 6

Static Calculation

6.1 Introduction

In the static calculation the theory of the basic reactor and neutron physics is firstly introduced as the fundamental background, which can be used for the deterministic theoretical approaches in the future. Now in this work the basic physics is calculated for a steady-state reactor configuration using Monte Carlo approaches. Based on the geometry described in Sec. 5.1, the U-Pu fuel type is investigated. The results are grouped under subjects and the details corresponding to this fuel type are then discussed.

6.2 Criticality

6.2.1 Theoretical Analysis

The effective multiplication factor $k_{eff}$is defined as the quotient of the number of fissions in one generation divided by the number of fission in preceding generation [LB01, pp.117]. A graphic demonstration can be found in Fig. 6.1, in which compared to the conventional nuclear reactors such as Light Water Reactors, where thermal fission mainly occurs, the DFR, a fast reactor, has a simpler process in the life cycle of the neutrons and, therefore, a different definition of the multiplication factor.

For the thermal reactors in the figure N means the neutron population in the ith or $(i+1)$th generation, ϵ is known as the fast fission factor, P_{FNL} is the fast non-leakage probability, p is the resonance escape probability, P_{TNL} is the thermal non-leakage probability, f is the thermal utilization factor, and η is the thermal fission factor [LB01, pp.286]. The whole process describes the neutron life from its birth in the fission reaction to its induction of the next fission reaction. The six-factor formula [DH75] is then used to determine the multiplication factor of a nuclear chain reaction:

$$k_{eff} = \eta f p \epsilon P_{FNL} P_{TNL} \tag{6.1}$$

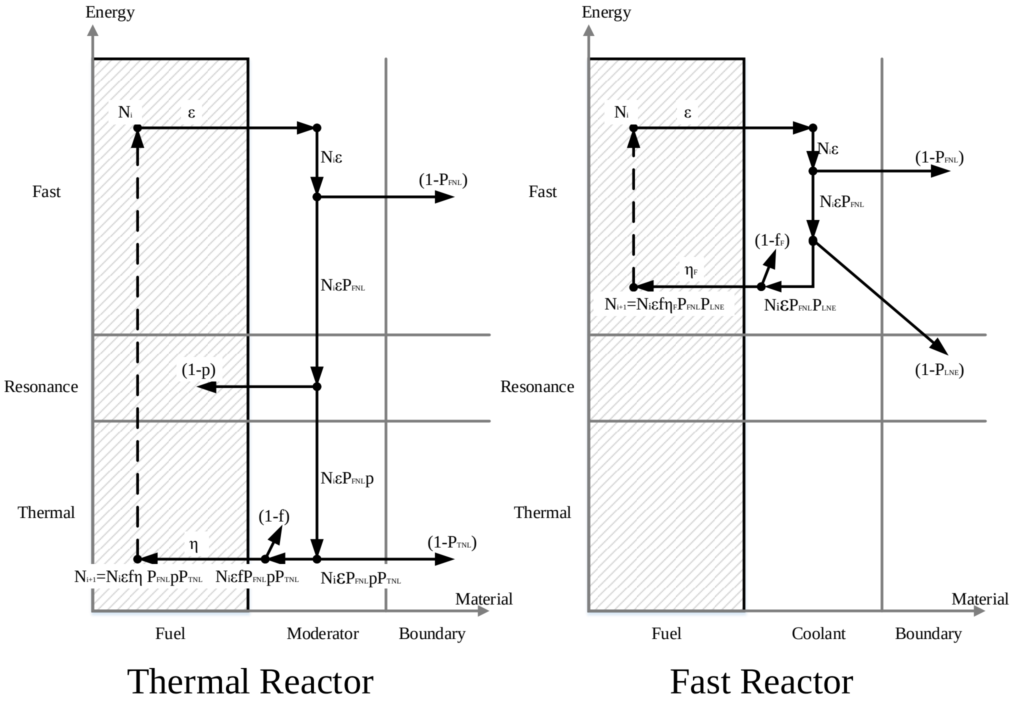
Energy
Fast
Resonance
Thermal
Ni
ε
Niε
(1-PFNL)
NiεPFNL
(1-p)
NiεPFNLp
(1-f)
η
(1-PTNL)
Ni+1=Niεfη PFNLpPTNL
NiεfPFNLpPTNL
NiεPFNLpPTNL
Material
Fuel
Moderator
Boundary
Thermal Reactor
Energy
Fast
Resonance
Thermal
Ni
ε
Niε
(1-PFNL)
NiεPFNL
(1-fF)
ηF
Ni+1=NiεfηFPFNLPLNE
NiεPFNLPLNE
(1-PLNE)
Material
Fuel
Coolant
Boundary
Fast Reactor

Figure 6.1: Graphic demonstration of the multiplication factor k_{eff}

For the fast reactor, however, no moderator is available inside the core. Thus, the neutrons are rarely moderated into the lower energy regions. In the right figure it can be seen that almost all the process is carried out in the fast neutron region and limited to the fuel salt and the coolant. The number of neutrons from the N_i generation is firstly scaled by ϵ to get the total neutron number, though in the fast reactor almost all the neutrons come from fast fission. Inside of a reactor with limited boundaries, if the fast neutrons do not escape from the core to the outside of the boundary (probability P_{FNL}), they have to undergo collisions and scatterings inside the core. In the DFR, there is lead as the coolant/reflector and light elements in the structures. These light elements will slow down the neutrons, though only a few of them will be truly “moderated”. Therefore, P_{TNL} is replaced by P_{LNE}, which indicates the probability that the the neutrons are not scattered into the lower energy regions. Even though in a fast reactor there is no moderator, the coolant and the structure materials, nevertheless, scatter neutrons. The utilization factor f_F differs from f in that it represents the utilization factor of the fast neutrons, describing how many fast neutrons are absorbed by the fuel salt. These neutrons are then capable of inducing fast fission reaction and producing the N_{i+1}th generation multiplied by the fast fission factor. The expression of the multiplication factor can be consequently written as

$$k_{eff} = \eta_F f_F \epsilon P_{FNL} P_{LNE} \tag{6.2}$$

From the definition it is easy to see that if $k_{\mathit{eff}}$is larger than 1, the number of fissions increases and the reactor is "supercritical", while conversely it is called "subcritical" if k is smaller than 1. Only in the special case where k is equal to 1, the fission generations proceed unchanged in their amount of neutrons and the reactor is said to be "critical".

In order to establish the model for the further calculation, the time-dependent Boltzmann neutron transport equation for the angular flux is introduced:

$$\begin{aligned}\underbrace{\frac{1}{v}\frac{\partial\psi(\vec{r},E,\hat{\Omega},t)}{\partial t}}_{\textit{Time dept. change}} = &-\underbrace{\hat{\Omega}\cdot\vec{\nabla}\vec{J}(\vec{r},E,\hat{\Omega},t)}_{\textit{Diffusion}}\\ &-\underbrace{\Sigma(\vec{r},E)\psi(\vec{r},E,\hat{\Omega},t)}_{\textit{Absorption}}\\ &+\underbrace{\int_0^\infty \mathrm{d}E'\int_{4\pi}\mathrm{d}^2\Omega'\Sigma_s(\vec{r},E'\to E,\hat{\Omega}\cdot\hat{\Omega}')\psi(\vec{r},E)\psi(\vec{r},E',\hat{\Omega}',t)}_{\textit{Scattering from higher energy region}}\\ &+\underbrace{\chi(E)\int_0^\infty \mathrm{d}E'\nu(E')\Sigma_f(\vec{r},E')\int_{4\pi}\mathrm{d}^2\Omega'\psi(\vec{r},E',\hat{\Omega}')}_{\textit{Neutron from fission}} \qquad (6.3)\\ &+\underbrace{s(\vec{r},E,\hat{\Omega},t)}_{\textit{External source}}\end{aligned}$$

where $\vec{r}$ is the space vector, E, E' are the energy group of the neutrons, $\hat{\Omega}, \hat{\Omega}'$ are unit vector of the neutron velocity. ψ stands for the angular neutron flux, v is the neutron velocity, ν is the neutron number produced per fission, and $\chi(E)$ is the energy distribution of the fission neutrons. This equation is very difficult and computer resource intensive to solve for a full reactor. For this reason a simplified form of this equation called the Neutron Diffusion Equation is derived from it by applying a series of assumptions and simplification that eliminate the energy dependency (energy integration) or reduce it to a few energy groups, and the transformation of the angular flux into the scalar flux independent of the neutron movement direction $\hat{\Omega}$ by using the Fick's Law.

The simple form of the diffusion equation over all neutron energies (one single neutron energy group) and over all of the angular space for a *bare reactor* with a homogeneous mixed core and without reflector and the breeding blanket, can be written as

$$\frac{1}{v}\frac{\partial\phi}{\partial t} = D\nabla^2\phi - \Sigma_a\phi + \Sigma_s\phi + \nu\Sigma_f\phi + s \qquad (6.4)$$

by introducing the "diffusion coefficient" D in the Fick's Law:

$$\nabla J = -D\nabla^2\phi \qquad (6.5)$$

The simplest case should be first of all considered. In the one energy group approximation for a homogeneous reactor core without reflector or the external source in the steady-state, the Eqn. 6.3 can be simplified in the following form by setting the term on the left-hand side as well as the third and the last term on the right-hand side to zero:

$$D\nabla^2\phi - \Sigma_a\phi + \nu\Sigma_f\phi = 0 \tag{6.6}$$

which describes a steady-state of neutrons in the reactor core with the consideration of the neutron loss, which includes the diffusion term and the absorption term, and the neutron gain, which is the fission term. The Laplacian term can be re-arranged as:

$$\nabla^2\phi = \frac{1}{D}\left(\Sigma_a - \frac{\nu\Sigma_f}{k_{\mathit{eff}}}\right) \tag{6.7}$$

where k_{eff} is the multiplication factor and for the static state it should be the value of 1. Let B^2 equals to the right hand term,

$$B^2 = \frac{1}{D}\left(\frac{\nu\Sigma_f}{k_{\mathit{eff}}} - \Sigma_a\right) \tag{6.8}$$

then the Eqn. 6.6 becomes:

$$\nabla^2\phi + B^2\phi = 0 \tag{6.9}$$

while the constant k_{eff} is presented for:

$$k_{\mathit{eff}} = \frac{\nu\Sigma_f}{DB^2 + \Sigma_a} \tag{6.10}$$

with B^2 the geometry buckling for the finite cylindrical reactor:

$$B^2 = \left(\frac{2.405}{\widetilde{R}}\right)^2 + \left(\frac{\pi}{\widetilde{H}}\right)^2 \tag{6.11}$$

where $\widetilde{R}$ and $\widetilde{H}$ are extrapolated radius and extrapolated height of the reactor, separately. With Eqn. 6.10 and Eqn. 6.11 k_{eff} and B^2 can be calculated and compared.

6.2.2 General Assessment

The assessment of the consistency between SERPENT 1.x, SERPENT 2.x and SCALE 6.x is given here by the effective multiplication factor calculation of the DFR reactor with U-Pu fuel salt in the full reactor scale, whose results are reported in the following Tab. 6.1. Meanwhile a graphical presentation of all the results is

Code	ENDF/B-VII		JEFF-3.1		JEFF-3.1.1	
	k_{eff}	rel.err.	k_{eff}	rel.err.	k_{eff}	rel.err.
SERPENT 1.1.19	1.02678	3.1E-4	1.02688	3.2E-4	1.02714	1.9E-4
SERPENT 2.1.19	1.02668	1.3E-4	1.02709	1.3E-4	1.02738	1.9E-4
SERPENT 2.1.23	1.02664	1.1E-4	1.02724	1.2E-4	1.02711	1.6E-4
SCALE 6.1.3 mg	1.02784	1.8E-4				
SCALE 6.1.3 ce	1.02987	2.5E-4				
SCALE 6.2b4 mg	1.02715	1.9E-4				
SCALE 6.2b4 ce	1.03708	2.0E-4				

Table 6.1: Assessment of U-Pu fuel salt k_{eff}

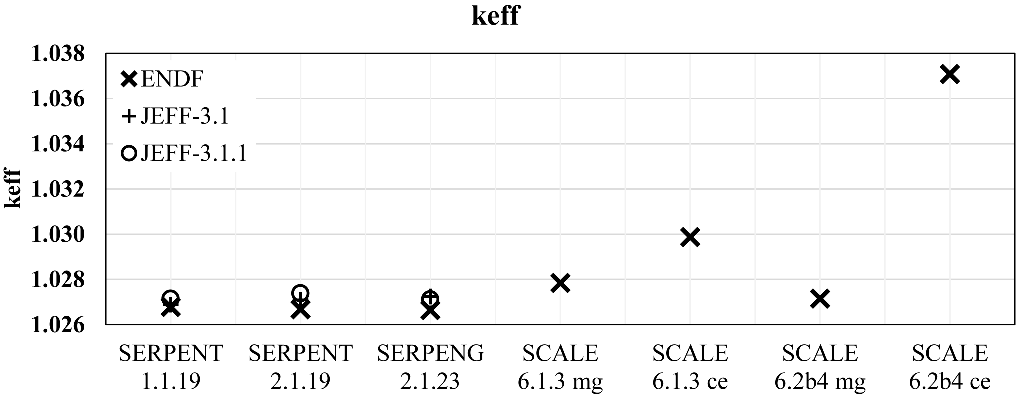

Figure 6.2: Assessment of U-Pu fuel salt k_{eff}

plotted in Fig. 6.2. “ce” is short for the continuous energy and “mg” is short for multi-group.

In this k_{eff} calculation, the results from SERPENT are based on 50 active cycles and 50 inactive cycles of 1 million neutrons for different versions. The nuclear data library selected is the ENDF/B-VII nuclear data library initially and then JEFF 3.1 as well as JEFF 3.1.1 nuclear data library later for the comparison. The reason for the decision of these three nuclear data libraries is that they are the newest libraries that are implemented in the SERPENT code and ENDF/B-VII is also the main data library in the SCALE code. The nuclear libraries ENDF/B-VI.8 and JEFF 2.2 are also available in the SERPENT, however they are out of date and some important isotopes for the DFR are missing in the library.

The results from KENO-VI are based on 1000 generations of 10000 neutrons per generation, for a total 10^8 histories. In the case ENDF/B-VII, continuous energy cross section data files and multi-group mode are both used.

In the comparisons the results from SERPENT 2 with ENDF/B-VII library are taken as reference. First of all, the results with the library ENDF/B-VII with different codes are examined. The results of SERPENT 1.1.19, 2.1.19 have a difference of $14pcm$ and $4pcm$, which is very small and they can be considered identical within

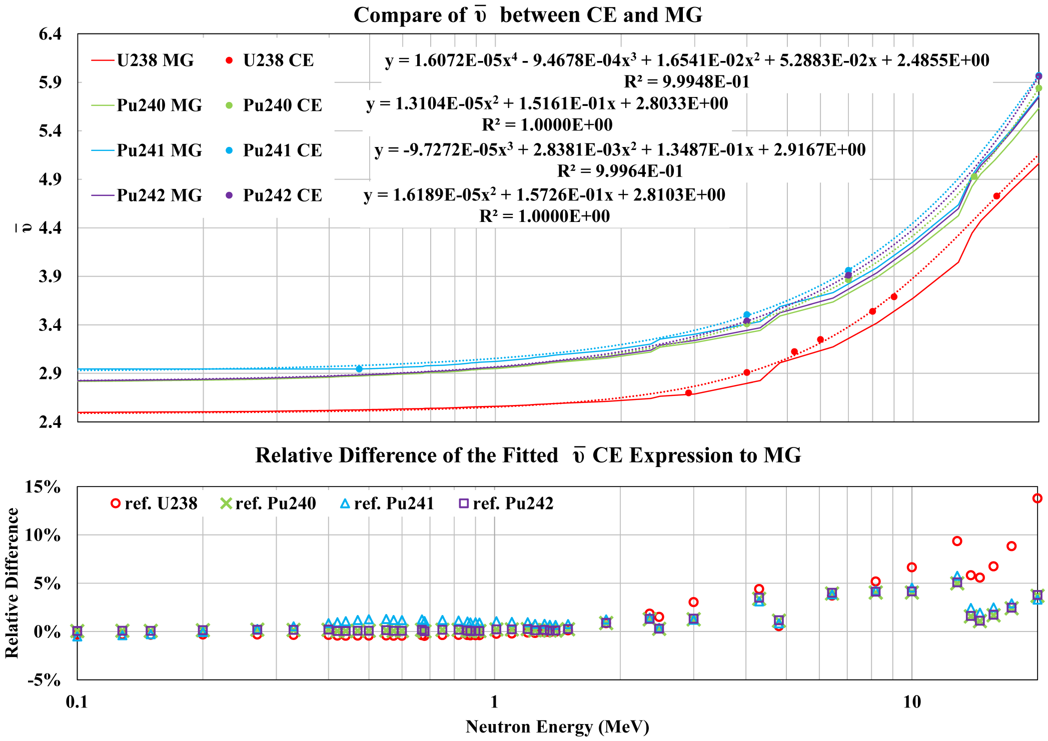

Figure 6.3: Comparison of $\bar{\nu}$ between SCALE CE and MG

the range of uncertainty. At the same time the difference between the reference result and that from KENO-VI in multi-group mode in SCALE 6.1.3 (120*pcm*) and in SCALE 6.2b4 (51*pcm*), can also be considered consistent or even identical in some cases.

Secondly, for the results of SCALE code system, the difference between the results from KENO-VI in continuous energy and in multi-group mode is more significant than that between SERPENT and KENO-VI in multi-group mode. For SCALE 6.1.3 in continuous energy mode the difference reaches 323*pcm* and for SCALE 6.2b4 it reaches even 1044*pcm* . Since SCALE 6.2b4 is provided as a beta version that the calculation data can not be retraced, the relevant data used by SCALE 6.1.3 in continuous energy mode and in multi-group mode is compared, including the fission cross section, capture cross section, absorption cross section and $\bar{\nu}$, which are directly related to the value of the k_{eff}. More specifically, the data files "ce_v7_endf" and "scale.rev07.xn238v7" in the "data" folder on the installation path of SCALE 6.1.3 are compared, which contains the information of the neutronics processed from the original ENDF nuclear data library. Each data file corresponds to each mode.

It turns out that there is no noticeable difference found between the cross section of both data files. Meanwhile $\bar{\nu}$ is compared and plotted in Fig. 6.3. In order to better interpret the figure with value comparisons, it has to be reminded that the points corresponds to the $\bar{\nu}$ value provided in the data files of the continuous energy mode. For the demonstrated four nuclides ^{238}U , ^{240}Pu , ^{241}Pu and ^{242}Pu the $\bar{\nu}$ given in the data file of the continuous energy mode is formed with only some points, while in the data file of the multi-group mode the $\bar{\nu}$ is always given with 238 data points.

Therefore, in order to compare the data of two energy modes of the calculations, the points in the plot of the *ce* mode are fitted with polynomials. The dashed curves shown in the figure are the corresponding fitted curves. The fitting process starts from a lower degree polynomial, during which the corresponding R^2 as well as the shape of the curve are observed and estimated. After the fitting, the relative difference of the fitted $\bar{\nu}$ *ce* expression to the *mg* data as the reference is presented in the lower figure of Fig. 6.3.

Now it is obvious that the $\bar{\nu}$ value in the continuous energy mode is distinctly larger than that in the multi-group mode. The points in the upper figure can also be matched with the points in the lower figure. This difference is significant in the energy range above $1MeV$. In the lower energy range, the relative differences are small and reduce to 0 in the thermal energy region. This means that these differences may not cause discrepancies for a thermal spectrum reactor, but they may become important for a fast spectrum reactor such as the DFR, especially for reactors with the elements mentioned above, this influence should be taken into account. Even though the reason for a higher k_{eff} calculated by SCALE 6.2b4 ce is still not clear, this could explain why k_{eff} calculated by SCALE 6.1.3 ce is higher than that by SCALE 6.1.3 mg.

Thirdly the results from different libraries are compared. The results with the ENDF library are smaller as those from the JEFF libraries. For SERPENT 2, the differences with JEFF-3.1 and JEFF-3.1.1 can be as much as $60pcm$ and $47pcm$ respectively. These two differences for SERPENT 1.1.19 and 2.1.19 are separately $10pcm$, $36pcm$ and $41pcm$, $70pcm$. On the order of magnitude these can be considered as identical, however the trend that the results calculated with JEFF libraries are larger than that with ENDF library is clear. From the comparison of the fission to capture ratio (generated with data from JANIS 4.0 [SBD14]), which is the ratio calculated with the fission microscopic cross section divided by capture microscopic cross section, of the nuclides in the fuel composition shown in Fig. 6.4 this result can be qualitatively proved. For different nuclides in the fuel composition, most of the curves are consistent over most of the energy range of interest. Obvious discrepancies can be observed over $1MeV$ or below $10eV$. In the energy range over $1MeV$ for ^{238}U and ^{239}Pu the ratio in the ENDF libraries is higher than that in the JEFF libraries by about one order of magnitude, while the ratios of ^{242}Pu are almost the same. The nuclides ^{238}Pu and ^{241}Pu have a considerable high ratio which is 2∼4 orders of magnitude larger in the JEFF libraries compared to the value given in the ENDF libraries. Although according to the composition the DFR fuel contains little ^{238}Pu and ^{241}Pu compared to the amount of the other nuclides, this overwhelming difference in the ratio still results the the discrepancy observed in the k_{eff} assessment.

6.2.3 Group Constants

From the theoretical analysis to the actual calculation, models with different assumptions and details are used in this section. In this section the group constants are calculated for successive changes in the reactor structure from “Only fuel” through

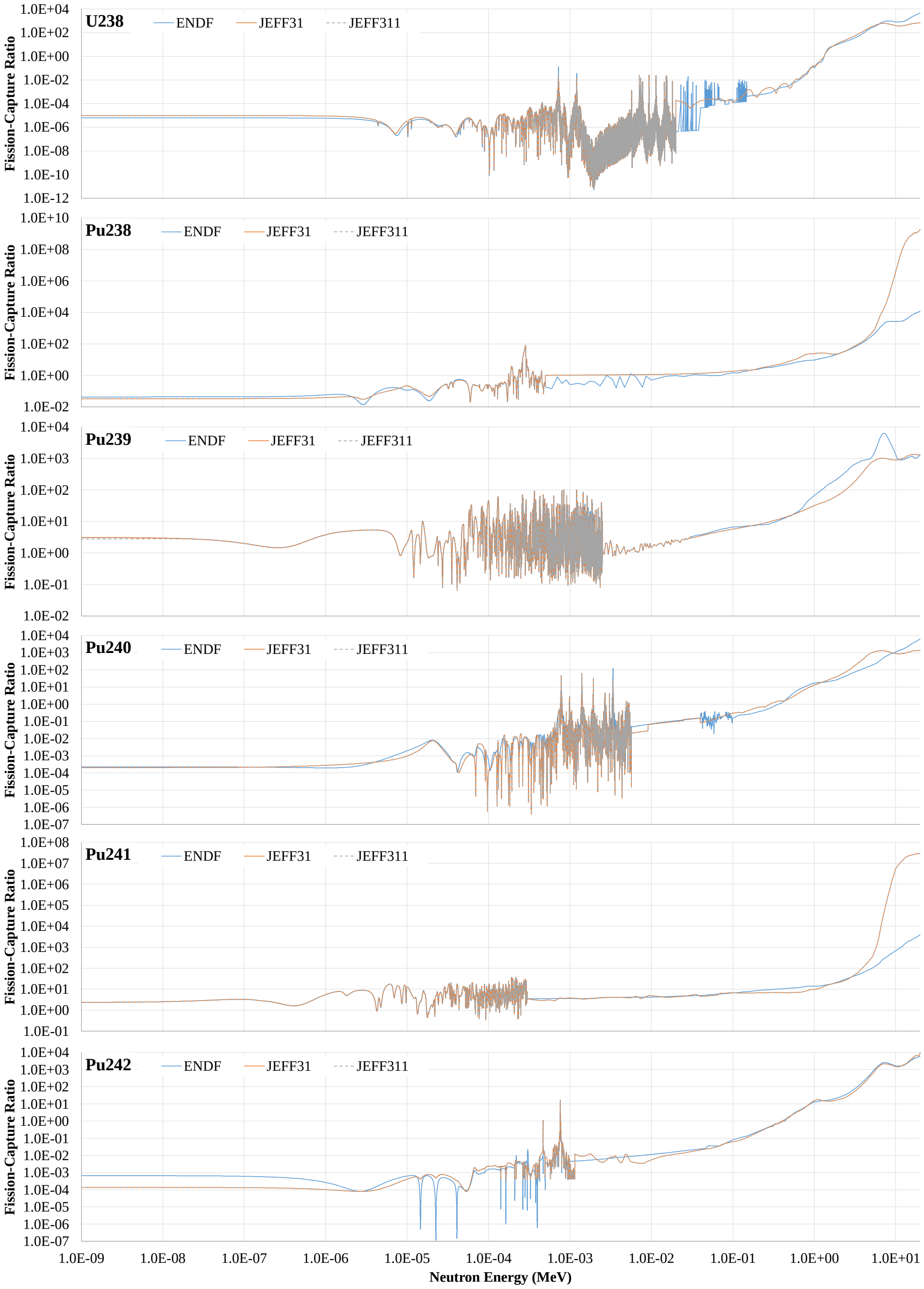

Figure 6.4: Fission-capture ratio of U-Pu fuel

Constants	Only fuel	With coolant	With reflector	With breeder	Units
Σ_{tot}	9.14310E-2	1.89890E-1	2.04703E-1	2.22776E-1	cm^{-1}
Σ_{cap}	8.22609E-4	1.03319E-3	1.08101E-3	1.34802E-3	cm^{-1}
Σ_a	1.52088E-3	1.74547E-3	1.81158E-3	2.08976E-3	cm^{-1}
Σ_f	6.98268E-4	7.12282E-4	7.30565E-4	7.41741E-4	cm^{-1}
Σ_{tr}	7.79896E-2	1.63560E-1	1.77921E-1	1.93537E-1	cm^{-1}
ν	2.93151	2.92235	2.92149	2.92040	
D	4.27407	2.03799	1.87349	1.72232	cm
$E_{fission}$	2.08243E+2	2.07975E+2	2.08315E+2	2.08312E+2	MeV

Table 6.2: Evolution of one-group constants with U-Pu fuel

Constants	1st Group	2nd Group	Unit
Σ_{tot}	2.22634E-1	3.14944E-1	cm^{-1}
Σ_{cap}	1.34709E-3	1.95548E-3	cm^{-1}
Σ_a	2.08973E-3	2.10926E-3	cm^{-1}
Σ_f	7.42643E-4	1.53785E-4	cm^{-1}
Σ_{tr}	1.93423E-1	3.13873E-1	cm^{-1}
ν	2.92041	2.87187	
D	1.72334	1.06200	cm
$E_{fission}$	2.08312E+2	2.07975E+2	MeV

Table 6.3: Two group constants of the whole reactor with U-Pu fuel

“Adding up coolant” and “Adding up reflector” to the final complete reactor. Group constants are calculated with SERPENT 2 and compared in Tab. 6.2 for one group and Tab. 6.3 for two groups, where $6.25\times10^{-7}\ MeV$ is the boundary between two groups, among which the 1st group has a higher energy than the 2nd group.

With more structures being added progressively, the reaction rates of various types of reactions in the DFR varies, not only capture reactions, but also absorption and fission reactions. Nonetheless, because of the different characteristics of the materials, the changes in the reaction rates show differences. These differences are reflects in the changes calculated in the macroscopic cross sections. For a given material in the DFR reactor and the U-Pu fuel composition, the change (increase) of the absorption macroscopic cross section is the most significant.

Compare to the one-group constants, they are almost the same as those of the 1st group in the two-group configuration. This is because the 1st group represents the fast or more specifically, the higher energy range above $6.25\times10^{-7}\ MeV$, which covers most of the neutron energies in the DFR core.

Precursors group	SERPENT 1	rel.err.	SERPENT 2	rel.err.
Total	3.44321E-3	7.33E-3	3.40194E-3	2.54E-3
1st	7.55608E-5	4.89E-2	7.51718E-5	1.92E-2
2nd	7.51583E-4	1.94E-2	7.41027E-4	5.87E-3
3rd	5.37744E-4	1.83E-2	5.30534E-4	8.34E-3
4th	1.34666E-3	1.33E-2	1.32089E-3	4.25E-3
5th	5.70659E-4	1.83E-2	5.75974E-4	6.58E-3
6th	1.60993E-4	3.50E-2	1.58350E-4	1.29E-2

(a) DNP effective fraction (-)

Precursors group	SERPENT 1	rel.err.	SERPENT 2	rel.err.
Total	6.26892E-1	1.80E-2	6.34962E-1	6.52E-3
1st	1.28891E-2	1.78E-3	1.28291E-2	8.90E-4
2nd	3.00274E-2	8.80E-5	3.00226E-2	3.00E-5
3rd	1.12083E-1	7.50E-4	1.12050E-1	3.50E-4
4th	3.20103E-1	4.60E-4	3.20087E-1	2.10E-4
5th	1.13384E+0	3.12E-3	1.13120E+0	1.33E-3
6th	6.18308E+0	1.86E-2	6.33237E+0	6.53E-3

(b) DNP decay constants (s^{-1})

Table 6.4: Constants of DNPs of U-Pu fuel

6.3 Delayed Neutron Data

The group constants of the delayed neutron precursors of the reactor with U-Pu fuel option are calculated by both SERPENT 1 and SERPENT 2 based on the Nauchi [NK06, NK05] method. The delayed neutron precursors are divided into 6 groups depending on their radioactive decay constant. The effective fraction of the delayed neutron precursors and the decay constants of the delayed neutron are listed in Tab. 6.4 a) and b). It has to be noted that these results are only valid for the fuel salt in the limit of zero flow velocity.

For the values in Tab. 6.4 (a), $\beta = \sum_{i=1}^{6} \beta_i = 0.00344$ with SERPENT 1 and 0.00340 with SERPENT 2, so the delayed precursors account for around 0.34% of all the neutrons.

6.4 Generation Time

6.4.1 Introduction

The "generation time" with the commonly used meaning of "the time between the birth of a neutron and subsequent absorption-inducing fission" [LB01, pp.333] was firstly defined in 1960 by Lewins [Lew60] as the reciprocal of the product of ν, the total mean number of neutrons from fission, by the macroscopic fission cross-section:

$$\Lambda = \frac{1}{\nu v \Sigma_f}$$

In the following decades, however, the term “generation time” was widely discussed because it had been defined earlier by Hurwitz [Hur49] with another meaning, and because of its vague definition. In 1980 “generation time” was finally replaced as the “reproduction time”, which means the mean time for one neutron to be replaced by another neutron on fissioning media [Lew81]:

$$\begin{aligned} \Lambda &= \textit{prompt neutron reproduction time} \\ &= \frac{1}{\nu v \Sigma_f} \end{aligned}$$

and the original “generation time” by Hurwitz [Hur49] is defined as:

$$\begin{aligned} \tau &= \textit{prompt generation time} \\ &= \frac{1}{v \Sigma_f} \end{aligned}$$

which represents a time for one neutron to produce a “family” of ν neutrons. The “prompt” mentioned here is special for the neutrons immediately taking part in fission after the production and the ones produced through delayed neutron precursors but without delay time.

In order to clarify similar concepts, *neutron lifetime* defined as “the mean time for one neutron to be removed from the reactor”, is also given here

$$l = \frac{1}{(\Sigma_a + DB^2)v} \tag{6.12}$$

The SERPENT code calculates the *neutron reproduction time.* The “generation time” [Oak11, F11.3.14] calculated by SCALE also has the meaning of the “reproduction time” [Lew81].

For the *generation time* the following results are provided in Tab. 6.5. The “IFP” is referred to the *adjoint-weighted generation time* [LAF+14] by using the iterated fission probability method.

Moreover, the generation times in two-energy groups are also provided in Tab. 6.6. It can be seen that the SERPENT results are quite close to the result of the 1st group in the two-group energy structure, which is also reasonable since the DFR is indeed a fast reactor in which the reactor generation time is mainly contributed by the neutrons with energies over $6.25\times10^{-7}\,MeV$. SCALE mg results have also shown the same conclusion, while the results calculated by SCALE ce seem to be much closer to the result of the 2nd group.

Code	Nauchi	rel.err.	IFP	rel.err.	Perturbation	rel.err
SERPENT 2.1.19	2.62449	2.6E-3	2.38930	5.6E-3	2.50775	6.5E-4
SERPENT 2.1.23	2.54412	1.7E-3	2.31276	3.5E-3	2.42932	7.7E-4
SCALE 6.1.3 mg	2.58907	3.3E-3				
SCALE 6.1.3 ce	2.85865	3.3E-3				
SCALE 6.2b4 mg	2.57778	3.2E-3				
SCALE 6.2b4 ce	2.83391	3.1E-3				

Table 6.5: Generation time of U-Pu fuel (10^{-6} s)

Energy Groups	Nauchi	rel.err.	IFP	rel.err.
over 6.25E-7MeV	2.54255	1.7E-3	2.31147	3.6E-3
below 6.25E-7MeV	3.00442	2.0E-2	2.70707	2.7E-2

Table 6.6: Generation time of U-Pu fuel in two energy groups (10^{-6} s)

This result, however, should be considered as a coincidence, but not has anything to do with the 2nd group (thermal energy region). The reason should be the same as the reason for the larger k_{eff} value observed in the criticality calculation. A lower $\bar{\nu}$ means fewer neutrons will be produced in the fission reactions, which will reduce the neutron density, as well as, the collision probability with fissile nuclides to induce the next fission reaction. This process will increase the generation time, as shown by Eqn. 6.12.

6.5 The In-hour Equation

Based on the delayed neutron data and generation time obtained in the previous sections, the time-dependent response of the DFR can be approached by the so-called "Nordheim Equation" in France or "Inhour Equation" in English-speaking countries [Reu08, pp. 124], whose name comes from the fact that the value of ω were quoted as "inverse hours" in the early days of reactor technology.

$$\rho = \omega\Lambda + \sum_{i=1}^{N} \frac{\beta_i \omega}{\omega + \lambda_i} \tag{6.13}$$

where N is the number of delayed neutron groups, normally 6. The graphical solution of this equation as applied to the DFR is plotted in Fig. 6.5. The horizontal axis used for ω is logarithmically scaled, while the vertical linear axis stands for reactivity. The asymptotic lines between the curves represent the value of λ_i.

From the plot it is not difficult to find out that for a certain reactivity, a horizontal line can be drawn intersecting the solution of the In-hour equation. For a positive reactivity, among all seven ω values corresponding to the intersections there is only one ω which can be positive in Quadrant I and this positive value indicates the time

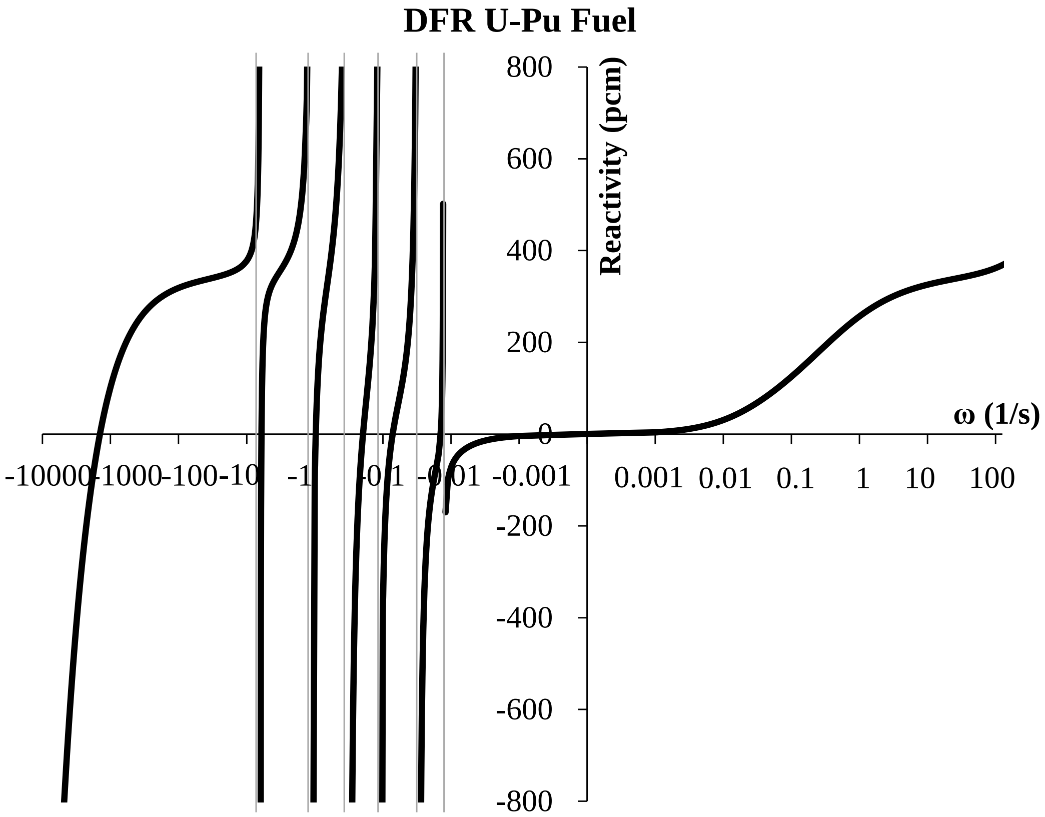

Figure 6.5: Graphical solution of the In-hour equation of the DFR (U-Pu fuel salt)

the DFR requires to rise the reactor power, defined as:

$$\tau = \frac{1}{\omega} \tag{6.14}$$

Similarly, for a negative reactivity, all the values of ω are negative in Quadrant III. The least negative one corresponds to the decay of the longest-lived precursor group (1st).

6.6 Neutron Spectrum

6.6.1 Introduction

In a fission reaction most of the neutrons are emitted immediately when the reaction happens and are referred to as prompt neutrons, while those being emitted by the decay of fission products are called delayed neutrons. In this work the energy spectrum of the prompt fission neutrons of the DFR is mainly considered. Neutron interactions depend strongly on the range of the neutron energy involved and, therefore, the final reactor spectrum is also a function of the reactions taking place in

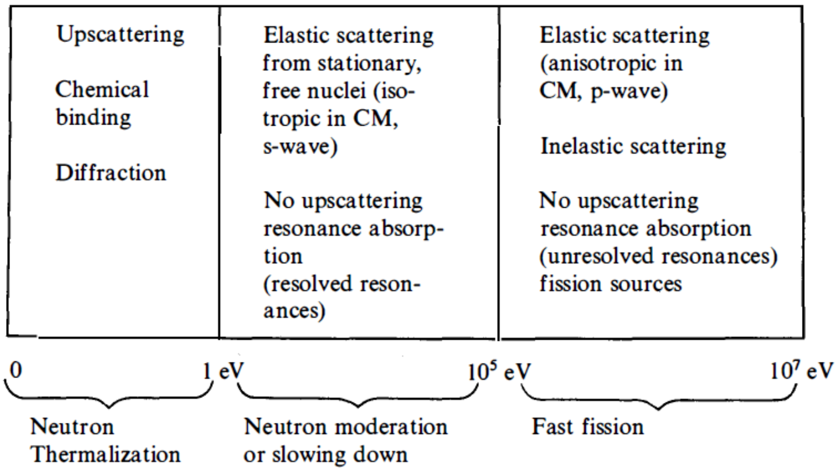
Upscattering
Chemical binding
Diffraction
Elastic scattering from stationary, free nuclei (isotropic in CM, s-wave)
No upscattering resonance absorption (resolved resonances)
Elastic scattering (anisotropic in CM, p-wave)
Inelastic scattering
No upscattering resonance absorption (unresolved resonances) fission sources
0
1 eV
10⁵ eV
10⁷ eV
Neutron Thermalization
Neutron moderation or slowing down
Fast fission

Figure 6.6: Various interactions of neutrons at different energy ranges [LB01]

the core, as can be referred in Fig. 6.6. This section discusses the neutron energy spectrum characterizing fast neutrons as generated in the DFR.

Initially, an assessment between the theoretical results, as well as, between different points of views is carried out. The assessment is performed to discuss the differences in the results given by different codes regarding the energy group structure used and the nuclear databanks. The in-core characteristics of the neutron spectrum depending on the materials used in the reactor is also investigated. Finally, the most significant reactions which shape the neutron spectrum are discussed.

6.6.2 Neutron Energy Distribution

The neutron spectrum of DFR reactor using U-Pu fuel composition is plotted in Fig. 6.7 in both linear and logarithmic scales in the form of activity per unit lethargy [DH75, pp.322]. In this calculation the spectrum has been averaged over all of the space in the reactor. All the results in this figure were generated with 238-energy-group structure.

It can be observed that, since the DFR is expected to be a fast reactor, the main neutron spectrum is shifted the fast neutron region. The core averaged spectrum is represented in the energy range from $10^{-9}\,MeV$ to $20MeV$. The peak area extends from ca. $100eV$ to ca. $10MeV$, with its center at about $0.1MeV$.

6.6.2.1 Evaluation of different Codes and Versions

Comparisons have been made between the spectra as calculated by SCALE continuous energy (ce) and multi-group (mg), and SERPENT 1 and 2 by setting the results calculated by SCALE(ce) as the reference values; see the lower chart in Fig. 6.7. In this comparison all the results were calculated with ENDF/B-VII nuclear data library.

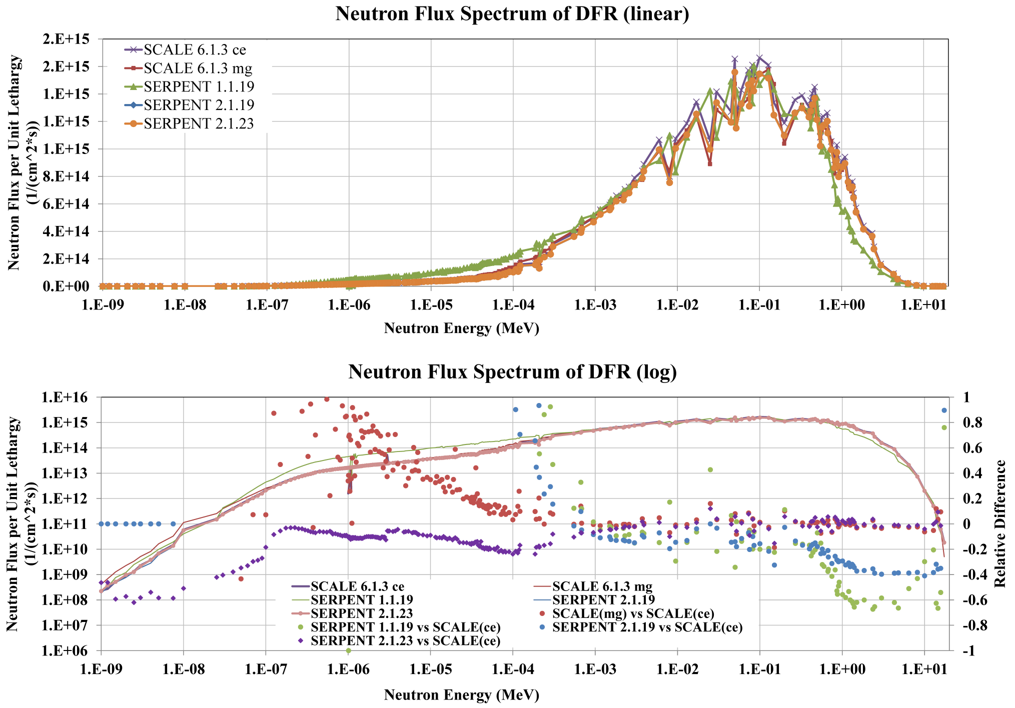

Figure 6.7: Total neutron spectrum of U-Pu fuel

The relative difference, which is defined as

$$\textit{Relative Difference} = \frac{\textit{Actual Difference}}{\textit{Reference Value}} \tag{6.15}$$

between SCALE(mg) and SCALE(ce) is constrained to a small energy range from $10^{-4}\,MeV$ to $20MeV$, mostly around 5%, and in the energy region below $10^{-4}\,MeV$ the spectrum of the results from SCALE(mg) is higher than that from SCALE(ce). This discrepancy can be interpreted as the statistic error of the results due to the small amount of neutrons in this energy range. The larger relative differences appear between the spectrum of SERPENT, both versions, and SCALE(ce).

The relative differences in the results from SERPENT and SCALE(ce) indicate a spectral shift between the two codes. Overall the SCALE(ce) spectrum is a bit harder than the one calculated with SERPENT (especially harder than that with SERPENT 1). Taking the curve from SCALE(ce) as reference, it can be observed that from $20MeV$ down to $0.2MeV$ the relative differences between SERPENT 1 and the reference stay around -60% and between SERPENT 2.1.19 are around -40%, while SERPENT 2.1.23 shows a good consistency (around 0%) with the reference. From $0.2MeV$ down to $10^{-3}\,MeV$ the relative differences between all SERPENT results and the reference results reduce to around -20%. Below $10^{-3}\,MeV$ the discrepancies of the results between SERPENT 1.1.19 as well as 2.1.19 and the reference increase rapidly. This can be easily observed in the upper figure, where there is a small shift between the curves. For the curve from SERPENT 2.1.23 the discrepancies remain

Internal Name	Total Groups	Groups $<1eV$	Groups $1eV \sim 100keV$	Groups $>100keV$	Description
scale44	44	20	13	11	SCALE 44-group
cas70	70	31	30	9	CASMO 70-group
scale238	238	49	145	44	SCALE 238-group
nj2	239	6	79	154	CSEWG 239-group
nj21	315	38	175	102	TRIPOLI 315-group
nj20	1968	70	1263	635	ECCO 1968-group

Table 6.7: Different energy group structures

smaller than -20% from $0.2MeV$ till $10^{-7}\ MeV$. For all practical purposes, however, these results can be still considered consistent.

6.6.2.2 Different Energy Group Structures

The neutron spectrum can vary because of different energy group structures due to their non-homogenous distribution of energy groups. Especially for different reactor types, for example, light water reactor as thermal reactor and molten salt reactor as fast reactor, their spectrum will differ and have peaks over different energy ranges. For fast reactors, more energy groups must be considered in the energy region where the peak of the spectrum is located.

The energy group structures that are been considered in this work are provided by SERPENT itself and the following Tab. 6.7 shows the internal names and the energy group distribution of these structures. In the Table all the energy groups are classified into three categories corresponding to the neutron energy ranges. The thermal neutrons are in the energy groups below $1eV$ [Mot70, pp.7], the intermediate neutrons are in the energy range between $1eV$ to $100keV$ [Mot70, pp.77], and the fast neutrons have energies over $100keV$ [Mot70, pp.141].

It can be seen that the percentage of the energy groups over $1eV$ varies from 54.5% to 97.5%. Especially for the last four energy group structures, they have over 79% energy groups specified for neutrons within the intermediate and fast energy range. Considering that the DFR reactor is a fast reactor, then most of the neutrons have a relative high energy from $1eV$ to $10MeV$. The high percentages of the energy groups ensures that the fast neutron spectrum can be well described by these energy group structures. The cas70 energy group has even fewer groups in the fast energy range than scale44, which is more suitable for the representation of the thermal or intermediate (epithermal) energy neutron spectra.

Figure 6.8 depicts the neutron spectrum calculated with different energy group structures by SERPENT 2.1.23 with the ENDF-B/VII data library. Generally, the results with different energy group structures are well consistent in most of the energy regions.

The 44-group structure shows a lack of energy points necessary to produce a detailed shape of the DFR neutron spectrum. The 70-group and 238-group structures describe

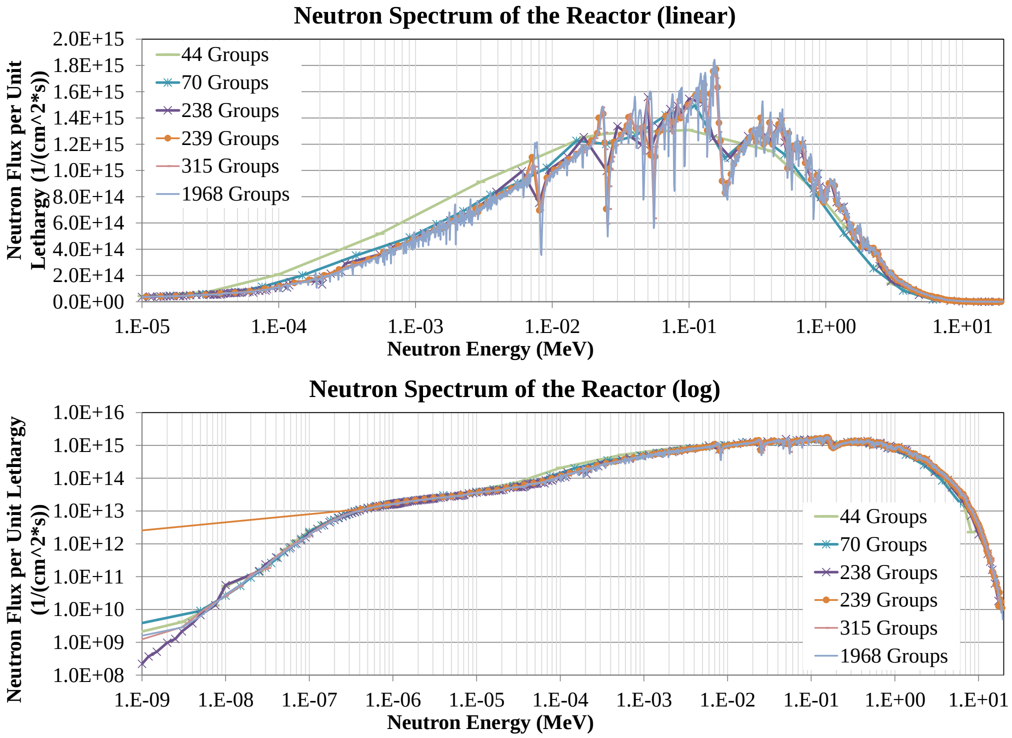

Figure 6.8: Neutron spectrum in different energy groups

well the basic shape and trends of the spectrum, but, as can be observed in the upper plot of Fig. 6.7, the roughness of the spectrum is portrayed without any details. The 239-group structure has only 1 group more than the 238-group one, but there are many more energy groups located in the high energy region than in the case of the 238-group structure. Therefore, the 239-group, the 315-group and the 1968-group structures are more capable of describing the particulars on the DFR spectrum, especially the crests and troughs on the spectrum, which will be discussed later. Meanwhile in the low energy region the 239-group structure has only 1 group over $10^{-11}\,MeV$ to $4.14\times10^{-7}\,MeV$, which is why its curve behaves so differently compared to other group structures. The 44-group, 70-group, 315-group structures and even 1968-group structure also have this problem, but the energy span is two orders of magnitude smaller than that of the 319-group structure.

6.6.2.3 Different Nuclear Data Libraries

In this section the results that calculated by SERPENT but with two different nuclear data libraries are compared. The selected nuclear data libraries are ENDF/B-VII and JEFF-3.1.1, and combined with various energy groups that listed earlier in Tab. 6.7.

The plots in Fig. 6.9 show the relative differences for the JEFF 3.1 and 3.1.1 nuclear data bases taking the results from ENDF library as a reference. They show results of spectrum calculations for a series of energy group structures as given in the plots.

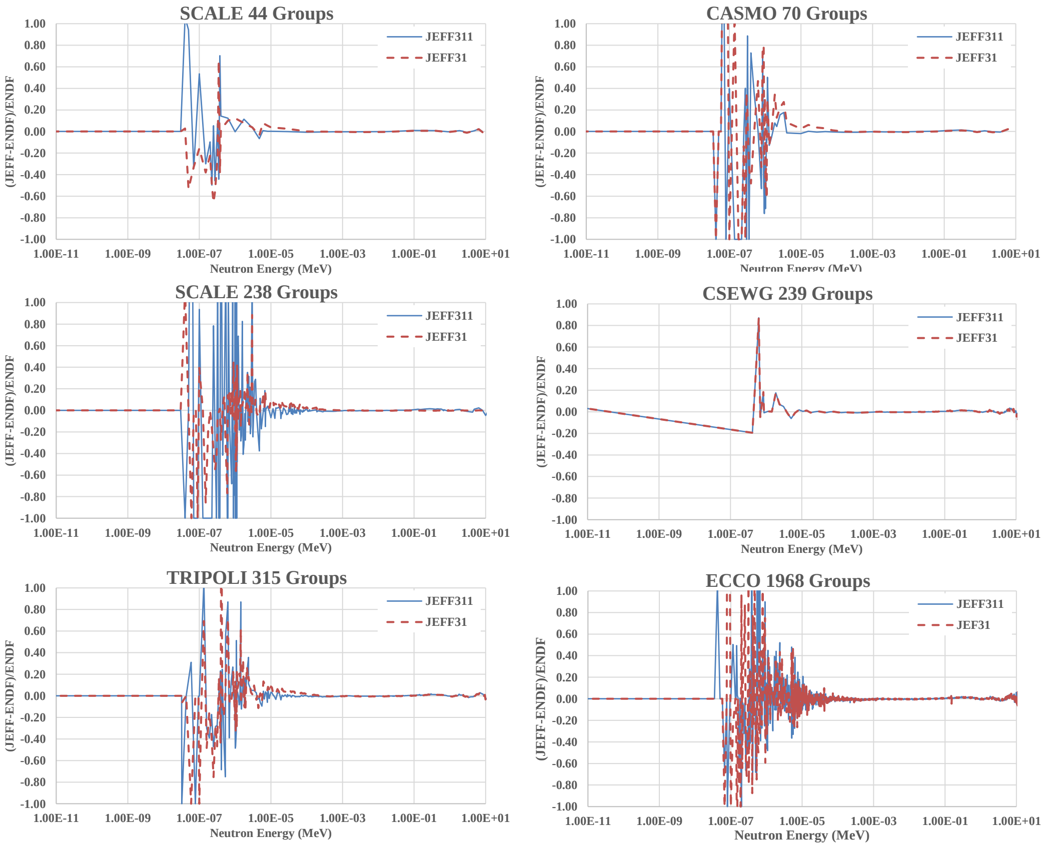

Figure 6.9: Difference of neutron spectrum in libraries

It can be seen that, in almost all the energy groups, the two JEFF libraries have a satisfactory consistency in the energy range over $10^{-5}\,MeV$, the relative difference is smaller than 5%. In the low energy range, most of the energy group structures cut off at $10^{-8}\,MeV$ or even $10^{-7}\,MeV$, so in the energy range lower than this limit, no data or deviations between the results can be observed. Between $10^{-7}\,MeV$ and $10^{-5}\,MeV$ fluctuations can be observed in all the charts. These fluctuations are caused by the statistical errors due to the low neutron counts of the calculations in these energy ranges for a DFR type of spectrum. Therefore, the nuclear libraries with the investigated energy groups structures analyzed can be considered consistent.

6.6.2.4 Neutron Energy Shift

The system of the DFR consists of different materials such as the fuel salt, the fuel tube wall (SiC), the coolant (lead), the reflector (lead) and the breeder material in the breeder blanket, as well as, other structural materials. Some of these materials contribute to inducing fission and generating power, while others cause an energy shift in the neutron spectrum due to other kinds of reactions occurring between these materials and the neutrons. This effect is discussed in this subsection by adding up new materials gradually, from an initial basic reactor model.

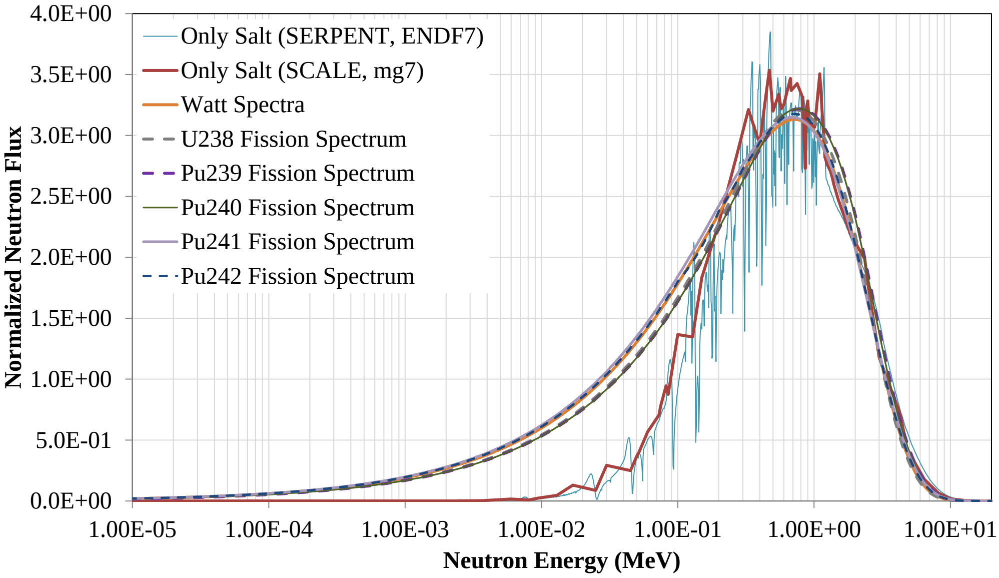

Figure 6.10: Neutron spectrum in U-Pu fuel salt vs. theoretical spectra

A fission spectrum is the energy distribution of prompt neutrons emitted from the fission process [Mot70, pp.142]. Together with the Maxwell fission neutron spectrum, the Watt spectrum is also in use today. The complete expression of the Watt fission spectrum is represented by the equation [Mad90, pp.202]:

$$\phi(E) = \frac{e^{-E_f/T_w}{}^{0.5}}{\pi E_f T_w} e^{-E/T_w} sinh\left(2\frac{(E_f E)^{0.5}}{T_w}\right) \tag{6.16}$$

where E is the laboratory neutron energy, E_f is the average fission-fragment kinetic energy per nucleon, T_w is the effective Watt temperature, which can be calculated or obtained from the experiments [Mad82] [Mad90] [Mad06]. The Eqn. 6.16 can be therefore reduced to [Mot70, pp.142]:

$$\phi(E) = 0.484 sinh(\sqrt{2E})e^{-E} \tag{6.17}$$

Therefore, the theoretical fission spectrum and the emitted neutron energy distribution (generated with data from JANIS 4.0 [SBD14]) are then compared with the calculated neutron spectrum in the fuel salt of the DFR reactor, which is shown in Fig. 6.10.

The “Neutron Flux per Unit Lethargy”-axis does not represent absolute values of the neutron spectrum, but only the normalized values converted with a z-score normalization:

$$Normalized\ Value = \frac{Original\ Value - Mean\ Value}{Standard\ Deviation}$$

After the normalization the minimum value is subtracted from all the values to make

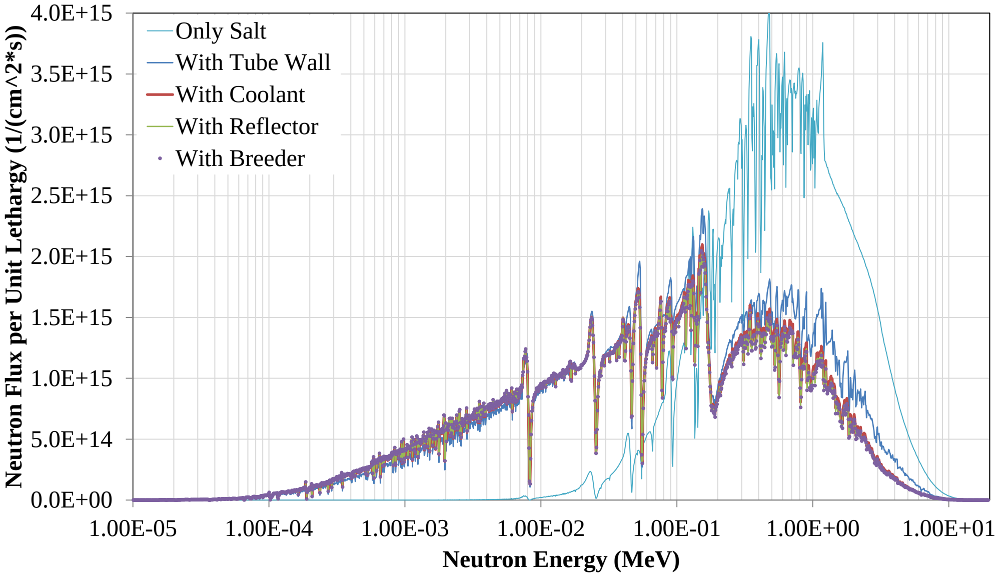

(a) Neutron spectrum while adding materials (linear, $10^{-5}\ MeV$ to $20 MeV$)

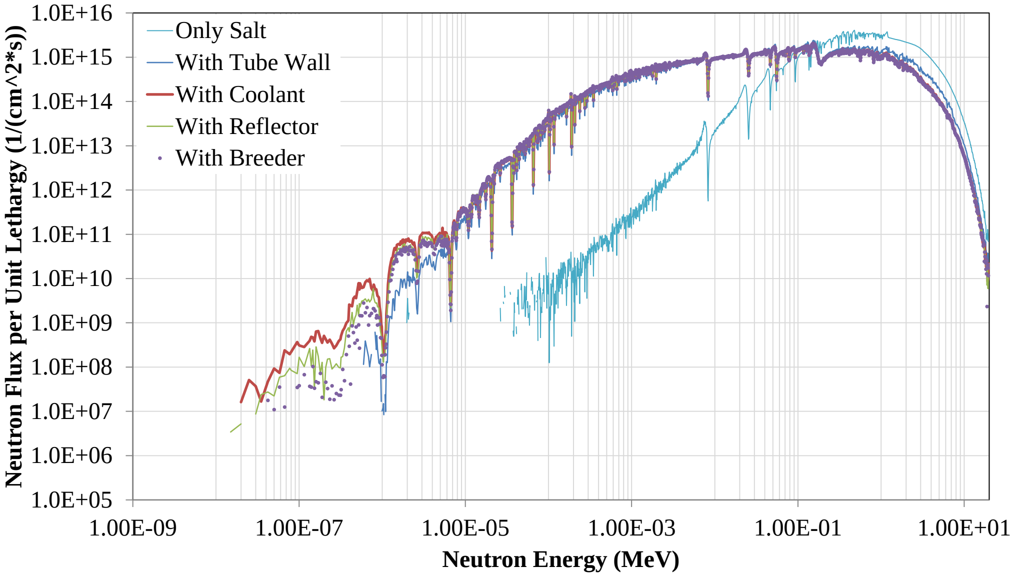

(b) Neutron spectrum while adding materials (logarithmic, $10^{-9}\ MeV$ to $20 MeV$)

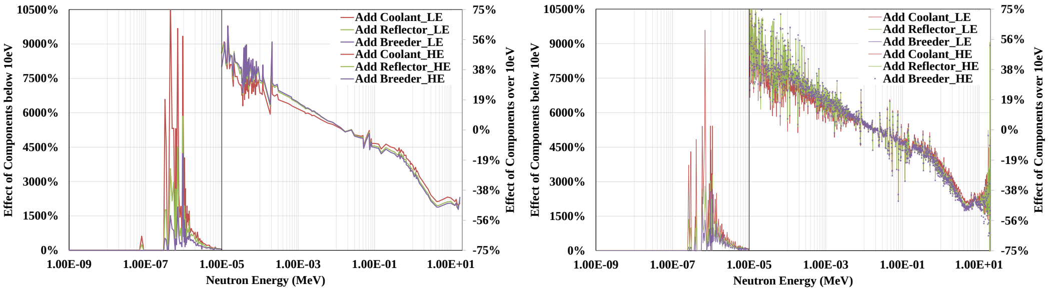

(c) relative difference refers to the spectrum in the fuel salt (left: 238-group, right: 1968-group)

Figure 6.11: Effect of the materials on the spectrum in the fuel salt

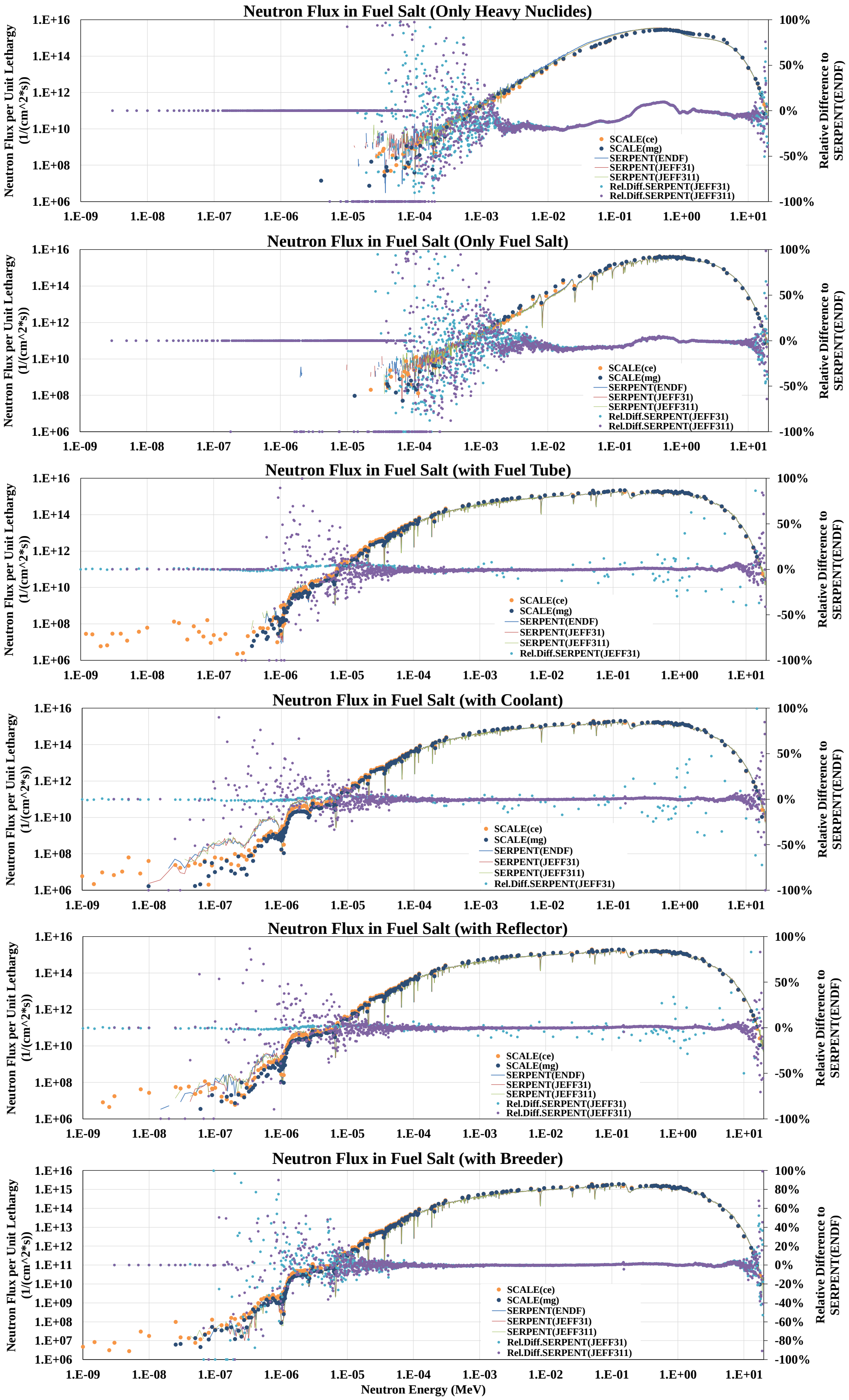

Figure 6.12: Dependency of neutron spectrum on neutron data libraries

them positive. The figure shows the neutron spectrum in the fuel salt, since fission occurs mainly there. The neutron energy axis is scaled to $10^{-5}\,MeV \sim 20MeV$ in order to check the spectra with more details in the regions of interest. The light blue and red curves describe the neutron spectrum of the fuel salt under the circumstance that in the reactor there is only this material: fuel salt, while all the other materials are replaced with simple air. The difference between these two curves is that the light blue one is generated by SERPENT with the ENDF/B-VII library with a 1968-energy-group structure and the red one is by SCALE also with the ENDF/B-VII library but in the multi-group mode (mg) with 238 energy groups. The orange curve, which almost overlaps with the other two curves, shows the Watt fission spectrum described above as applied to the DFR reactor in Sec. 6.16.

The rest of the curves are the emitted neutron energy distribution of the different fissionable materials present in the composition of the fuel salt, which are also normalized and plotted as reference. The emitted neutrons from the listed fissionable nuclides (^{238}U, from ^{239}Pu to ^{242}Pu) have their peak in the distribution at around $1MeV$.

It can be seen that over $1MeV$ all the spectra overlap perfectly each other. From $1MeV$ downwards, the calculated neutron spectra are perturbed, no matter whether it is calculated by SERPENT or by SCALE. In this energy range some significant troughs and crests can be observed around $10^{-2}\,MeV$. These are caused by elastic scatterings and the phenomena are interpreted later in Sec. 6.6.2.6. From $0.1MeV$ downwards, the spectra decrease rapidly compared to the theoretical spectra of the fissionable nuclides. The reason for this can be traced to the stark neutron absorption of the heavy nuclides in the fuel salt. Since only fuel salt is present in this calculation, moderation or scattering by other components in the reactor is not possible. The neutrons either escape the reactor or are absorbed.

Further results on the relationship between other materials and the neuron spectrum in the DFR are presented in Fig. 6.11. Figures 6.11(a) and (b) show, in both linear and logarithmic scales, how the DFR neutron spectrum evolves from the sole material fuel salt to the complete reactor by adding up different materials. The plotted data are results calculated by SERPENT 2 with the ENDF/B-VII library with a 1968-energy-group structure. In order to show the most interesting details, plot (a) depicts the neutron energy from $10^{-5}\,MeV$ to $10MeV$, while plot (b) utilizes an energy scale from $10^{-9}\,MeV$ to $10MeV$. During this process of progressively adding materials to the reactor core, the neutrons are increasingly moderated. The maximum values of the spectral shift occur from $1MeV$ to around $0.1MeV$. In the new spectra, which means here the spectra in the fuel salt with new adding materials, besides the troughs and crests mentioned in the last section between $5\times10^{-3}\,MeV$ to $0.1MeV$, more characteristic shape deformations can be observed, especially the one at about $0.2MeV$. This behaviour will also be explained in Sec. 6.6.2.6.

It is obvious that the existence of the fuel tube wall changes the neutron spectrum the most and forms the basic shape for the following spectra. The following spectra, that is, the spectra in the neutron spectrum after adding up the coolant, the reflector and the breeder, have only a slight influence on the neutron spectrum in the fuel salt. This can be better explained with the help of the two plots labelled as Fig. 6.11(c).

These two plot show details of the spectra that cannot be clearly distinguished in Fig. 6.11(a) and (b), for two different energy group structures.

The data in these two figures are shown as the relative difference of each spectrum (from "With Coolant" to "With breeder") with respect to the reference spectrum "With Tube Wall", because the spectrum "Only Salt" is far more different to these spectra and there is no need to do the comparison. Since the results span several orders of magnitude, each figure is divided at $10^{-5}\,MeV$ into two parts, left and right, for the low energy range and high energy range respectively. For this reason, each figure also has two y-axis presenting the percentage of the relative difference.

From higher energy to lower energy, that is to say, from $20MeV$ to $0.1MeV$, the neutron counts decrease by assembling new materials, while the counts increase from $0.1MeV$ to $10^{-5}\,MeV$. This means that with more materials in the reactor, the neutrons become scattered in greater numbers and, in consequence, losing their energy, they drop from the higher energy region to the lower energy region. In the energy range lower than $10^{-5}\,MeV$, however, where resonance and absorption dominate, more neutrons disappear when more materials, especially the breeder material is added, which is full of ^{238}U.

Figure 6.12 presents this phenomenon from another perspective. All the horizontal axes stand for neutron energy from $10^{-9}\,MeV$ to $20MeV$. The vertical axis on the left side is for the neutron spectrum and the right side shows the relative differences with respect to the reference values, for which the results calculated by SERPENT 2 with the ENDF/B-VII library (SERPENT(ENDF)) have been chosen. In each chart the results calculated by SCALE 6.1 in (ce) and (mg) modes, SERPENT 2 with ENDF, JEFF-3.1 and JEFF-3.1.1, as well as, the relative differences of the last two series are included. It can be seen that in most cases, which means in the energy range from $1MeV$ to the tail part (downwards $\sim 2\times10^{-3}\,MeV$, $\sim 10^{-2}\,MeV$, $10^{-4}\,MeV$, $10^{-4}\,MeV$, $10^{-4}\,MeV$, $10^{-4}\,MeV$), the different plots have shown a good consistency. Outside of the mentioned energy range, however, especially from the lower energy limit mentioned above till the end of the available neutron energy, the relative differences show a distribution with large values. This is mainly because of the statistical error due to low counts of neutrons, as has been indicated already several times before.

In the fourth ("with Coolant") and fifth ("with Reflector") plots more discrepancies can be observed in the energy range lower than $10^{-5}\,MeV$. the neutron spectra calculated by SERPENT are obviously higher than that by SCALE, though they have similar shapes.

There is another notable region in the figures. It can be noticed that in the first two plots ("Only Heavy Nuclides" and "Only Fuel Salt") the relative differences show fluctuations in the energy range near $10MeV$. However, in the next four charts, these fluctuations relocate in the energy range where the neutron spectra is mostly present, namely from $0.1MeV$ to $1MeV$. Since the curves show the relative difference between the results calculated with the ENDF and the JEFF libraries, this could reveal that due to the added materials, the additional reactions are the causes for these discrepancies coming from the nuclear data for these materials contained in each library. Considering only the JEFF-3.1 and JEFF-3.1.1 libraries, a better consistency

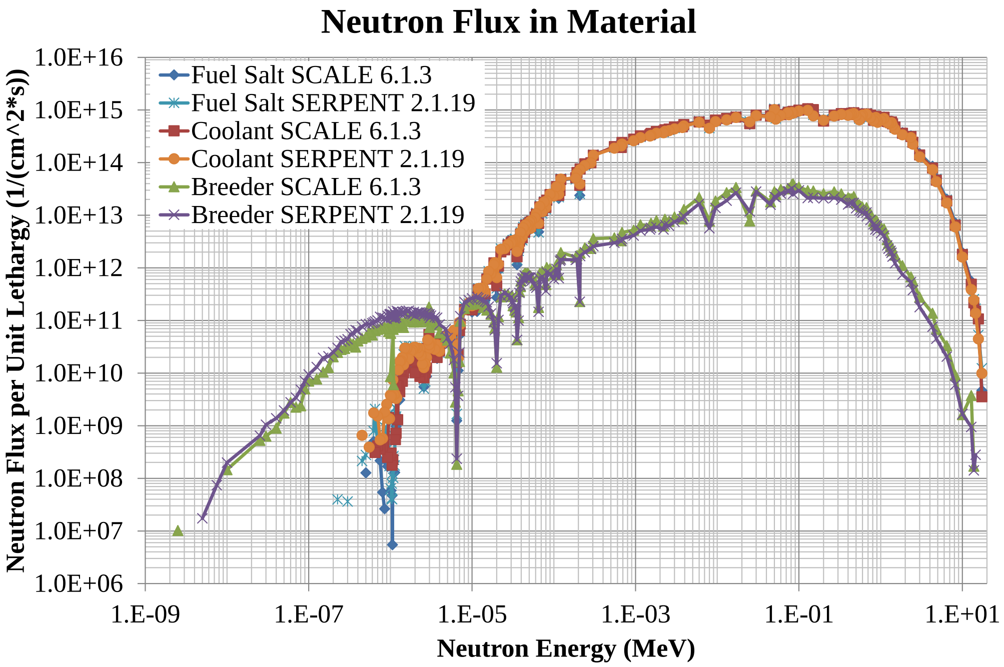

Figure 6.13: Neutron spectra in materials

between JEFF-3.1.1 and ENDF/B-VII can be concluded.

6.6.2.5 Different Materials

The previous section has introduced the neutron spectrum *in the fuel salt* as influenced by different materials, and this section is about the neutron spectrum calculated *in the different materials*. In Fig. 6.13 the neutron spectra in the fuel salt, in the liquid lead coolant, and in the breeder blanket are shown for comparison. Since the reflector lead and the coolant lead have the same properties and their thermodynamic conditions are close to each other, the spectrum in the reflector does not appear in the figure. All the neutron spectra in the figure are shown for a complete reactor with all the materials in each zone added, not separately calculated as in the previous section.

The spectra in the fuel salt and in the coolant lead overlap because of the spectrum homogenization effect in the central fission zone. It is noteworthy that the spectra in the breeder are shifted towrads lower energies, which is a manifestation of thermalization as the neutrons leak out of the fission zone. The troughs on the neutron spectra of the breeder are caused by their absorption, which is explained with details in Sec. 6.6.2.6.

6.6.2.6 Nuclear Reactions

The neutron spectrum of the DFR is not smooth at all compared to an ideal neutron spectrum due to the interactions between the nuclides in the reactor and the mostly fast neutrons. There are some significant crests and troughs that should be considered. Figure 6.14 shows 5 most significant troughs in the neutron spectrum and their corresponding characteristic peaks in the energy range from $10^{-4}\,MeV$ to 20 MeV (upper figure) and 6 in the energy range from $10^{-7}\,MeV$ to $10^{-3}\,MeV$ (lower figure). The emitted neutrons from fission reactions encounter first light nuclides inside the fuel salt composition, $^{37}\mathrm{Cl}$, and suffer elastic scatterings losing certain amount of energy. They then encounter the nuclides in the fuel salt tube material,$^{28}\mathrm{Si}$, and undergo elastic scattering again losing once more energy in the process. The smaller crests next to the troughs with lower energy indicate the neutrons after elastic scattering and subsequent energy loss. The troughs marked with numbers in the upper figure have the following characteristic energies:

1 $8.32{\times}10^{-3}\,MeV$: by $^{37}\mathrm{Cl}$;

2 $2.55{\times}10^{-2}\,MeV$: by $^{37}\mathrm{Cl}$;

3 $4.67{\times}10^{-2}\,MeV$: by $^{37}\mathrm{Cl}$;

4 $5.56{\times}10^{-2}\,MeV$: by both $^{28}\mathrm{Si}$ and $^{37}\mathrm{Cl}$;

5 $1.89{\times}10^{-1}\,MeV$: by $^{28}\mathrm{Si}$.

By analyzing the neutron spectrum in view of the the elastic scattering cross section of other important nuclides in the DFR reactor, one can reach the conclusion that the roughness of the spectrum observed in energies lower than $10^{-5}\,MeV$ is mainly caused by heavy metals like $^{238}\mathrm{U}$ and from $^{239}\mathrm{Pu}$ to $^{242}\mathrm{Pu}$, which exist in the fuel salt and breeder blanket. The roughness at higher energies is caused by isotopes of Pb, such as $^{204}\mathrm{Pb}$, $^{206}\mathrm{Pb}$, $^{207}\mathrm{Pb}$, and $^{208}\mathrm{Pb}$ present in the coolant and the reflector.

The troughs in the lower energy region of the neutron spectrum shown in Fig. 6.14 (lower plot) are very significant and a consequence of the resonant absorption of neutrons by $^{238}\mathrm{U}$ and other heavy nuclides, among which the most important ones are $^{239}\mathrm{Pu}$ to $^{242}\mathrm{Pu}$. The most interesting difference between the absorption troughs and elastic scattering ones is the small crests next to the troughs at lower energies, which exist only for elastic scattering reactions.

For the spectrum in the lower energy region there are also some recognizable troughs, namely:

1 $\sim 0.2eV$ to $\sim 0.4eV$: troughs packet by $^{239}\mathrm{Pu}$ and $^{241}\mathrm{Pu}$;

2 $1.05eV$: by $^{240}\mathrm{Pu}$;

3 $2.66eV$: by $^{242}\mathrm{Pu}$;

4 $6.75eV$: by $^{238}\mathrm{U}$;

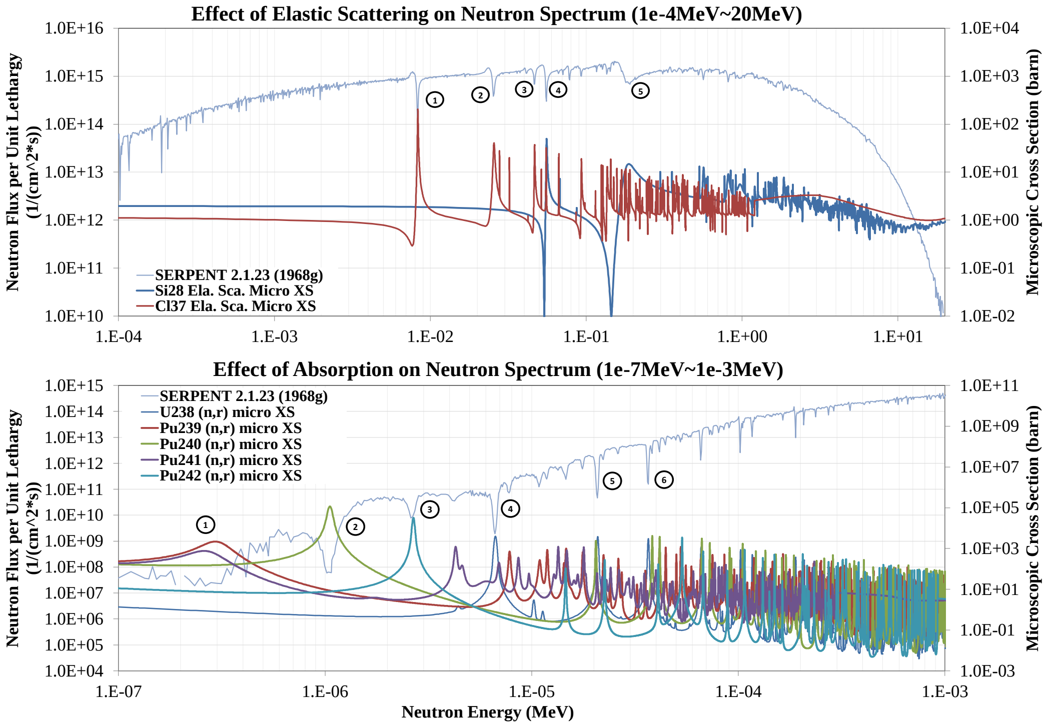

Figure 6.14: Characteristic peaks

5 $20.0eV$: troughs packet mainly by ^{238}U and ^{240}Pu ;

6 $38.4eV$: troughs packet mainly by ^{238}U and ^{240}Pu .

A less significant roughness, with smaller troughs and crests, can also be recognized in other energy regions and explained by the cross section values of certain nuclides at these energies, but they are not as important for the DFR as the ones discussed above, and will not be analyzed here.

The conclusions presented in this subsection have considered the presence of certain nuclides as the main influence on the shape of the neutron spectra analyzed caused by the magnitude of their macroscopic cross sections and the type of reactions they mainly have with the neutrons in the DFR. Since the conclusions reached have been only qualitative, that is, without data on reaction rates, the values of these macroscopic cross sections are not provided in the thesis.

6.6.3 Spatial Distribution of the Neutron Flux

The neutron flux is defined as the product of the neutron density $n(E, r)$ and its velocity $v(E)$:

$$\phi(E, r) = n(E, r)\ v(E)$$

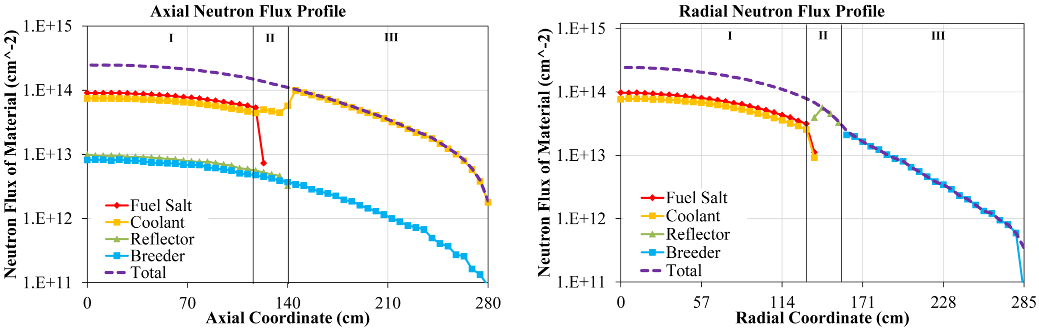

(a logarithmic

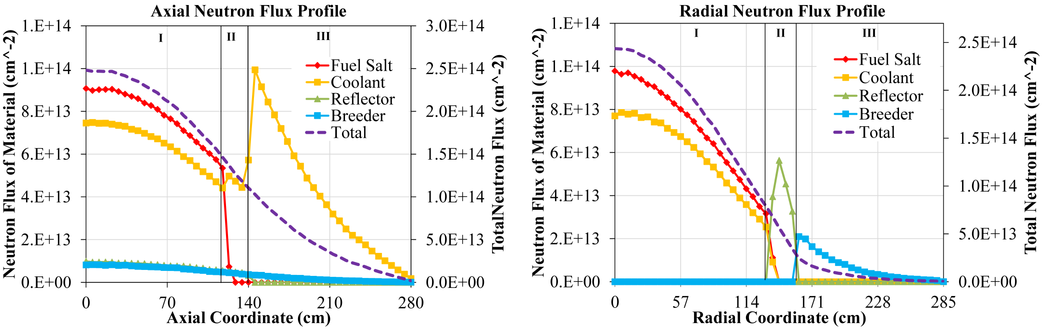

(b normal

Figure 6.15: Spatial neutron flux distribution for U-Pu fuel in the reactor

Therefore the neutron flux in the core describes the spatial distribution (r) and energy distribution (E) of the neutrons inside of the core. The spatial flux distribution is important for a neutron physics analysis, because is determines the distribution of the reaction rates and, ultimately, of the power density generated.

The neutron flux distribution integrated over the entire neutron spectrum $\phi(r)$ is shown in Fig. 6.15 for the symmetric DFR model. The results are shown in both axial and radial directions. The flux is normalized over the volume and has units of $1/(cm^2 s)$. Though each figure is divided into three regions, the meaning of the regions are different. In the "Axial Flux Profile" region I stands for the fission zone ($0 \sim 120cm$), region II is for the top outlet plenum ($121 \sim 140cm$) while the remaining region III means the top liquid lead plenum ($141 \sim 280cm$). In the "Radial Flux Profile" region I starts from the center of the fission zone to its boundary ($0 \sim 135cm$), region II is marked for the reflector ($136 \sim 155cm$), and finally region III is for the breeding blanket ($156 \sim 280cm$). Since the plots show the flux distribution inside the reactor, it is not surprising to find flux in some certain materials existing in all the regions where the materials involved are located, e.g. breeding material.

The boundaries of the reactor zones, such as both sides of the reflector or both sides of the in-/outlet plenum, show flux discontinuities of the flux in the different materials, but the total flux, is obviously continuous across these boundaries. In the "Axial Flux Profile" the descending neutron flux in the fuel salt material towards to the outlet of the reactor is, therefore, expected. A higher neutron flux observed in the outlet plenum and also in the liquid lead plenum means that the neutrons accumulate and reflect inside of the coolant lead without being absorbed or escaping. Compared to the axial distribution, the flux in the fuel salt and in the coolant diminishes at the boundary of the inner surface of the reflector, while the flux in the reflector rises inside of the reflector and the flux in breeder rises at the outer surface of the reflector, because of their ring-form geometry.

6.7 Reaction Rates

The general definition of the reaction rate density as a function of energy E and location r is given in reference [LB01, pp.61] as the product of the macroscopic cross section for the certain reaction and the neutron flux:

$$R(E,r) \;=\; \Sigma(E,r)\;\phi(E,r)$$

Both spatial and energy dependent reaction rate are calculated by SERPENT 2 and SCALE 6. In order to reflect the different reaction rates in various materials and volumes, the volume and energy integrated reaction rate density is calculated. The calculation uses the collision estimate of the neutron flux by averaging the integration of the mentioned product over all the volume and energy groups of interest [Lep13, pp.95]:

$$R = \frac{1}{V}\int_V \int_0^\infty \Sigma(r,E)\phi(r,E)d^3rdE \tag{6.18}$$

where R is the reaction rate density, V is the volume for each reaction in the reactor and $\Sigma(r,E)$ represents here for different macroscopic cross sections to the corresponding reactions. The most important reaction rate densities calculated in the DFR are listed in Tab. 6.8.

All the plots in Fig. 6.16 show the over volume normalized reaction rate density in the entire reactor's volume perpendicular to the plotted axis. The axial coordinate of the plots extends from the center of the fission zone (0∼120cm) through the top of the outlet plenum (121∼140cm) until the top of the liquid lead plenum (141∼280cm), while the radial coordinate starts from the center of the fission zone (0∼135cm), through the reflector (136∼155cm), the breeding blanket (156∼280cm), and reaches the reactor vessel wall (281∼285cm). Since each direction covers three structural parts of the reactor, these parts are separated with vertical lines in the plots.

In the Fig. 6.16 (c) it is possible to see that the neutron capture reaction density in the fuel salt along the axial direction is concentrated in the fission zone and extends into the outlet plenum. At the boundary between the outlet plenum and the liquid lead plenum a slight rise of reaction rate density can be observed. This can be attributed to the reflection of neutrons from the liquid lead plenum because this part is full of liquid lead and has a thickness about ca. 140cm.

The neutron capture reaction rate density in the breeder is smaller than that in the

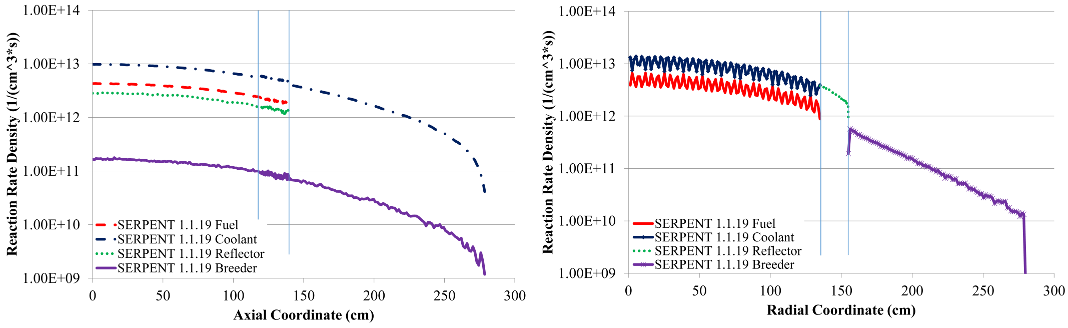

(a Axial, total

(b Radial, total

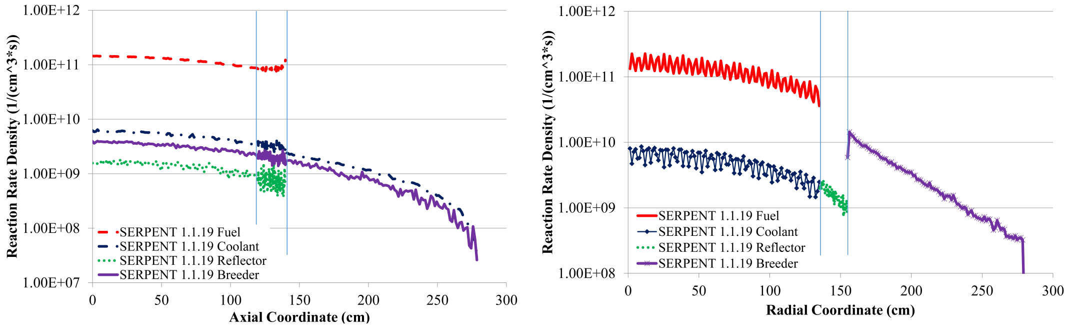

(c Axial, capture

(d Radial, capture

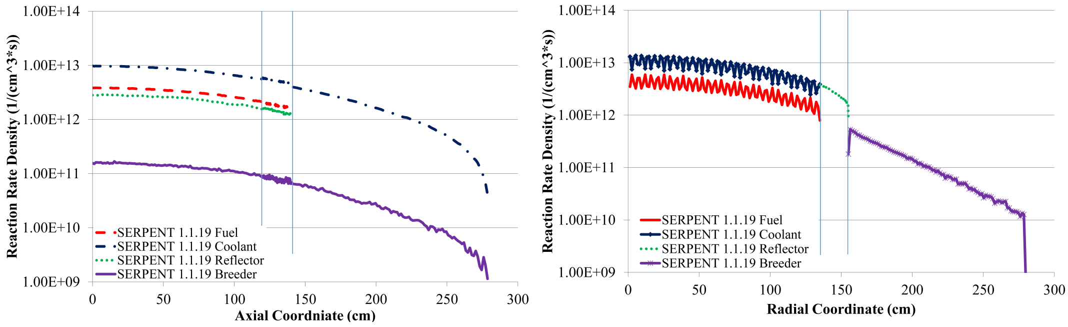

(e Axial, elastic scattering

(f Radial, elastic scattering

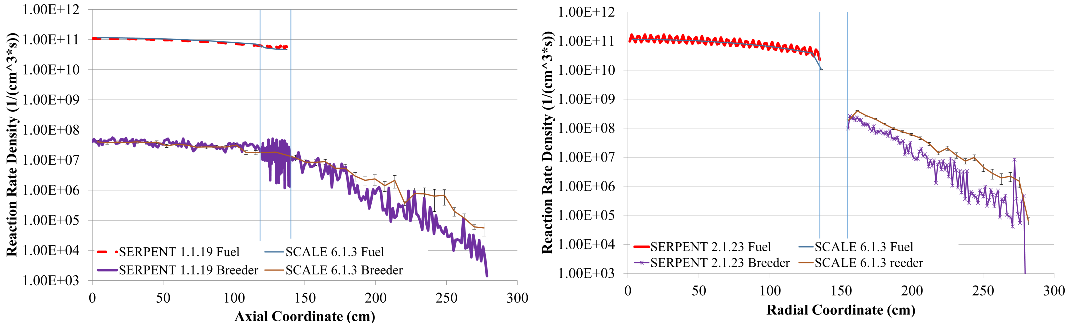

(g Axial, fission

(h Radial, fission

Figure 6.16: Reaction rate density

Reaction	SERPENT 2		
	ENDF-B/7	JEF-3.1	JEFF-3.1.1
Total flux	1.21065E23	1.21205E23	1.21195E23
$\mathrm{R}_{f,^{238}U}$	5.47027E18	5.41947E18	5.41835E18
$\mathrm{R}_{f,^{239}Pu}$	5.93034E19	5.88782E19	5.88464E19
$\mathrm{R}_{f,^{240}Pu}$	3.70056E18	3.69071E18	3.68786E18
$\mathrm{R}_{f,^{241}Pu}$	1.96906E19	1.97925E19	1.97863E19
$\mathrm{R}_{(n,\gamma),^{238}U}$	1.03884E20	1.03547E20	1.03629E20
$\mathrm{R}_{(n,\gamma),^{239}Pu}$	2.81673E19	2.83051E19	2.82804E19
$\mathrm{R}_{(n,\gamma),^{240}Pu}$	1.09305E19	1.07358E19	1.07428E19
$\mathrm{R}_{(n,\gamma),^{241}Pu}$	4.28807E18	4.52118E18	4.53306E18
$\mathrm{R}_{f,total}$	8.98866E19	8.97723E19	8.97723E19
$\mathrm{R}_{(n,\gamma),total}$	1.62823E20	1.62504E20	1.62520E20
rel.err.	<0.00127	<0.00113	<0.00151

Table 6.8: Reaction rates (1/s) of selected nuclides of U-Pu fuel

coolant because fewer neutrons are able to pass through the lead coolant and reach the breeder blanket.

The elastic scattering reaction (Fig. 6.16 (e)) is highest in the coolant. This causes also the highest count for the coolant in the total reaction rate density (Fig. 6.16 (a)). In fact, because the elastic reaction rate density is so high, it dominates the shape and the trend of the total reaction rate density. Different reaction rate densities fluctuate in the outlet plenum, this is because, compared to the fission zone, the flow direction in this region of the fuel salt is reversed with respect to the coolant lead flow.

The fission reaction density (Fig. 6.16 (g)) is highest in the fuel salt, while that in the breeder is about four orders of magnitude lower. The reaction rate density of the fuel salt and the breeder calculated by SERPENT and SCALE are consistent both in the fission zone and in the outlet plenum. But in the coolant plenum region, because the counts for the fission reaction are already very low, larger statistic errors appear and, therefore, the results obtained with these two codes have discrepancies. A more intuitive view of the fission reaction rate is shown in Fig. 6.17.

For the plots (Fig. 6.16 (b), (d), (f), (h)) along the radial direction, all the values are taken only between the altitude of Âś120cm and averaged over this volume, which is exactly the fission zone and excludes the in-/outlet plenum or the liquid lead plenum. The boundaries of the materials can be observed by the sudden change of the reaction rate densities. The periodic variation of the reaction rates in the fuel salt and the coolant is due to the periodic lattice of the fuel salt tubes in the fission zone.

For the capture reaction the reaction rate density (Fig. 6.16 (d)) of the fuel salt is much higher than the other material in the fission zone. The number of the capture reaction in the breeder is less than that in the fuel salt and it decreases faster than any other materials, because in the breeder the neutron density is already quite low.

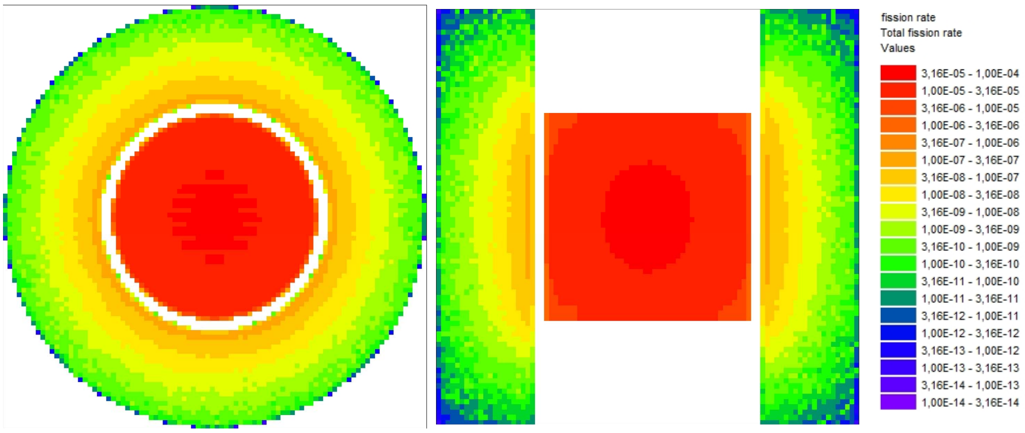

Figure 6.17: Visualization of fission reaction rate

The coolant and the reflector hang together smoothly at the boundary of the fission zone and the reflector zone, since they are actually the same material.

The elastic scattering reaction rate density (Fig. 6.16 (f)) in the radial direction acts similarly to that in the axial direction, and still dominates the total reaction rate density (Fig. 6.16 (b)).

The fission reaction rate density (Fig. 6.16 (h)) stops at the boundary of the fission zone and also has a satisfied consistency between the results from SERPENT and SCALE. The reaction starts again in th breeder and decreases fast towards the outer boundary of the reactor. The short of counts in the breeder bucket is again the reason for the difference between codes and for the larger error. This can also be seen in Fig. 6.17

6.8 Power Distribution

The power distribution of the DFR reactor is obtained from the Monte-carlo calculated counts of the deposited power generated by fission reactions in the materials. The fission power distribution is, therefore, shown in Fig. 6.18. The the power distributions in the coolant, reflector and the structures of the reactor are zero, while the distributions in the fuel in the core, in the fuel in the in-/outlet plenum regions, and in the breeder blanket are represented in both radial and axial directions. Figure 6.18(a) presents the radial and axial distribution of the fission power, as well as a color-coded plot of the fission power distribution in the whole reactor in plot (b). The longitudinal power distribution can be fitted as

$$P(z) = C \cdot \left[2.22 \cos \left(\frac{\pi z}{H + 2\delta} \right) + 3.16 \right], \tag{6.19}$$

where C is a constant containing the average reactor P_{avg} that multiplies a shape expression. The term H represents the half height of the reactor core and δ is its extrapolated length.

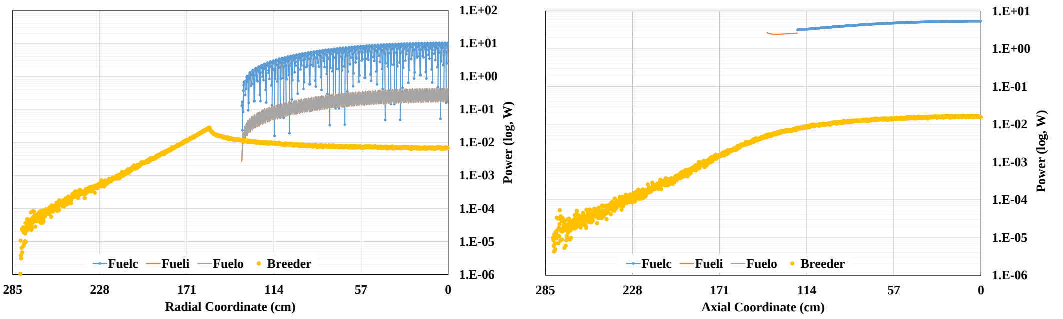

(a Fission power in the reactor

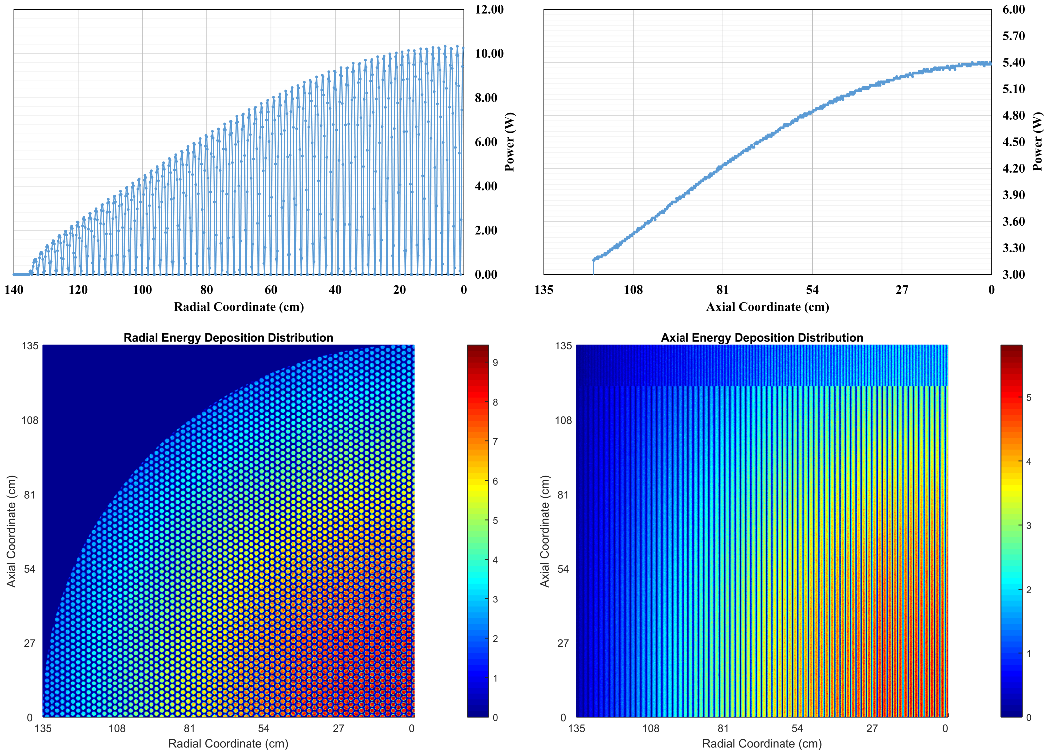

(b Fission power in the core

Figure 6.18: Fission power distribution

6.9 Conclusions

In the k_{eff} calculation the first parameter to be defined should be the total number of fuel tubes. Although the number is calculated in Sec. 5, it only covers complete fuel tubes. At the boundary of the core, however, there must be *incomplete* fuel salt tubes between the complete fuel tubes and the boundary. Even though these incomplete fuel salt tubes do not exist in the actual DFR core, the fuel salt in them assumed in the model can make a difference in the value of the calculated k_{eff}. This is especially important when the model for criticality calculations with the neutronic codes is developed by setting the lattice of the fuel salt tubes with an ***infinite*** 3D x- or y-type hexagonal prismatic lattice, or by setting up a ***finite*** array of fuel tubes larger than the horizontal geometric cross section of the reactor in order to leave no blank spaces. For this reason, the differences observed in the comparisons between code results may not be significant, but the results of the calculated k_{eff} may over estimate its vale compared to an actual DFR.

The neutronic analysis of the DFR reactor covered the entire geometry including the fission zone, reflector and breeder blanket. In the static calculation performed at the beginning of this chapter, the criticality of the DFR design was firstly verified and assessed with the codes SERPENT and SCALE. The results of this study show that the criticality of the DFR design can be ensured, the relative differences between the results calculated by different codes or with different nuclear data libraries are small enough so that the results can be considered as consistent.

The group constants as well as other information related to the neutronics characteristics of the DFR were then obtained from the Monte-Carlo based calculation results. With this information, a theoretical neutronic analysis of the reactor can be carried out and detailed models of the DFR can be developed.

The next step entailed the verification of the neutron spectrum, which, according to the design, is located in the high neutron energy region. This chapter concentrated on discussing the reasons for the shape of the calculated spectra and attempted to explain the differences caused by codes, energy group structures, reactor materials, and nuclear data libraries. The final spectrum is proven to have a satisfactory consistency in every energy region.

Since the DFR structure has several well-defined zones and each zone consists of a specific combination of materials, each zone has a different impact on the neutron spectrum as a result of the reaction rates between the neutrons and these materials. This impact was studied in the energy shift of the DFR spectrum, and the results allowed to identify those materials with the highest impact on the neutron spectrum in the different zones of the DFR.

Chapter 7

Sensitivity Analysis

7.1 Nuclide Importance

For a fuel mixture containing various nuclides, it is interesting to find out which nuclides are the most important ones, or have the largest influence on the k_{eff} for a certain fuel salt composition. The macroscopic cross sections are the most important nuclide's property that determines its importance in the criticality of the reactor. The macroscopic cross sections are a function of the temperature and material density and, therefore, depend strongly on the core's conditions.

In this section the importance of the nuclides is investigated based on the assessment of the effect of relative changes of the nuclides' cross sections on the relative changes in the system's multiplication factor k_{eff}. The investigation is carried out by using the **S**ensitivity **A**nalysis **M**odule for **S**CALE (SAMS) module called TSUNAMI-3D [RHE^{+}03] embedded in SCALE, which uses, for this purpose, linear perturbation theory [RPJW11]. The SAMS module is specialized in providing an evaluation of the sensitivity of the k_{eff} to the nuclear cross section data used in the calculation. The complete sensitivity coefficient [RPJW11, F22.2.8] is defined for a given nuclide i, reaction x and energy group g as

$$\left(S_{k,\Sigma^i_{x,g}}\right)_{complete} = \left(S_{k,\Sigma^i_{x,g}}\right)_{explicit} + \left(S_{k,\Sigma^i_{x,g}}\right)_{implicit}$$

that is, the total sensitivity coefficient is the sum of an explicit and an implicit sensitivity coefficient. The original complete expressions can be found in the original references and will not be cited here.

The explicit part of the sensitivity coefficient shows the relationship between the sensitivity of the k_{eff} to the "problem-dependent resonance self-shielded multi-group cross section data used in the critical analysis" while the implicit part is "the sensitivity of the resonance self-shielded multi-group cross section data to the data input to the resonance self-shielded calculation" [RPJW11, F22.2.1]. This means that for a fast reactor the explicit part is sufficient, for the resonance self-shielding of the nuclides in the fuel salt has no significant impact, and the implicit part is not strictly

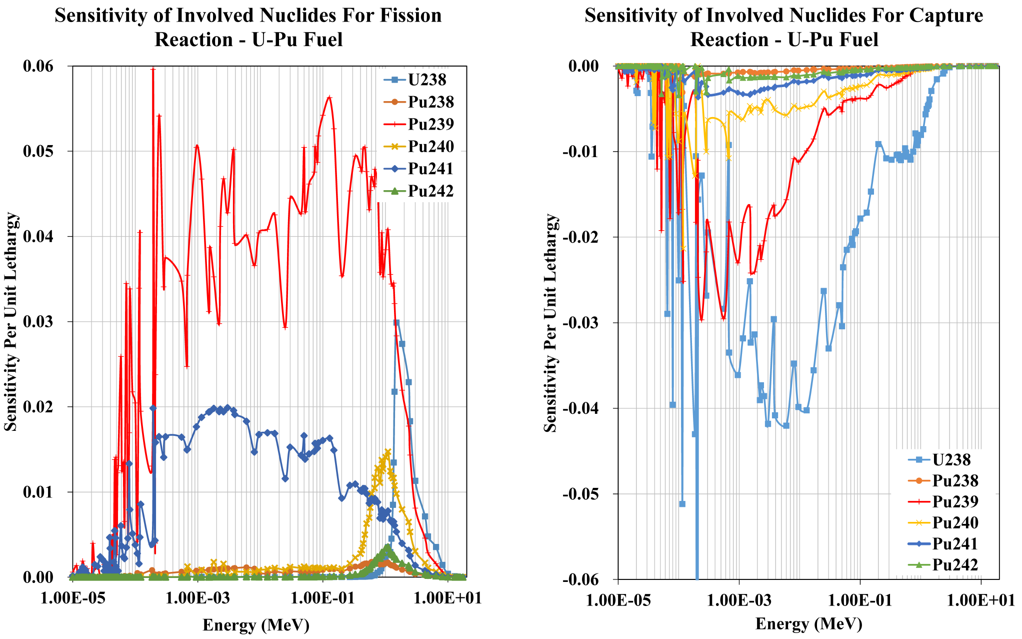

Figure 7.1: Sensitivity of k_{eff} with regard to the most important nuclides in U-Pu fuel

necessary.

Next the sensitivity analysis is carried out for the two fuel salt options of the DFR. The total sensitivity of each actinide will be determined and the values of the explicit and implicit parts will also be given.

Based on an analysis carried out previously [WSM15], Fig. 7.1 shows the total sensitivity coefficient for the U-Pu fuel salt. The left plot in the Figure for the fission reaction shows that in the energy range from $10^{-5}\,MeV$ to $20 MeV$ the value of k_{eff} is most sensitive to the fission cross section of $^{239}\mathrm{Pu}$ and $^{241}\mathrm{Pu}$, while $^{238}\mathrm{U}$ is only significant in the energy range above $1 MeV$. The fourth significant nuclide is $^{240}\mathrm{Pu}$, which becomes influential in the energy range from $0.1 MeV$ to $20 MeV$.

On the right plot the sensitivity to the macroscopic capture cross sections of $^{238}\mathrm{U}$, $^{239}\mathrm{Pu}$ and $^{240}\mathrm{Pu}$ clearly shows that they are the most important for the determination of k_{eff}. The sensitivities are negative because a reduction in the macroscopic neutron capture cross sections will, as expected, increase the value of k_{eff}. Other nuclides in the fuel show a smaller impact on the k_{eff} for neutron capture, at least in the energy range of interest.

Since the value of S reflects the relationship between the macroscopic cross sections (see Fig. 7.2 left) and the value of k_{eff}, for the fission reaction, the calculated sensitivities, on one hand, mirror the differences in the magnitude in the microscopic fission cross sections of $^{239}\mathrm{Pu}$ and $^{241}\mathrm{Pu}$, which both have a larger fission cross section over the DFR energy spectrum compared to the other fissionable nuclides. On the other hand according to Tab. 5.1, the number density of $^{239}\mathrm{Pu}$ is much larger than that of any other Pu nuclide, so, again, $^{239}\mathrm{Pu}$ is destined to dominate the sensitivity chart.

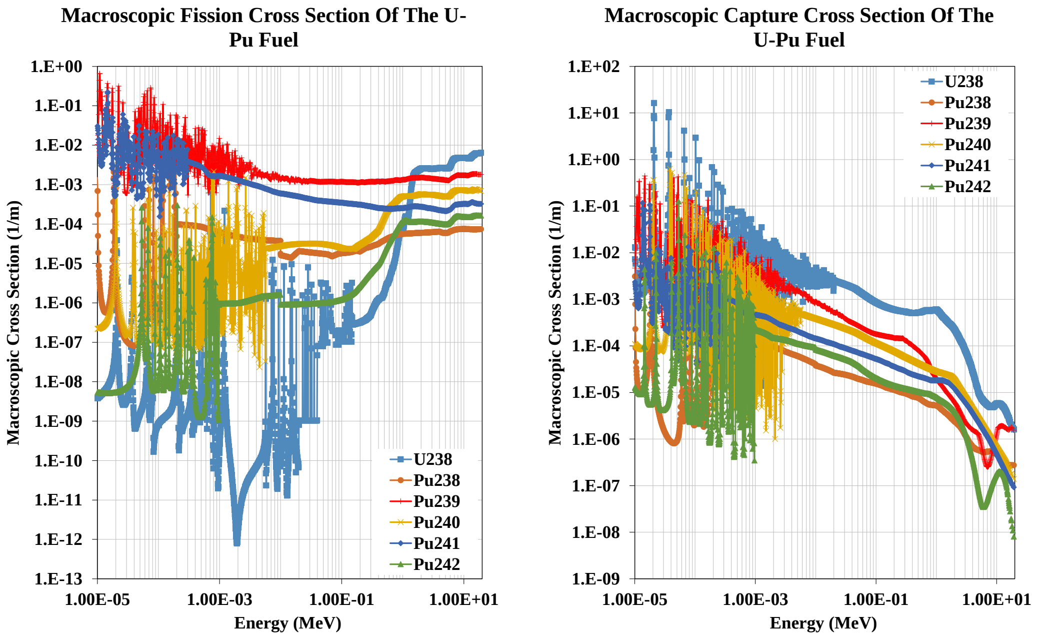

Figure 7.2: Macroscopic cross section of fissionable nuclides in U-Pu salt fuel

The macroscopic fission cross section of ^{238}U becomes comparable to that of ^{239}Pu only above $1 MeV$, which explains the late, noticeable contribution of ^{238}U in the plot.

For the neutron capture reaction, it can be observed that in the energy range till about $10^{-4}\, MeV$ the curves are mixed together and cannot be clearly distinguished. In the higher energy region the order and magnitude of the curves have the same trend as the macroscopic cross sections of the nuclides (see Fig. 7.2 right), analog to the analysis for the fission reaction above.

The implicit sensitivity coefficient calculated in this analysis is about a hundred times smaller than the explicit sensitivity coefficient for both fission and capture reactions for the fuel salt actinide, which means that for the U-Pu fuel salt composition in the DFR, the explicit sensitivity is accurate enough to describe the relationship between the cross section data and the k_{eff}.

7.2 Geometry Feedback Coefficient

7.2.1 Description

This part of the sensitivity analysis is mainly based on the results presented in a previously published work part of this thesis [WSM15]. As mentioned in section 5.1, names and definitions of the components in the DFR reactor are already given based on Fig. 5.2, 5.1 and 5.3. The aim of this series of calculations is to find out how consistent the geometric parameters of the DFR are.

1. Radius of fuel tube
    - Inner radius of fuel tube: 5mm-8.5mm, ref: 7mm, outer radius remains
    - Outer radius of fuel tube: 7.5mm-10.5mm, ref: 9mm, inner radius remains
    - Inner radius of fuel tube: 7mm-11mm, ref: 7mm, thickness remains
2. Pin pitch: 18mm-30mm, ref: 22mm
3. Radius of fission zone: 1300mm-1700mm, ref: 1500mm, divided in two cases: the size of breeder zone changes together and the size of breeder zone remains conscent as buffer
4. Thickness of reflector: 0mm-300mm, ref: 150mm
5. Thickness of breeder: 240mm-1500mm, ref: 1030mm
6. Other Parameters of the Breeder Zone
    - Number of breeder coolant tubes: 0-10, ref: 6
    - Radius of breeder coolant tube: 5mm-35mm, ref: 12mm, thickness of tube wall remains
    - Radius of breeder coolant tube ring: 1850mm-2550mm, ref: 2210mm

All the Monte-Carlo based calculations were carried out with 500k neutrons in 100 active cycles and 100 inactive cycles.

7.2.2 Results

Since the DFR is still in its conception stage, geometric dimensions can still vary in future design refinements. This series of calculations for the geometry is aimed to understand the design of the DFR better. And with these calculations, it is better to evaluate other results in this chapter, since the information on the sensitivity of the geometric parameters is obtained. In the upcoming section the serial numbers in the description are referred.

Figure 7.3(a) shows the relationship between three geometric parameters of the fuel salt tube and the k_{eff}, which corresponds the cases in the legend. It has to be mentioned that the first blue line "d inw. increases"(Nr. 1) refers the case in which the fuel tube inner radius is changed, while the outer radius remains unchanged; the case on the second line "d outw. increases"(Nr. 2) with red lines means the opposite process, and the last case "outer r increases"(Nr. 3), with a green line, means that both radii change together, while the thickness of the tube wall remains unchanged. The statistical errors of the result are around 2×10^{-4} ; hence they are too small to be displayed in the chart. It can be seen that a fuel salt tube with a larger inner radius (Nr. 1) can contain more fuel salt in it (without considering limits to its structural strength, of course), which enhances the core's reactivity and increases the value of k_{eff}. In contrast, when the inner radius remains constant, a fuel salt tube (Nr. 2) with a larger outer radius increases the thickness of the tube, which could not

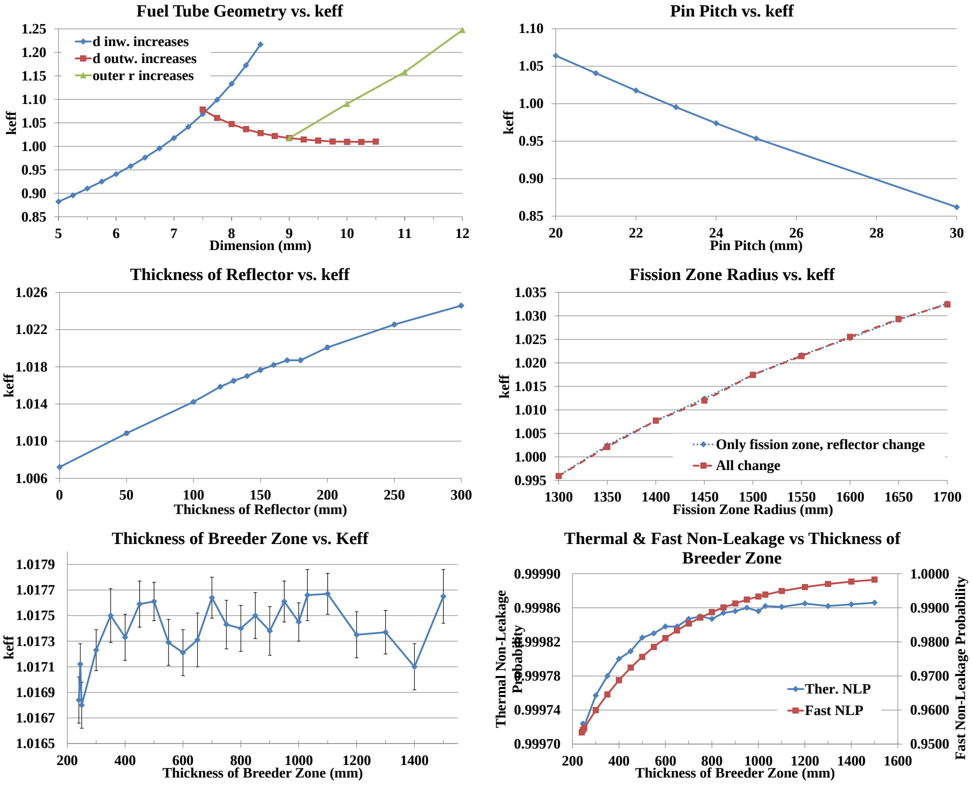

Figure 7.3: Geometry coefficients (top: a, b; middle: c, d; bottom: e,f)

only hinder the transport of neutrons through it, but also the neutrons emitted from fission have to travel a longer distance to interact with other fissile material and the average density of fissile material in the reactor decreases.

When the volume of the fuel tube increases but the wall thickness remains unchanged (Nr. 3), the increase of k_{eff} is smaller compared to (Nr. 1), because the tube wall in (Nr. 3) is thicker than that in (Nr. 1) in this case.

Figure 7.3 (b) shows how the k_{eff} changes as a function of the pin “pitch”. The errors of the results are smaller than 2×10^{-4}; hence they are too small to be displayed. The reason for the behavior of the curve is also related to the fuel-to-coolant ratio in the volume of the fission zone. With a larger pin pitch there will be less fissionable material in the fission zone and neutrons will need more time to travel to interact with fissionable material in the neighboring fuel salt tubes.

The effect due to the thickness of the reflector on the k_{eff} is shown in Fig. 7.3(c). The statistical errors of the result are around 2×10^{-4}; hence, they are too small to be displayed. Though the geometry sensitivity coefficient of the thickness of the reflector over the whole investigated thickness range (0∼500mm) is changing from 7.280pcm/mm (0∼50mm) to 2.360pcm/mm (450mm∼500mm), this value is still about ten times larger than the joint temperature coefficient caused by the density change of both coolant and reflector, as shown in Section 7.3.

Therefore, for reactivity fine tuning it may be possible to have a flexible reflector with changing effective thickness by dividing it into concentric layers and permitting or stopping the liquid lead from flowing into some of the layers.

From Fig. 7.3 (e) and (f) it can be seen how the thickness of the breeder blanket influences the breeding efficiency. Since the ^{238}U of the breeder should absorb or reflect most of the incoming neutrons, the non-leakage probability is one of the most important variables for the investigation. The thermal and the fast non-leakage probability rise for thicker breeder blankets, as expected. Beyond about 40cm of breeder thickness the marginal gain in the fast non-leakage probability becomes progressively less attractive.

7.3 Thermal Feedback Coefficient

7.3.1 Description

This part of the analysis of the thermal feedback coefficient is based mainly on the previously published approach as part of this thesis [WSM15]. In order to reduce the error caused by statistical fluctuations, each calculation in this section performed with SERPENT 1.x and 2.x consists of 5 separate runs with different random numbers, which are then averaged. Each run was carried out with 5×10^5 neutrons in 100 active and 100 inactive cycles. The data library ENDF-VII was selected with a 238 energy group structure. The calculation parameters for KENO were the same as those used for the k_{eff} calculation.

Independent temperature effect calculations of different materials in the reactor are compared to the standard design temperature reference from Tab. 3.3 in order to investigate, in particular, the behavior and feedback of the individual reactor zones and components due to a change of the material density and temperature. The total temperature coefficient (including Doppler and Density) is provided. The results are then combined to determine the joint temperature response of the lead in both coolant and reflector. For this purpose two cases are considered, one with the lead in both coolant and reflector at identical temperature, while the second one allows for a temperature difference of 300K between the lead in these two different zones.

7.3.2 Results

The results of the combined temperature reactivity feedback (i.e. density plus Doppler Effect) of the individual reactor components are reported in Tab. 7.2 and the plots for the different materials are shown in Fig. 7.4. The temperature coefficient is defined as

$$\alpha_X = \frac{dk_{eff}}{dT_X}\$ = \frac{d\rho}{dT_X} \tag{7.1}$$

where the X signifies the property of a certain material, such as the fuel salt, the coolant lead or the reflector lead and ρ stands for the reactivity. The plots of the

Region	Temperature range
Independent temperature effect	
Fuel	1300K-1700K
Coolant	1100K-1400K
Reflector	1100K-1400K
Breeder	1100K-1300K
Joint temperature effect (identical temperature)	
Coolant/Reflector	1100K-1400K
(coupled)	1100K-1400K
Joint temperature effect (with temperature difference)	
Coolant/Reflector	1100K-1400K
(coupled)	800K-1100K

Table 7.1: Calculation design for temperature effect of U-Pu fuel

	SERPENT 1	SERPENT 2	KENO-VI
Fuel	−40.30	−40.26	−31.74
Coolant	0.3609	0.2603	0.2447
Reflector	−0.1269	−0.068 83	−0.1009
Breeder	−0.1885	−0.2224	−0.1231

Table 7.2: Independent temperature effect results ($pcm\,/\Delta$K)

results from SERPENT and KENO refer each to its own k_{eff}-axis, because only in this way the detailed value points can be clearly delineated. All the data points are plotted with error bars, however, for some data points, the error bar is too small to be recognized.

It needs to be mentioned that in these calculations average, estimated reference temperatures of the reactor components were used. In the future, when more elaborate thermal analyses become available, these calculations can be repeated with a more realistic temperature profile. Furthermore, it has to be noted that Doppler broadening for these calculations were done on-the-fly with the code's built-in modules instead of with a rigorous cross section generation procedure for the appropriate temperatures.

The negative temperature coefficient of the k_{eff} for the fuel salt is a direct consequence of a decreased number density of fissionable nuclides in the fission zone due to the density decrease and, hence, the decreased macroscopic cross section of fissionable materials. Increased resonance absorption due to the Doppler-Effect also contributes its part.

More attention should be given to the temperature reactivity feedback for the coolant and the reflector. Both materials have the same composition, but the behavior is opposite to each other. The coolant produces a positive temperature reactivity feedback, while the reflector has a negative one. The reason can be explained as

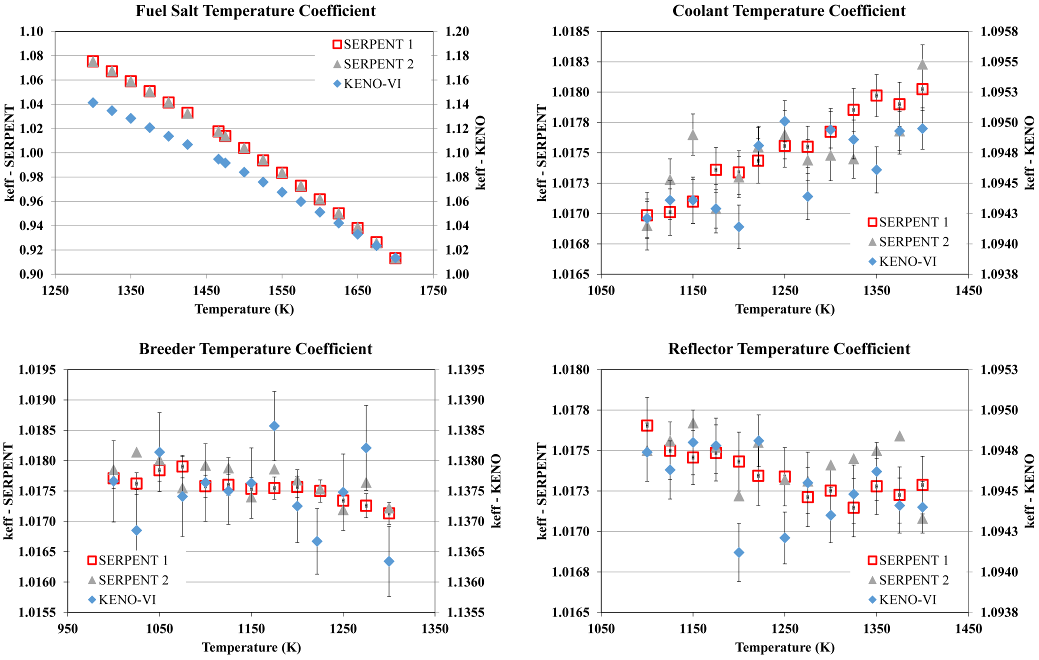

Figure 7.4: Temperature coefficient of the different DFR zones

follows: since the DFR is a fast reactor, neutrons generated from fission do not need to be moderated into a much lower energy region to induce new fission events, but directly contribute to the fast fission chain reaction. For the normal operation, the fuel is not only cooled by the coolant, the neutrons are also reflected/scattered by the high density lead. With a dense coolant the newly produced neutrons will stay more likely inside the fuel tube where they are born, as they encounter a reflecting coolant with many scattering atoms per cm^3 when they try to escape, though there may still be a lot neutrons that escape into other fuel tubes. Consequently, a decrease of coolant density can enhance the probability that neutrons pass through the coolant area and re-enter the next fuel salt tube taking part in the reaction. Compared to the normal case, the neutrons have more “options” on where they take part in the fission reaction. The neutron economy inside of the core is improved.

However for very large density changes of the coolant test calculations up to 1800K have shown that the reactivity contribution will turn negative. The reason for the ultimate decrease is thought to be that without the scattering of the lead, neutrons will have a higher escape probability from the fission zone, leading to a fictitious absorption term.

The negative temperature coefficient of the reflector reveals that the higher temperature causes decrease of the density, which leads to the enhanced leakage of neutrons and less effective reflection.

The negative temperature coefficient for the breeder blanket is similar to that of the reflector, which is also caused by the enhanced leakage of neutrons due to the decreased number density of nuclides in the breeder blanket. It needs to be noted that with the above mentioned neutron statistics this coefficient still has a significant

Condition/Codes	SERPENT 1	SERPENT 2
identical temperature	0.1661	0.1306
with 300K difference	0.1249	0.1226

Table 7.3: Joint temperature effect results (*pcm* /ΔK)

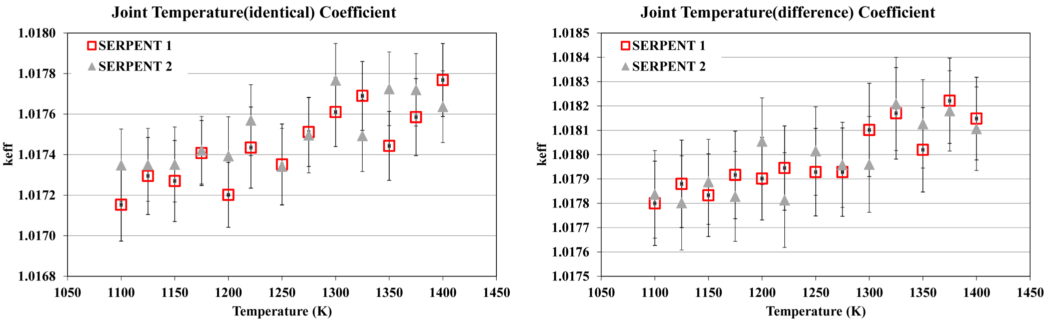

Figure 7.5: Joint Temperature coefficient of Coolant/Reflector

statistical fluctuation for the 5 different runs (±20*pcm*).

As mentioned before in Sec. 3.2.4 the coolant in the fission zone and in the reflector can be exchanged. This leads to an acceleration of the temperature rise of the lead in the reflector. The results for the two cases: that the lead in the coolant and in the reflector have an identical temperature, and a 300K temperature difference are shown in the second line of Tab. 7.3. They are also plotted in Fig. 7.5.

Compared with previous temperature coefficients it has been found that the joint temperature coefficient of the lead in both coolant and reflector is smaller than the summation of the temperature coefficients of the coolant and the reflector separately. Although slightly positive it is still very much smaller in magnitude than the negative feedback of the fuel salt and, therefore, it does not pose an operational problem for the DFR.

7.4 Conclusions

Based on the studied design, the DFR has shown a sufficient neutronic stability facing possible changes in the fuel salt composition, in the geometry or in the temperature of the reactor's materials.

The importance of the nuclides in the fuel salt has been also investigated, which will be helpful for the replacement of the nuclides in new fuel salt compositions. The geometrical design has been verified by the geometry sensitivity calculation and by studying the influence of changing the geometric reactor parameters on the criticality state of the reactor through the value of k_{eff}.

The geometry sensitivity analysis reveals that the selection of the dimensions and the size of the reactor are quite suitable for the design power level. In addition, the influence of the geometry was also examined and showed that the fluctuation of k_{eff} with the changes of geometry considered is acceptable.

The most noticeable is the thermal feedback coefficient, which is almost the only way to control the reactor during operation. The negative temperature feedback coefficient is significant compared to other molten salt reactor designs. The MSFR has a thermal feedback coefficient of -6∼-7pcm/K for ^{233}U-started case or -3∼-7pcm/K for TRU-started case [BMLR$^+$13, pp.34-35], or in the case of the MSRE it has a salt temperature feedback coefficient smaller than -10pcm/K [RSBB70, pp.21]. It is not difficult to conclude that during the operation, the DF will be very stable, and its safe response to increases in temperature very fast.

Unfortunately it has to be mentioned that, because of its large negative temperature coefficient, it may be difficult to shut the reactor down without a large reserve of negative reactivity, e.g. control rods, or to reduce its power rapidly in other transient situations in which the reactor temperature decreases significantly. This will be detailed discussed in later chapters.

Part III

Burnup Calculation

Chapter 8

Introduction

One of the important differences between the DFR and conventional, thermal LWRs is its fast neutron spectrum. This spectrum allows the FR to efficiently breed fuel and fission minor actinides. Therefore, the study of the burn-up process in the DFR will focus on the online fuel processing capability, the development of the specific nuclide inventory during the burn-up, and the determination of its breeding gain and breeding ratio. In this thesis fuel re-processing is only mentioned in specific contexts, but no detailed study is offered.

Prior to performing the burn-up calculations, the discretization of the fission zone into different depletion sections, not only in the radial but also in the axial direction, was considered. In the end, such a refined nodalization it was not adopted, because, for a reactor with a liquid fuel salt core, as is the case of the DFR, the fuel salt is distributed from a common well mixed source into the fuel tubes into the fission zone and, in a few seconds, the fuel salt flows out of the zone and is mixed in the outlet plenum. Therefore, inside of the fission zone there are no regions with different burn-ups.

Burn-up with and without online processing involving various nuclear fuel types is studied in this Chapter, without regard to the details on how the fission products and other nuclides are extracted from the flowing salt. In each case general information about the fuel salt composition and the reactor configuration are given, and the results obtained for the evolution of k_{eff} and the salt inventory are presented and analyzed. Finally, the breeding characteristics of each case are discussed.

The following section offers a complete discussion on the topic of the calculation options. Since a burn-up calculation involves many nuclides and materials, it needs important calculation resources. Based on the resources available at the time of this thesis work, adequate parameters for the calculations should be carefully selected, so that they are performed as accurate and efficiently as possible. The study presented in Sec. 8.1 assesses different combinations and obtains the proper parameters for an efficient burn-up calculation of the DFR reactor. The results reported in subsequent sections are based on calculations following the conclusions reached in this first section.

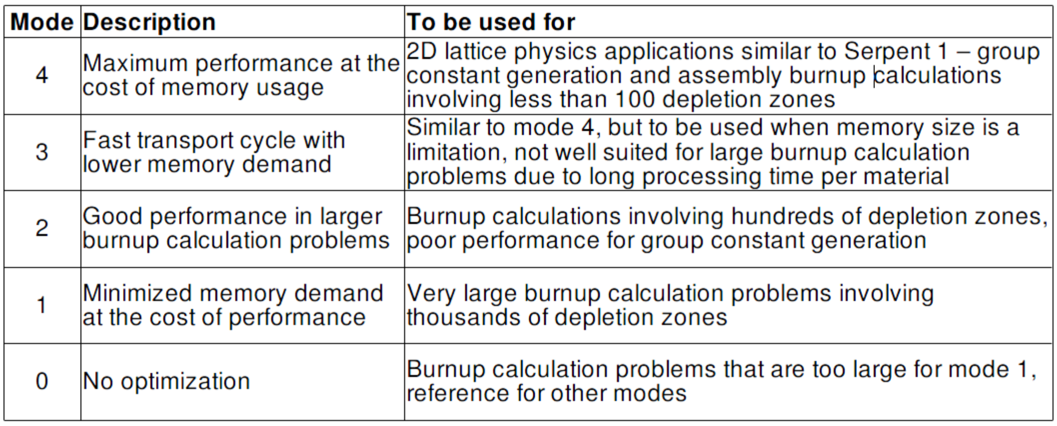

Mode	Description	To be used for
4	Maximum performance at the cost of memory usage	2D lattice physics applications similar to Serpent 1 – group constant generation and assembly burnup calculations involving less than 100 depletion zones
3	Fast transport cycle with lower memory demand	Similar to mode 4, but to be used when memory size is a limitation, not well suited for large burnup calculation problems due to long processing time per material
2	Good performance in larger burnup calculation problems	Burnup calculations involving hundreds of depletion zones, poor performance for group constant generation
1	Minimized memory demand at the cost of performance	Very large burnup calculation problems involving thousands of depletion zones
0	No optimization	Burnup calculation problems that are too large for mode 1, reference for other modes

Figure 8.1: Optimization mode

8.1 Calculation options

The code SERPENT provides various calculation and optimization modes for specific needs. Because the burn-up calculation always consumes a large amount of time and computer memory, first, an assessment of the results generated by different calculation options is carried out, in order to achieve a balance between time, calculation resources and precision of the results.

8.1.1 Parameters

The assessment has investigated the effect of the following parameters depletion calculation:

1. **bumode** gives the probability to choose the method for solving the Bateman equations from Transmutation Trajectory Analysis [Iso13] (TTA), Chebyshev Rational Approximation Method [PL12] (CRAM) or the variation TTA.
2. **egrid** defines the energy grid used for the reconstruction of the continuous-energy cross sections to accelerate the calculation. By changing the fractional reconstruction tolerance, the total allocated memory is changed. Because of some loss of data, the consequence due to the reduction of the grid on the results is not significant until the tolerance is raised above $\times 10^{-2}$ [Lep13, pp.25].
3. **dix** means double-indexing mode, which is not available in SERPENT 2, but only functional in SERPENT 1.
4. **opti** provides 4 different modes to balance the memory usage and the calculation time, while maintaining the quality of the results. A detailed optimization description can also be found in Fig. 8.1 [LI12].
5. **pcc** balances the calculation time and the accuracy of the estimation of isotopic changes during each burn-up step by activating the predictor-corrector

	ref	bumode		dix	egrid			opti				pcc	xscalc
		1	3		4	3	2	1	2	3	4		1
bumode1	×	◯	×	×	×	×	×	×	×	×	×	×	×
bumode2	+	×	×	+	+	+	+	+	+	+	+	+	+
bumode3	×	×	◯	×	×	×	×	×	×	×	×	×	×
dix	×	×	×	◯	×	×	×	×	×	×	×	×	×
egrid5	+	+	+	+	×	×	×	+	+	+	+	+	+
egrid4	×	×	×	×	◯	×	×	×	×	×	×	×	×
egrid3	×	×	×	×	×	◯	×	×	×	×	×	×	×
egrid2	×	×	×	×	×	×	◯	×	×	×	×	×	×
opti1	×	×	×	×	×	×	×	◯	×	×	×	×	×
opti2	×	×	×	×	×	×	×	×	◯	×	×	×	×
opti3	×	×	×	×	×	×	×	×	×	◯	×	×	×
opti4	+	+	+	+	+	+	+	×	×	×	◯	+	+
pcc	×	×	×	×	×	×	×	×	×	×	×	◯	×
xscalc1	×	×	×	×	×	×	×	×	×	×	×	×	◯
xscalc2	+	+	+	+	+	+	+	+	+	+	+	+	×

Table 8.1: Optimization Options

calculation [DKSL13]. Although this is not really an optimization mode, the activation of the option will double the number of transport runs and, therefore, increase the running time and the desired precision.

6. **xscalc** provides two modes to deal with the one-group transmutation cross sections during the transport cycle. The default value in the reference is expected to reduce the time by a factor up to 4, but affect the statistical accuracy compared to a direct calculation of the cross section [Lep13, pp.113].

All the calculations were carried out with 10 threads on Intel® Xeon® L7555 1.87 GHz processors. Moreover, it is worthy to note that the results depend significantly on the number of burnable materials considered, which is set in the cut-off option.

8.1.2 Results

A burn-up case with U-Pu fuel salt was selected to be used in the test calculations. This case has 23 burn-up steps and a neutron population of 100,000 in 50 active and 50 inactive cycles. A total of 292 nuclides were considered in each step of the burn-up calculation.

The reference calculation adopted the default optimization options, which are listed and compared with other test calculations in Table 8.1. In the table the symbol "◯" means that this parameter was assigned the corresponding value or that this option was activated, while "×" means there was not such a parameter or option in this case or it was deactivated, and "+" means default parameter values or values assigned by the program automatically, if they are not specified.

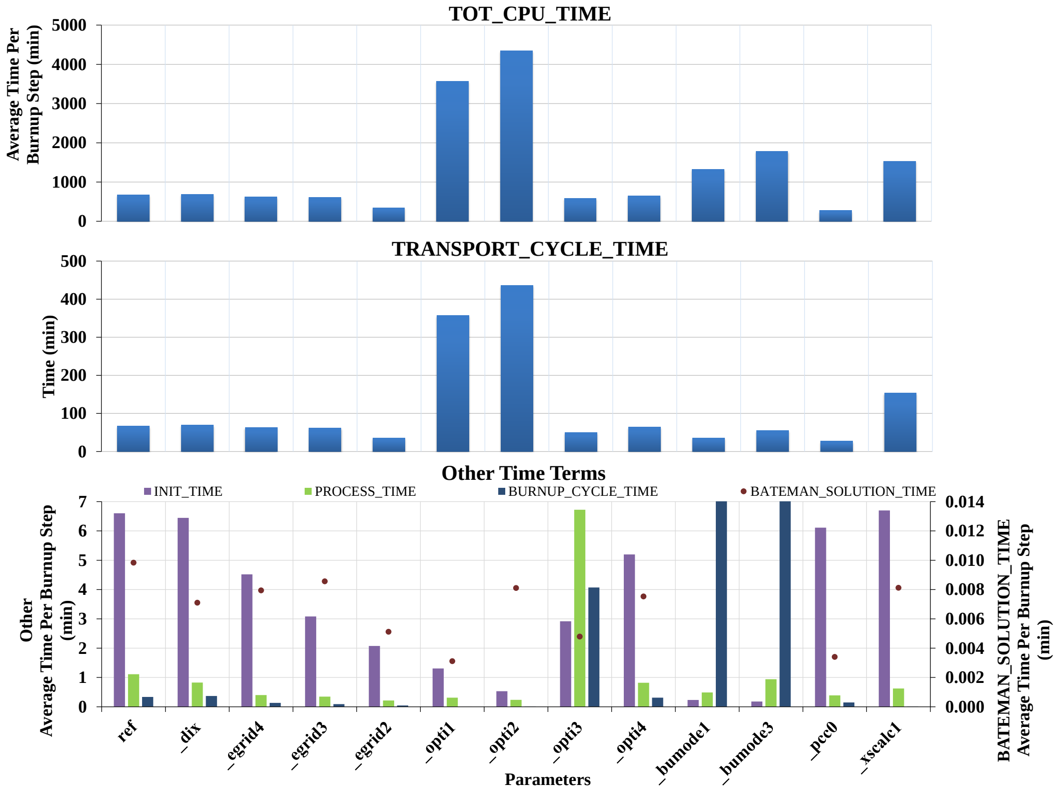

Figure 8.2: Time comparison between parameters

It has to be mentioned that for the parameter “egrid”, in the table the number behind the name means the power of 10 of the tolerance. For example, “egrid5” means a tolerance of 10^{-5} and so on. In the optimization mode “opi 3” overrides the energy grid thinning with the thinning tolerance set to 0.

It needs to be remarked that the results shown are exclusively valid for the case, for which the calculation was performed. For other different cases the results may vary. The results are classified into parameter groups: referenced with parameter “bumode”; referenced with parameter “egrid”; referenced with parameter “opti” and referenced with other parameters.

8.1.2.1 Balance of Time and Memory

1. **Time**

   The time comparison between parameters is shown in Fig. 8.2. For the burn-up calculation the total time, following the calculation sequence, can be divided into “Initial time (INIT_TIME)”, “Process time (PROCESS_TIME)”, “Transport time (TRANSPORT_CYCLE_ TIME)” and “Burn-up time (BURNUP_CYCLE_TIME)”.

   The top figure shows the comparison of the “Total CPU Time”, which uses TOT_CPU_TIME to calculate the average CPU time used for each burn-

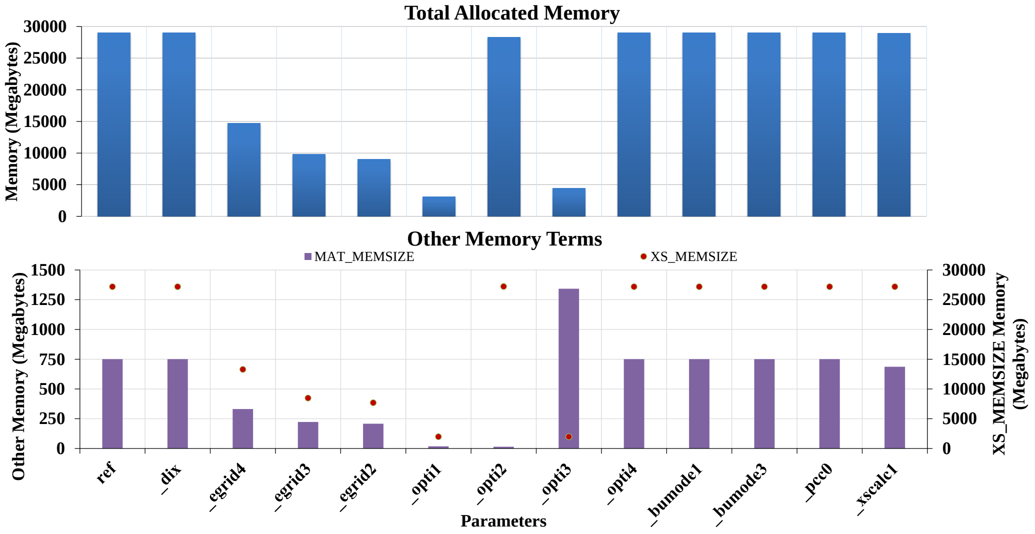

Figure 8.3: Memory comparison between parameters

up step. Since each calculation is OMP [omp15] parallelized with 10 threads, TOT_CPU_TIME is the product of the real running clock time (RUNNING_TIME) and the real CPU usage (CPU_USAGE). The middle figure reveals the "The Transport Time", the time used for the transport cycle. The bottom one summarizes four other time terms. The time used for solving the Bateman equations, displayed as red dots, refers to the right axis, and the other three terms as columns refers to the left axis.

It can be clearly observed that, even though the change of the "egrid" value has an obvious trend in the other time terms, the most important "Transport Time" only affects the calculation time when the tolerance is set to 10^{-2}. The time used between the "opti"s depends on the corresponding purposes as shown in Fig. 8.1. Setting "pcc" to 0 causes a time reduction of almost half of the total time for the calculation compared to other parameters. And the default "xscalc" setting reduces the total CPU time, as well as, the transport cycle time. Nonetheless, for other time terms the difference is not significant.

2. Memory Requirements

The memory usage in SERPENT consists of several terms: memory used for material (MAT_MEMSIZE), memory used for cross section (XS_MEMSIZE), other memory consumption (MISC_MEMSIZE) and terms that not be grouped (REST_MEMSIZE).

Figure 8.3 (upper plot) shows that in this case only some parameters ("egrid" and "opti") have effect on the memory usage of the SERPENT depletion calculation. The amount of memory needed for other parameters almost does not change. Since in the reference (ref) calculation the "egrid" adopts the fractional reconstruction tolerance of 10^{-5}, the tolerance level on 10^{-4} reduces the memory usage dramatically from nearly 30GB to around 15GB, while the tolerance level on 10^{-3} and on 10^{-2} reduces this usage less, which result in

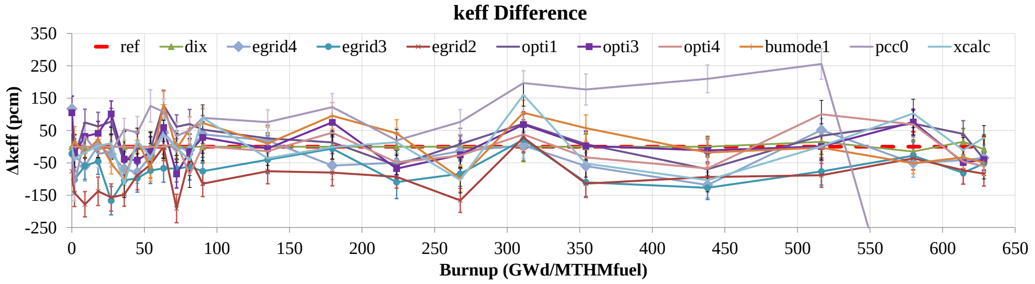

Figure 8.4: k_{eff} comparison between parameters

a memory usage of 10 GB and 9 GB respectively. The parameter “egrid” describes the minimum relative difference between two grid points, below which both points are combined into a single one. THus, the higher the tolerance, the less memory is needed to store the energy grids.

The optimization mode “opti” has also a noticeable impact on memory usage. The option “opti 1” requires a minimum of memory, around 3GB, whereas the other options consumes increasingly more, until the option “opti 4” stabilizes the memory requirements.

On the other memory terms, the comparison of which are showed in the lower figure, “egrid” series also have significant impacts on the memory usage. The memory usage of the cross section generation of “opti1” and “opti2” are nearly none.

8.1.2.2 Evolution of k_{eff}

In this subsection, the k_{eff} calculated with different combinations of computational parameters are compared and discussed. Figure 8.4 shows the relative differences with respect to the reference settings. The depletion calculated in this evaluation is expected to be as long as possible in order to investigate the accumulated differences caused by the options used. Therefore, a total depletion of 630 GWd was chosen.

With the “ref” results (red line and first column in Table 8.1) are taken as a reference, most of the k_{eff} values spread in a range between -200pcm and 150pcm, which can be considered acceptable for general evaluations. The k_{eff} for the case “pcc0”, however, begins to diverge at about $200 GWd/MTHM_{fuel}$. The Δk_{eff} of this case reaches the boundary of the variations of the other cases at about $520 GWd/MTHM_{fuel}$ and exceeds it at $550 GWd/MTHM_{fuel}$.

8.1.2.3 Material Inventory

In order to evaluate the differences introduced by the material inventory, the nuclides ^{238}U, ^{239}Pu and ^{241}Pu were selected for comparison. Figure 8.5 shows that the material inventories in the burn-up region of interest are consistent except for the combination of parameters labeled “dix” with the double indexing mode.

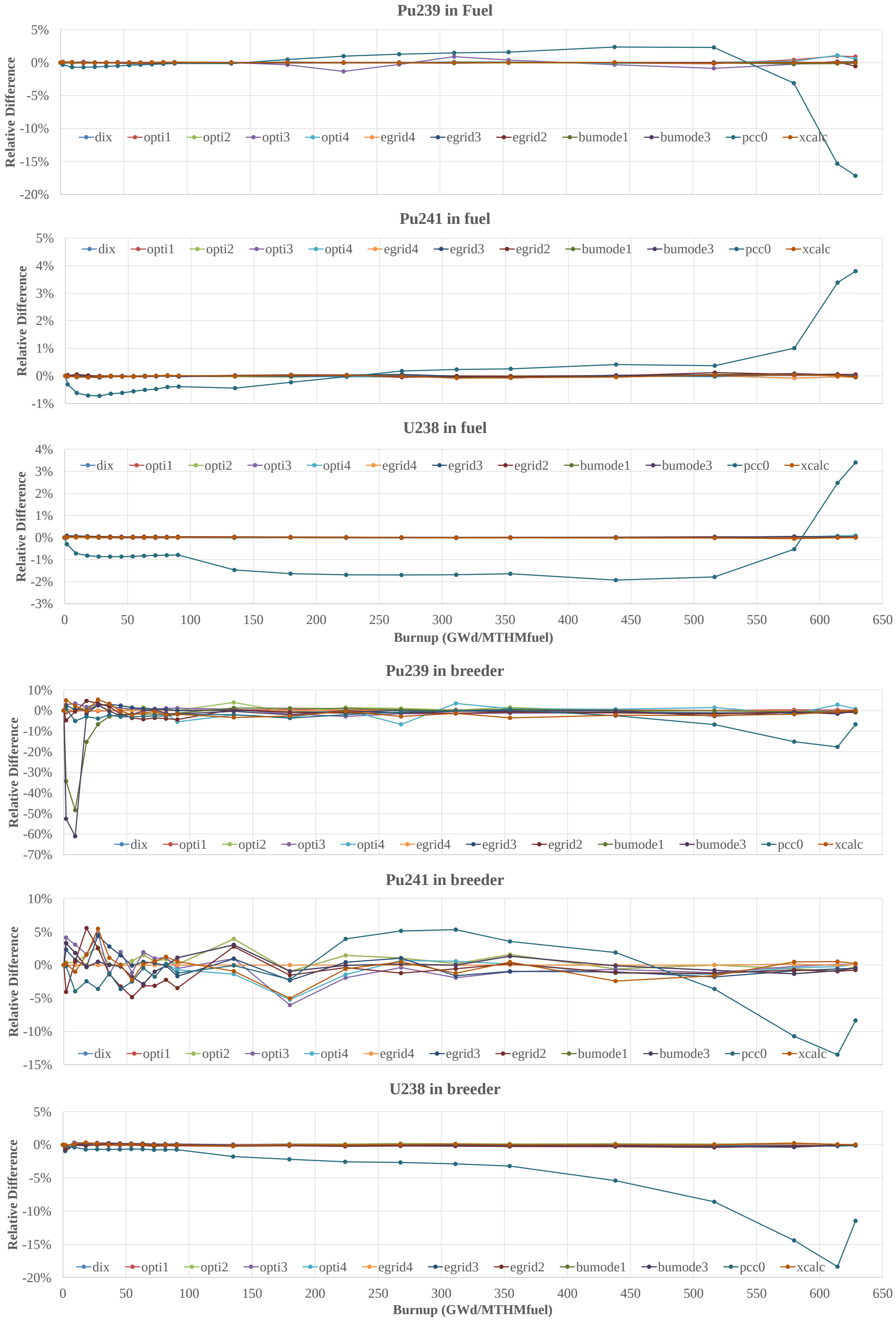

Figure 8.5: Inventory comparison between parameters

Isotope	U-Pu Fuel			
	Cell	Core	Reactor	Breeder
^{37}Cl	0.4391	5885.96	7300.99	121277.52
^{238}U	0.7347	9849.27	12217.11	260036.48
^{238}Pu	0.0043	57.19	70.94	
^{239}Pu	0.1194	1601.30	1986.26	
^{240}Pu	0.0512	686.27	851.26	
^{241}Pu	0.0256	343.14	425.63	
^{242}Pu	0.0128	171.57	212.81	
Total	1.3870	18594.76	23064.99	381314.00

Table 8.2: Initial loading of the fuel salt (kg)

8.2 Initial Load of Fuel Salt

The initial load of the fuel salt listed in Table 8.2 shows not only the total weights of the fuel salt loaded at the beginning of the depletion for both kinds of fuel salts, but also the detailed masses of the nuclides in the composition of the fuel salt. The weight under "Core" includes only the fuel salt inside of the core region, while the values under "Reactor" contain also the fuel salt in the inlet and outlet plena.

The masses of heavy metal (HM), as used for the depletion calculation for the U-Pu fuel, are $0.9480kg$ HM in one single fuel tube, 12,708.74kg HM in the core, and 15,764.01kg HM in the reactor. In the breeder the mass of the heavy metal reaches about $260ton$HM.

Chapter 9

Depletion without online-Processing

9.1 Single Fuel Tube Approach

9.1.1 Burnup Chain

Based on the composition of the fuel salts, the burn-up calculations aim to understand the physics and behavior of the nuclide population during the burn-up process. Therefore, before an study for the entire reactor, a simplified burn-up chain has been established, which describes the fundamental physical phenomena of importance to follow the change of the nuclide population during burn-up. The chain makes use of the depletion equations with the appropriate source and sink terms for each nuclide of importance for a simplified model of the DFR with a one single fuel tube.

The geometry of the model is an hexagonal single fuel cell including a cylindrical fuel tube and the coolant between the fuel tube and the hexagonal cell boundary. It has reflective boundaries, so that no leakage is considered. The details related to the geometry of the single fuel tube are described in Sec. 5.1. The total initial fuel salt inventory of the DFR core is divided by the total number of fuel tubes, in order to determne the initial inventory for a single fuel tube.

The model considers only main nuclide branches with basic reactions including neutron capture $(n,\ \gamma)$, $(n,\ 2n)$ as well as $(n,\ 3n)$ and fission reactions (n, f), and basic radioactive decay chains, including α-, β^--decay, electron capture and internal conversion.

Considering both fuel salt composition options, it can be noticed that most burn-up chains are common. For simplicity, only actinides are taken into account in the calculation. Hence, the burn-up chains of each fuel salt composition can be merged into a single one, as shown in Fig. 9.1. Generally, the solid violet arrows indicate the direction of $(n,\ \gamma)$ reactions, the green arrows point out the EC/β^--decay by different directions, the red arrows show $(n,\ 2n)$ reactions, the blue curve arrows show $(n,\ 3n)$ reactions, and the orange arrows stand for the α-decay.

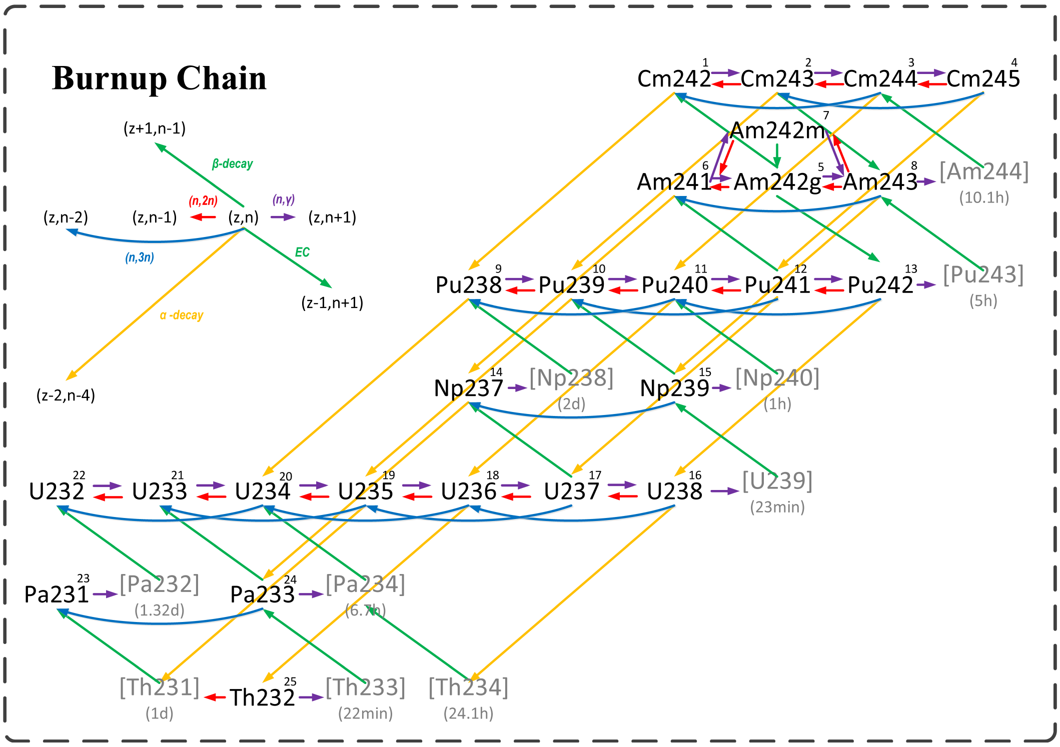
Burnup Chain
(z+1,n-1)
β-decay
(n,2n)
(n,γ)
(z,n-2)
(z,n-1)
(z,n)
(z,n+1)
(n,3n)
EC
(z-1,n+1)
α -decay
(z-2,n-4)
1 Cm242
2 Cm243
3 Cm244
4 Cm245
7 Am242m
6 Am241
5 Am242g
8 Am243
[Am244]
(10.1h)
9 Pu238
10 Pu239
11 Pu240
12 Pu241
13 Pu242
[Pu243]
(5h)
14 Np237
[Np238]
(2d)
15 Np239
[Np240]
(1h)
22 U232
21 U233
20 U234
19 U235
18 U236
17 U237
16 U238
[U239]
(23min)
23 Pa231
[Pa232]
(1.32d)
24 Pa233
[Pa234]
(6.7h)
[Th231]
(1d)
25 Th232
[Th233]
(22min)
[Th234]
(24.1h)

Figure 9.1: Burnup chain of the fuel salts (modified and reproduced from [wim16])

Since the model is simplified, some decay and formation processes that are not relevant or some nuclides that have a short half-life, whose names are marked with square brackets and its half-life in grey color, were not individually considered and their inventories were not calculated separately. The burn-up processes and the nuclides considered are discussed below.

- ^{242g}Am (5.) decays about 17.3% via β^+ to ^{242}Pu and 82.7% via β^- to ^{242}Cm [MPDS15].
- ^{241}Am (6.)'s neutron capture product can be ^{242g}Am (5.) and ^{242m}Am (7.) that ^{242}Am is ground state and ^{242m}Am is the excited state. The braching ratio is approximated as 12% for the branch from ^{241}Am to ^{242m}Am and 79% for that to ^{242}Am [wim16].
- ^{243}Am (8.)'s neutron capture product ^{244}Am with a half-life of $10.1h$ is assumed to decay instantly into ^{244}Cm (3.) [MPDS15].
- ^{242}Pu (13.)'s neutron capture product ^{243}Pu with a half-life of $4.956h$ is assumed to decay instantly into ^{243}Am (8.) [MPDS15].
- ^{237}Np (14.)'s neutron capture product ^{238}Np with a half-life of $2.117d$ is assumed to decay instantly into ^{238}Pu (9.). The further neuron capture to produce ^{239}Np is not considered [MPDS15].
- ^{239}Np (15.)'s neutron capture product ^{240}Np with a half-life of $1.032h$ is assumed to decay instantly into ^{240}Pu (11.) [MPDS15].

- ^{238}U (16.)'s neutron capture product ^{239}U with a half-life of 23.45min is assumed to decay instantly into ^{239}Np (15.). Its decay product ^{234}Th with a half-life of 24.1h is assumed to decay instantly into ^{234}U and then into ^{234}U [MPDS15].
- ^{231}U (23.)'s neutron capture product ^{232}U with a half-life of 1.32d is assumed to decay instantly into ^{232}U (22.) [MPDS15].
- ^{233}U (21.)'s neutron capture product ^{234}U with a half-life of 6.7h is assumed to decay instantly into ^{234}U (20.) [MPDS15].
- ^{232}Th (25.)'s neutron capture product of ^{233}Th with a half-life of 22.3min is assumed to decay instantly into ^{233}U (24.) [MPDS15].

By combining the burn-up branches and the balance of production and depletion of each considered nuclide n, from the decay and reactions of nuclides i, j that yield n, the ODE set of depletion equations for the U-Pu fuel salt can be written in the following form

$$\frac{dN_n(t)}{dt} = -(\lambda_n + \sigma_n \phi) N_n + \sum_i \sigma_i \phi N_i \eta_i + \sum_j \lambda_j N_j \eta_j \tag{9.1}$$

where λ is the decay constant, η is corresponding branch ratio of the formation reactions or decay paths that lead to the formation of nuclide n, σ is the corresponding total microscopic cross section for the reactions involved, which includes fission[1], neutron capture[2], (n,2n)[3] and (n,3n)[4], and ϕ is the neutron flux. This system of differential equations can be expressed in the form of a vector matrix

$$\frac{d\vec{N}}{dt} = A\vec{N} \tag{9.2}$$

where $\vec{N}$ is the vector of nuclide number densities:

$$\vec{N}_{UPu} = [N_{^{245}Cm}, N_{^{244}Cm}, ..., N_{^{234}U}]^T \tag{9.3}$$

and A represents the matrix of coefficients. Among all the coefficients, the decay constants λ are calculated from half-life data compiled in the JANIS 4.0 data base [SBD14]) with the following expression

$$\lambda = \frac{ln(2)}{t_{1/2}} \tag{9.4}$$

---

[1] corresponds to the "total fission" which is numbered as MT=18 in the ENDF neutron reactions. However for the nuclides that do not have MT=18, the 1st-chance fission (n,f) MT=19 is used.

[2] corresponds to the (n, γ) reaction MT=102

[3] corresponds to the (n,2n) reaction MT=16

[4] corresponds to the (n,3n) reaction MY=17

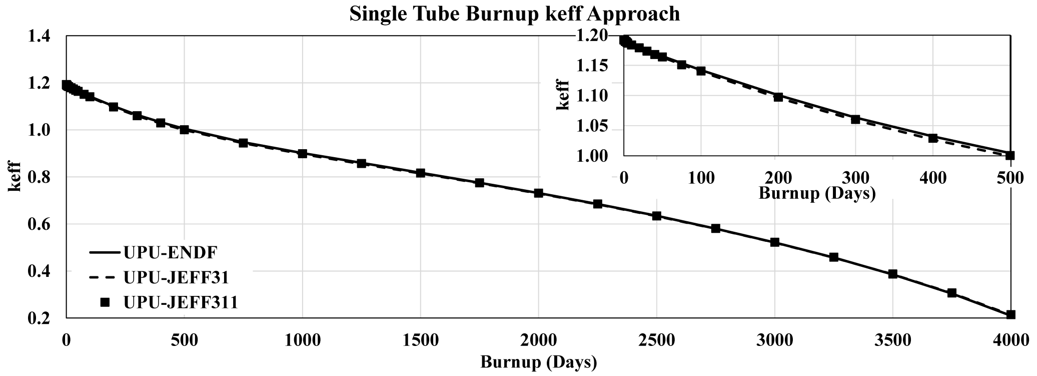

Figure 9.2: k_{eff} of the single fuel tube burnup

The neutron flux, as well as, the one group cross sections for the considered reactions of the given nuclides are obtained from SERPENT calculation results by using appropriate detector settings.

9.1.2 Results

The results of the calculation without online processing are presented in this section. Since the total design thermal power of the reactor is $3GW_{th}$ and there are 13406 fuel tubes, for each fuel tube the power output is calculated as $223.78kW$. Considering the fuel salt inventory loaded in a single fuel cell, the power of one single fuel cell is $0.1613GW/MTHM_{fuel}$. A fuel burn-up of $80GWd/MTHM_{fuel}$ corresponds to about 500 days in the calculation. The total calculation was extended to 4000 days, in order to show the difference between the simplified analytical and Monte Carlo calculations.

Figure 9.2 shows the assessment of the k_{eff} for the U-Pu fuel option in a single fuel tube burn-up calculation. The large plot shows the total development of 4000 burn-up days, while the zoomed plot on the right side shows the first 500 burn-up days. Since the single fuel tube model with reflective boundary conditions does not consider neutron leakage, at the beginning of the burn-up the k_{eff} is well over 1. It can be observed that k_{eff} decreases to k_{eff}=1 at about 500 burn-up days. Few differences can also be found when the plot is zoomed to 500 burn-up days. Considering the different nuclear data libraries that were used, the results show a good comparison for the U-Pu fuel salt, since for most of the data points the relative difference referred to the ENDF/B-VII results remains less than ±1% and only at 4000 days rises up to 1.45% for the JEFF-3.1 and for JEFF-3.1.1 2.10%.

The change of the inventories of the fuel salt during the burn-up is plotted in Fig. 9.3. As mentioned in the analysis and demonstrated in Fig. 9.1, 25 nuclides were considered in the calculation. Ten of them have been selected to be presented in this figure, because they contribute with larger masses and are the most important in determining the neutronic characteristics of the reactor compared to others. Generally speaking for all the nuclides considered there is a consistency of the inventory change within $80GWd/MTHM_{fuel}$ (500 days). Except ^{241}Am , whose neutron capture product was approximated and simplified, for other nuclides, like ^{238}U , ^{238}Pu to ^{242}Pu , ^{243}Am , ^{244}Cm and ^{245}Cm , the consistency till 2000 burn-up days is still acceptable, though, due to accumulated errors and the simplifications of the model, at the end of the calculation the inventories start to diverge. For ^{241}Pu , ^{242}Pu and ^{244}Cm the consistency of the results lasts up to 3000 burn-up days, since they are located in the center of the burn-up chain. For ^{245}Cm , the differences between the results with difference nuclear data libraries slightly exceeds 10%. The differences between the theoretical calculation and the simulations can be, therefore, accepted.

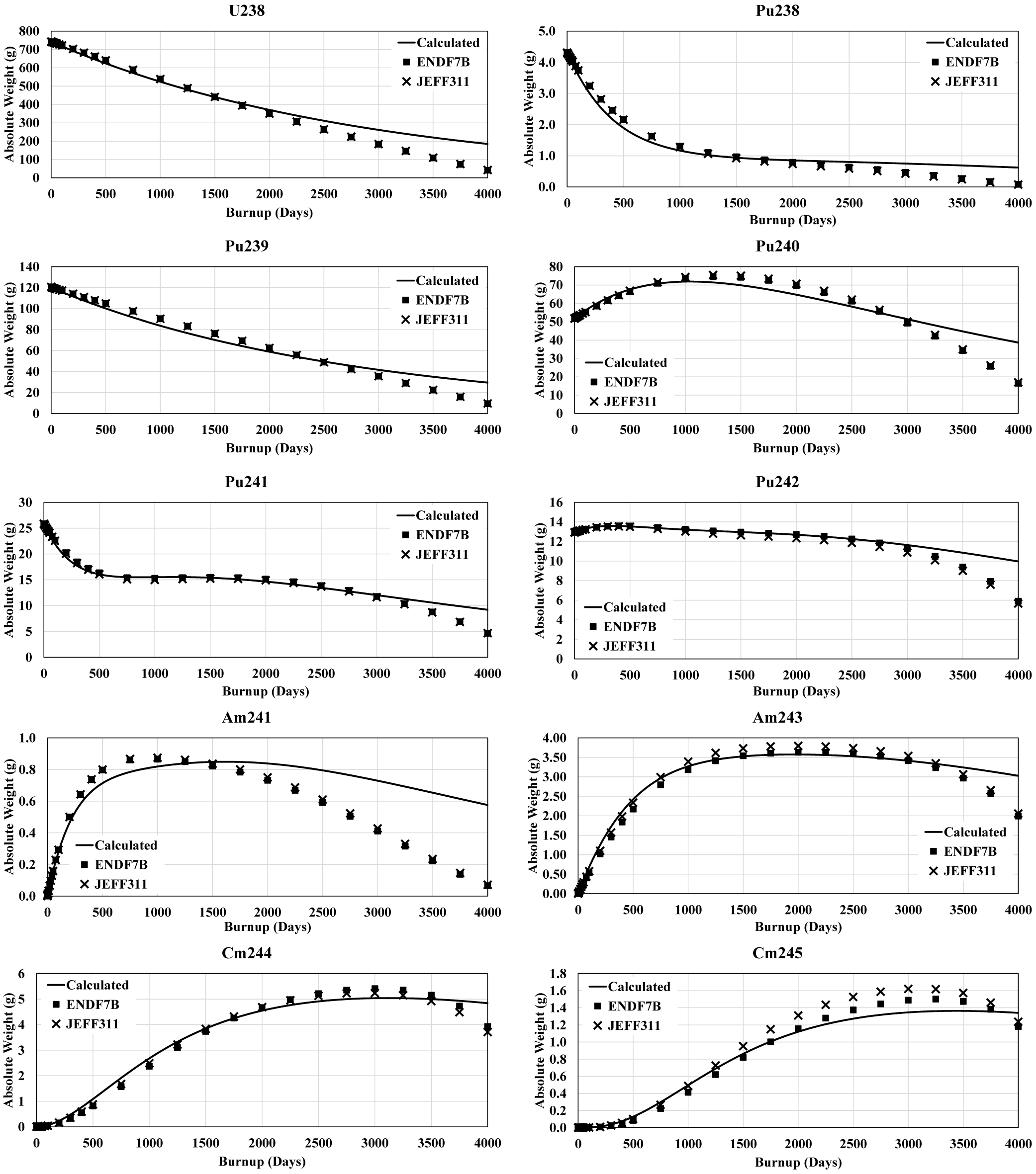

Figure 9.3: Interested nuclide inventories of the fuel in single fuel tube burnup

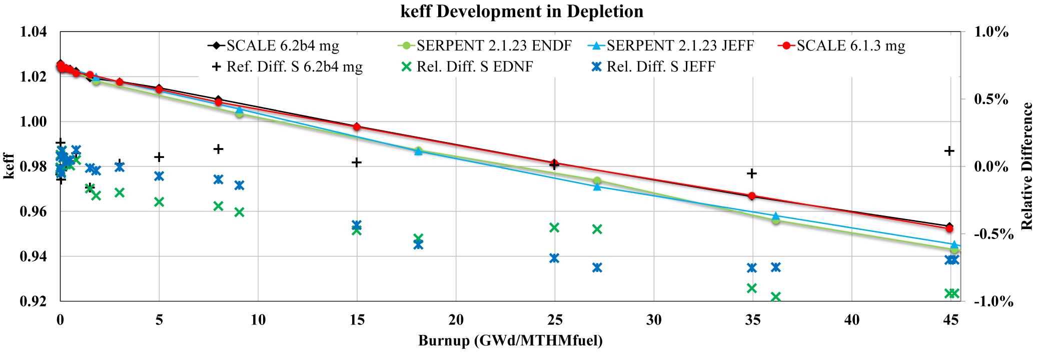

Figure 9.4: Evolution of k_{eff} in depletion of U-Pu fuel

9.2 Full Core Approach

9.2.1 Description

The burn-up calculation for the entire core was carried out with the TRITON 6 module in the SCALE code system, versions 6.1.3 and 6.2b4, in multi-group mode and with SERPENT 2.1.23 with both ENDF/B-VII and JEFF-3.1.1 nuclear data libraries. As mentioned in Sec. 8.2, the DFR with U-Pu fuel salt has $15764kg$ of heavy metal in the fuel salt inside of the complete reactor and about 260 tons in the breeder material in the breeder blanket. Considering that the thermal power is expected to be $3GW_{th}$, this means that the burn-up power is around $0.2GW/MTHM_{fuel}$, which is slightly higher than the burn-up power in the single fuel cell, because the fuel salt in the inlet and outlet distribution zones is also included. For the purpose of the burn-up calculation, a target of $45GWd/MTHM_{fuel}$ was set, which means a total burn-up time of 225 days. Some results of this analysis were already presented in [WSM15].

9.2.2 Evolution of k_{eff}

The evolution of the k_{eff} and the neutron yield during the depletion are shown in Fig. 9.4. A continuous reduction of the k_{eff} can be observed from 1.02482 to 0.99342 ($3121pcm$) for a total burn-up of $20GWd/MTHM_{fuel}$. Until $15GWd/MTHM_{fuel}$ (75 days) the k_{eff} is still larger than 1, which satisfies the requirement of an initial design burn-up duration of a minimum of 14 days. Further on, till the 225th day the k_{eff} has dropped to around 0.952 according to the SCALE results and to 0.945 in the case of the SERPENT results.

9.2.3 Evolution of Inventory

During the depletion, the fission material is consumed and fission products are produced in the fuel salt. Figure 9.5 provides an overview of the most important nuclides in the fuel composition. The figure shows the differences between the nuclide inventory at the beginning and at the end of the depletion, which represents the absolute change of the inventory for the burn-up time considered.

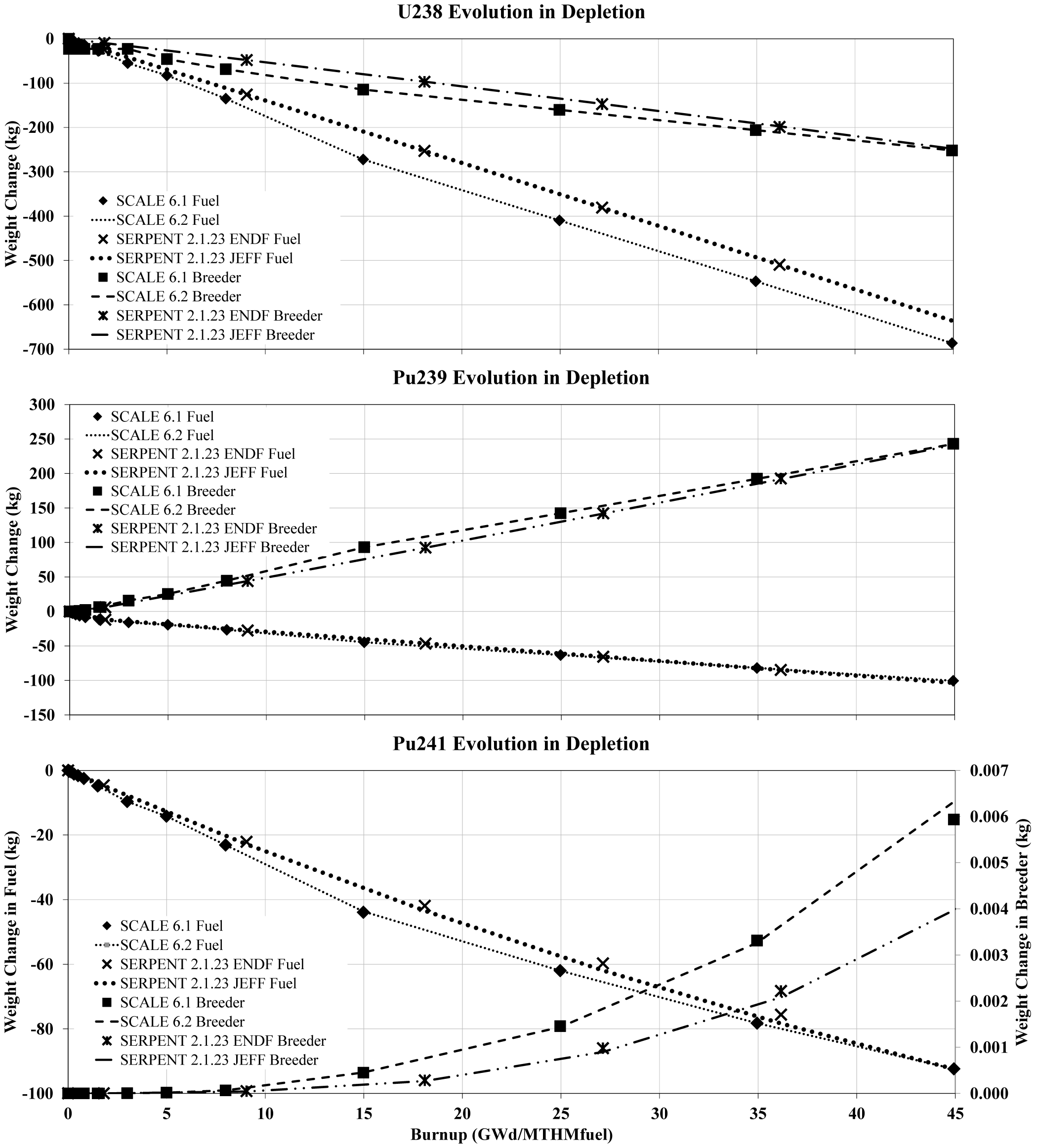

Figure 9.5: Evolution of selected inventories in the depletion of U-Pu fuel

The results shown in Fig. 9.5 prove that, in the fuel salt, fissionable nuclides, such as ^{239}Pu and ^{241}Pu are consumed and take part in the fission reactions. ^{238}U as a fissionable nuclide in the fast neutron region also contributes to the fission reaction. Additionally, ^{238}U is consumed because of the neutron capture reaction which converts ^{238}U into ^{239}Pu, and newly produced ^{239}Pu can then contribute to the chain reaction or it can capture neutrons to yield further conversions.

In the depletion calculation of the entire core, it is important to take into consideration the breeding blanket. As can be seen in Fig. 6.13 in Sec. 6.6.2.5, the neutron spectrum in the breeder blanket is much flatter than that in the fuel salt, which reduces significantly the influence of the neutron population in the energy range around $1MeV$ on the fission reaction as compared to the fuel salt. This can be inferred from Fig. 6.4 in Sec. 6.2.2. In the energy range over $0.1MeV$, the fission to capture ratio is much higher than 1. In the breeder blanket, with a flat neutron spectrum, however, the capture reaction becomes much more significant compared to the fission reaction and the importance of neutron capture is much higher than in the core fission zone. As a result, in the breeder blanket, ^{239}Pu and ^{241}Pu are produced in a larger amount from ^{238}U neutron absorptions than consumed in the fission reaction. They are "bred" in large quantities in the breeder blanket.

By observing Fig. 9.5 discrepancies can also be found between the different codes used. The calculated inventories of ^{239}Pu from SERPENT 2.1.23 with two nuclear data libraries and from two SCALE versions show a good consistency, especially in the fuel salt, in which the change in inventory calculated by both codes is similar. The results in the breeder blanket present, however, discrepancies during the depletion and disappear at the end of the burn-up period. After a burn-up of $15GWd/MTHM_{fuel}$ the results from SERPENT and SCALE seem to approach gradually, ultimately converging to a final common value at $45GWd/MTHM_{fuel}$. The results of ^{238}U in the breeder blanket show a similar behavior, as well as, the results of ^{241}Pu in the fuel salt. But the relative differences of the results of ^{238}U in the fuel salt reach up to 7% with respect to the results from SCALE. The most significant difference can be observed between in the evolution of the ^{241}Pu inventory in the breeder blanket, in which the relative difference reaches a maximum of 30% with respect to the results from SCALE at the end of the depletion time. Fortunately, because the increment of ^{241}Pu in the breeder is very small, the 30% relative difference represents only $0.002kg/d$, which might not be significant in the calculation of the breeding ratio.

9.2.4 Breeding Ratio

The breeding ratio has specific definitions depending on the reactor characteristics [NKLvdH10]. In this thesis, for the DFR concept, the entire burn-up duration is considered as a complete closed fuel cycle.

Based on a generalized formulation the conversion ratio can be defined as [Von76, p.5],

$$Conversion\ ratio = \frac{Rate\ of\ fuel\ generation}{Rate\ of\ fuel\ destruction}$$

For a given operation time the the total amount produced or consumed can be obtained by the multiplication of the rates by this time. Because the breeding of fissile nuclides in the core is the main reason for calculating the *Conversion Ratio*, we can then turn this ratio into the *Breeding Ratio* as

$$\textit{Breeding ratio} = \frac{\textit{Production of fissile nuclides}}{\textit{Consumption of fissile nuclides}}$$

The production and the consumption of fissile nuclides in both the fuel salt and the breeder blanket are taken into consideration for this determination. The consumption of ^{238}U in both fuel salt and breeder blanket is shown in Fig. 9.5 (upper). The consumption ratio of ^{238}U in the fuel is $2720g/d$ and in the breeder is $1140g/d$. During the depletion, ^{239}Pu is not only consumed by taking part in the fission chain reaction, but is also bred from ^{238}U by neutron capture (Fig. 9.5 (middle)). In the fuel salt, due to the high neutron flux, the change of ^{239}Pu inventory is -$446g/d$, while in the breeder blanket is $+933g/d$. For changes of ^{241}Pu (see Fig. 9.5 (bottom)) in the fuel salt and breeder blanket, the gain and loss are, respectively, -$437g/d$ and $+4.48\times10^{-3}\,g/d$ from SERPENT and $6.50\times10^{-3}\,g/d$ in the breeder blanket from SCALE (practically the same value as SERPENT for the fuel salt).

In the breeder blanket of the DFR, the following reactions dominate the production of fissile nuclides:

$$\begin{aligned} n +^{238}\mathrm{U} &\rightarrow^{239}\mathrm{U} \rightarrow^{239}\mathrm{Np} + \beta^- \\ ^{239}\mathrm{Np} &\rightarrow^{239}\mathrm{Pu} + \beta^- \\ n +^{239}\mathrm{Pu} &\rightarrow^{240}\mathrm{Pu} + \beta^- \\ n +^{240}\mathrm{Pu} &\rightarrow^{241}\mathrm{Pu} + \beta^- \end{aligned}$$

In order to determine the breeding ratio of the DFR with U-Pu fuel composition, the nuclides ^{239}Pu and ^{241}Pu are selected, since other fissile nuclides such as ^{235}U and ^{233}U are present in much smaller quantities. Based on the linear characteristic of their depletion-breeding process, the breeding ratio can be expressed as the *Conversion Ratio* and obtained as

$$\textit{Breeding ratio} = \frac{933g/d + 4.48 \times 10^{-3}g/d}{446g/d + 437g/d} = 1.0566$$

If the amount of ^{241}Pu in the breeder blanket predicted by SCALE is used for the calculation, the difference is so small compared with the SERPENT values, that it can not be reflected in the result of the breeding ratio given above. For this reason it has not been taken into account.

9.3 Conclusion

The analysis of the burn-up without online-processing allows to examine the change in inventory of the DFR as a conventional, solid-fuel based reactor. In the single tube approach the consistency between the theoretical analysis and the calculation results using Monte-Carlo based codes (SERPENT and SCALE) can be considered as acceptable. Better performance can be achieved when more detail and nuclides are included in the theoretical model. In this thesis, 25 nuclides, considered the most important ones for the DFR charateristics, were taken into account for the calculation. It turns out that for a depletion of about $50 GWd/MTHM_{fuel}$ a good consistency can be achieved for most of the nuclides included. This result points to the possibility of developing more detailed theoretical models in future that can yield fast predictions of nuclide inventories during the DFR depletion with an acceptable accuracy. By using such models, it should be possible a *real-time prediction* of the concentration of nuclides in the DFR core and breeding blanket in order to plan online reprocessing and the addition or removal of fissile isotopes to maintain critical operation.

The single tube approach has been followed by the full core approach. The full core approach considers the burn-up of the entire core with the power and neutron flux spectrum and distribution calculated in the previous chapters. SCALE and SERPENT were used for the calculations with a full core inventory. The value of k_{eff} shows good consistency between the results from different codes and with different nuclear data libraries: relative differences are around ±1%. The change of the inventory has also been assessed and it has been found that the differences between the results of different verions of SCALE is much smaller than that between the results of SCALE and SERPENT. For a preliminary DFR analysis, without a final detailed design fixed, this level of difference can be accepted.

In the future both approaches can be greatly improved. For the single tube approach, more nuclides and more reactions can be included to create a more accurate, fast-running theoretical model. For the full core approach, the results discussed in this work still rest on the assumption that the core is homogeneous and not divided in smaller zones. A core model with more zones which can take into account the three-dimensional neutron flux distribution should be considered for a more accurate depletion calculation in future DFR design and safety calculations.

Chapter 10

Depletion with Online-Processing

10.1 Description

10.1.1 Reprocessing Techniques

Just as the origin of the nuclear science can be traced to military applications, the reprocessing techniques of spent nuclear fuel (SNF) were also used for the extraction of plutonium for nuclear weapons. Some early methods, such as the "Bismuth Phosphate Process" [BNG$^+$01, p.1241-p.1256], were widely used for this purpose. Nonetheless, these methods could not recover the uranium in the SNF and increased the volume of the waste by adding significant, unnecessary amount of material to the final radioactive waste. Such a characteristic precluded the use of those technologies for civilian applications.

The development of reprocessing techniques for civilian applications accompanied the commercialization of the nuclear power with the following goals:

- Recovery of the valuable fissile nuclides for further reuse as nuclear fuel;
- Reduction of the total amount/volume of the radioactive wastes;
- Extraction of specially valuable or needed nuclides.

The extracted plutonium and uranium were recovered and put back into the fuel cycle for the thermal reactors as Mixed Oxide Fuel (MOX), so that the plutonium would not be diverted for the development of nuclear weapons, thus contributing to the non-proliferation goals set by the International Atomic Energy Agency (IAEA).

The PUREX (**P**lutorium and **U**uranium **R**ecovery by **EX**traction) reprocessing technology was first developed in 1949 at ORNL and is still in practice today. As an aqueous organic reprocessing technique, PUREX is similar to other processes in the class of hydro-metallurgy. It is, however, not suitable for online reprocessing, because it must let the fuel cool for not less than 5 years and then it converts the fuel into a highly acidic solution for further processing (see Fig. 10.1).

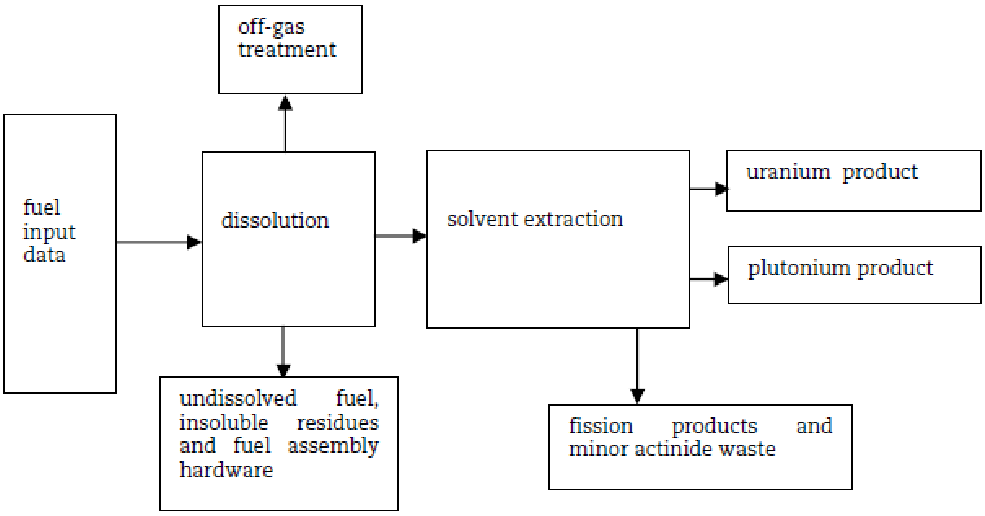
off-gas treatment
fuel input data
dissolution
solvent extraction
uranium product
plutonium product
undissolved fuel, insoluble residues and fuel assembly hardware
fission products and minor actinide waste

Figure 10.1: Standard PUREX flowsheet [NEA67]

Compared to the PUREX method, which operates at low temperature, pyroprocessing technology [Iiz01] [WW06] is a method suitable for high temperature situations, such as on-line reprocessing. The method was developed at the Argonne National Laboratory in the Integral Fast Reactor (IFR) [IFR] project. It dissolves the spent nuclear fuel in molten salts and molten metals, and then uses electro-refining or distillation to separate the fission products. The most obvious difference between hydro-metallurgy and pyro-metallurgy is that the former one uses a water-based solvent, while the latter uses a molten salt or metal as solvent. The use of a molten salt solvent confers this method with a higher compatibility than aqueous methods, which avoids the transportation of spent fuel and its related security issues. The spent fuel can just be stored on-site instead. Yet, this possesses also the disadvantage that the processed salt is less suitable for conversion into glass form if needed by the waste management strategy. In Russia, for instance, the pyro- and hydro-processing techniques are combined to profit from both advantages and to avoid their disadvantages [SVD$^+$13].

In the IFR project a reprocessing unit using the pyro-metallurgical method was established on-site, which was already the embryonic form of the online processing envisioned for the DFR. Its succeeding project, the S-PRISM, has also used this processing technique, but abandoned the on-site design, by relocated the reprocessing facility to an off-site place [FLC$^+$89].

With on-line reprocessing in the molten salt reactor it is possible to realize its unique advantage, that the reactor can keep normal operation while undergoing on-site, continuous removal of the fission products generated from the liquid fuel by chemical and physical methods. Nevertheless, pyro-processing is just one possible option. Since on-line reprocessing improves the performance of the reactor and the neutron economy, as well as, the breeding ratio by reducing the inventory of absorbers, it has been investigated from the very beginning as an integral part of the development of the molten salt reactor concept. Already in the course of the ARE project in

1959 [CC59], a coupled liquid HF dissolution procedure with fluorination for the recovery of the uranium and the solvent salt was developed.

Another example is the fuel processing facility integrated in the MSRE reactor building in order to remove any accumulated oxides in the fuel or flush salt by chemical reactions with H_2-HF and to recover the original fissionable nuclides for further reactor operation [Lin69, p.1]. Based on the successful experience of the MSRE project, the MSBR [McW70] project was designed with an on-line processing unit from the start, which was an improved processing method to separate thorium from the rare earth fission products. It required a single molten salt mixture LiF-BeF_2-ThF_4-UF_4 [Nee71]. Unfortunately, this idea was not to be realized because of the eventual cancellation of the MSBR project [CN72].

In the optimization of the MSFR project, a combined fuel salt management mechanism combining a salt control unit, an on-line gaseous extraction system, and an off-line lanthanide extraction component by pyro-chemistry was introduced. This system extracts gaseous elements with a removal period of $30s$ and a fraction of the fuel is then withdrawn to extract the lanthanides in an off-line procedure, the rate of which depends on the desired breeding performance. With a rate of $40l$/day, the whole core can be reprocessed in 450 days. The fission products are slowly removed at a rate of $0.4l$/day, which results in a total clean up of the fertile salt volume ($7.3m^3$) in 52.7 years [BMLR$^+$13, p.12-p.13].

10.1.2 Fuel Reprocessing of the DFR

The DFR is designed to have an on-line processing unit for the purification of the fuel, for the removal of the fission products, and for the processing of the breeder salt. Considering the composition of the fuel salt and the fission products, there are generally four different categories of fission products that need to be removed:

- Gaseous elements or compounds
- Non-soluble elements or compounds
- Lanthanide and other elements or compounds
- Actinide elements or compounds

Based on the composition described in the previous sections, the fuel salt is supposed to remove the first three categories: gaseous, non-soluble, as well as, lanthanide elements or compounds; all elements whose Z<90. The gases have a very low solubility in the molten salts (approximately $10^{-8}\,moles/cm^3$) and they diffuse towards the core boundaries [ABC$^+$08, p.14]. These elements are, thus, 100% removed, which means that at the beginning of each cycle their amount is set to 0. The elements whose Z is larger than 90, the actinides, are handled individually.

The capture-to-fission ratios of the actinides are plotted in Fig. 10.2. Depending on this value, it is clear to decide which nuclide should remain in the salt and which will be removed. From the point of view of the neutron population inside the reactor, if

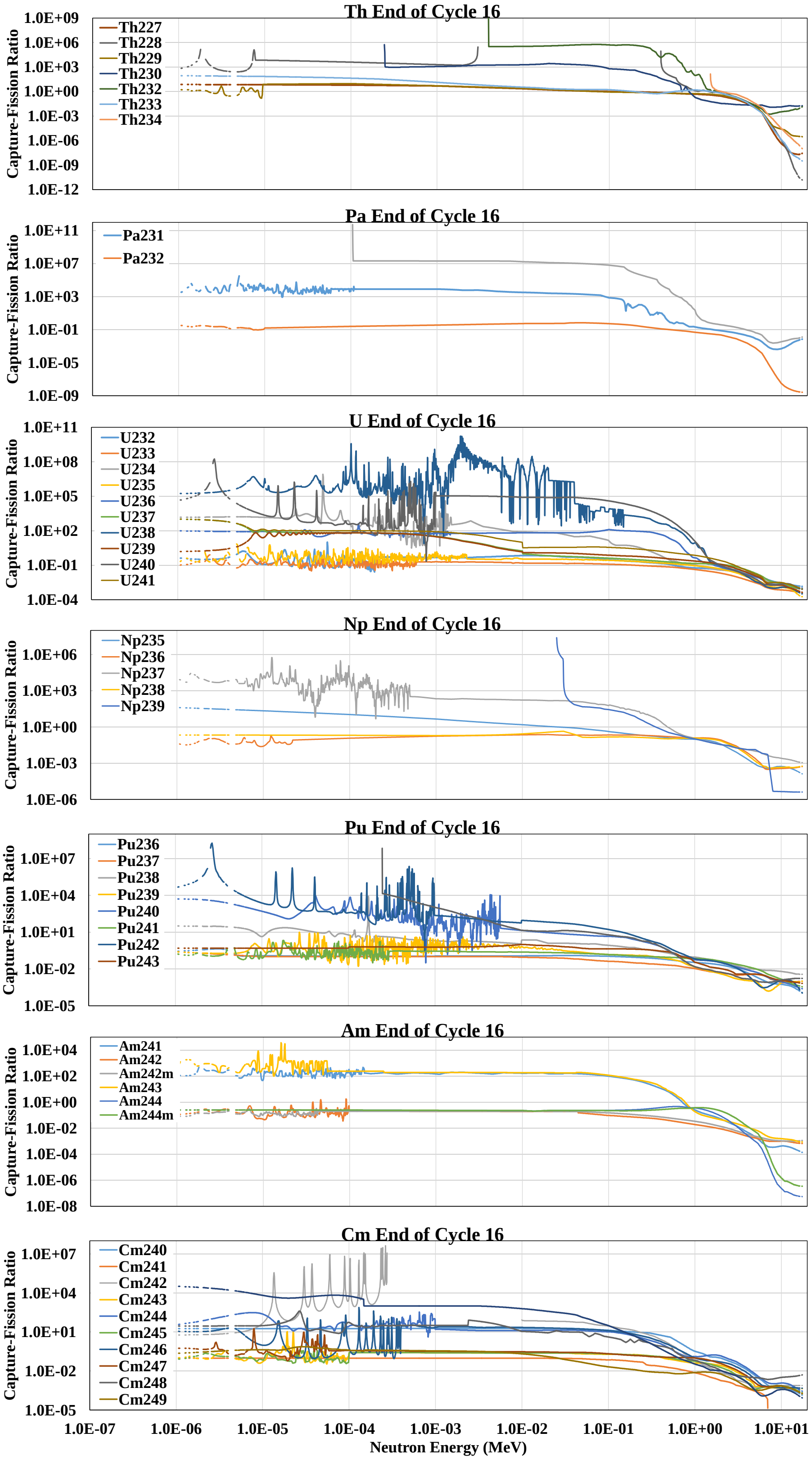

Figure 10.2: Capture-to-fission ratio of actinides for U-Pu fuel salt composition (reproduced with data from JANIS 4.0 [SBD14])

the ratio is larger than 1, it means that the capture reaction is predominant, and the nuclide absorbs more neutrons, whereas, for the case that the ratio is smaller than 1, the fission reaction is more likely than the capture one and, therefore, more neutrons are produced. From top to bottom the Z increases from 90 to 96, which represent the isotopes of thorium, protactinium, uranium, neptunium, plutonium, americium and curium. The curves in the figure indicate that the capture-to-fission ratio of most isotopes falls below 1 in the energy range over $1MeV$ or $100keV$. Other actinides (^{232}U , ^{232}U , ^{233}U , ^{234}U , ^{236}Np , ^{238}Np , ^{236}Pu , ^{237}Pu , ^{239}Pu , ^{241}Pu , ^{243}Pu , ^{242}Am , ^{242m}Am , ^{244}Am , ^{244m}Am , ^{241}Cm , ^{243}Cm , ^{245}Cm , ^{247}Cm , and ^{249}Cm) have a ratio under 1 from $10^{-7}\,MeV$ to $20MeV$. Without considering the difficulties involved in their extraction, these isotopes are worthy to stay in the reactor to be burnt and to contribute to the reactivity.

The removal of the actinides requires not only energy, but also financial investment for the processing materials. For this reason the frequency of the fuel salt processing is an important issue for the DFR. Nevertheless, the deciding factor is not just the expense. According to the investigation in the last section, the more frequent (or even continuous) the chemical reprocessing is done, the higher the breeding ratio is. Based on this argumentation, the adequate on-line processing strategy should be selected.

For the study of several scenarios with on-line reprocessing, the depletion calculation was carried out with SERPENT 2.1.23, while external MATLAB scripts were used for the removal or feed procedures.

10.1.2.1 Scenario I

In the first scenario, a simplified method of on-line processing is considered, in that the fission products whose Z<90 in the fuel salt are removed together simultaneously at the end of a given cycle. Among the nuclides whose Z>90 only those which existed in the initial composition of the fuel salt are kept or added if necessary to recover to their initial percentage in the fresh fuel composition. Other actinides are removed in the same way as the elements whose Z<90. So this scenario represents not a real continuous on-line reprocessing, but a regular extraction strategy which keeps the DFR reactor critical during operation and refuels the reactor so that it can reach criticality until the next load fuel salt is added. The material in the breeding blanket is not processed in this scenario. The results are reported in Sec. 10.2.1. A schematic description of the process is presented in Fig. 10.3

A burn-up duration of about 28 days (4 weeks) is envisaged in order to optimize the load of the on-line processing unit. The reference burn-up calculation was based on this time frame.

10.1.2.2 Scenario II

In this scenario the method of extraction proposed in reference [BMLR^{+}13, p.12-p.13] is utilized, which was originally developed for Transuranium (TRU) fuel composition

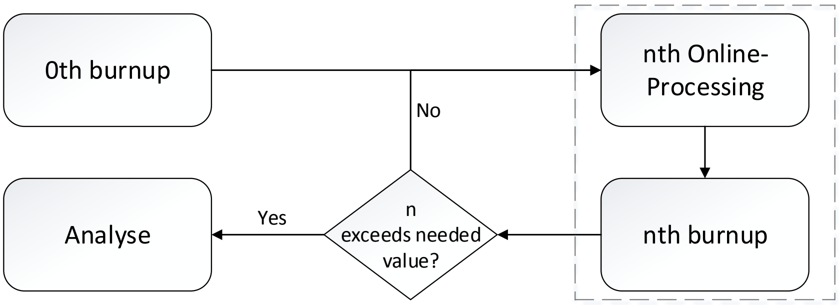

Figure 10.3: Scheme for the on-line processing Scenario I

in the MSFR reactor. This method is combined with an on-line gaseous extraction system and an off-line fission product extraction system, which can be performed by means pyro-chemical methods. The gaseous extraction system removes all gaseous and non-soluble fission products by using injected helium bubbles, in which the noble metals, rare gases and other gaseous fission products are carried away. In the calculation the elements with Z=1, 2, 7, 8, 10, 18, 36, 41∼47, 51, 52, 54 and 86 were supposed to be removed with an extraction period of one day, instead of every $30s$, as in the original reference. This is, nevertheless, still a heavy computational task for the resources available, as can be seen in Fig. 10.4. In one week, for example, there is be a removal for this group of isotopes every day, from both the fuel salt or from the breeding blanket material. In fact, the research program on the thorium cycle by the CNRS [ABC$^+$08, p.9] has revealed that this procedure, the He-bubbling extraction, at least for the fuel salt with the binary LiF-ThF$_4$ composition and other heavy nuclides with longer extraction period would have little effect on the TMSR-NM system properties [heu06, MLHA$^+$07, MLHB$^+$06, MLHB$^+$07].

Other elements with Z smaller than 90, such as fission products, are also removed (except Z=17), but the extraction period depends on the balance of the performance of the reactor and economical considerations. The period varies with regard to the number of liters per day, which results in a total time constant for the reprocessing rate of soluble fission products of several thousand days [FAC$^+$13, p.157]. In this work, however, this time constant is set as one week, as can be seen in Fig. 10.4, so that on the seventh day other fission products, together with gaseous fission products in the fuel salt, are removed. In the breeding blanket only the plutonium is removed and eventually added back to the fuel salt. This can be realized with a storage tank as a buffer, unlike other processing methods mentioned in the references [FAC$^+$13, p.155] and [ABC$^+$08, p.14]. Actinides remain in the core untouched to be further burnt, which simplifies the process of them being removed and re-injected into the core in practice.

After the initial loading of the fuel salt, in order to maintain the reactivity of the reactor, fissile materials are fed into the salt as needed. For the case of operation with the U-Pu fuel composition, the possible feeding options are $^{238}\mathrm{U}+^{239}\mathrm{Pu}$ and $^{238}\mathrm{U}+^{241}\mathrm{Pu}$. The Pu isotopes come from the production in the breeding blanket. The breeder blanket is supplemented only with $^{238}\mathrm{U}$.

In order to clarify the different feeding options, a schematic representation is shown

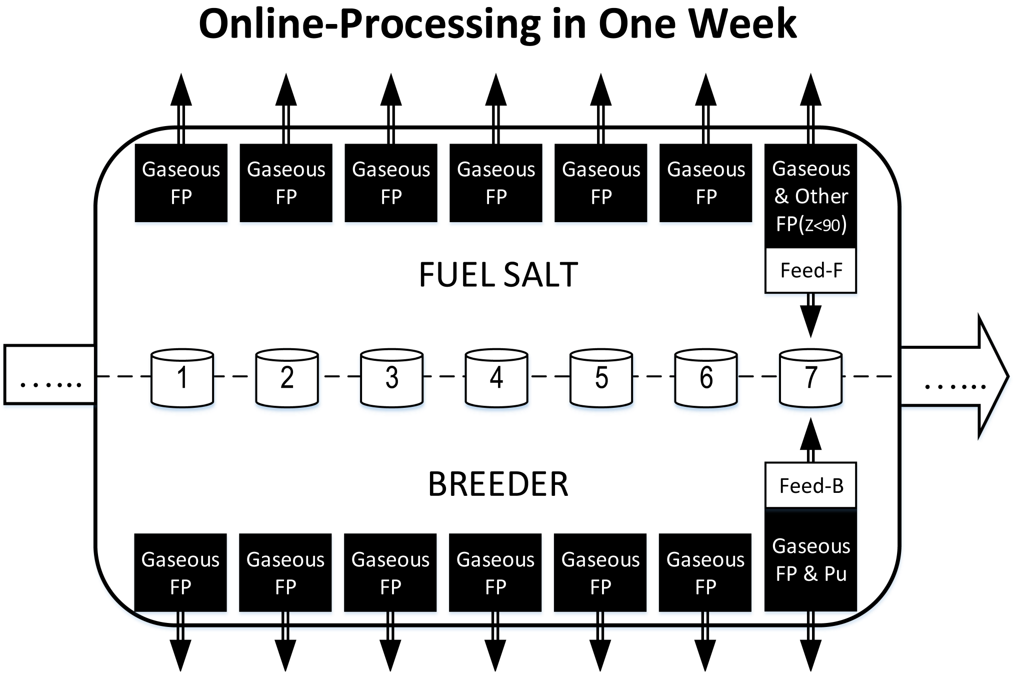
Online-Processing in One Week
Gaseous FP
Gaseous FP
Gaseous FP
Gaseous FP
Gaseous FP
Gaseous FP
Gaseous & Other FP(Z<90)
FUEL SALT
Feed-F
……
1
2
3
4
5
6
7
……
BREEDER
Feed-B
Gaseous FP
Gaseous FP
Gaseous FP
Gaseous FP
Gaseous FP
Gaseous FP
Gaseous FP & Pu

Figure 10.4: Scheme for the online processing in scenario II

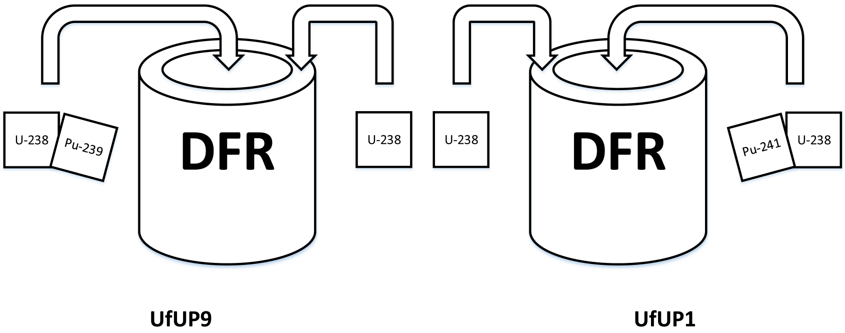
U-238
Pu-239
DFR
U-238
U-238
DFR
Pu-241
U-238
UfUP9
UfUP1

Figure 10.5: Schematic representation of the investigated feed options

in Fig. 10.5. Information for the options is also available in Table 10.1. The name of the options starts with **U**(ranium), followed by “f” for feed option, and 9 for ^{239}Pu and 1 for ^{241}Pu. In the column “Extraction” under “Breeder” the isotopes with arrows mean that the extracted bred isotopes are fed directly into the fuel, whereas other nuclides (Pu) are also extracted and taken away for other uses.

Option	Fuel	Fuel feed	Breeder Extraction	 Feed
UfUP9	U-Pu	^{238}U + ^{239}Pu	←^{239}Pu, Pu	^{238}U
UfUP1	U-Pu	^{238}U + ^{241}Pu	←^{241}Pu, Pu	^{238}U

Table 10.1: Brief information of the investigated feed options

10.2 Results

10.2.1 Results Of Scenario I

10.2.1.1 Evolution of k_{eff}

The calculation of the Scenario I was only carried out with SERPENT 2.1.23. In the scenario the k_{eff} changes between 1.025 and 1.014 in a cycle of 28 days. At the begin of each cycle the k_{eff} has the highest value due to the new fuel salt added. During the cycle the fuel salt is depleted of fissile material, and the k_{eff} decreases progressively as shown in Fig. 10.6 (each dot in the figure represents a daily data point).

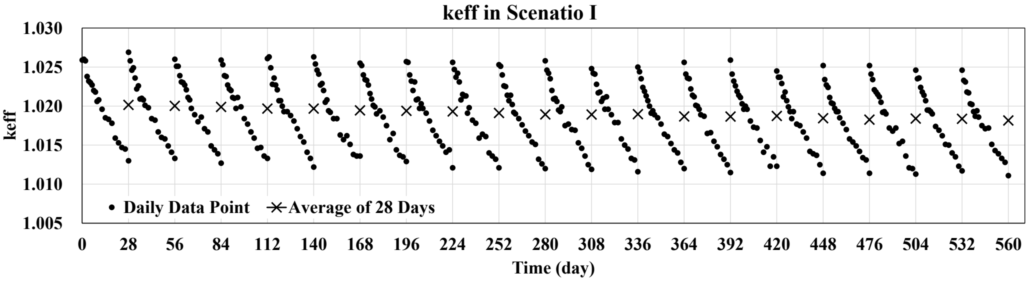

Figure 10.6: Change of k_{eff} in burnup with 28d-cycle fuel reprocessing

Each cross in the plots of Fig. 10.6 represents the averaged value of k_{eff} for each one of the 28-day cycle. A descending trend is evident in the average k_{eff} values, which is coudl be a result of an insufficient amount of fissile nuclide feed. The rate of the decrease is, however , small: about -9.98pcm /cycle.

10.2.1.2 Evolution of the Core Inventory

The fuel undergoes changes in compositions during operation depending on the duration of the feeding cycles. In each 28-day cycle about $70kg$ of ^{238}U are consumed in the fuel salt and about $31kg$ in the breeding blanket. In the fuel salt the inventory of ^{238}U is recovered at the beginning of each cycle, but in the breeding blanket it decreases at a constant rate.

At the same time ^{239}Pu and ^{241}Pu are burned in the fuel salt but produced in the breeding blanket. The inventory of ^{239}Pu in the fuel salt fluctuates between $1888kg$ to $1909kg$ and that of ^{241}Pu between $395kg$ to $409kg$ in each cycle. In the breeding blanket, during the cycle, the inventory of ^{239}Pu has increased in $575kg$, while that of ^{241}Pu has increased in $43.3kg$.

10.2.1.3 Breeding Ratio

The breeding ratio of Scenario I is similar to the breeding ratio calculated for the full core approach in Sec. 9.2.4. The nuclides involved in its determination are restricted

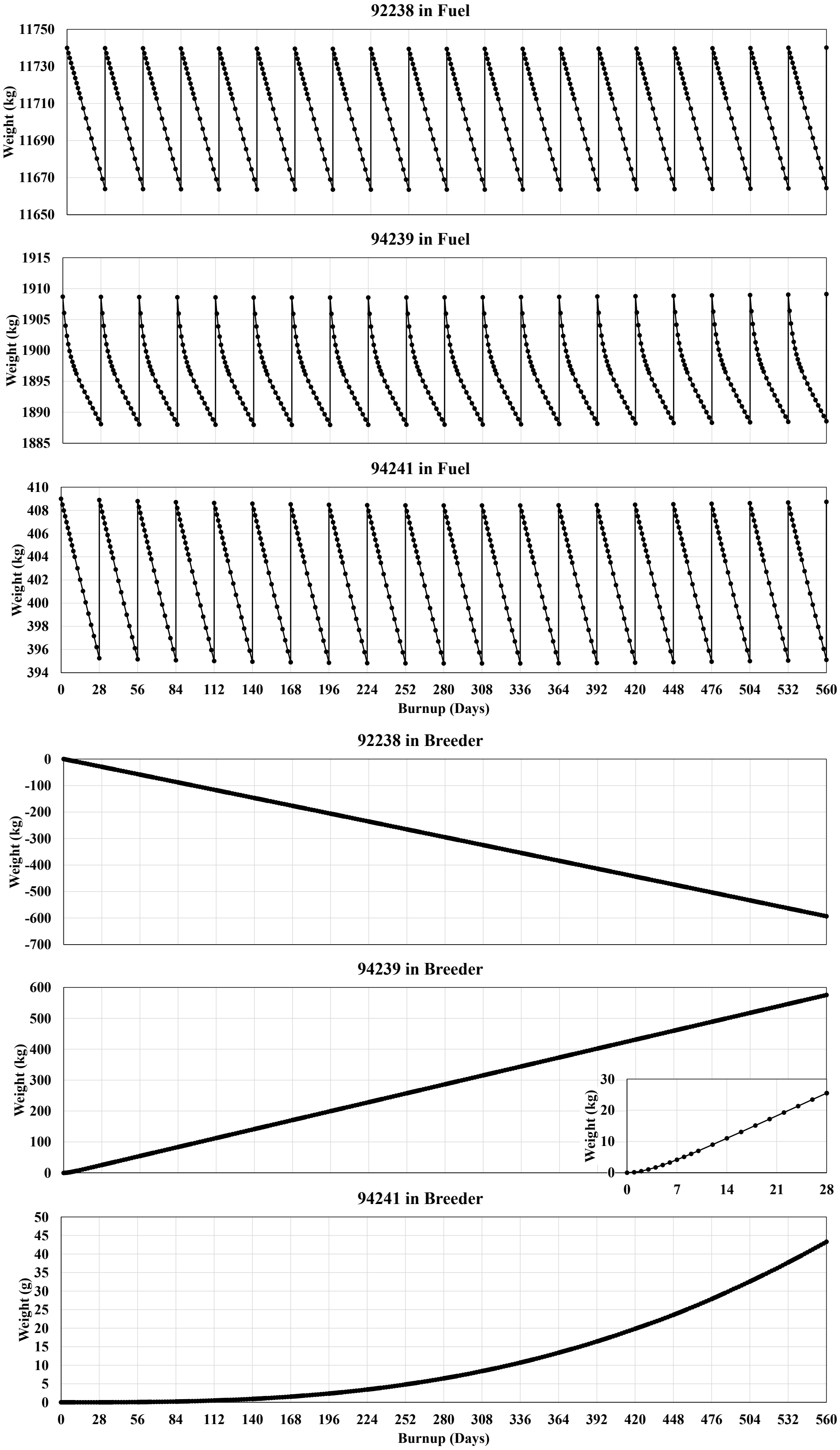

Figure 10.7: Change of fuel composition in burnup with 28d-cycle fuel reprocessing

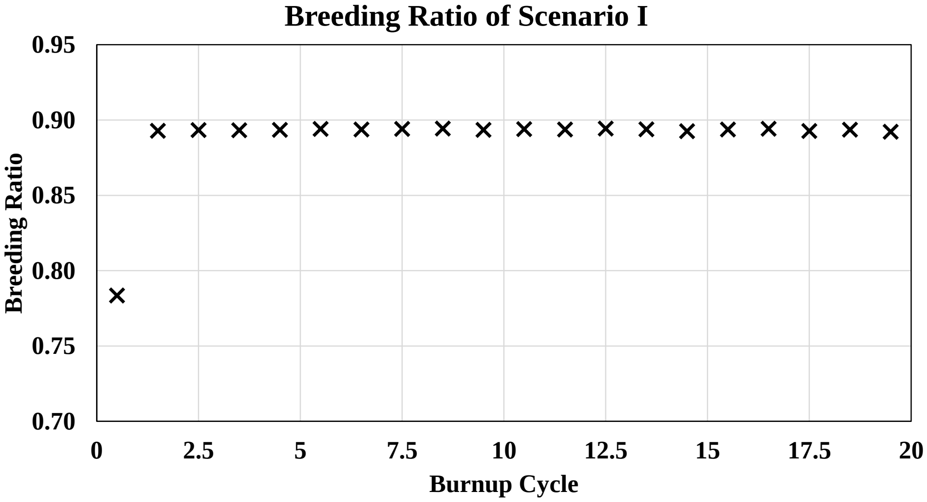

Figure 10.8: Change of breeding ratio of scenario I

to ^{239}Pu and ^{241}Pu . The considered time interval is a cycle of 28 days, since the the removal and feed is performed every four weeks. The change of the breeding ratio during the entire operating time (twenty 28-day cycles) is plotted in Fig. 10.8. The figure shows that the breeding ratio rises in the second cycle and remains almost unchanged at 0.89, which is smaller than 1. Even taking into consideration the possible difference, as mentioned in Sec. 9.2.3, that the results for the breeding of ^{241}Pu yielded by SERPENT could be 30% less than those by SCALE, into account, the small amount of the increment of ^{241}Pu plays no significant role in the the evolution of the breeding ratio. A plausible explanation for the sudden change of the breeding ratio from the first to the second cycles can be that in the first cycle the gain of the fissile nuclides ^{239}Pu and ^{241}Pu is about 12.25% less than the gain in the following cycles, which is caused by ^{239}Pu reaching an equilibrium concentration in the first week of the first cycle. This can be observed in the zoomed plot in Fig. 10.7 for ^{239}Pu in the breeding blanket. For ^{241}Pu the increase is clearly not linear, but compared to ^{239}Pu its increase can be considered negligible.

10.2.2 Results Of Scenario II

For feed option UfUP9 of Scenario 2 four data sets and for feed option UfUP1 only one data set were calculated. The total mass of the feed should be the mass removed. The total operation time calculated is around 9000 days for all the data sets because of the limitations in computation time and resources. This time corresponds to ca. 25 yeas (9125 days for 365 days/year). Although long, this operation time is not optimal for a long term study of the reprocessing strategy when compared to the much longer operation time considered in reference [BMLR$^+$13]. It is also not long enough to establish the equilibrium in the development of the nuclide inventories. Therefore, the results presented in this subsection cover from the beginning of reactor operation to the some time point in the future before the equilibrium is reached.

Dataset		U9_40	U9_35	U9_32	U9_30	U1_25
UfUP9	^{238}U	60%	65%	68%	70%	
	^{239}Pu	40%	35%	32%	30%	
UfUP1	^{238}U					75%
	^{241}Pu					25%

Table 10.2: Detailed information of the investigated feed options

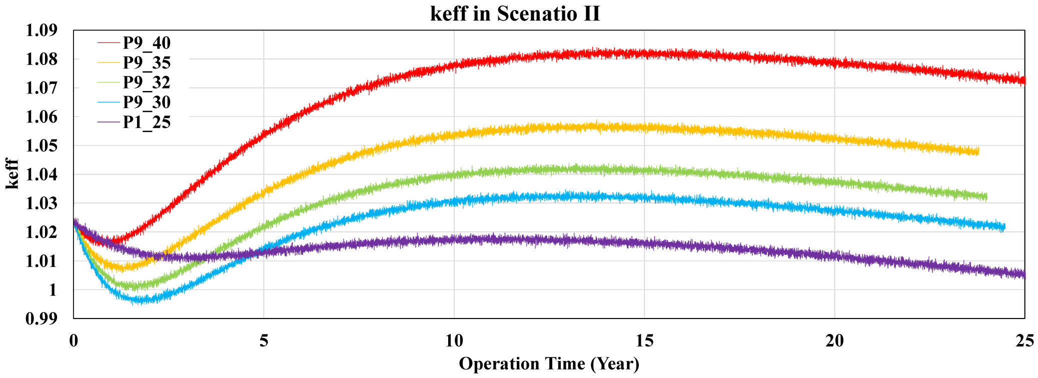

Figure 10.9: Change of k_{eff} in scenario II

Five data sets were considered for the calculation. They differ in the type and the composition of the fed nuclides. The detailed information for each data set is given in Table. 10.2.

10.2.2.1 Evolution of k_{eff}

The development of k_{eff} is presented in Fig. 10.9. It can be seen that the feed option UfUP9, in all its data sets, has a completely different behavior to UfUP1. The value of k_{eff} in the results of UfUP9 diminishes initially and then increases due to the fissile nuclides fed into the fuel salt, until a maximum value is reached in the period between the 10th and the 15th year. The evolution of k_{eff} in the UfUP1 case is relatively flat and its value changes gently as the years of operation pass. In both cases after a maximum value of k_{eff} is reached, it decreases.

Considering all the data sets of UfUP, it can be seen that the less amount of fissile nuclides is fed, the deeper k_{eff} drops after the beginning of the reactor operation. For all the data sets, the descending rates after the highest point are the same. It revels that the fed nuclides considered may be less than the amount needed, so that the fuel salt could not provide enough activities to remain a constant k_{eff}. Further studies should try to correct the fed amounts as the operation extends in time so as to maintain the desired k_{eff}.

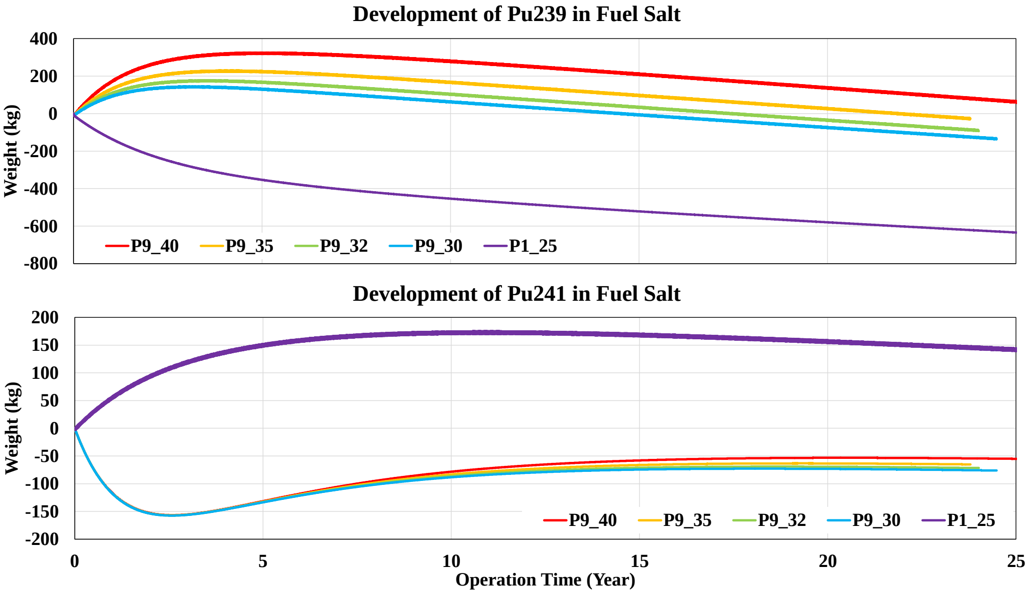

Figure 10.10: Development of fissile nuclides in fuel salt in scenario II

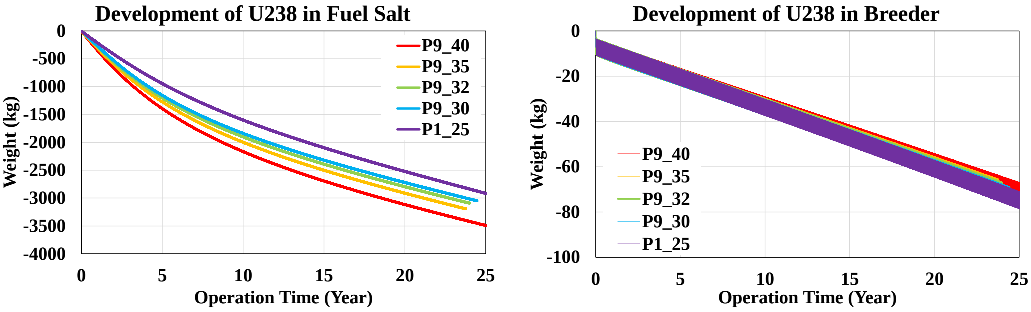

Figure 10.11: Development of ^{238}U in scenario II

10.2.2.2 Evolution of the Core Inventory

Since each feed option adds fissile nuclides to the fuel salt regularly, the inventory of the added fissile nuclides increases to its highest value first, as they accumulate, and then begins to decrease, as shown in Fig. 10.10. For UfUP9 the highest inventory appears between the 2.5th to the 5th year, while for UfUP1 at about 10th year.

In the evolution of the inventory of ^{241}Pu it can be observed that without the feed of ^{241}Pu, the results of the data sets of UfPU9 make ^{241}Pu reach its equilibrium inventory from the 15th year. Such an equilibrium, however, is not reached for the inventory of ^{239}Pu.

The change of the inventory of ^{238}U is depicted in Fig. 10.11. On the left side of the figure, corresponding to the fuel salt, the curves have a sawtooth-like appearance, similar to that observed in the plot on the right side, corresponding to the breeding blanket, caused by the weekly feed. It can be concluded that, even though ^{238}U is the major portion of the feeding added to the fuel salt and to the breeding blanket, the

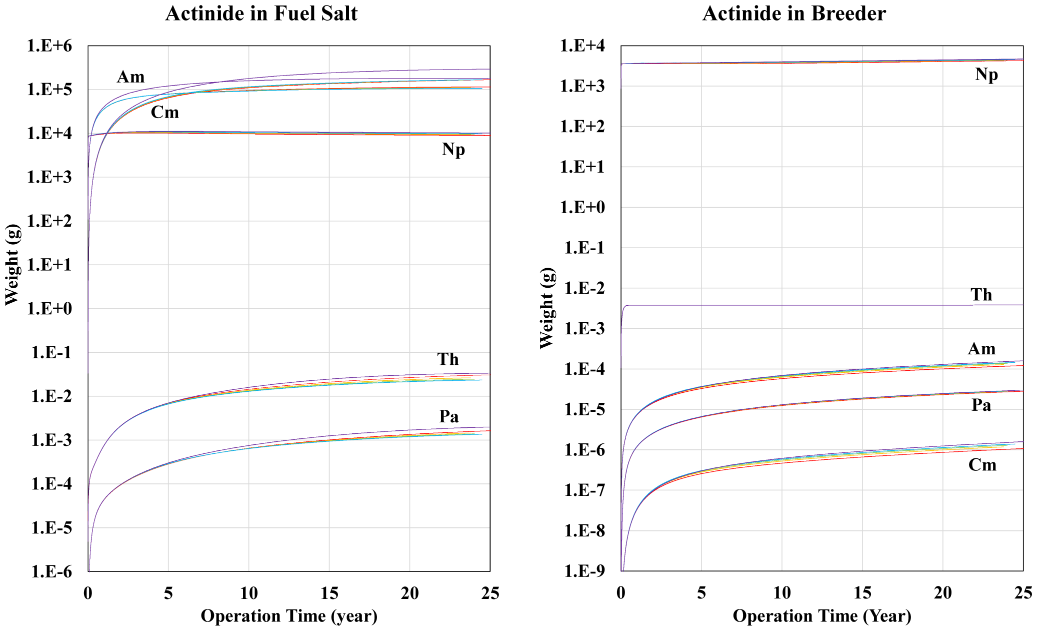

Figure 10.12: Development of other actinides in scenario II

total inventory of ^{238}U decreases continuously in both core zones. Though the rate of decrease slows down in the fuel salt, the decrease of the inventory in the breeding blanket maintains the same rate through the operation time considered. ^{238}U is continuously removed because of its absorption of neutrons in capture reactions in the breeding process, but also because of fast fissions.

For other actinides, their inventory elocutions are plotted in Fig. 10.12, in both fuel salt and in the breeding blanket. In the fuel salt Np reaches its equilibrium inventory at the beginning of the operation with about $10kg$. Americium reaches its equilibrium at about $113kg$. Other nuclides seem to increase continuously, but after a fast rate of increase, it slows down. For Th, Pa and Np the difference between UfUP9 and UfUP1 is not as significant as the difference observed for Cm and Am. This can be explained with help of Fig. 9.1. From ^{241}Pu through β-decay ^{241}Am is directly produced and, therefore, a series of Am and Cm nuclides are produced. For this reason, in the fuel salt the inventories of Am and Cm for the case UfUP1 are higher than those for UfUP9.

In the breeding blanket Th has established its equilibrium inventory in the first year at about $0.002g$. The equilibrium of Np his not reached in the 25 years of operation and its inventory maintains a growing trend.

10.2.2.3 Breeding Ratio

In Scenario II, the breeding ratio is also considered as the gained mass of fissile nuclides divided by the mass of burned up fissile nuclides. The difference between the two scenarios is the complexity of the on-line reprocessing. The added fissile nuclides are considered in the calculation, but the burned fissile nuclides are not, since they can come from the already produced fissile nuclides extracted from the breeding blanket. Therefore, the net loss of fissile nuclides can be obtained by subtracting their initial inventory from the inventory on the last day of a cycle. The loss and gain of the relevant fissile nuclides are plotted in Fig. 10.13.

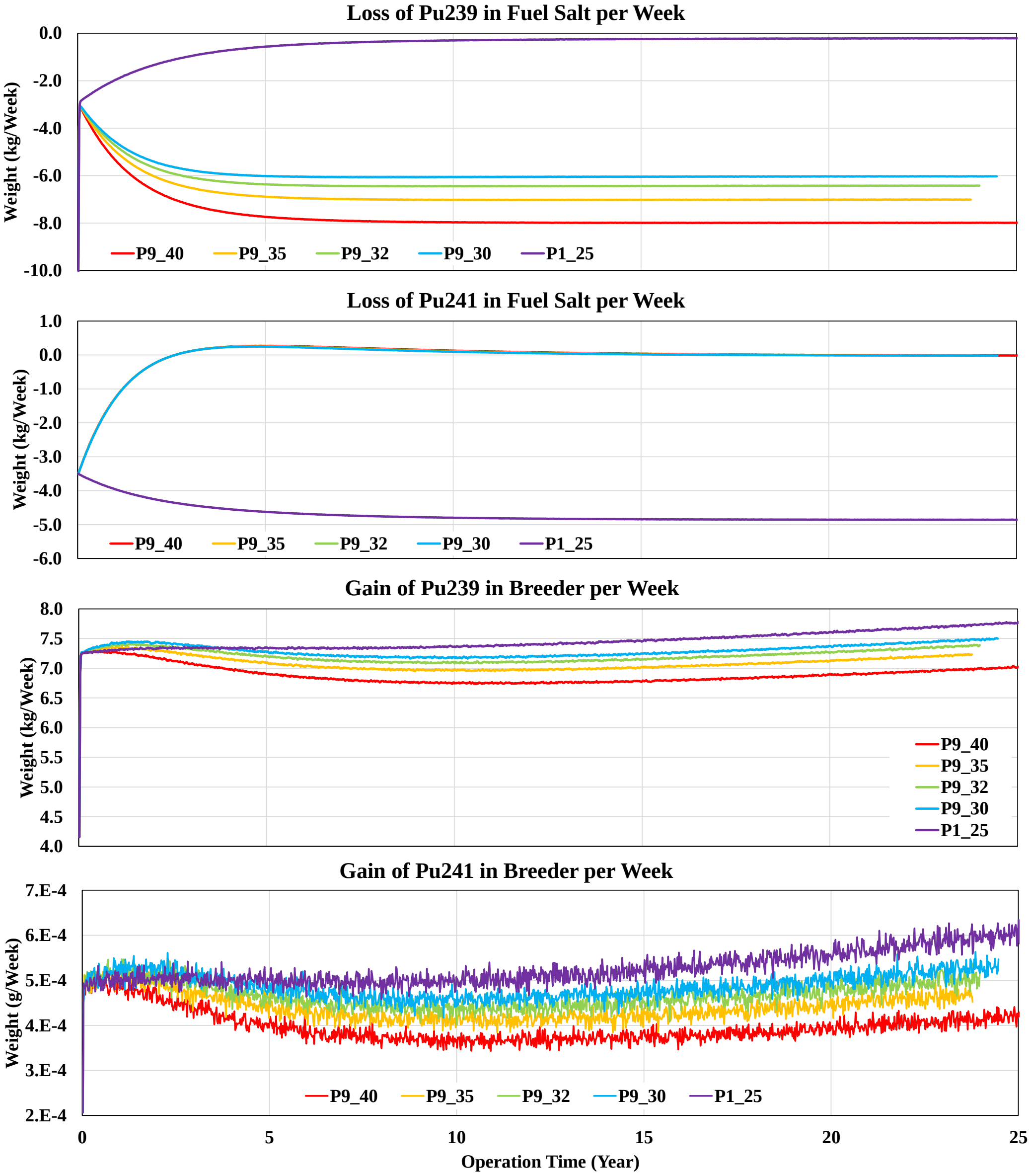

Figure 10.13: Gain of fissile nuclides per week in scenario II

After the beginning of the reactor operation, the rates of consumption of ^{239}Pu and ^{241}Pu become constant in 5 years, while just after a short time both nuclides are produced at a relatively constant rate. The consumption rates of these nuclides are quite different depending on the data sets. For ^{239}Pu the P1_25 has a minimal consumption near almost 0. The data set P9_40 has the maximal consumption at $8kg/week$, while P9_30 has a minimal consumption rate in the UfUP9 feed option of $6kg/week$. For ^{241}Pu the feed option UfUP9 shows a consistent result of nearly

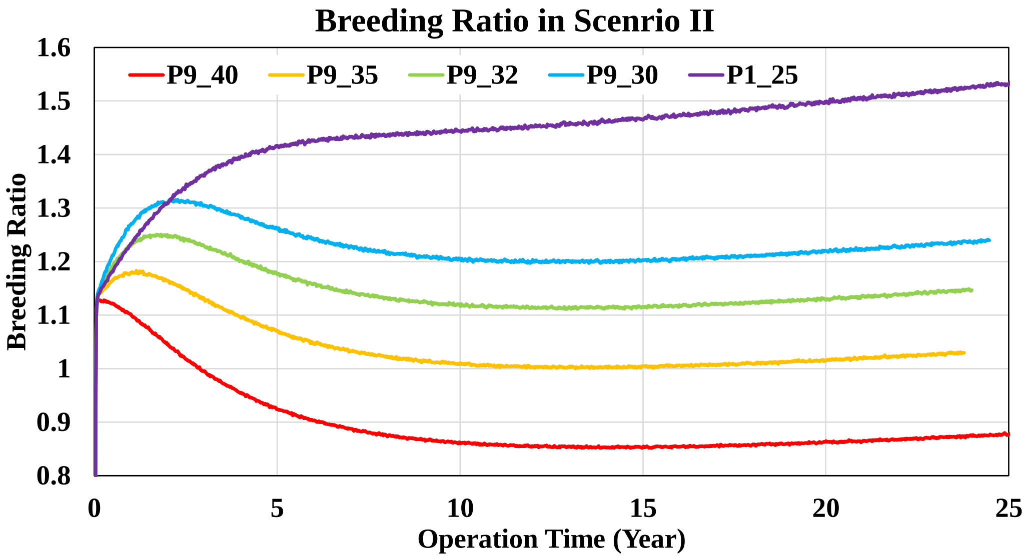

Figure 10.14: Change of breeding ratio of scenario II

$0 kg/week$, while P1_25 has a consumption of about $5 kg/week$. From Fig. 10.13 it can be concluded that

1. The feed of one fissile nuclide suppresses the consumption of the other;
2. The more a fissile nuclide is fed, the more of it will be burned.

But for the gain rate the values do not diverge substantially. The gain rate of ^{239}Pu is about $7 \sim 7.7 kg/week$, and for ^{241}Pu the gain rate is about $4\times10^{-4} \sim 6\times10^{-4}\ g/week$.

The final breeding ratio were calculated for time units of a week and plotted in Fig. 10.14. Based on the discussion above, the data set P1_25 has a maximal breeding ratio over 1 and, with the increase of the operation time, the breeding ratio can reach values over 1.5. The breeding ratio of data set P9_40 was calculated to be over 1 for a short time of 2.5 years and then dropped to values smaller than 1. The other three UfUP9 data sets all have breeding ratios over 1.

10.3 Conclusions

This Chapter has focused on a first approach to the on-line reprocessing method for the DFR concept, and its analysis. Scenario I and II have been studied and, although they are simpler than those considered for other MSR in previous work [BMLR$^+$13] and [FEA12], interesting insights in fundamental neutron parameters of the DFR have been gained.

Scenario I provides a simplified processing option which assumes that the fuel salt is totally renewed at the beginning of each cycle, while the breeding blanket remains untouched. This “complete or nothing”-way has shown to yield a breeding ratio smaller than 1, because of the processing of both the fuel salt and the breeder.

In the scenario II a more realistic on-line processing procedure has been proposed and calculated. In this scenario the gaseous fission products in the fuel salt are removed every day, while the other fission products with $Z<90$ are removed every week. In the breeding blanket the gaseous fission products are removed every day, while all the Pu inventory is removed every week. In order to keep a constant mass in the core, a mixture of ^{238}U and fissile nuclides is fed in the fuel salt and only ^{238}U is fed in the breeding blanket every week. The results suggest that in this scenario the breeding ratio is larger than 1 and the DFR meets the requirement of a true breeder.

Regarding the calculation procedure employed, some conclusions drawn from the evaluation of the results point that in Scenario II the fed mass should be *exactly* the same as the removed mass, otherwise, in a reasonable reactor operation time, the accumulated imbalance can be enormous. The operation time in the calculations should be extended until an equilibrium in the inventory of the most important nuclides is reached. Only at this time will the results be consistent and stable and appropriately describe the characteristics of the depletion in the DFR’s fuel salt. Finally, the current calculation method must be improved. So far the neutronics and depletion calculation of the two scenarios has been carried out with SERPENT, and the feed, removal of the materials is realized with a purpose-built MATLAB script. Further studies with improved feed and removal process modeling should be implemented in SERPENT, which could significantly increase not only the efficiency but also the accuracy of the results.

Part IV

Thermal-Hydraulic Calculation

Chapter 11

System Analysis

11.1 Introduction

The complexity of the a nuclear reactor has shown that it is not sufficient to investigate the whole system only with reactor physics. A coupled computational system with both reactor physics and thermal-hydraulic analysis is now considered better capable for the analysis of the behavior on nuclear reactors.

In this part, the zero- and one-dimensional coupled thermal-hydraulic neutronic analyses focus on the DFR system response to changes in reactivity by using a neutron point-kinetics model for the reactor. The neutronic analysis is restricted to the fission zone of the core. The inlet and outlet distribution zones are not included. The decision was made based on the consideration that the structure of the reflector and the breeding blanket do not have a large impact not only on the neutronic behavior of the core, but also on the heat transfer from the fuel salt to the coolant lead. The first assumption has been verified in the Sec. 7.4 and the second one is a working assumption. The outer structure of the fuel salt circulation and the coolant circulation loops are nor considered.

Since the core of the DFR is made up of hexagonally arranged fuel cells with fuel tubes at their centers, for the certain core size, the total number of fuel tubes can be determined. In order to simulate the entire reactor and establish a satisfactory approach, the validity of the assumptions and the similarity of behavior of the computational model to the actual reactor has to be proved.

For this purpose, various equivalent models were prepared for the simulations, instead of a single one based on the original DFR geometric data and configuration. In Subsection “Modeling” the characteristics of the point kinetic model and the consideration on the thermal-hydraulic model are presented. This is followed by the description of the zero-dimensional model and its parameters. The section describing the one-dimensional model is similarly structured. The one-dimensional model is based on the previously developed zero-dimensional model with the consideration on an axial spatial dimension.

With these models several simulations were performed and their results are presented and discussed in the following sections, including, not only the steady-state conditions, but also transient states. The results are also compared in order to investigate the differences introduced by the models.

11.2 Modeling Approaches

11.2.1 Zero-Dimensional Model

11.2.1.1 Point Kinetics Model

Several methods can be used to investigate the dynamics of nuclear systems, among which the coupled neutron physics and thermal-hydraulic approach with the point kinetics model (PKM) is always the first step. As a highly simplified but useful model, it has been used for various applications including the molten salt reactor in the past. Keepin [Kee64, pp.162] developed the point kinetics model in the integral form for the first time in the formulation used today. A full model with the consideration of the delayed neutrons and their precursors was, however,too difficult to use routinely at that time. In order to simplify the solution of the point kinetic model, Keepin and Nobrega [Nob71] tried to use a constant reactivity insertion and a constant neutron source to substitute the time dependent term, however this treatment proved computationally expensive. At almost the same time, Vigil [Vig67] tried to solve the model with a Taylor Series in time discretization, which was a significant advance compared to the model by Nobrega. In the following decades, many efforts [CA85, San89, AH02, LCLZ09] tried to develop a simple, reliable, and robust algorithm to solve the point kinetic model. Izumi [IN70] combined the Runge-Kutta method with repeated Richardson extrapolation to improve the calculation scheme and achieve a convergence acceleration, while Kinard [KA04] solved the equations for eigenvalues at each time interval.

Related to the application of the PKM, especially for the molten salt reactors, Lapenta [LMR01] proposed the general PKM for the fluid fuel system and discussed the modified system of equations. Zhang [ZQS09] developed a safety analysis code with PKM for the MOSART system. Cammi [CFS10] performed preliminary analysis with PKMs for the MSRE. Guerrieri [GCL13] conducted the dynamics and stability analysis for the MSFR and MSBR.

The simplest way to investigate the delayed neutron precursor (DNP) decay outside of the core is to adopt the classical lumped model for 6 groups of delayed neutron precursors [Kee64]:

$$\frac{dN(t)}{dt} = \frac{\rho(t) - \beta}{\Lambda} N(t) + \sum_{i=1}^{n} \lambda_i C_i(t), \text{ for i = 1...6} \tag{11.1}$$

$$\frac{dC_i(t)}{dt} = \frac{\beta_i}{\Lambda} N(t) - \lambda_i C_i(t) - \frac{C_i(t)}{\tau_{core}} + \frac{C_i(t - \tau_{ext})}{\tau_{core}} e^{-\lambda_i \tau_{ext}} \tag{11.2}$$

where $N(t)$ stands for the neutron density, C_i is the DNP concentration in the i, $\rho(t)$ stands for the reactivity, Λ is the neutron generation time. The variables β_i and β represent the effective DNP fraction of each DNP group i and the total DNP fraction respectively, λ_i and λ_C for the DNP decay constants of each DNP group and the DNP decay constant inside of the core, τ_{core} and τ_{ext} for the flow time inside of the core and in the external loop respectively. In order to present the effect on the delayed neutrons in the core due to the flowing fuel, the 3rd and the 4th terms on the right side of Eqn. 11.2 are added. The 3rd term stands for the precursor loss and the 4th term for the precursor re-entering in the core region. The initial value of C_j and ρ can be calculated by solving Eqn. 11.1 and Eqn. 11.2 for a stationary state by setting the time derivatives equal to zero. Hence

$$C_{i,0} = \frac{\beta_i n_0}{\Lambda\left[\lambda_i + \frac{1}{\tau_{core}}(1 - e^{-\lambda_i \tau_{ext}})\right]}, \text{ for i} = 1...6 \tag{11.3}$$

$$\rho_0 = \beta - \sum_{i=1}^{6} \frac{\beta_i \lambda_i}{\lambda_i + \frac{1}{\tau_{core}}(1 - e^{-\lambda_i \tau_{ext}})} \tag{11.4}$$

The reactivity total $\rho(t)$ consists of the initial reactivity, the inserted reactivity and the real- time reactivity change, which is also represented in the model. The real-time change of the reactivity $\rho(t)$ depends on the temperature feedback due to the temperature change in the fuel and in the coolant, because with the increasing temperature the density of the material decreases and the Doppler-Effect begins to rise, as explained in Sec. 7.3. Thus the total reactivity as a function of time can be calculated as

$$\rho(t) = \rho_0 + \alpha_f(\overline{T}_f(t) - \overline{T}_{f,0}) + \alpha_c(\overline{T}_c(t) - \overline{T}_{c,0}) + \rho_{insert} \tag{11.5}$$

where α is the temperature reactivity coefficient and $\overline{T}$ is the average temperature in the material. The variables with (t) have real-time values in the calculations. Subscript f stands for the property in the fuel and c in the coolant. The subscript *insert* means inserted value from outside, and the variables with 0 are the initial values of each property. The reactivity ρ_{insert} is only used for transient calculations and, therefore for steady state is set to 0.

The power generation in the model is calculated by the product of the macroscopic cross section of the fission materials, the neutron flux and the energy released per fission integrated over the whole reactor volume

$$P = E_f \int_V \int_{E=0}^{\infty} \Sigma_f(E)\phi(r,E)dEdV$$

for the zero-dimensional, one-group approximation, this expression can be simplified

$$\begin{aligned} P &= E_f \Sigma_f \phi V \\ &= E_f \sigma_f N_f(t,T) N(t,T) v V \end{aligned} \tag{11.6}$$

and, therefore, the initial neutron density is

$$N(0) = \frac{P_{thermal}(0)}{E_f \sigma_f N_f(0) v V}$$

where E_f is the energy released per fission, σ_f the one-group microscopic fission cross section (in units of $10^{-28} m^2$), $N_f(t,T)$ the time, temperature dependent number density of the fissile nuclides ($1/m^3$), $N(t,T)$ is the time, temperature dependent neutron density ($1/m^3$), v the neutron speed (m/s) and V the reactor volume (m^3). Except for the time dependent variables, the other variables are considered as constants.

11.2.1.2 Thermal-Hydraulic Model

The zero-dimensional, thermal-hydraulic model is based only on a simple energy balance between the fuel salt, the fuel tube wall and the lead coolant. The DFR concept is unlike a conventional Light Water Reactor in that in the primary side the working fluid takes away all the available thermal power and transfers it the coolant in the secondary side, and also unlike the Molten Salt Reactor proposed in the Gen-IV Forum (see Fig. 1.2) in that the fuel salt in the primary produces fission power in the reactor core and gives all this generated heat in the heat exchanger to the cooling fluid in the secondary side. The heat transfer in the DFR uses once-through heat transport with the fuel salt flowing out of the core with a high temperature and containing still a large amount of heat expected to be transferred outside of the core, where the coolant also flows, but not given to the coolant. This heat can be used to provide power to the on-line fuel processing facility.

In the model developed for the anaylsis presented in this Chapter the properties of the fuel salt and the tube walls (SiC) are described by approximate relationships. The heat transfer efficiency strongly depends on these thermal properties, and the results obtained should not be taken as the final design values, but as an approximation to what should be expected in an eventual DFR.

Assuming the materials have temperature dependent properties and that all the fluids are compressible the energy balance in the fuel, wall material and coolant can be expressed as

$$M_f c_{p,f} \frac{d\overline{T}_f(t)}{dt} = \dot{m}_f c_{p,f} [T_f^{in}(t) - T_f^{out}(t)] + P(t) - h_{f\to w} [\overline{T}_f(t) - \overline{T}_w(t)] \tag{11.7}$$

$$M_w c_{p,w} \frac{d\overline{T}_w(t)}{dt} = h_{f\to w} [\overline{T}_f(t) - \overline{T}_w(t)] - h_{w\to c} [\overline{T}_w(t) - \overline{T}_c(t)] \tag{11.8}$$

$$M_c c_{p,c} \frac{d\overline{T}_c(t)}{dt} = \dot{m}_c c_{p,c}[T_c^{in}(t) - T_c^{out}(t)] + h_{w\to c}[\overline{T}_w(t) - \overline{T}_c(t)] \tag{11.9}$$

where M is the mass (kg) of the corresponding material, c_p is the specific heat ($kJ/(kg \cdot K)$), $\dot{m}$ is the mass flow rate (kg/s), T is the temperature (K) of the material, P is the power (W) generated in the fuel salt, and h is the overall heat transfer coefficient for the heat transfer interface. The subscript f stands for the fuel salt, w for the wall, and c for the coolant. Some of the variables are distinguished by superscripts for different situations. Thus, the superscripts *in* and *out* stand for the variable at the inlet and outlet of the core respectively.

The first term on the right side of Eqn. 11.7 represents the energy taken away by the fuel salt itself out of the core. The third term is the energy transferred to the fuel tube wall, that is, the difference between the energy transferred from the fuel salt and the energy transferred to the coolant, which causes the temperature change of the tube wall. In the fuel tube wall it is assumed that no energy is lost, as described in Eqn. 11.8. On the right side of Eqn. 11.9 the second term means the energy through the fuel tube wall while the first term is the energy that the coolant transfers to the external heat exchanger. The variable $\overline{T}$ represents the averaged temperature in each material, which is obtained from

$$\begin{aligned} \overline{T}_f(t) &= \frac{T_f^{in}(t) + T_f^{out}(t)}{2} \\ \overline{T}_c(t) &= \frac{T_c^{in}(t) + T_c^{out}(t)}{2} \end{aligned} \tag{11.10}$$

This set of equations describes the change of the internal energy of the fuel, which is expressed on the left term of Eqn. 11.7 as the sum of the change of the internal energy of the fuel salt mass flow and the heat transfer between the fuel salt and the wall. The change of the internal energy of the wall (Eqn. 11.8) is the sum of both heat transfers from the fuel salt to the wall and from the wall to the coolant. The change of the internal energy of the coolant (Eqn. 11.9) is the sum of the change of the internal energy of the coolant mass flow and the heat transfer from the wall.

The heat transfer coefficients in Eqn. 11.7, 11.8, and 11.9 are specified for the interface between the materials which in contact with forced-convection, turbulent flows and are defined as [Hol14, pp.452]

$$\begin{aligned} h_{f\to w} &= \frac{1}{\dfrac{1}{h_f A_f} + \dfrac{ln(r_{outer}/r_{inner})}{2\pi k L}} \\ h_{w\to c} &= \frac{1}{\dfrac{1}{h_c A_c} + \dfrac{ln(r_{outer}/r_{inner})}{2\pi k L}} \end{aligned}$$

where h_f and h_c are the heat transfer coefficients ($W/(m^2 \cdot K)$) of the fuel salt and

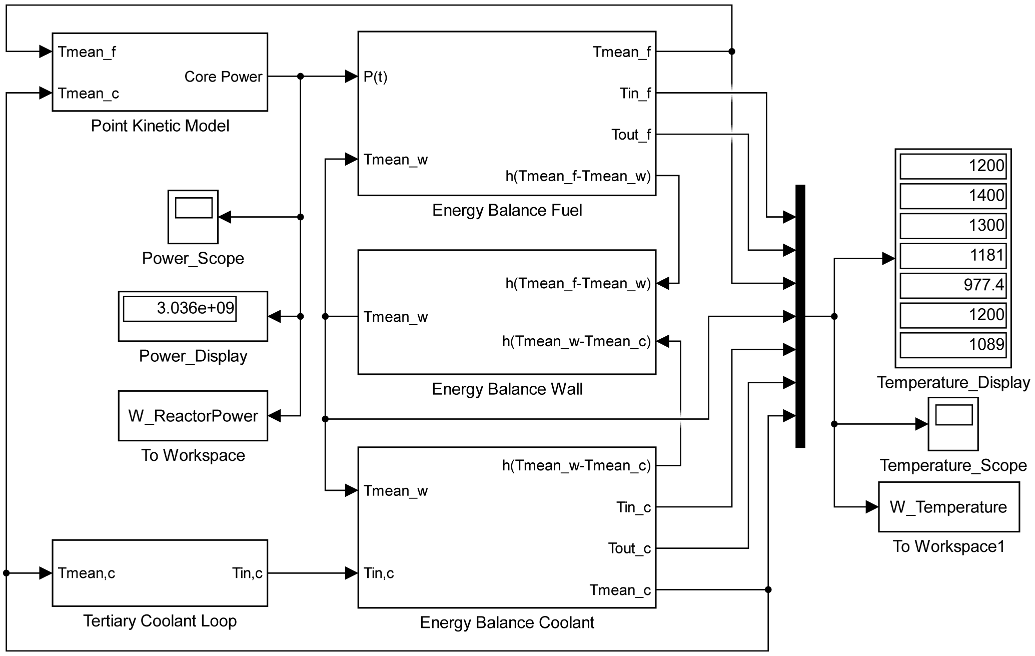
Tmean_f
Tmean_c
Core Power
Point Kinetic Model
P(t)
Tmean_w
Tmean_f
Tin_f
Tout_f
h(Tmean_f-Tmean_w)
Energy Balance Fuel
Power_Scope
3.036e+09
Power_Display
W_ReactorPower
To Workspace
Tmean_w
h(Tmean_f-Tmean_w)
h(Tmean_w-Tmean_c)
Energy Balance Wall
Tmean_w
Tin,c
h(Tmean_w-Tmean_c)
Tin_c
Tout_c
Tmean_c
Energy Balance Coolant
Tmean,c
Tin,c
Tertiary Coolant Loop
1200
1400
1300
1181
977.4
1200
1089
Temperature_Display
Temperature_Scope
W_Temperature
To Workspace1

Figure 11.1: Layout of the DFR-0D system with subsystems

the coolant, k is the thermal conductivity ($W/(m \cdot K)$) of the wall material, r_{inner} and r_{outer} are the inner and outer radii (m) of the fuel tube respectively.

Since in the last equations c_p, ρ, $\dot{m}$ and M are dependent on the temperature, a temperature feedback on these variables is also considered. Other properties are taken from tables in Sec. 3.3.4.

11.2.1.3 System Description

As mentioned in the previous Section, the zero-dimensional modeling approach for the system was followed in order to understand the thermal behaviour of the DFR under homogeneous, simplified conditions, so that the system responding to the reactivity change can be easily investigated.

The zero-dimensional system model was developed with SIMULINK by means of representing all the equations introduced above in the form of functional blocks. The final diagram of the system, divided into five main parts, is shown in Fig. 11.1. The point kinetic model for the power generation is the “Point Kinetic Model” module, and each equation of Eqn. 11.10 is included in the “Energy Balance” module for each material. The “Point Kinetic Model” module takes T_{mean_f} and T_{mean_c} as inputs for the temperature feedback on the reactivity and other variables that affect the “Core Power”. The removed power of the reactor is modeled in the block “Tertiary Coolant Loop”, in which a certain cooling capacity is set. For the desired system variables, displays or scopes as well as outputs are connected to the system model for the monitoring of the variables.

	Fuel salt	Coolant	Unit
ρ_{ini}	4961.4	10 161.5	kg/m^3
μ	0.000 45	0.0013	$Pa \cdot s$
ν	0.907	1.304	$\times 10^{-7}\, m^2/s$
D_h	14.5	4.0	mm
Re	1.9184	2.6132	$\times 10^5$
Pr	0.09	0.0092	
Pe	17 265.6	2415.3	

Table 11.1: Hydraulic parameters related to flow properties

In order to ensure the validity of the SIMULINK model, another model written in m-file form was also established with MATLAB, which proved equivalent to the SIMULINK model in practice. The point kinetics model was realized as a MATLAB *function* and constructed with 18 equations, where the first 7 equations come from Eqn. 11.1 and Eqn. 11.2 as the DNP concentration and the neutron density, the 8^{th} equation is Eqn. 11.5 as the reactivity depending on the temperature feedback; the 9^{th} to 15^{th} equations are from Eqn. 11.7, Eqn. 11.8, Eqn. 11.9, and Eqn. 11.10 describing the heat transfer process. The last three equations are written for the temperature dependent density and specific heat of the materials. The equation set is solved with the embedded *dde (delayed differential equation)* solver because in the equation set the time delayed terms are involved due to the delayed neutron precursors.

11.2.1.4 Parameters

The zero-dimensional model was developed and solved for the U-Pu fuel salt composition. In Sec. 11.2.1.1 the initial value of the DNP concentration and the initial reactivity were presented with formulas. The delayed neutron data including $C_{j,0}$ used in this section were obtained from the results of the static calculation in section 6.3 by SERPENT. The temperature coefficients of the materials adopted the values from the results of the temperature feedback from Sec. 7.3. The initial temperatures were taken from Table 3.3. The running time was set to $100s$, with a time step of $0.0001s$ for a detailed overview on the stabilization of the static calculation. A further running time of up to 10 $000s$ with a time step of $1s$ was then selected for system behavior simulations.

The flow of the fuel salt and the coolant in the DFR follows a turbulent flow pattern with the liquid-metal properties listed in the Table 11.1. The values at the flow inlet are assumed as the initial values for the simulation.

In Table 11.1 D_h is the hydraulic diameter, Re, Pr, Pe and are the dimensionless numbers *Reynolds Number* [TK90a, pp.372], *Prandtl Number* [TK90a, pp.413] and *Peclet Number* [TK90a, pp.450] defined as

$$Re = \frac{D_h v \rho}{\mu} \tag{11.11}$$

$$Pr = \frac{c_p \mu}{k} \tag{11.12}$$

$$Pe = Re \cdot Pr = \frac{D_h v \rho c_p}{k} \tag{11.13}$$

where v is the flow velocity, μ and ν are dynamic and kinematic viscosities of the fluid, and k is the fluid's thermal conductivity.

The Reynold numbers of the fuel salt and the lead coolant in each of their flow channels indicate turbulent flow (>2000). The Prandtl number of the fuel salt is much smaller than 1 and of the same order of magnitude as the value of the liquid metal, which suggests that in both, fuel salt and liquid lead, the thermal diffusion dominates, that is, that for both fluids the heat conduction is much more significant than the convection. Therefore, it is reasonable to treat the fuel salt also as a liquid metal.

11.2.2 One-Dimensional Model

In this section a one-dimensional thermal-hydraulic analysis of the DFR is carried out based on a model developed with MATLAB. The thermal-hydraulic model is combined with zero-dimensional neutronics (PKM). In the primary circuit of the DFR, where the fuel salt flows, the point kinetic model in the core calculates the neutron density and provides power to the fuel salt. The fuel salt gives the heat through the fuel tube wall to the coolant. In the secondary circuit the coolant gives the heat to the outside environment and flows back into the core. The heat transfer between the coolant and an external heat radiator is not explicitly considered. Since the zero-dimensional point kinetics model was already introduced in the Sec. 11.2.1.1, only the thermal-hydraulic part is new compared to the previous model. The layout of the nodalization employed in the calculations is demonstrated in Fig. 11.2.

11.2.2.1 One-dimensional Thermal-Hydraulic Model

The one-dimensional thermal-hydraulic model is governed by a set of conservation equations introduced below and based on the zero-dimensional thermal-hydraulic model. Assuming that the core is divided into n nodes, then the space between two adjacent nodes can be considered as a control volume (CV), which results in n CVs. The conservation equations inside of a CV with lower boundary ni and upper boundary no are based on Eqn. 11.7 to Eqn. 11.9. After rearrangement, the expressions from Eqn. 11.17 to Eqn. 11.19 for the n-th CV are

$$P_n + \frac{dT_f^{no}(t)}{dt} = \frac{\dot{m}_f}{M_f^{no}} T_f^{ni}(t) - \left(\frac{\dot{m}_f}{M_f^{no}} + \frac{h_{f\to w}}{M_f^{no} c_{p,f}} \right) T_f^{no}(t) + \frac{h_{f\to w}}{M_f^{no} c_{p,f}} T_w^{no}(t) \tag{11.14}$$

$$\frac{dT_w^{no}(t)}{dt} = \frac{h_{f\to w}}{M_w^{no} c_{p,w}} T_f^{no}(t) + \frac{h_{w\to c}}{M_w^{no} c_{p,w}} T_c^{no}(t) - \frac{h_{f\to w} + h_{w\to c}}{M_w^{no} c_{p,w}} T_w^{no}(t) \tag{11.15}$$

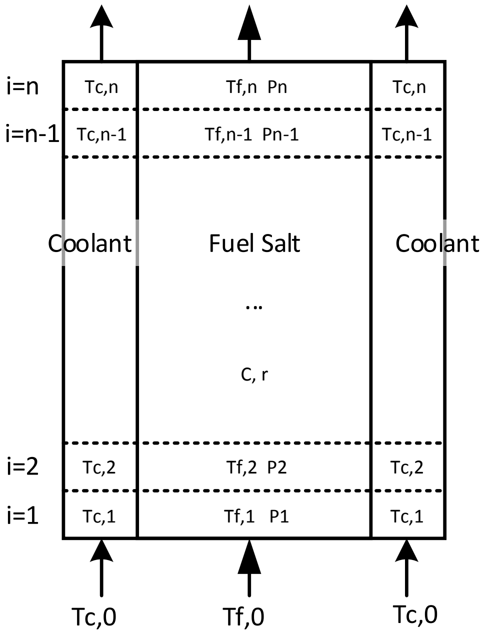

Figure 11.2: Layout of the node in the DFR-1D system

$$\frac{dT_c^{no}(t)}{dt} = \frac{\dot{m}_c}{M_c^{no}} T_c^{ni}(t) - \left(\frac{\dot{m}_c}{M_c^{no}} + \frac{h_{w\to c}}{M_c^{no} c_{p,c}}\right) T_c^{no}(t) + \frac{h_{w\to c}}{M_c^{no} c_{p,c}} T_w^{no}(t) \tag{11.16}$$

where P_n is the power distribution calculated for each node. The variables defined as input and output of each CV can be relocated to the CV and represent the properties in the CV

$$P_n + \frac{dT_f^n(t)}{dt} = \frac{\dot{m}_f}{M_f^n} T_f^{n-1}(t) - \left(\frac{\dot{m}_f}{M_f^n} + \frac{h_{f\to w}}{M_f^n c_{p,f}}\right) T_f^n(t) + \frac{h_{f\to w}}{M_f^n c_{p,f}} T_w^n(t) \tag{11.17}$$

$$\frac{dT_w^n(t)}{dt} = \frac{h_{f\to w}}{M_w^n c_{p,w}} T_f^n(t) + \frac{h_{w\to c}}{M_w^n c_{p,w}} T_c^n(t) - \frac{h_{f\to w} + h_{w\to c}}{M_w^n c_{p,w}} T_w^n(t) \tag{11.18}$$

$$\frac{dT_c^n(t)}{dt} = \frac{\dot{m}_c}{M_c^n} T_c^{n-1}(t) - \left(\frac{\dot{m}_c}{M_c^n} + \frac{h_{w\to c}}{M_c^n c_{p,c}}\right) T_c^n(t) + \frac{h_{w\to c}}{M_c^n c_{p,c}} T_w^n(t) \tag{11.19}$$

For the CV$_{n=1}$ no externally connected CV is considered. The CV's temperature in Eqn. 11.17 and 11.19 has to be replaced by a constant input temperature, which is assumed to be obtained by

$$P_n + \frac{dT_f^1(t)}{dt} = \frac{\dot{m}_f}{M_f^1} T_f^{in} - \left(\frac{\dot{m}_f}{M_f^1} + \frac{h_{f\to w}}{M_f^1 c_{p,f}}\right) T_f^1(t) + \frac{h_{f\to w}}{M_f^1 c_{p,f}} T_w^1(t)$$

$$\frac{dT_c^1(t)}{dt} = \frac{\dot{m}_c}{M_c^1} T_c^{in} - \left(\frac{\dot{m}_c}{M_c^1} + \frac{h_{w\to c}}{M_c^1 c_{p,c}}\right) T_c^1(t) + \frac{h_{w\to c}}{M_c^1 c_{p,c}} T_w^1(t)$$

These equations can be expressed as a set of differential equations, and for all the CVs, the equation set of the unknown variables T_f^1, T_f^2, $\cdots$, T_f^{n-1}, T_f^n, T_c^1, T_c^2, $\cdots$, T_c^{n-1}, T_c^n, T_w^1, T_w^2, $\cdots$, T_w^{n-1}, T_w^n can be solved.

The equations above can be written in matrix form as

$$\mathbb{A} \cdot \mathbb{X} = \mathbb{B}$$

where $\mathbb{A}$ is the coefficient matrix, $\mathbb{X}$ is the vector array of temperature variables, and $\mathbb{B}$ is the vector of characteristic system parameters including constant terms, boundary conditions, and power profile. The solution of the unknown variables is obtained by $\mathbb{X}=\mathbb{A}^{-1}\mathbb{B}$. The time-dependent temperature of the different nodes can then be averaged to calculate the overall mean temperature of the fuel salt and the coolant as a function of time. This mean temperature is used to produce the feedback for the point kinetic model and to adjust the reactor power output.

11.2.2.2 Power Profile

The power of the one-dimensional model is based on the calculated power distribution in Sec. 6.8. Since the reactor is divided into several nodes, the power profile was also discretized and simplified to yield power profile that describes the power distribution in the nodes along the longitudinal axis.

The power profile in a bare cylindrical reactor can be approximated based on the product of a cosine function and a Bessel function [LB01, pp.280]

$$P = A J_0 \left(\frac{2.405 r}{\widetilde{R}} \right) \cos \frac{\pi z}{\widetilde{H}} \tag{11.20}$$

where A is the product of various reactor parameters, $\widetilde{R}$ and $\widetilde{H}$ are the extrapolated radius and height of the reactor, calculated as $\widetilde{R} = R + d$ and $\widetilde{H} = H + 2d$, with d the extrapolated length. The geometric variables r and z are radius and axial location (middle height $=$ 0), and J_0 represents the Bessel function of the 1st kind J_n for $n = 0$.

In the DFR the presence of the reflector flattens the power profile, as plotted in Fig. 6.18(b), which is the power profile actually implemented as a user defined function along the axial direction for the calculations. In the radial direction the power is assumed to be unchanged, because for the single fuel tube located in the center of the reactor, its radial power profile can be approximately considered as constant. For this reason the relationship between P_{max} and P_{total} in the axial direction can be expressed by substituting the Bessel function for an averaged value, for which the calculated and fitted power profile Eqn. 6.19 in Sec. 6.8 can be used

$$P_{total} = \int_{-H/2}^{H/2} P(y) \mathrm{dy} \tag{11.21}$$

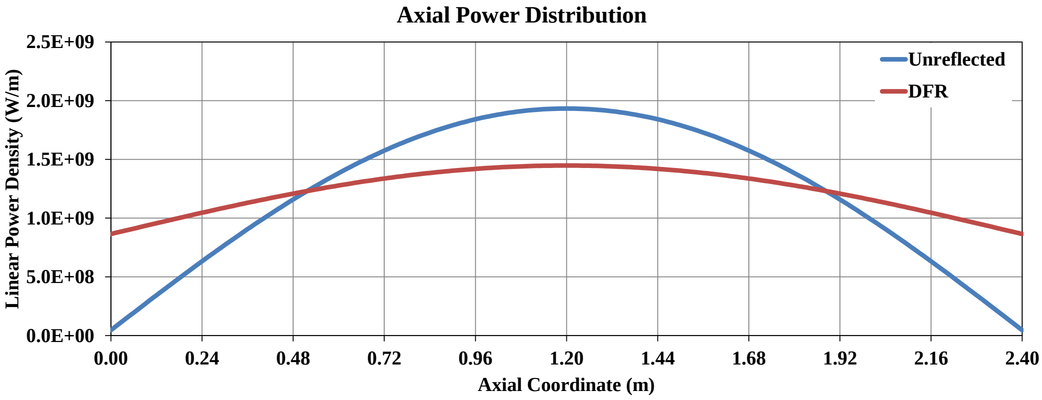

Figure 11.3: Axial power distribution of the DFR in the simulation

$$
\begin{aligned}
&= \int_{-H/2}^{H/2} P_{coef}\left[2.22\cos\left(\frac{\pi y}{H+\delta}\right)+3.16\right]\mathrm{dy}\\
&= P_{coef}\left[\frac{2.22(H+\delta)}{\pi}\sin\frac{\pi y}{H+\delta}+3.16y\right]\Bigg|_{-H/2}^{H/2}\\
&= (H+\delta)\left(\frac{4.44}{\pi}+3.16\right)P_{coef}\approx 11.14P_{coef}
\end{aligned}
$$

for an extrapolated height of $\delta = 0.037m$. So the expression of $P(y)$ is

$$
P(y) = \frac{P_{total}}{11.14}\left[2.22\cos\left(\frac{\pi y}{H+\delta}\right)+3.16\right] \tag{11.22}
$$

This expression as the axial power distribution is presented together with that of the unreflected cylindrical reactor in the form of a cosine function as a reference in Fig. 11.3. Both distributions have a total power of $3GW$. From the figure it is clear that the DFR's power profile is much flatter than the unreflected cosine profile, due to the existence of the reflecting material.

For the one-dimensional thermal-hydraulic model the power distribution depends on the number of nodes in the core. The power fraction in each node is integrated from Eqn. 11.21, where the total power output equals to the total thermal power generated in the core. In the two- and three-dimensional models discussed later, however, the direct power profile is used.

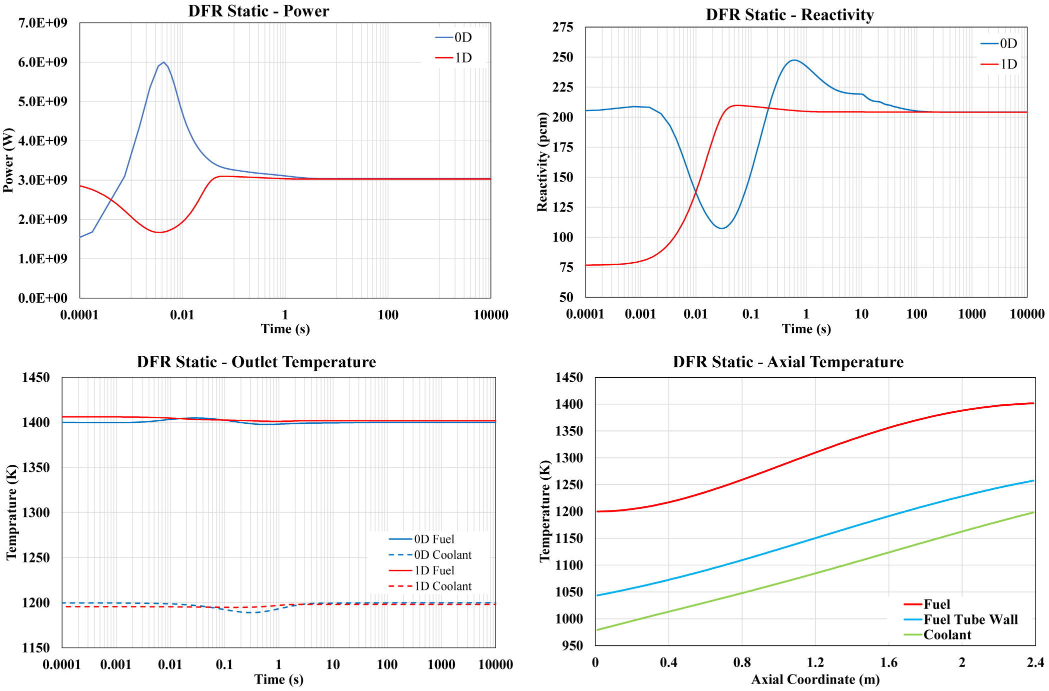

Figure 11.4: System Steady-state Results

11.3 Results of the Simulations

11.3.1 Steady-State Results

The steady-state calculation considers the stable state of the DFR system with the given initial design conditions. The results of thermal power, reactivity, outlet temperatures of the fuel and the coolant, and the spatial temperature distribution are shown in Fig. 11.4.

The x-axes of the figures show the calculation time, except for the axial temperature, which shows the axial coordinate, while the y-axes identify the investigated system variables. In the figures showing power, reactivity and temperature, the blue color is for the zero-dimensional results and the red color for the one-dimensional ones; the dashed lines in the temperature plot correspond to the coolant temperature and the solid line to the fuel temperature. In the plot of the axial temperature distribution, the curves for different materials are colored with a rainbow color set. The results of the axial temperature distribution come from the one-dimensional model since in the zero-dimensional model there is no spatial information.

In the steady state-analysis only the final stable values reached are relevant. In the power plot the result is 3.036×10^9 W, which is very close to the initial design power of 3×10^9 W, a relative difference (d_r) smaller than 1.2%. The reactivity responds to the temperature feedback, which is a consequence of power changes, and affects the power output directly. It is reasonable to expect that the reactivity compensates for the loss of the delayed neutron precursor and keeps the power stable. The final stable reactivity of the fuel is 213.4*pcm* , which has a d_r of 4.5% with respect to the initially set value of 204.2*pcm* .

Thanks to the self-regulation of the reactivity, the temperature of the fuel salt does not fluctuate much with time, but shows a satisfactory stability, regardless of the temperature of the fuel salt or of the coolant. The steady-state temperatures are 1400.0 / 1401.6K for the fuel and 1199.9 / 1198.1K for the coolant, for zero- and one-dimensional thermal-hydraulics model respectively, whose d_r are all smaller than 0.2%.

11.3.2 Transient Results

The main task of the transient analysis of the zero- and one-dimensional model is to set a baseline for the more complex simulations. The transient simulation results reflect how the DFR responds to disturbances in operation conditions. Since no transient calculations for the DFR have been done before, the reliability and consistency of the results are assessed by comparisons between results calculated with various initial parameters and models.

Transient responses are set to be triggered when the DFR system is operating in steady-state. In this section, the transient analysis is organized in the following several parts: the response to a small step reactivity change of up to ±500*pcm* , which corresponds to a typical reactivity insertion during normal operation of the system, and the response to a large step reactivity change up to ±2000*pcm* , which generally will only happen in the case of an accident. The actual limits of these two responses can be vague, so the suggestion from reference [CFS10, pp.105] was taken that a ±600*pcm* change of reactivity is comparable to the uncontrolled insertion or withdrawal of three control rods in a conventional reactor, while a ±800*pcm* change equals to an unprotected control rods extraction event. It has to be noticed that in these two scenario the velocity of the hypothetical control rods is not considered since the change of the reactivity is assumed to happen instantaneously: step change.

The scenario with the consideration of the velocity of the insertion/ withdrawal is simulated in the a later section, in which the total insertion/withdrawal takes a certain time in the form of a ramp. At the end of the ramp the reactivity will remain steady until the end of the simulation.

11.3.2.1 Response to a small Step Reactivity Change

The small reactivity change is defined between -500*pcm* to 500*pcm* into 8 data sets. This is approximately the reactivity generated by the system due to fuel temperature changes of 10K (as a reminder, the temperature feedback coefficient of the fuel salt is about -40*pcm* /K).

The results are plotted in Fig. 11.5. In the eight plots included, there are four properties investigated, namely total power, overall reactivity, fuel salt temperature and coolant temperature at the exit of the reactor. Since each plot includes eight data sets, the results of zero- and one-dimensional models are plotted in neighboring plots. The comparison between zero- and one-dimensional models can be carried out directly.

Because of the strong negative temperature feedback of the U-Pu fuel salt, when a step-wise reactivity is inserted into the system, it recovers in a very short time. For the zero-dimensional model, after a positive step of reactivity of $50pcm$, the DFR core needs only $0.002s$. After a negative step of reactivity of $-50pcm$, the time for the system to recover is about 3 times longer than the positive step. With increasingly larger positive reactivity steps, the system power reaches a larger power peak before settling back to the initial value, as shown in the power plot of Fig. 11.5. This larger power peak significantly increases the recovery time. For a large insertion of $500pcm$ the recovery time can last up to $0.3{\sim}0.4s$ and $0.1s$ for the positive and negative insertion respectively, while for the positive insertion the peak of maximum power lasts for only $0.002s$. The power after the transient is restored at between $3.13GW$ for $500pcm$ and $2.91GW$ for $-500pcm$, which means the perturbations considered cause fluctuations in the system final power within $\pm 5\%$.

The temperature changes permanently after the inserted reactivity. It can be seen from the plot of the temperature of the fuel salt in Fig. 11.5, that, after a fast transient peak value, the fuel salt temperature stabilizes at a certain value depending on the inserted reactivity. The change of the coolant temperature is smoother, because, due to the heat transfer's time constant, a sudden change of the temperature is damped. For an inserted reactivity of $500pcm$ the fuel salt's and the coolant's temperatures rise up to $1426K$ and $1213K$ respectively, and for a negative insertion of $-500pcm$ the temperatures decrease to $1376K$ and $1187K$.

The results of the one-dimensional model show that the power and the reactivity do not behave as in the zero-dimensional model. The most obvious difference can be found in the time that the peak values last due to the sudden insertion of reactivity. Their duration has been extended by 3 times for the power and by about 2 times for the reactivity. The recovery times after the peaks are, however, almost similar. This can be explained because in the zero-dimensional model the effect caused by sudden changes in reactivity are transferred instantly to the point-like system, whereas in the one-dimensional model the time taken for the flow to transport energy along the system has been taken into account. Thanks to this, the temperature at the exit of the reactor does not change so fast and in such a large amount in the one-dimensional model compared to the zero-dimensional model, since the effects of power changes are propagated from one node to another. The peak temperatures are, therefore, smaller and their final changes are also smaller. The final temperature for the one-dimensional model is $1422K$ (+) / $1207K$ (-) in the fuel salt and $1381K$ (+) / $1189K$ (-) in the coolant, each for a positive and a negative insertion of $500pcm$ and $-500pcm$ respectively.

11.3.2.2 Response To large Step Reactivity Changes

Large step reactivity insertions represent situations in which the system has encountered some severe accidents that induce large reactivity fluctuations. Five different insertions, from $2000pcm$ to $-5000pcm$, are investigated. All the results are plotted in Fig. 11.6. The number, the settings and the contents of the plots are the same as in the previous analysis for the response to small step reactivity changes.

The system can still restore the stability after large reactivity perturbations, as is displayed in the plot of the power and the reactivity. In both plots the magnitudes of the peaks and the oscillations due to the insertion of the reactivity have shown satisfactory consistency between the zero- and one-dimensional models, and the DFR system seems to recover to a steady state in a similar length of time, for the reactivity data sets from $2000 pcm$ to $-2000 pcm$.

Pronounced differences appear, however, between the two models in the recovery time of the system with the data set of $5000 pcm$. In the calculation with the zero-dimensional model the recovery time reaches $2.55s$, while with the one-dimensional model the time is around $0.8s$ less for the reactivity. For power both times are $2.95s$ and $1.95s$ respectively.

A similar behaviour can be observed also in the plots of the temperature. The fuel salt and the coolant temperatures reach new steady-state values after the insertion of reactivity with values from $2000 pcm$ to $-2000 pcm$, however. A reactivity insertion of $-5000 pcm$ be seems to have exceeded the valid range that can simulated with the zero-dimensional model. Compared to this, the one-dimensional model can handle this extremely large negative reactivity insertion successfully and bring the system back to a new steady state. The maximal relative differences of both the fuel salt and coolant temperatures between the two models reach only around 1% at $\pm 2000 pcm$, with respect to the results of zero-dimensional model.

11.3.2.3 Response to a Ramp Reactivity Change

The system response to a ramp insertion of reactivity is discussed in this section. Compared to the step-wise insertion, the ramped change of reactivity is more moderate. The system is supposed to have a longer time to react. With this intention, the types of ramp insertions of reactivities investigated are listed in Table 11.2, which contains four simulation cases from the ORNL reports [HE62, pp.27] and two extra added cases. The change of reactivity is supposed to be triggered during a steady-state of the system for a certain duration. After this time, the reactivity maintains the value at which the ramp stops and lasts until the end of the simulation.

	Total ρ (pcm)	Ramp slope (pcm/K)	Duration (s)
Ramp1	1000	33	33.33
Ramp2	1000	50	20
Ramp3	1000	100	10
Ramp4	1500	150	10
Ramp5	2000	200	10
Ramp6	3000	300	10

Table 11.2: Ramped insertions of reactivity

The results are plotted in Fig. 11.7, in which the time axis is logarithmic in order to have a clearer view of the transient process. Compared to the transient response to a step reactivity change, the transients in this section are already much longer. The reactivity changes over $200s$ for all the cases, while the changes in the power and temperatures stop closely after the change of the inserted reactivity. When the inserted reactivity remains as a constant, the power and the temperatures find their new steady-state values.

The ramp reactivity change brings smaller effects on the system. It can be seen in the plots of the power in Fig. 11.7 that the final power output level is only related to the total inserted reactivity (Ramp1 to Ramp3). However the shorter the duration of the ramp is, or to say the larger the ramp slope is, the more significant is the magnitude of the power rise (Ramp3 to Ramp6).

The total reactivity response in the reactivity plot shows the resulting effect of the temperature feedback and the inserted reactivity. Unlike the step insertion, the large negative feedback due to the gradual increase of the reactor temperature suppresses a pulse-like reactivity change. It can be observed that the longer the duration is, the smaller the total reactivity at the end of the ramp.

By comparing the results between the two models it can be found that the amplitudes predicted by the one-dimensional model are smaller than that of the zero-dimensional model, with the differences smaller than 2%. The reason for this can be found in that in the zero-dimensional model the properties of the fluids are set to be an averaged value. Therefore, when the power rises due to the increased reactivity, the one-dimensional model is more capable of distributing the energy produced in the core and keeps the system at a relatively lower overall temperature level.

11.4 Conclusions

From the simplified transient analysis discussed above, a general behavior of the system response to the selected disturbances can be inferred. The results of the zero- and one-dimensional models have shown that a satisfactory consistency between two models can be achieved.

Since there are no other analyses of the DFR to use as a reference for comparison, these two models with different methods can, somehow, provide a certain level of reliability to ensure that the results may not be too far away from the expected real behavior of the DFR. Moreover, the analysis of the system with zero- and one-dimensional models can be refined and modified based on the results of the analyses reported in the next chapter applied to a single fuel cell.

The consistent results reveal that the DFR system is stable against the sudden external change of reactivity. In the simulations, the maximum considered step-wise reactivity insertion reached up to $\pm 2000pcm$, but the system recovered back to its normal state in less than $2s$, thanks to the strong negative thermal feedback of the fuel salt itself. The change in the temperatures of the fuel salt and the coolant are also small enough to be acceptable from a safety point of view. The ramped reactivity insertion causes a smaller impact on the system variables and there is no very high and rapid peak values. Ramped reactivity insertions, with a smaller insertion rate but a longer time, change the state of the system, especially the power production, but less abruptly than step-wise insertions, as is observed in most nuclear reactor types.

Though the comparisons have shown satisfactory consistency between two models employed, as a preliminary approach, these models themselves are only useful for simplified analyses. Several improvements must be made in the models to increase their applicability and reliability. Some proposed improvements are:

- **More core regions:** It has been mentioned that in the one-dimensional model there are already 100 nodes along the axial direction, but the arrangement of nodes is only for the thermal-hydraulic calculation. For the neutronics calculation the reactor should also be discretized, so that the delayed neutron precursors in different axial nodes can be compared and verified, since the spatial neutron flux has its own shape in the reactor. Based on a complete one-dimensional model for both neutronics and thermal-hydraulics, a radial discretization should also be implemented, in which the radial distribution of both the neutron flux and the power density are explicitly considered.

- **Tertiary Circuit:** The tertiary circuit means the circuit where another coolant flows to extract the energy that the lead coolant takes from inside of the reactor. Due to the need to reduce the complexity of the calculations, the simulations carried out with both models focused only on the reactor itself: fuel salt and lead coolant circuits. The heat exchanger, as well as, further auxiliary systems were not considered. The input temperature of the first node of the thermal-hydraulic model was, therefore, set as a constant vlaue boundary condition, which is not real. This temperature should be set by a balance of the removed power from the reactor to the tertiary loop. Moreover, the time employed by the out-coming lead coolant flowing through the heat exchanger between the secondary and the tertiary circuits should also be considered, so that the response time of the inlet temperature can be more realistic compared to the current model.

- **More equipment:** Except for the tertiary circuit with the heat exchanger, the pump accurate modeling should also be addressed. By studying the description of the DFR system, it is not difficult to see the importance of the driving force of the fuel salt and, especially, of the lead coolant. The powerful pumps needed to move the fluids have to be taken into account in a comprehensive safety analysis. Additionally, in order to perform more comple transient analyses, the functionality of the designed drain tank system must also be evaluated.

- **More accurate parameters:** It is already known that the thermal-hydraulic properties of the fuel salt are based on approximations. For a more accurate system analysis, these properties are supposed to be validated and fitted with experimental data. The constant values of the properties used in this study could then be replaced by more accurate functions or empirical relationships.

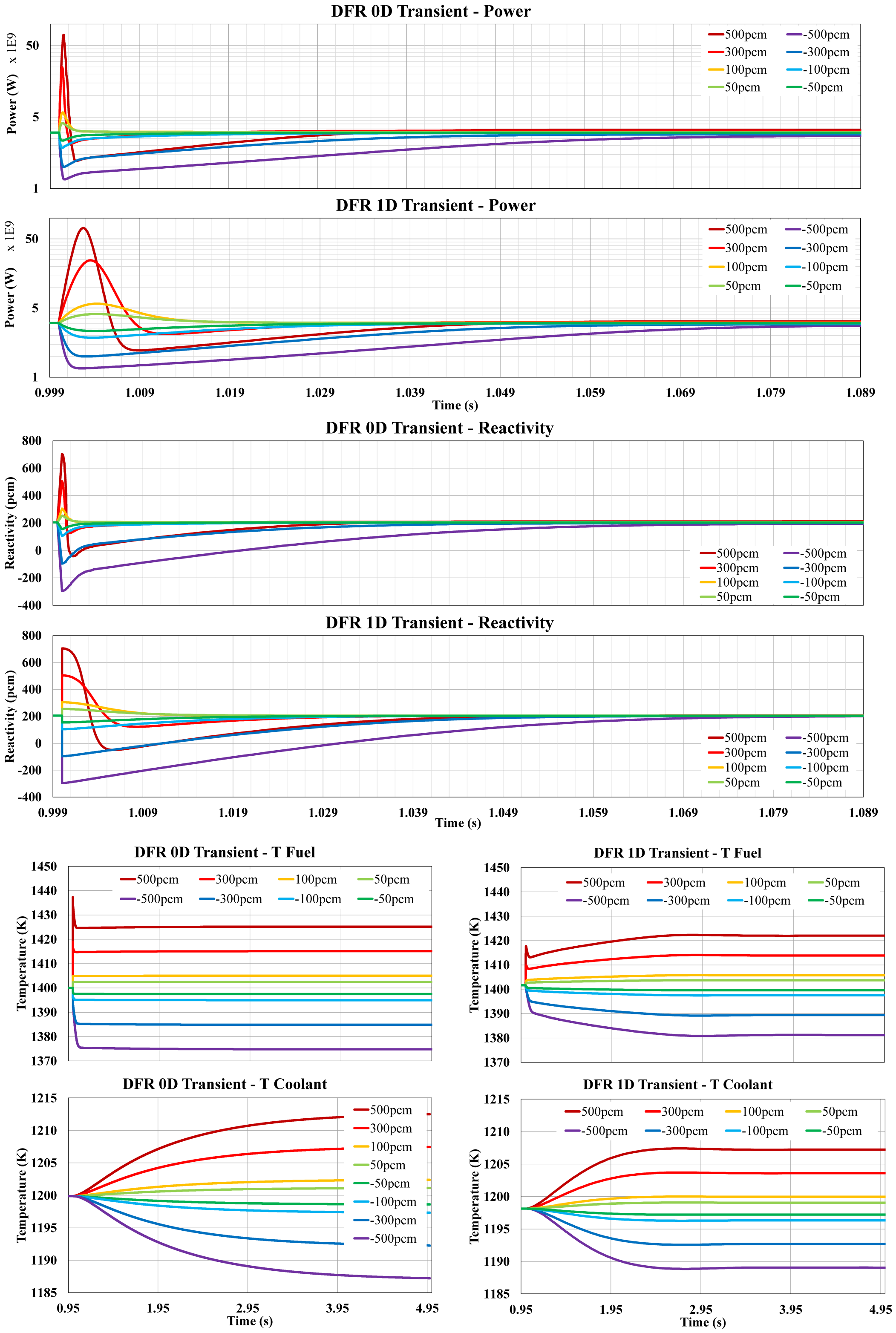

Figure 11.5: Transient results on small insert reactivities in step form

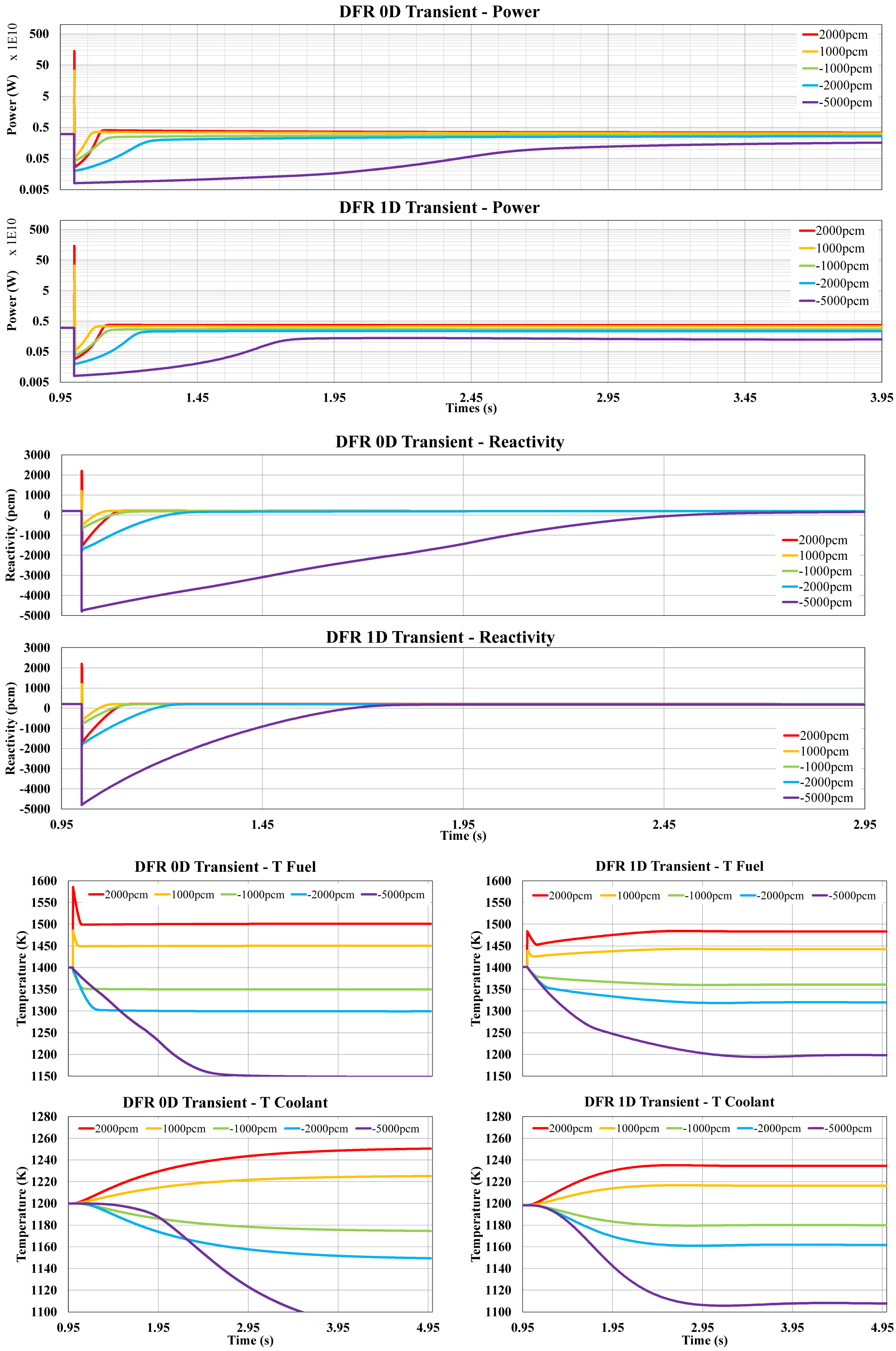

Figure 11.6: Power transient on insert reactivities in step form

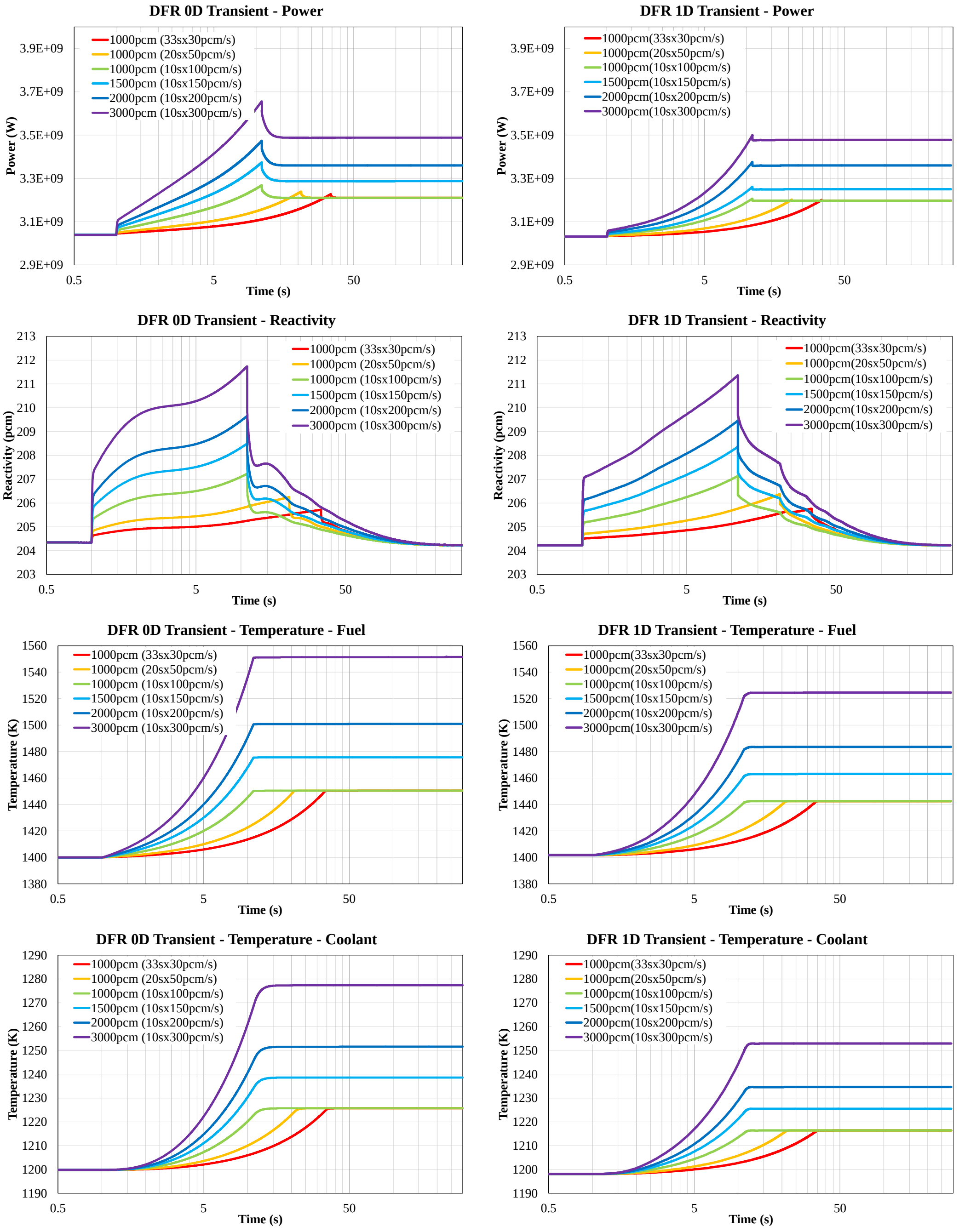

Figure 11.7: Transient results on insert reactivities in ramp form

Chapter 12

Single Cell Analysis

12.1 Introduction

With more considerations and more details, the analysis of the DFR needs more powerful computation resources and longer times when a realistic model in two- or in three-dimensions is used. Therefore, the size of the reactor has to be scaled and the structure has to be simplified without losing generality or similarity. For a nuclear reactor, the core radius is a significant criterium which determines the inner structure and arrangements of the core and also the amount of fuel. Since the core of DFR consists of hexagonal arranged fuel tubes where the fuel salt flows inside of the tubes and the coolant flows outside of the tubes, the volumetric ratio of the fuel salt and the coolant can be considered as the key factor of the heat transfer between the two fluids, so that the similarity between the model and the real reactor can be ensured by the unchanged volumetric ratio of both fluids.

Based on this principle, with an increasing core radius the evolution of the DFR cross sectional flow areas and the corresponding ratios of the fluids can be found in Fig. 12.1, from which it is possible to find an appropriate scale, and, on this scale, a simplified model can be developed with less error and also with less resources. The increased core radius enables more fuel tubes in the core. As a result the cross sectional flow area for both fuel salt and coolant, not only in the core, but also in the plena increase continuously at the same time as indicated on the left vertical axis. The right vertical axis indicates the ratio of the correspondent volumes, since, for the thermal-hydraulic analysis, the volumetric ratio is much more important than the absolute volume.

Inside of the core, with the increase of the core radius and the total number of the fuel tubes, the fuel-coolant ratio is an asymptotic curve that reaches a value about 1.16. This means that in the core the volumes of the fuel and the coolant are quite close. For the fuel salt only, the ratio of the flow area in the core and that in the plenum has grown asymptotically up to 0.699, while for the coolant the corresponding ratio reaches 2.18. This means that both fluids undergo significant changes in their flow areas at the boundary of the core with the plenum. For a constant mass flow rate in the plenum the velocity of the coolant can be almost double than the velocity

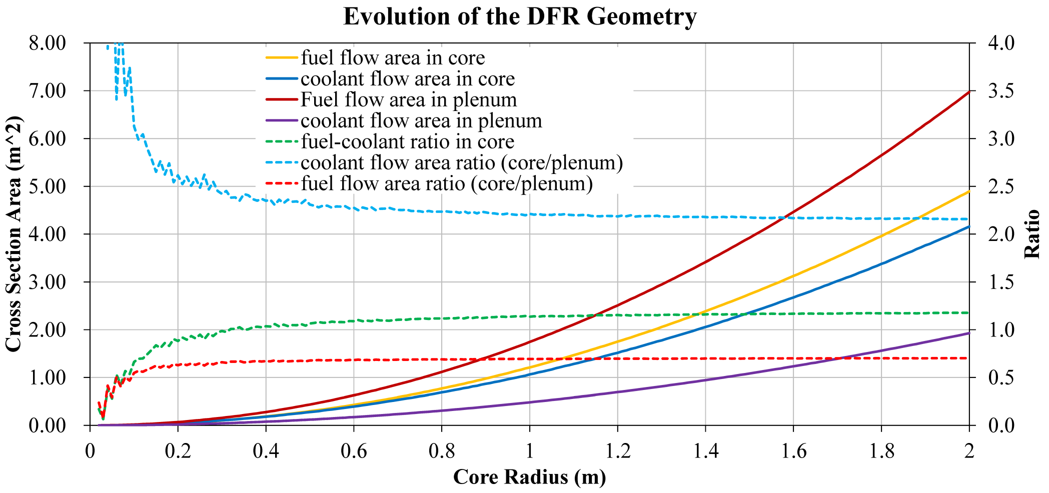

Figure 12.1: Evolution of the Geometry of the DFR

	fuel-coolant		fuel core/plenum		coolant core/plenum	
r$_{core}$	value	rel.diff.	value	rel.diff.	value	rel.diff.
0.20	0.88	-23.91%	0.63	-10.15%	2.61	20.01%
0.40	1.04	-10.64%	0.67	-3.94%	2.35	7.78%
0.60	1.09	-6.10%	0.68	-2.28%	2.28	4.43%
0.80	1.12	-3.57%	0.69	-1.34%	2.24	2.59%
1.00	1.14	-2.05%	0.69	-0.81%	2.21	1.54%
1.20	1.15	-0.47%	0.70	-0.13%	2.18	0.28%
1.35	1.16	0.00%	0.70	0.00%	2.18	0.00%

Table 12.1: Values and relative differences of the characteristic ratios

parallel to the bundles in the core, while the velocity of the fuel salt can be decreased to half of the velocity in the fuel tubes in the core. Consequently local pressure drops are also expected at the boundaries between the different reactor zones. The three ratios begin to get close to their asymptotic values from r_{core}=0.4m upwards. In fact, at r_{core}=0.4m the relative differences of the characteristic ratios with respect to the actual value at r_{core}=1.35m are around, or smaller than, 10%, which can be considered as acceptable. A scaled DFR model with r_{core}=0.4m still contains ca. 1135 fuel tubes, which is less than 1/10 of the actual total number of fuel tubes. The relative differences between the three ratios related to the final values at r_{core}=1.35m are summarized in Table 12.1.

Due to limited calculation resources, the simplified model with r_{core}=0.4m is still impossible in the current work. For this reason, in this chapter only a single unit hexagonal cell is modeled and simulated. The general flow pattern and the flow properties are calculated in both two-dimensional and three-dimensional geometries, while a sensitivity analysis are carried out only with the two-dimensional model.

12.2 Model Development

12.2.1 Two-Dimensional Model

This section presents the two dimensional thermal hydraulic analysis of the fuel salt tube in the core region, which is the most basic component of the DFR concept. The zero-dimensional and one-dimensional analysis in the previous chapters generated approximated results but neglected the thermal-hydraulic detailed features of the fluid flow, which are analyzed in this chapter with a simplified two-dimensional geometry.

The two-dimensional analysis tries to achieve the general description of the thermal hydraulic features of the single fuel cell without a very large computational cost. For this reason two-dimensional simulations are a convenient platform to validate thermal hydraulic assumptions and carry out sensitivity studies. Therefore, the fundamental task in this chapter is to investigate the thermal hydraulic behavior of both DFR fluids by setting up an axial-position-dependent heat source in the fuel salt, which produces the same heat per unit volume as the real thermal power. Information about the heat transfer, temperature, pressure drop, change of velocity and density due to the changes in the core temperatures, as well as, other fluids properties can be obtained from these simulations. Moreover, some sensitivity studies regarding nodalization, wall functions and variation of the thermal properties of the tube wall material SiC can be performed to find out the robustness of the calculations and the possible limitations of the results.

The calculations presented in this Section were performed with COMSOL and FLUENT in order to compare their results. Since COMSOL itself consists of quite a number of modules with different functionalities, the two-dimensional model was set up with the Multi-physics module that consists of *Turbulent* and *Heat Transfer in the Fluids*. As the name indicates, the *Turbulent* part deals with the turbulent flows while the other part focuses on the heat transfer between fluids and solids. The Multi-physics module combines two physical processes and formulates them as a coupled one.

12.2.1.1 Geometry

The two-dimensional fluid model of the fuel salt tube is shown on the left side plot in Fig. 12.2 (generated by COMSOL, scaled 1:100). Since the original form of the unit cell of the fuel-coolant heat transfer is a hexagonal prism, it has different axial projections on the $x-y$ plane through the central axis of the hexagonal prism. In order to achieve comparable results, an equivalent axi-symmetric cylindrical model was established, so that it had the same volumetric fuel-to-coolant ratio as the original hexagonal prism. In the left plot the edge on the x-axis represents the radial direction of the hexagonal channel, which, from $0m$ to $0.00725m$, is the fuel salt flow channel, from $0.0095m$ to $0.01155m$, instead of $0.011m$ as inscribed radius, or $0.0127m$ as the out-scribed radius of the hexagonal prism, is the coolant flow channel. The area between them is the fuel tube wall. The edge on the y-axis represents

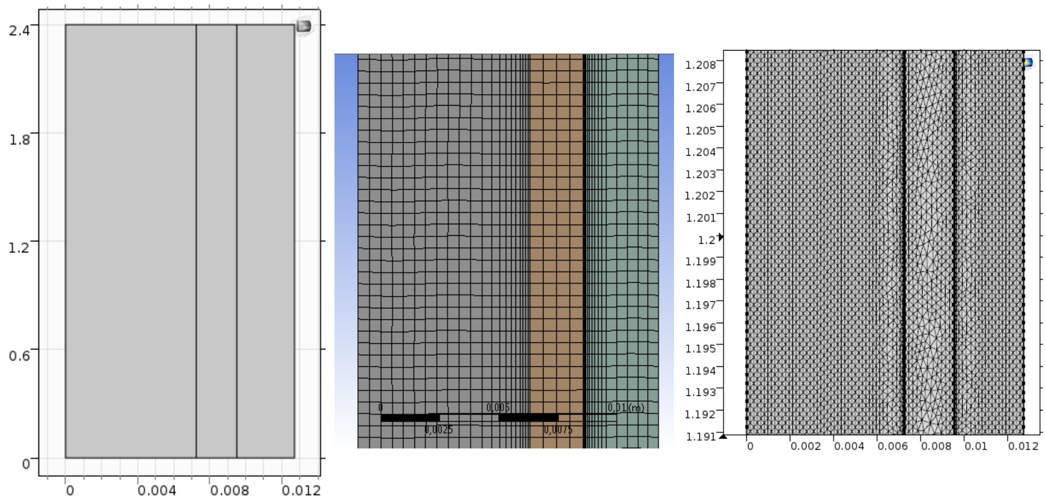

Figure 12.2: 2D model and meshes of the fuel salt tube (FLUENT(m), COMSOL(r))

the height of the cell. The symmetry axis of the model is at x=0.0 [1]

12.2.1.2 Materials

For simplification there are only three materials considered in both two- and three-dimensional models: two liquids, which are the U-Pu fuel salt and the liquid lead coolant, and one solid material which is the wall structure made of SiC. The features and properties of the materials can be found in Table 3.4 and Table 3.5.

12.2.1.3 Mesh

The mesh plays a very important role in Computational Fluid Dynamics (CFD) simulation. In order to carry out a sensitivity study on the mesh size and to ascertain the effect of different meshes on the simulation results of the DFR fuel cell, several possibilities are considered. Generally two mesh types, the *triangular* and *quadrangular*, which is also known in FLUENT as *CutCell*, were used. Based on these two types of meshes, parameters are set and alternated for the considered ranges. A local demonstration of the geometry with both kinds of meshes is shown in the middle (generated by FLUENT) and on the right side in Fig. 12.2 (generated by COMSOL). The detailed mesh data used for the calculation are listed in each section.

12.2.1.4 Turbulence Models

Since research on turbulence modeling started in 1960's, turbulence models based on the determination of the turbulence kinetic energy have dominated the field.

---

[1] However in the model the symmetry axis in COMSOL is the z-axis(with a $z-r$ coordinate system) and in FLUENT is y=0.0 (Cartesian coordinate system). For the axis-symmetric calculations it is worthy to be mentioned that in FLUENT the model must be and only can be located in the first and second quadrants so that the symmetry axis is y=0.0

In the decades past one- two-equation models have been developed and have been distinguished for their completeness in the application range [Wil93, pp.73]. Among the two-equation models, the most used and preferred k-ϵ model was applied in this work.

The detailed forms of the model applied by COMSOL and FLUENT are not exactly the same. In FLUENT there are two variations of *Standard* k-ϵ [LS72] and *Realizable* k-ϵ [SLS+95] turbulence models and in COMSOL the turbulence effects are formulated by *Standard* k-ϵ with realizability constraints [COM15, pp.56], [Wil93, pp.89]. Compared to the *Standard* k-ϵ model the *Realizable* k-ϵ model uses a modified transport equation for the dissipation rate of kinetik energy ϵ and a new eddy viscosity formulation. The formulations of these turbulent models can be summarized as follows.

The transport equation for turbulence kinetic energy k:

$$\rho(\vec{\mathbf{u}}\cdot\nabla)k = \nabla\cdot\left[\left(\mu+\frac{\mu_T}{\sigma_k}\right)\nabla k\right] + \mathrm{Term_k} - \rho\epsilon \tag{12.1}$$

and the transport equation for the dissipation rate ϵ:

$$\rho(\vec{\mathbf{u}}\cdot\nabla)\epsilon = \nabla\cdot\left[\left(\mu+\frac{\mu_T}{\sigma_\epsilon}\right)\nabla \epsilon\right] + \mathrm{Term_\epsilon} \tag{12.2}$$

where for each model $\mathrm{Term_k}$ and $\mathrm{Term_\epsilon}$ have their own expressions:

$$\begin{aligned}
&\mathrm{Term_k}\\
\text{FLUENT } k-\epsilon:\quad & G_k + G_b - Y_M + S_k\\
\text{COMSOL } k-\epsilon:\quad & P_k\\
&\mathrm{Term_\epsilon}\\
\text{FLUENT standard } k-\epsilon:\quad & C_{1\epsilon}\frac{\epsilon}{k}(G_k + C_{3\epsilon}G_b) - C_{2\epsilon}\rho\frac{\epsilon^2}{k} + S_\epsilon\\
\text{FLUENT realizable } k-\epsilon:\quad & C_{1\epsilon}\frac{\epsilon}{k}C_{3\epsilon}G_b + C_2\rho\frac{\epsilon^2}{k+\sqrt{\nu\epsilon}} + (C_1\rho+1)S_\epsilon\\
\text{COMSOL } k-\epsilon:\quad & C_{1\epsilon}\frac{\epsilon}{k}P_k - C_{2\epsilon}\rho\frac{\epsilon^2}{k}
\end{aligned}$$

with G_k the generation of turbulence kinetic energy due to the mean velocity gradients, G_b the generation of turbulence kinetic energy due to buoyancy, Y_M as the contribution of the fluctuating dilatation in compressible turbulence to the overall dissipation rate, and μ_T the Eddy Viscosity [SLS+95, pp.3]:

$$G_b = \beta g_i\frac{\mu_T}{Pr_T}\nabla T, \quad Y_M = 2\rho\epsilon M_T^2, \quad \mu_T = \rho C_\mu\frac{k^2}{\epsilon},$$

$$\begin{aligned}
C_1 &= \max\left[0.43, \frac{\eta}{\eta+5}\right], \quad \eta = \sqrt{2S_{ij}S_{ij}}\frac{k}{\epsilon}, \\
G_k &= -\rho\overline{\mathbf{u}_i'\mathbf{u}_j'}\nabla\mathbf{u} \\
&= \rho\left(C_\mu\frac{k^2}{\epsilon}(\nabla\mathbf{u}+(\nabla\mathbf{u})^T) - \frac{2}{3}k\delta_{ij}\right)\nabla\mathbf{u} \\
&= \mu_T\left(\nabla\mathbf{u} : (\nabla\mathbf{u}+(\nabla\mathbf{u})^T) \qquad\qquad\qquad\qquad \right) - \frac{2}{3}\rho k\nabla\cdot\mathbf{u} \\
P_k &= \mu_T\left(\nabla\mathbf{u} : (\nabla\mathbf{u}+(\nabla\mathbf{u})^T) - \frac{2}{3}(\nabla\cdot\mathbf{u})^2\right) - \frac{2}{3}\rho k\nabla\cdot\mathbf{u}
\end{aligned}$$

and with the following closure coefficients as constants: $C_{1\epsilon}$=1.44, $C_{2\epsilon}$=1.92 (for realizable k-ϵ model C_μ is no longer a constant [ANS13, pp.53]), C_2=1.9, C_μ=0.09, σ_k=1.0, σ_ϵ=1.3 (1.2 for realizable k-ϵ model). Among the rest of parameters, $\mathbf{u}$ is the velocity field, S_k and S_ϵ are defined source-terms, β is the thermal expansion coefficient, g_i is the i component of the gravitational vector and M_T is the turbulent Mach number. The derivation of G_k has been intentionally left blank to compare with P_k. It shows that the P_k in the COMSOL k-ϵ model represents only the generation of turbulence kinetic energy due to the mean velocity gradients (G_k), and the extra term compared to G_k is also related to the velocity. However, the generation of turbulence kinetic energy due to buoyancy (G_b) and the contribution of the fluctuating dilatation in compressible turbulence to the overall dissipation rate (Y_M) do not appear in the COMSOL k-ϵ model.

12.2.1.5 Velocity Profile

In order to investigate the flow condition, the boundary layer has to be considered for not only hydraulic calculation but also for the heat transfer model. A Pr number much smaller than 1 means also a thicker boundary layer. Since the flow develops inside of a rounded channel, the development of the velocity boundary layer is depicted in Fig. 12.3 [mek11, pp.325]:

The hydrodynamic entrance region can be therefore calculated by [SB87b]:

$$\begin{aligned}
L_{h,fuel} &= 1.359 \times D_h Re_D^{0.25} \\
&= 0.41m
\end{aligned}$$

The result of this calculation shows that the entrance region takes up only one fifth of the total length of the flow channel and, after that, the flow can be considered as fully developed, while the boundary layer with increasing thickness merges in the center of the fuel salt tube. Therefore, in the two-dimensional case, the radial velocity profile can be set to a uniform velocity at the entrance of the system.

At the same time, a completely developed flow profile in the entire flow channel is also adopted, which approaches the situation that the fluids enter the flow channel with a fully developed velocity profile. A parabolic velocity profile is therefore implemented

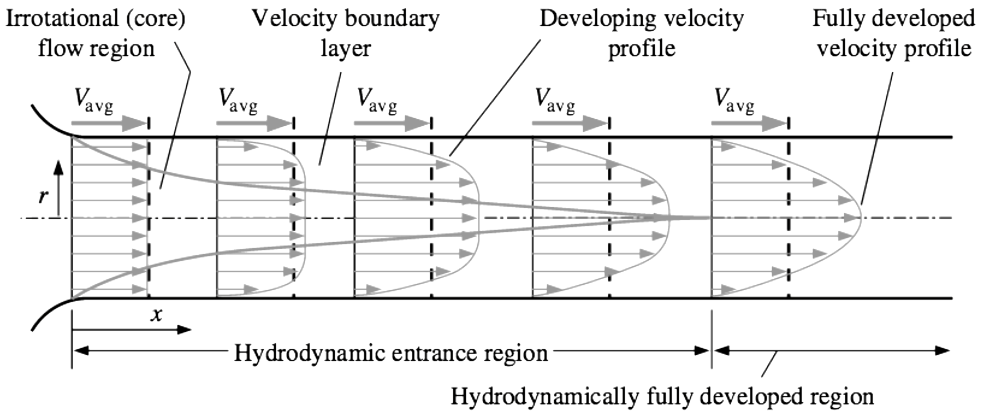
Irrotational (core) flow region
Velocity boundary layer
Developing velocity profile
Fully developed velocity profile
V_{avg}
r
x
Hydrodynamic entrance region
Hydrodynamically fully developed region

Figure 12.3: Development of the velocity boundary layer

in the two-dimensional model. According to Fig. 12.3, the relationship between v_{avg} and v_{max} is expressed as

$$\begin{aligned} v_{avg} &= \frac{1}{A}\int v(r)dr \\ \text{or for 2D} \quad v_{avg} &= \frac{1}{D}\int v(r)dr \end{aligned} \tag{12.3}$$

where A is the flow area of the inlet and D is the length of the inlet as a dimensionality reduction of A. Therefore the velocity profile, which is considered flatter as the parabolic profile for the laminar flow, for the symmetric flow channel in the two-dimensional model has the form [TK90a, pp.378]

$$v(x) = Cv_{avg}\left(1-\frac{r}{R}\right)^{1/7}$$

Substituting the velocity profile into Eqn. 12.3 and interate

$$v_{avg,f} = \frac{1}{D}\int_{x=0}^{x=D} C_f\left(1-\left(\frac{x}{D}\right)^{1/7}\right)dx = \frac{2C_f}{3}$$

So the final parabolic velocity profile for the fuel salt and coolant in the equivalent cylinder geometry of the model can be expressed as

$$v_f(x) = 1.5v_{avg,f}\left(\frac{0.00725-x}{0.00725}\right)^{1/7}, \quad 0 \le x \le 0.00725 \tag{12.4}$$

$$v_c(x) = 1.5v_{avg,c}\left(\frac{x-0.0095}{0.01155-0.0095}\right)^{1/7}, \quad 0.0095 \le x \le 0.01155 \tag{12.5}$$

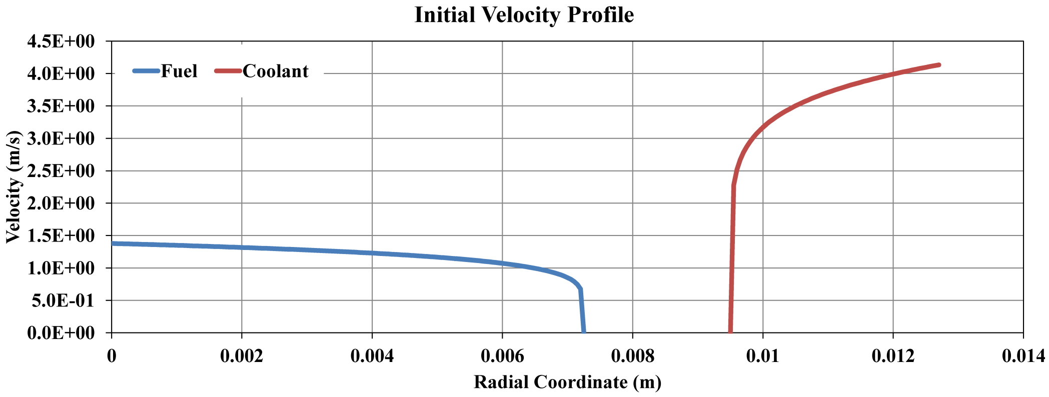

Figure 12.4: Radial initial velocity profile

The both velocity profiles are presented in the following Fig. 12.4

12.2.1.6 Pressure Drop

Since the fuel salt and the coolant in the later thermal hydraulic calculations have the real features like compressibility and viscosity, it is necessary to reconsider the pressure drop of the fluids. Nowadays the research of the pressure drop of the fuel salt as well as of the liquid metal is achieved by assessing correlations for the flow pattern and the friction factor with the limited results from experiments. The IAEA report [iae13, pp.23-pp.40] summarized the hydrodynamic models for the bare-rod bundle with grids and in wire-wrapped rods. However the flow pattern of the fuel salts and the coolant lead is out of the limitation of the valid application range of the models, the following estimations are found on more basical correlations.

Generally the pressure drop Δp of a single-phase fluid in a heated channel can be constructed as the summation of several pressure terms as mentioned in the last section, derived in the literature [TK90b, pp.117]:

$$\begin{aligned}\Delta p =& p_{in} - p_{out} = \Delta p_{acc} + \Delta p_{gravity} + \Delta p_{fric} + \Delta p_{form} \qquad (12.6)\\ \text{where: } \Delta p_{acc} =& G_m^2 \left(\frac{1}{\rho_{out}} - \frac{1}{\rho_{in}} \right)\\ \Delta p_{gravity} =& \int_0^L \rho_{mean} g dz\\ \Delta p_{fric} =& \int_0^L \frac{f G_m |G_m|}{2 D_h \rho_{mean}} dz\\ \Delta p_{form} =& \sum_i K_i \frac{G_m |G_m|}{2\rho_{mean}}\end{aligned}$$

where in Eqn. 12.6 Δp_{acc} represent the pressure loss (Pa) due to the change of the cross section of the flow channel, $\Delta p_{gravity}$ is for the pressure loss due to the gravity, especially in the vertical flow channels, Δp_{fric} gives the pressure loss due to the friction of the fuel tube, and Δp_{form} is the term due to the sudden change of the flow channel. In the expressions f stands for the Darcy's friction coefficient and K for the local form loss coefficient. G_m is the mass flow density in $(kg/(m^2 \cdot s))$ and can be calculated by:

$$G_m = \frac{\dot{m}}{A}$$

Based on the boundary condition of the one-dimensional model, the cross sectional area of the flow channel does not change, the friction is not considered, and the sudden change at the core inlet and oulet is not yet considered. So the total pressure loss of the one-dimensional model can be simplified as the following expression with the values of certain variables from zero-dimensional calculations or calculated according to the equations in Sec. 3.3.4

$$\begin{aligned}\Delta p &= \Delta p_{acc} + \Delta p_{gravity} + \Delta p_{fric} \\ &= G_m^2 \left(\frac{1}{\rho_{out}} - \frac{1}{\rho_{in}}\right) + \int_0^L \rho_{mean} g dz + \int_0^L \frac{f G_m |G_m|}{2 D_h \rho_{mean}} dz \qquad (12.7)\end{aligned}$$

if the friction factor f is a function of Re, the pressure drop of the fuel and the coolant is expressed as

$$\Delta p_f = 9.2546 \times 10^4 + 8.1191 \times 10^5 f(Re) \qquad (12.8)$$

$$\Delta p_c = 2.3987 \times 10^5 + 4.7677 \times 10^7 f(Re) \qquad (12.9)$$

The exact expression of $f(Re)$ has then to be found. Starting from the Darcy's friction factor [DIBL05, pp.490] is defined as

$$f(Re) = \frac{D_h}{L} \frac{\Delta p^*}{(1/2)\rho V^2} \qquad (12.10)$$

where Δp^* is the piezometric pressure drop over a length L. In reality *f(Re)* is determined from the Moody's Chart or evaluated with appropriate correlations. Depending on the relationship between $f(Re)$ and the Re number, and also strongly depending on the Reynolds-Number itself, a value can be determined from the correlation, especially when the coolant and the fuel salt are liquid metals or liquid metal-alike materials. Some well-known correlations are investigated and plotted as a function of the Re number in Fig. 12.5 for both fluids.

For fluids in a circular duct,

McAdams [Rus79] ($3\times10^4 < Re < 10^6$)	$f = 0.184 Re^{-0.2}$
Pfann [Pfa77, pp.162] ($2300 < Re < 1.668\times10^6$)	$f = \left(\frac{0.28}{\log Re - 0.82}\right)^2$
Drew et al. [nas12, pp.5] ($3000 < Re < 3\times10^6$)	$f = 0.0014 + 0.125 Re^{-0.32}$

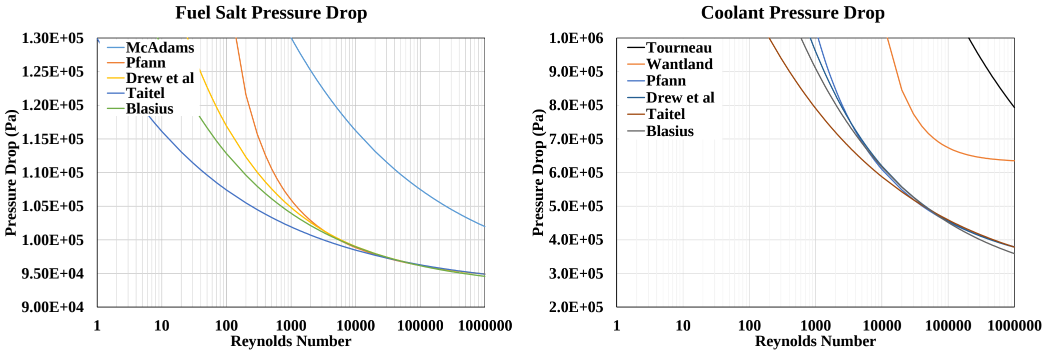

Figure 12.5: Theoretical pressure drop

$$\text{Taitel \& Dukler [TD76] } (3000{<}Re{<}10^5) \qquad f = 0.046Re^{-0.2}$$
$$\text{Blasius [Bla13] } (3000{<}Re{<}10^5) \qquad f = 0.079Re^{-0.25}$$

for fluids in a bundle,

$$\text{Tourneau [Rus79] (tri p/D=1.12, } 3000{<}Re{<}10^5\text{))} \qquad f = 0.184Re^{-0.2}$$
$$\text{Wantland [TJ79] (tri p/D=1.19, } 2000{<}Re{<}10^4\text{))} \qquad f = 0.0082 + 90Re^{-1.0}$$

Among these relationships, the ones from Pfann, Drew, Taitel and Blasius are specified for liquid metals [Pfa77], while other listed relationships can also be used for other working fluids. It can be seen that for the fuel salt, the expression of f proposed by McAdams is far away from other expressions for Re<1,000,000. The rest of the expressions have also shown discrepancies for Re$< 10,000$. At the same time for the lead coolant the relationships specialized for bundles are far away from the ones applicable to a circular duct, while other expressions have a cross point before Re=10,000 and begin to differ just after this point.

As mentioned in the last paragraphs, the theoretical pressure drop of the fluids in the flow channel for the two-dimensional model can be updated by substituting Eqn. 12.7 with Eqn. 12.8 and 12.9. Therefore, with the Re numbers listed in Table 11.1, the pressure drops can be calculated in advance by using the relationships between f and Re, or by using the chart data in Fig. 12.5 for the approximation. The calculated results are listed in Table 12.2, which can be compared later with the simulation results.

12.2.1.7 Heat Transfer

The heat transfer model deals with conduction heat transfer inside of each material and convective heat transfer at the interfaces between the fuel salt and the fuel tube wall as well as between the wall and the coolant.

The convective heat transfer coefficient h for the flow can be expressed in terms of

	Fuel salt	Coolant
McAdams/Tourneau	107 921	822 891
Wantland	104 626	573 691
Pfann	100 670	262 414
Drew et. al	102 225	382 557
Taitel	102 268	385 867
Blasius	102 118	373 581

Table 12.2: $f - Re$ dependent pressure drop (Pa)

the dimensionless Nusselt Nu number [TK90a, pp.417] by

$$h = \frac{Nuk}{D_h} \tag{12.11}$$

Depending on the geometry of the flow channel and the features of the flow itself, the *Nusselt* number, determines the heat transfer coefficient at the interface fluid-solid. The definition of the *Nusselt* number is

$$Nu = \frac{hD_e}{k} \tag{12.12}$$

where D_e is the effective diameter of the flow channel, k is the thermal conductivity of the material, and h is the heat transfer coefficient. From this definition, it can be seen that the value of h can be obtained from Eqn. 12.12 and, therefore, Nu needs to be calculated with appropriate correlations. The *Nusselt* number can be correlated in terms of other dimensionless numbers as introduced in the last section [LB01, pp.439] and can be expressed in quite a number of forms. Since there are two working liquids, which is specified as liquid metal or liquid-metal-like fluids, in the DFR concept and both are in forced turbulent flow conditions, as shown in Table 11.1, the discussion of the Nu is then divided into two parts focusing on the geometrical differences of their flow channels with respect to the boundary condition of "circumferentially constant wall temperature and axially constant wall heat flux" [SB87a, 3.9]:

$$\begin{aligned} q''_w &= q''_w(r, z) \\ T_w &= T_w(r) \end{aligned}$$

With the development of the molten salt reactor, the research on its thermal-hydraulic features of the molten salt has accumulated many experiments and theoretical analysis. Since the molten salt in the DFR has a low Pr number smaller than 0.1, it can be considered as a liquid metal as well. Selected correlations for circular duct flow are listed below in Eqn. 12.13 to Eqn. 12.20:

$$Nu = 5.6 + 0.0165Re^{0.85}Pr^{0.86} \tag{12.13}$$

$$Nu = 7 + 0.025\left[Pe - \frac{1.82Re}{(0.037Re\sqrt{f})^{1.4}}\right]^{0.8} \tag{12.14}$$

Name	Equation	Pr	Re	Nu	h
Chen [CC81]	(12.13)	0-0.1	10^4-5×10^6	56.75	1.26E5
Dwyer [Dwy63]	(12.14)	0-0.1	10^4-5×10^6	56.18	1.25E5
Lee [Lee83]	(12.15)	0.001-0.02	510^3-10^5	8.11	1.80E4
Lubarski [LK55]	(12.16)	0-0.1	10^4-10^5	27.78	6.16E4
Lyon [Lyo51]	(12.17)	0-0.1	10^4-5×10^6	56.40	1.25E5
Notter [NS72]	(12.18)	0.004-0.1	10^4-10^6	50.04	1.11E5
Sleicher [ST57]	(12.19)	0-0.1	10^4-5×10^6	49.89	1.11E5
Skupinski [STV65]	(12.20)	0-0.1	10^4-5×10^6	52.05	1.15E5

Table 12.3: Assessment of Nu number correlations for fuel salt

$$\text{where} \quad \frac{1}{\sqrt{f}} = 1.7372\ln\frac{Re}{1.964\ln Re - 3.8215}$$

$$Nu = 3.01Re^{0.0833} \tag{12.15}$$

$$Nu = 0.625Pe^{0.4} \tag{12.16}$$

$$Nu = 7.0 + 0.025Pe^{0.8} \tag{12.17}$$

$$Nu = 6.3 + 0.0167Re^{0.85}Pr^{0.93} \tag{12.18}$$

$$Nu = 6.3 + 0.016Re^{0.91}Pr^{1.21} \tag{12.19}$$

$$Nu = 4.82 + 0.0185Pe^{0.827} \tag{12.20}$$

The results of the assessments of these correlations, as well as the comparison of their application ranges are shown in Table 12.3. A good consistency can be observed for the models whose application range covers the fuel salt of the DFR. The value of the Nu number ranges from 49.89(Sleicher(Eqn. 12.19)) to 56.75(Chen(Eqn. 12.13)), while the heat transfer coefficient ranges from 1.11×10^5 $W/(m^2{\cdot}K)$ to 1.26×10^5 $W/(m^2{\cdot}K)$. In this work the model from Lyon [Lyo51] was adopted for the rest of calculations.

The interest in molten salt reactors using liquid metals as coolant has induced a number of experimental and theoretical investigations to determine the expression of the most appropriate Nu numbers. The results are always compared to each other, from case to cas,e in order to evaluate the applicability of the empirical formulas or fitting expressions. The fundamentals of the experimental and theoretical work were carried out in the middle and late 20^{th} century. As summary, Lubarsky and Kaufman [LK55], Kutalteladze et al. [KBNF58] and the literature from OECD/NEA [nea15] gave detailed introductions to most of the experimental work, while Kirillov and Ushakov [KU01] presented a comprehensive review of the studies on liquid metal coolants in the former USSR back to 1940s. The report from IAEA [iae13] covers not only liquid lead or lead-bismuth but also other liquid metal and molten salt coolants. In this work, the assessments of the Nu number is based on the correlations summarized in the NEA handbook specialized for liquid lead. The heat transfer correlations for liquid metal flowing along triangular rod bundles with constant heat flux are selected as follows:

$$
\begin{aligned}
Nu &= 24.15\log\left[-8.12+12.76\left(\frac{P}{D}\right)-3.65\left(\frac{P}{D}\right)^2\right] \\
&\quad + 0.0174\left\{1-exp\left[-6\left(\frac{P}{D}-1\right)\right]\right\}(Pe_c-200)^{0.9} && (12.21) \\
Nu &= 0.93+10.81\left(\frac{P}{D}\right)-2.01\left(\frac{P}{D}\right)^2+0.0252\left(\frac{P}{D}\right)^{0.273}(\phi_c Pe_c)^{0.8} && (12.22) \\
Nu &= 7+3.8\left(\frac{P}{D}\right)^{1.52}+0.027\left(\frac{P}{D}\right)^{0.27}(\phi_c Pe_c)^{0.8} && (12.23) \\
Nu &= 0.25+6.2\left(\frac{P}{D}\right)+\left[0.32\left(\frac{P}{D}\right)-0.007\right]Pe_c^{0.8-0.024\left(\frac{P}{D}\right)} && (12.24) \\
Nu &= 4.0+0.16\left(\frac{P}{D}\right)^5+0.33\left(\frac{P}{D}\right)^{0.38}\left(\frac{Pe_c}{100}\right)^{0.86} && (12.25) \\
Nu &= 6.66+3.126\left(\frac{P}{D}\right)+1.184\left(\frac{P}{D}\right)^2+0.0155(\phi_c Pe_c)^{0.86} && (12.26) \\
Nu &= 0.047\left\{1-exp\left[-3.8\left(\frac{P}{D}-1\right)\right]\right\}(Pe_c^{0.77}+250) && (12.27) \\
Nu &= 0.58\left[\frac{2\sqrt{3}}{\pi}\left(\frac{P}{D}\right)^2-1\right]^{0.55}Pe^{0.45} && (12.28) \\
Nu &= 7.55\left(\frac{P}{D}\right)-20\left(\frac{P}{D}\right)^{-13}+\frac{3.67}{90}\left(\frac{P}{D}\right)^{-2}Pe_c^{0.19\left(\frac{P}{D}\right)+0.56} && (12.29) \\
Nu &= 4.0+0.33\left(\frac{P}{D}\right)^{3.8}\left(\frac{Pe_c}{100}\right)^{0.86}+0.16\left(\frac{P}{D}\right)^{5.0} && (12.30) \\
\text{where}\quad \phi_c &= 1-\frac{1.82}{Pr\left\{exp\left[0.864\ln Re-0.24\left(\frac{P}{D}\right)-2.12\right]\right\}^{1.4}}
\end{aligned}
$$

(P/D) is the pitch-to-diameter ratio of the fuel rod bundle which is a fixed value and can be calculated with the data in Table 3.1.

The results of the assessment of the Nu number correlations is reported in Table 12.6. The calculated Nu and h are on the right side of the table. The assessment involved most of the correlations specified for rod bundle geometry. There are some correlations, however, whose application range does not cover the DFR case. They are already marked with colors. Differences can be clearly observed for the liquid lead conditions in the DFR concept between the correlations from Kazimi(Eqn. 12.25), Mikityuk(Eqn. 12.27), Subbotin(Eqn. [SUK$^+$65]) and Westinghouse(Eqn. 12.30), whose application range covers the DFR case. These have an acceptable consistency compared to other correlations, though a relative difference of 21%(Kazimi) to the averaged value still exists. The derived heat transfer coefficient for the liquid lead ranges then from $2.10\times10^4\ W/(m^2\cdot K)$ to $2.99\times10^4\ W/(m^2\cdot K)$ for the given DFR expected temperatures. It was recommended in the NEA report [nea15, pp.701] that,

Name	Equation	P/D	*Pe*	*Nu*	*h*
Borishanskii [Bor69]	(12.21)	1.1-1.5	200-2000	29.90	6.67E4
Dwyer [nea15]([DT60])	(12.22)	1.375-10	10-10^5	23.34	5.21E4
Friedland [nea15]([Fea61])	(12.23)	1.375-10	10-10^5	25.23	5.63E4
Gräber [nea15]([GR72])	(12.24)	1.2-2.0	150-4000	148.37	3.31E5
Kazimi [KC76]	(12.25)	1.1-1.4	10-5000	9.41	2.10E4
Maresca [MD64]	(12.26)	1.3-3.0	70-10^4	23.68	5.29E4
Mikityuk [Mik09]	(12.27)	1.1-1.95	30-5000	13.38	2.99E4
Subbotin [Mik09]([SUK$^+$65])	(12.28)	1.1-1.5	80-4000	12.47	2.78E4
Ushakov [nea15]([UZM77])	(12.29)	1.3-2.0	1-4000	18.29	4.08E4
Westinghouse [KC76]	(12.30)	1.1-1.4	10-5000	12.41	2.84E4

Table 12.4: Assessment of *Nu* number correlations for liquid lead

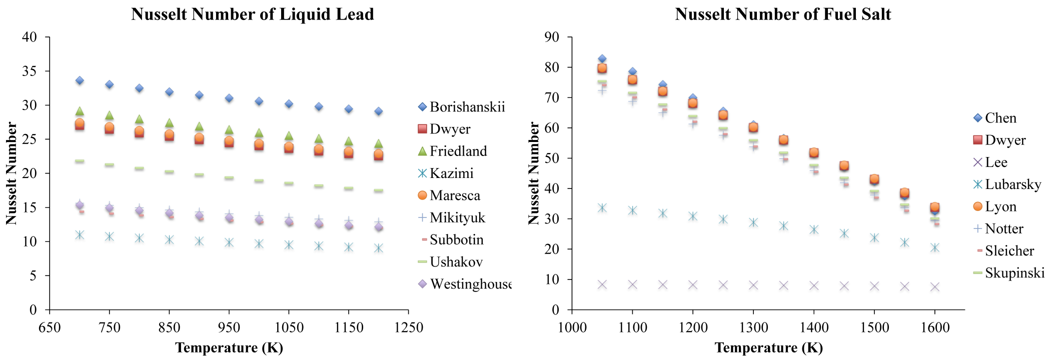

Figure 12.6: Temperature dependent *Nu* number of both liquids

after the comparison, the correlation from Mikityuk [Mik09] is suitable for the design purposes due to its wider range and the best statistical results. Therefore in this work all the *Nu* number used in the simulations are calculated with Eqn. 12.27.

The values in the tables above are calculated for a certain bulk temperature of the fluids. For the total temperature range, the change of the *Nu* number is plotted in Fig. 12.6. It can be seen that for the fuel salt, there are still some correlations yielding similar results to the Lyon correlation, namely Chen, Notter, Stleicher and Skupinski, among which the Nusselt Number calculated by Chen agrees the best with Lyon from $1300K$ to $1600K$. For liquid lead, the curve calculated by Westinghouse and Subbotin have a good consistency with the seelcted Mikityuk correlation.

Other parameters used in the heat transfer model are included in Table 12.5.

12.2.1.8 Wall Function

In the model describing turbulence, the wall function for the so called “near-wall” modeling approximates the physics of turbulence in the near wall region. The wall function has a significant impact on the numerical simulations, since the turbulent flows are affected by the “no-slip” wall condition. Because of continuity, the velocity

	Fuel salt	Coolant	Unit
T_{in}	1200.0	977.0	K
T_{out}	1400.0	1200.0	K
$\phi_{heat,\rightarrow wall}$	1.9359	1.4774	MW/m^2
h	9424.8	74 144.0	$W/(m^2K)$

Table 12.5: Extra model parameters related to flow properties

of the fluids at the wall has to be 0, while in the center of the duct the fluid velocity reaches its maximum. In the boundary layer development the velocity of the fluids is dragged by the wall and large gradients appear, affecting the flow turbulence characteristics. Thus, for a detailed thermal-hydraulic analysis the boundary layer has to be considered in detail and the impact of various models of wall functions on the fluid needs to be investigated.

Generally, a wall function is defined by means of dimensionless variables. In the case of turbulent flow in a circular duct, the velocity of the flow and the distance to the wall can be non-dimensionalized as follows [LS74]:

$$u^+ = \frac{u}{\sqrt{\tau_w/\rho}} \tag{12.31}$$

$$y^+ = y\frac{\sqrt{\tau_w/\rho}}{\nu} = y\frac{\sqrt{\tau_w\rho}}{\mu} \tag{12.32}$$

where u is the free stream velocity, y is the distance to the wall, and τ_w is the wall shear stress. For the different layers, the relationship between u^+ and y^+ can be shown to be

$$y^+ < 5,\ u^+ = y^+ \tag{12.33}$$

$$5 < y^+ < 30,\ u^+ = -3.05 + 5.0\text{ln}y^+ \tag{12.34}$$

$$y^+ > 30,\ u^+ = 5.5 + 2.5\text{ln}y^+ \tag{12.35}$$

Eqn. 12.33 to Eqn 12.35 describe the sublayers in the boundary layer near the wall: laminar sublayer, buffer sublayer and turbulent core.

In COMSOL the wall function is simplified to have the same logarithmic form as Eqn. 12.35 [COM15, pp.149] [FBA$^+$11, pp.6]:

$$u^+ = \frac{1}{\kappa}\text{ln}y^+ + B \tag{12.36}$$

where κ is the *Kármán* constant set to default value 0.41 and B is a constant set to 5.2 by default.

ANSYS provides two kinds of related wall functions which are *Standard Wall Func-*

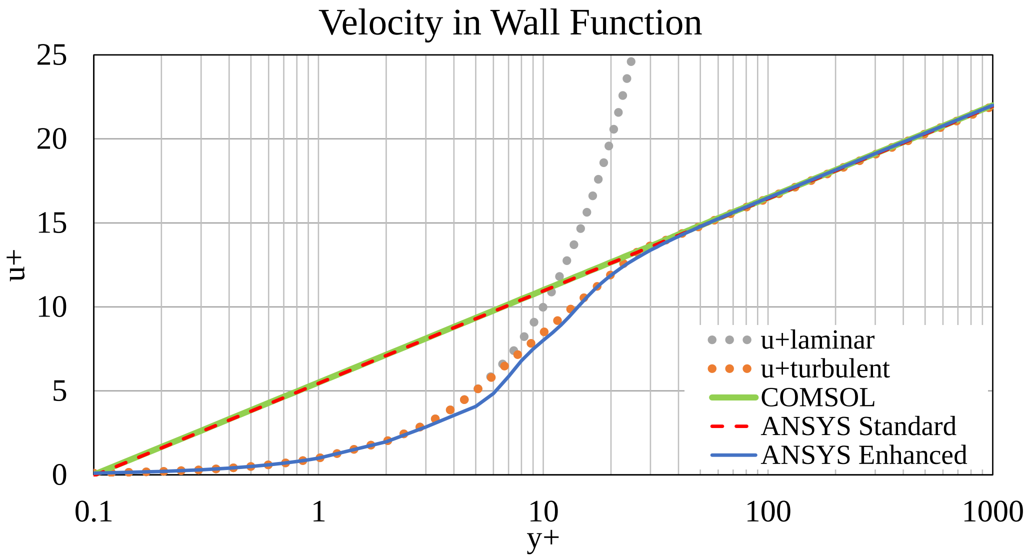

Figure 12.7: Comparison of wall functions

tion and *Enhanced Wall Function* with the following expressions

$$\begin{aligned} \text{Standard} \quad u^+ &= \frac{1}{0.4187}\ln(9.793y^+) \\ &= 5.4494 + \frac{1}{0.4187}\ln y^+ \qquad (12.37) \\ \text{Enhanced} \quad u^+ &= e^{\Gamma}u^+_{lam} + e^{1/\Gamma}u^+_{turb} \qquad (12.38) \\ \text{where} \quad \Gamma &= -\frac{0.01(y^+)^4}{1+5y^+} \end{aligned}$$

In Eqn. 12.38 u^+_{lam} is actually Eqn. 12.33 while u^+_{turb} is Eqn. 12.35. It means that the *Enhanced Wall Function* describes the boundary layer in one formulation with a blending function Γ. In Fig. 12.7 all the mentioned wall functions are plotted and compared. The relationships describing the laminar sublayer and the turbulent core have good consistency when $y^+ < 5$. In the buffer sublayer the curves begin to diverge and finally behave quite differently. The wall function used in COMSOL is identical to the *Standard Wall Function* in FLUENT, which matches u^+_{turb} when $y^+ > 30$. The *Enhanced Wall Function* then shows a good agreement with u^+_{lam} in the laminar sublayer and with u^+_{turb} in the turbulent core. In the turbulent core ($y^+ > 30$) all the wall functions are consistent.

In order to estimate the value of y^+, y and τ_w in Eqn. 12.32 should be evaluated. The wall shear stress τ_w can be calculated by

$$\tau_w = C_f \cdot \frac{1}{2}\rho U^2_{freestream}$$

while C_f known as Fanning's friction factor [DIBL05, pp.490], or skin friction coef-

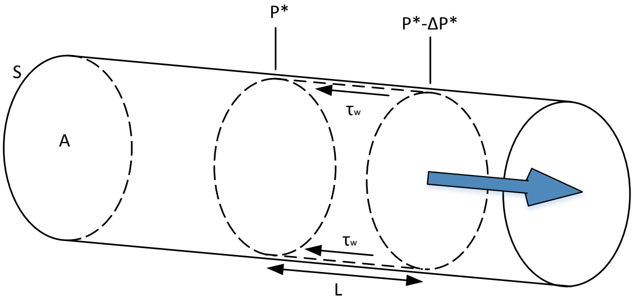

Figure 12.8: Force balance of a fluid control element in the duct with constant cross-sectional flow area

ficient, is defined for a fully developed flow through a closed duct as

$$C_f = \frac{\tau_w}{\frac{1}{2}\rho U^2_{freestream}}$$

It seems to be only the derived form of the previous formula. however, it is based on a force balance in a typical control volume of the fluid inside of a duct with constant flow cross sectional area (Fig. 12.8), and can be written as

$$\begin{aligned} C_f &= \frac{\frac{\Delta p^* A}{SL}}{(1/2)\rho U^2_{freestream}} = \frac{1}{4}\frac{D_h}{L}\frac{\Delta p^*}{(1/2)\rho U^2_{freestream}} \\ &= \frac{1}{4}f \end{aligned}$$

where f the Darcy's friction factor has been estimated in the previous Sec. 12.2.1.6. The value of y can be determined in the mesh by the appropriate size of the first mesh cell adjacent to the wall.

Since the *Enhanced Wall Function* performs better with the k-ϵ turbulence models and yields more physically reasonable results [ANS13, pp.114], the *realizable* k-ϵ turbulence model with the *Enhanced Wall Function* was finally selected as the reference model for all the calculations.

12.2.2 Three-Dimensional Model

This section presents the three dimensional fluid dynamic analysis of the flow in the DFR system. In addition to the two-dimensional axis-symmetric model a three-dimensional equivalent cylindrical model was investigated. In order to compare the equivalent model and the original hexagonal geometry, the original hexagonal prismatic cell was also modeled and used for simulations. For the DFR concept the most interesting parts from a thermal-hydraulic point of view are the hexagonal fuel-coolant fluid channel and the tube layout in the inlet and outlet plena. Because of the complexity of the reactor, especially the large number of fuel tubes, the needed computational resources can be tremendous fro a full core simulation and can not be fulfilled in this work. In consequence, a simulation of the whole reactor is not possible and has to be for the future.

The simulation of the flow with the three-dimensional model was carried out with FLUENT in steady-state by using the *pressure-based* solver. In the FLUENT modeling options, the *Energy* equation was enabled in order to compute the temperature profile of the fluids and to perform the heat transfer calculation. The *realizable k-epsilon* equation was adopted for the analysis of turbulence, as discussed before. Because in the simulations the heat transfer between fluids and structure is important, the *Enhanced Wall Treatment*, and *Thermal Effect* of the wall were included, together with the *coupled system* for the heat transfer calculation between the solid and fluids.

The calculation with COMSOL was also set as a three-dimensional *stationary* heat transfer problem conjugated with *Turbulence Flow, k-ϵ* and *Heat Transfer in Solids* physics.

12.2.2.1 Geometry

The structure of the fission zone as well as the fuel salt tube has already been discussed several times previously. In this section the analysis is carried out with two basic geometries. One of then is the equivalent cylinder model following the two-dimensional equivalent symmetric cylindrical model, which rotates around the symmetric central axis. The other one is the original hexagonal cell.

12.2.2.2 Mesh

For a sufficient precision of the calculation and with the consideration of calculation resources, some mesh parameters were selected to reduce the computational burden, instead of using the ANSYS-default mesh parameters. Since all the structures in the model are actually connected as a whole, in ANSYS *Assembly Meshing* instead of Part/Body Meshing was selected for nodalization. For the assembly meshing the *CutCell* algorithms, with a wide use, were selected. The detailed mesh information is listed in the discussion of each simulation results.

12.2.2.3 Power Profile

The heat generation in the three-dimensional calculations was simplified to follow the fluid with an appropriate power profile instead of the calculating the fission power. The power profile has the same form as taht use for the two-dimensional model in Sec. 11.2.2.2 by replacing the two-dimensional coordinate y by z:

$$P(z) = \frac{P_{total}}{11.14}\left[2.22\cos\left(\frac{\pi z}{H+\delta}\right) + 3.16\right] \tag{12.39}$$

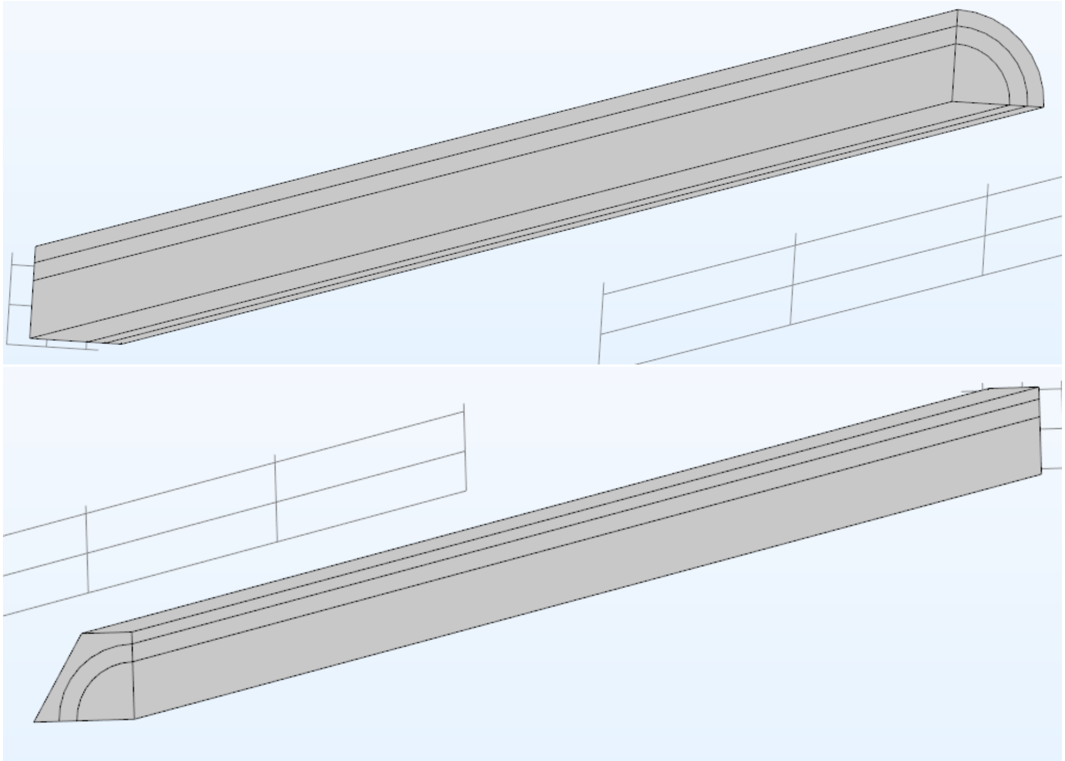

Figure 12.9: Layout of the three-dimensional model

12.2.2.4 Velocity Profile

Based on the velocity profile in Sec. 12.2.1.5 for the two-dimensional model, the proper velocity profile for the three-dimensional model could also be developed. For the equivalent cylindrical geometry the velocity profile is presented by replacing x with

$$r = \sqrt{x^2 + y^2}$$

in the two-dimensional velocity profile in Eqn. 12.4 and Eqn. 12.5:

$$v_f(r) = 1.5 v_{avg,f} \left(\frac{0.00725 - r}{0.00725} \right)^{1/7}, \quad 0 \leq r \leq 0.00725 \tag{12.40}$$

$$v_c(r) = 1.5 v_{avg,c} \left(\frac{r - 0.0095}{0.01155 - 0.0095} \right)^{1/7}, \quad 0.0095 \leq r \leq 0.01155 \tag{12.41}$$

12.2.2.5 Boundary Conditions

Based on the model described in the last section, the boundary conditions describing both fluids at the entrance of the DFR were set to velocity terms and the ones at

	Cylinder	Hex Prism	Unit
$D_{hydraulic,fuel}$	14.5	6.4	mm
$D_{hydraulic,coolant}$	4.0	40.0	mm
$T_{in,coolant}$	977.0		K
$T_{out,coolant}$	1200.0		K
$T_{in,fuel}$	1200.0		K
$T_{out,fuel}$	1400.0		K
$\phi_{heat,fuel \rightarrow wall}$	1.9359		MW/m^2
$\phi_{heat,wall \rightarrow coolant}$	1.4774		MW/m^2

Table 12.6: Extra model parameters related to flow properties

the exit to pressure terms for initialization. Because the pump was not considered in the system, a relative pressure drop instead of the precise pressure value was input.

Since all the models have two symmetry planes, the $x - z$ plane and $y - z$ plane, the faces on the symmetry planes are defined as *symmetry boundaries.* All the boundary conditions at the *solid structure* were set to *heat transfer* or *coupled system.* At the core *inlet* the boundary condition contained definitions on fluid velocity and initial temperature distributions, while at the *outlet* the pressure remained as default with a value of 0, and the temperature was set to an initialized outlet temperature. The flow and boundaries conditions are listed in Table 12.6.

12.3 Results

12.3.1 Steady State

The steady-state results of the single fuel cell demonstrate the thermal-hydraulic characteristics for the given boundary conditions. In this case, the flow in the axial direction and the temperature profiles of the fuel salt and the liquid lead at the exit of the cell are investigated. The relative pressure drop over the entire fuel cell is also examined and compared with the theoretical calculation carried out in Sec. 12.2.1.6. The design velocity is also validated by considering a parabolic velocity profile. Attention is also paid to the density change of the fluids as a reult of the temperature distribution.

From the analysis of the results some interesting points can be made. First, the geometry used for the steady-state simulation was the equivalent two-dimensional axis-symmetric model and the three-dimensional cylindrical model. Second, the mesh type of the geometry was prismatic for both codes in the two-dimensional case and for FLUENT in the three-dimensional case, while it was tetrahedral for COMSOL in the three-dimensional case. The model was meshed with the maximum number of mesh elements that the computation power could handle. Third, the simulations with FLUENT used the *realizable k-ϵ* model with *enhanced wall function* while the ones from COMSOL used the default k-ϵ model with default wall function, as already explained in Sec. 12.2.1.4 and 12.2.1.8. The rest of the relevant settings

Dimension	2D		3D	
Calculation tool	COMSOL	FLUENT	COMSOL	FLUENT
Series Nr.	(S1)	(S2)	(S3)	(S4)
Geometry	equivalen axissymmetric		equivalent cylinder	
Turbulence model	default k-ϵ	*realizable* k-ϵ	default k-ϵ	*realizable* k-ϵ
Wall function	default	*enhanced*	default	*enhanced*
Mesh type	quadrangle		tetrahedral	quadrangle
Mesh elements	317 555	240 037	3 406 285	3 558 205
Mesh ave. quality	0.78	0.58	0.26	0.65
Velocity Profile	parabolic		parabolic	

Table 12.7: Cases in the steady state analysis

and parameters used for the analyses are listed in Table 12.7. The results are plotted in Fig. 12.10 and 12.11 for the axial and radial directions respectively. The plots show the values of the selected variables on the left vertical axis and the relative differences referred to Case S2 on the right vertical axis. The horizontal axis shows the axial coordinate from entrance to the exit of the single cell in Fig. 12.10 and shows radial coordinate form the center of the single cell to the outer boundary in Fig. 12.11. The values of the variables are plotted with solid lines while the relative differences are plotted with hollow circles. In Fig. 12.12 rainbow diagrams of the results generated by COMSOL are shown. The rainbow diagrams represent both two- and three-dimensional models by rotating the two-dimensional model around its symmetry axis. In order to display details on the page with limited size, the y(2D)- or z(3D)-direction is scaled to the 0.01 times the origin.

In Fig. 12.10, for the temperature of both fluids, $T_{out,f}$ reaches 1400K/1409K/1410K/1418K (S1/S2/S3/S4), which have relative differences d_r smaller than ±0.8%, while $T_{out,c}$ reaches 1201K/1214K/1198K/1210K (S1/S2/S3/S4) with d_r ranging from -1.30% to 0.12%. The consistency of the values from the different cases is satisfactory. The quasi-linear curve describing the coolant temperature reveals that the heat transfer between the fuel tube wall and the coolant is saturated from the entrance of the fuel tube under the given power profile condition, which is not a linear curve. The curve of the fuel temperature tells the same story, that from the entrance of the fuel cell to the position of $0.7m$ the heat transfer behaves linearly, while, after $0.7m$ T_f, it has a steeper rise ($150K/m$) compared to the temperature rise in the first $0.7m$ ($71K/m$) for the fuel salt and ($95K/m$) for the lead coolant. The heat transfer between the tube wall and the coolant in this case works well, so that the temperature profiles of both materials are parallel. Near the outlet (from $1.7m$ to $2.4m$) the temperature rise slows down in the fuel salt, which corresponds well with the power profile introduced in Sec. 11.2.2.2.

The pressure drop of the fluids also shows acceptable consistency. It can be observed that the pressure drop in the coolant is much larger than the fuel salt $5.189/5.160/4.933/5.581\times10^5$ Pa (S1/
The relative difference d_r for the fuel salt in most of the region falls within -0.7%∼3% and for the coolant the range is larger with -4%∼7%. Comparing the results with the theoretical analysis reported in Table 12.2, it can be found that among all the

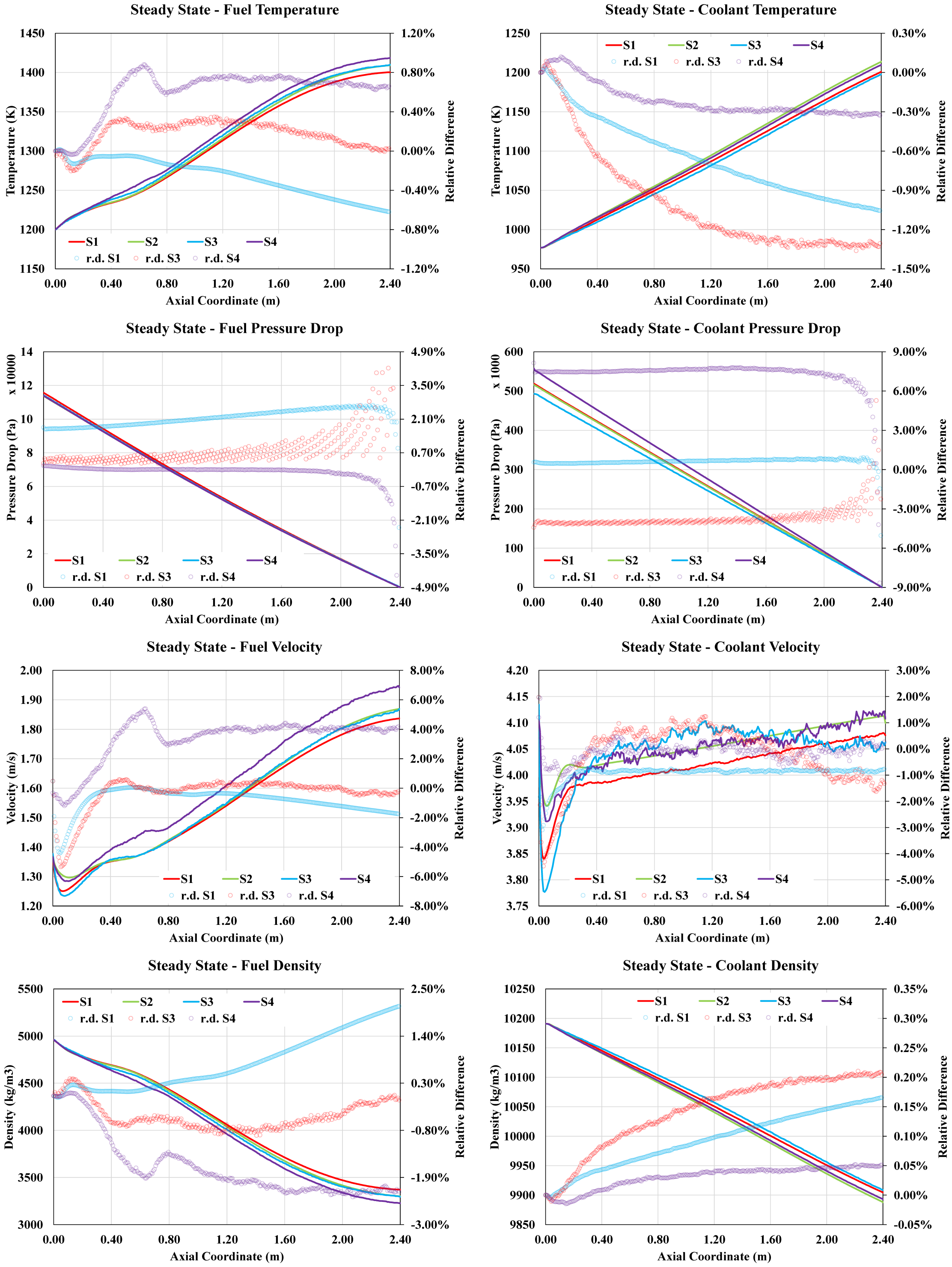

Figure 12.10: Steady state model performance (axial)

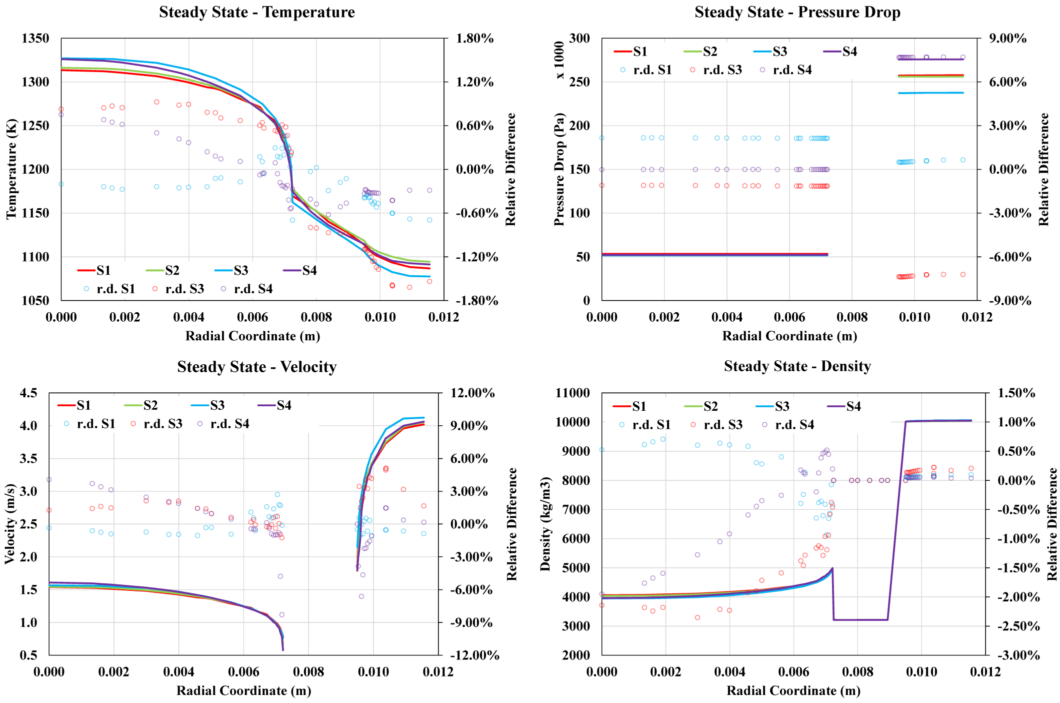

Figure 12.11: Steady state model performance (radial)

listed $f-Re$ relationships, for the fuel salt the one from McAdams has the best consistency with the results ($d_{r,\text{results}}$ <6.00%), while for the coolant, the results match better the pressure drop calculated with the $f-Re$ relationship from Wantland ($d_{r,\text{results}}$ <14.00%). Based on this observation the $f-Re$ relationships considered underestimate the pressure drop in the fuel salt, but for the coolant, especially for relationships (only the ones from Tourneau and Wantland) specified for fluid in a bundle, they overestimate the pressure drop in the liquid lead.

The velocity profiles of both fluids have a close relation to the change of the temperatures. The velocity profiles used at the entrance are parabolic, which is considered as fully developed velocity profiles. However, the axial velocity of the fluids experiences noticeable oscillations at the entrance. Afterward, the velocity increases since the temperature of the fluids also increases, and the density, therefore, decreases. Moreover, at about $0.7m$ a change in behavior can be found in all the velocity curves, which is caused by the accelerated temperature rise. At the exit of the single cell, the velocity of the fuel salt has reached $1.837/1.869/1.869/1.942m/s$ (S1/S2/S3/S4), while that of the fluid has reached $4.076/4.099/4.062/4.108m/s$ (S1/S2/S3/S4). The relative difference of the velocities for the fuel salt lay between -2.00% and 4.00%, while for the coolant, the relative difference is much smaller, less than ±1.00%.

The density of the fluids is directly related to the temperature of the fluids, which can also be seen in the figure. Because of the rise of the temperature, $\rho_{out,f}$ falls from $4961kg/m^3$ to $3370/3300/3295/3226kg/m^3$ (S1/S2/S3/S4) while $\rho_{out,c}$ decreases from $10191kg/m^3$ to $9904/9888/9909/9893kg/m^3$ (S1/S2/S3/S4) with a d_r within ±2.00% for the fuel salt and 0.05%∼0.20% for the coolant. The expression of the density

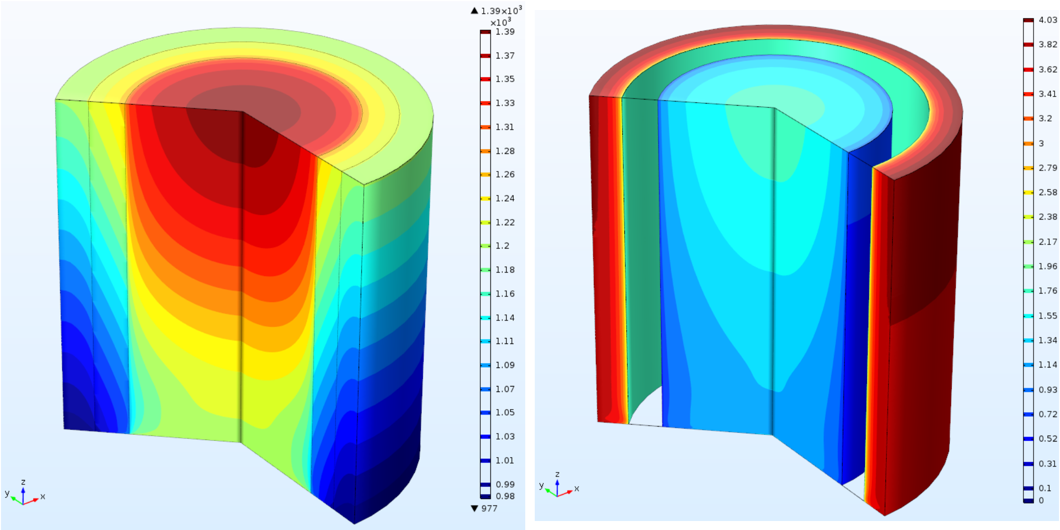
▲ 1.39×10³
×10³
1.39
1.37
1.35
1.33
1.31
1.28
1.26
1.24
1.22
1.2
1.18
1.16
1.14
1.11
1.09
1.07
1.05
1.03
1.01
0.99
0.98
▼ 977
4.03
3.82
3.62
3.41
3.2
3
2.79
2.58
2.38
2.17
1.96
1.76
1.55
1.34
1.14
0.93
0.72
0.52
0.31
0.1
0
z
y
x

(a Temperatue (K) (b Velocity (m/s)

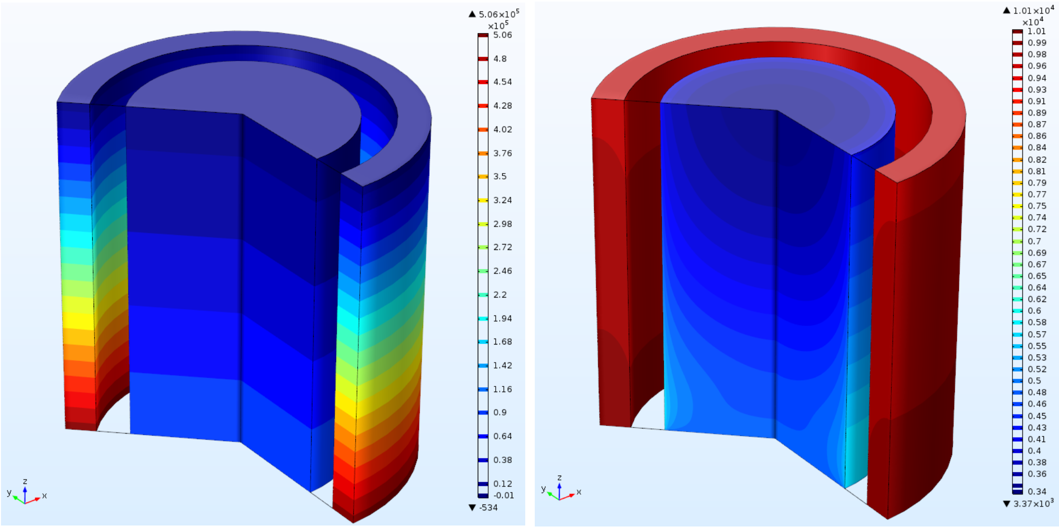
▲ 5.06×10⁵
×10⁵
5.06
4.8
4.54
4.28
4.02
3.76
3.5
3.24
2.98
2.72
2.46
2.2
1.94
1.68
1.42
1.16
0.9
0.64
0.38
0.12
-0.01
▼ -534
▲ 1.01×10⁴
×10⁴
1.01
0.99
0.98
0.96
0.94
0.93
0.91
0.89
0.87
0.86
0.84
0.82
0.81
0.79
0.77
0.75
0.74
0.72
0.7
0.69
0.67
0.65
0.64
0.62
0.6
0.58
0.57
0.55
0.53
0.52
0.5
0.48
0.46
0.45
0.43
0.41
0.4
0.38
0.36
0.34
▼ 3.37×10³
z
y
x

(c Pressure drop (Pa) (d Density (kg/m^3)

Figure 12.12: Steady state model performance (rainbow)

listed in Table 3.4 ensures that the difference in the temperature and that in the density has the same order of magnitude.

Generally speaking the results from different cases have the satisfactory consistency. However, for the pressure drop the relative difference is much larger than others, but this is fully to be expected. In the previous modeling and theory review in Sec. 12.2.1.4 it has been found that between the turbulent models, the model used by FLUENT has a bouyancy term more than that used by COMSOL. Yet does this bouyancy term have nothing to do with this discrepancy on the pressure drop, since S1 and S3 as well as S2 and S4 use the same model but actually they differ the most in the case of the pressure drop. The "consistency" between S1 and S2 can also be seen as "coincident" since in most all the properties the change of values of three -dimensional models (S3/S4) are higher than that of two-dimensional models (S1/S2) except for the pressure drop in the fuel salt, and the results from FLUENT (S2/S4) are higher than that from COMSOL (S1/S3) except for the pressure drop in the coolant.

In Fig. 12.11 the radial aspect of the results is compared. The data presents the values in the middle of the single cell. From the figure of the temperature and the velocity, the radial distribution of the fluid can be observed. At the near wall region, the drop of the value shapes the large gradient under the rule of the wall function.

12.3.2 Sensitivity

Though the steady state of the fuel channel is simulated, in order to characterize the system with the simulation results, some variables are selected to carry out sensitivity analysis. Based on the previous theoretical analysis, the wall function, the mesh settings as well as the turbulent model are chosen from various possibilities. When the fuel salt itself of the DFR is recalled, its properties are based on assumptions and approximations. Therefore it is necessary in this work to evaluate the impact on the performance of the thermal-hydraulic design, which relies on these variables. Analog to the steady state analysis, the following variables temperature, pressure, velocity and density are chosen to describe the system.

As investigated in the steady state analysis, the models with two- and three-dimensions have shown satisfactory consistency, which means that with the two-dimensional model the simulation can produce the desired results with less computational power and time. Therefore, in the sensitivity analysis below, except for the case that compares the results between the two geometric approaches, all comparisons have made used of two-dimensional models.

12.3.2.1 Velocity Profile

The purpose of the comparison of the velocity profile used in the models is to evaluate the necessity of establishing a parabolic velocity profile at the entrance of the single fuel cell and the differences in the results with a uniform velocity profile. This later profile sets the radial velocity inside the flow channel to the mean velocity of

Dimension	2D			
Calculation tool	COMSOL		FLUENT	
Series Nr.	(V1)	(V2)	(V3)	(V4)
Geometry	equivalent axis-symmetric		equivalent axis-symmetric	
Turbulence model	default k-ϵ		*realizable* k-ϵ	
Wall function	default		*enhanced*	
Mesh type	quadrangle		quadrangle	
Mesh elements	317 555		240 037	
Mesh ave. quality	0.78		0.58	
Velocity Profile	uniform	parabolic	uniform	parabolic

Table 12.8: Cases in the sensitivity to the velocity profile analysis

the fluid, while the parabolic velocity sets the radial velocity distribuiton with a parabolic shape. This shape can be considered as the approximated form of the fully developed flow. The theoretical calculations carried out in Sec. 12.2.1.5 have shown that the possible differences resulting from these profiles at the exit of the single fuel cell can be small enough to be accepted, since the flows have reached their fully developed form at about one fifth of the length of the fuel cell. The comparison is carried out with the two-dimensional models with prismatic meshes. The remaining model options an parameters are listed in Table 12.8. It has to be pointed out that V2 and V4 taken as the reference in this Section correspond to Cases S1 and S2 in the steady-state analysis.

The comparison of the results from both axial and radial directions are displayed in Fig. 12.13 and 12.14. The meaning of the axes is the same as that in the steady-state analysis, while in the sensitivity analysis to the velocity profile the reference Case is V4, which corresponds to the reference steady-state Case S2. In this section, the actual value of the variables will not be given since they were already given in the steady-state analysis, and these new curves can be compared with the reference values in both analysis. The radial results show values of the variables at the exit (for pressure drop at the entrance) of the single fuel cell, not in the middle of the cell as in the steady-state case.

The axial plots in Fig. 12.13 show similarity to the steady-state ones in that the results from FLUENT (V3/V4) present generally larger values than those from COMSOL (V1/V2), which can be especially observed in the temperatures, velocities and densities (reversed).

In the plot of the fuel salt velocity, the bundle of the curves obtained by using a uniform velocity profile is quite noticeable. They are cause by flow development inside of the flow channel. After $0.60m$ from the entrance, the velocity curves (V1/V3) of the fuel salt using uniform velocity profile become parallel to the curves (V2/V4) with parabolic velocity profile, which means that the flows in V1/V3 are fully developed. However, the value of the velocity shows discrepancies compared to the reference results (V4). The relative difference d_r of the results with uniform velocity profile (V1/V3) reaches from 3% to 5%, while the d_r of the results from COMSOL but with parabolic velocity profile (V2) stay within 0%∼-2%. The coolant velocity

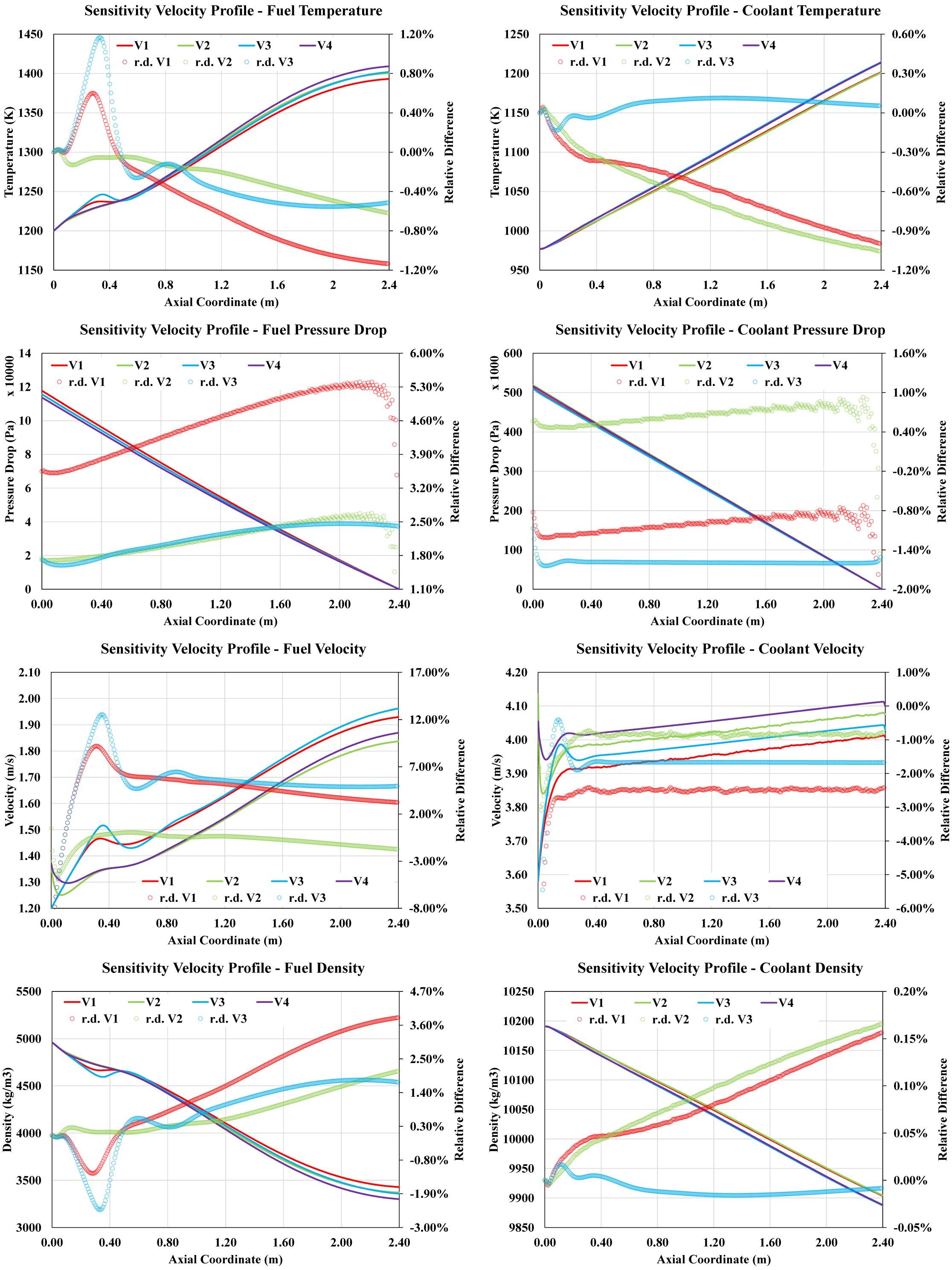

Figure 12.13: Sensitivity to velocity profile. Comparisons (axial)

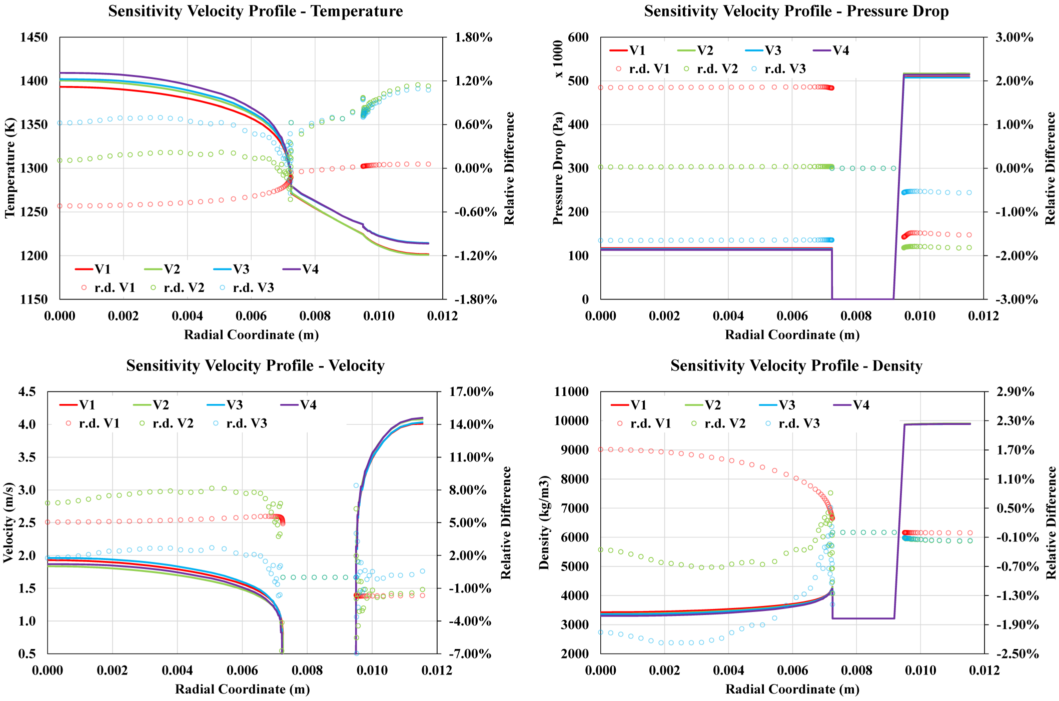

Figure 12.14: Sensitivity to velocity profile. Comparisons (radial)

has a similar behavior, though it is not so clear. The d_r of V1 and V3 are around -2.5% and -1.7% respectively, while the one of V2 is smaller than -1%.

In other diagrams this is not as significant as in the diagrams of the velocity. In the diagram of the fuel temperature the lump caused by the velocity development has also appeared, but the differences between the results do not particularly reflect the two velocity profiles. For temperature, pressure drop and density, the relative differences between the results at the exit (for pressure drop at entrance) are of the same level as that in the steady-state. For some properties, the relative difference is even smaller.

The same phenomena can also be found in radial plots in Fig. 12.14. The range of the d_r of the velocity becomes larger, while the ranges of all other d_r stay the same (temperature, density) or decrease to a smaller range (pressure drop).

Finally, it can be said that the parabolic velocity profile gives the flows a fully developed state, which can also be achieved with a uniform velocity profile, as long as the length of the flow duct is enough. But the parabolic velocity profile provides a more accurate value of the velocity. Other properties appear not to be strongly effected by the different velocity profiles. Considering the relative differences between the results, the replacement of a parabolic velocity profile by a uniform one is possible and acceptable for a preliminary analysis of the flow in the DFR fuel cells.

12.3.2.2 Wall Function and y^+

As mentioned in Sec. 12.2.1.8, a special wall function treatment is needed for the turbulent models that resolve the thermal-hydraulic interaction between the fluid flow and the tube wall. Not only does the mesh structure matter for the turbulence analysis, but also the size of the first mesh cell closest to the wall surface brings significant effects [CT06]. The turbulent model and the wall function are so tightly related that they should be considered together. Therefore, the assessment of effect of the value of y^+ also discusses the effect brought in by the turbulence models and the wall functions.

The first mesh's y^+ size is investigated inside of the range from 1 to 100, which corresponds to an actual distance to the wall of $0.00403{\cdot}(1 \sim 100)mm$ for the U-Pu fuel salt and $0.00136{\cdot}(1 \sim 100)mm$ for the liquid lead. However, y^+ is closely related to the wall treatment, so in this study the turbulence model, as well as, the wall function used are also taken into consideration. The whole plan for the study involving the turbulence models and wall functions is shown in Table. 12.9. The data set Ay010re is actually the same data set as Cases V4 or S2 in previous sections and served as reference for the y^+ analysis.

Model \ y^+	1	10	100
FLUENT standard k-ϵ, standard wall function	Ay001ss	Ay010ss	Ay100ss
FLUENT standard k-ϵ, enhanced wall function	Ay001se	Ay010se	Ay100se
FLUENT realizable k-ϵ, standard wall function	Ay001rs	Ay010rs	Ay100rs
FLUENT realizable k-ϵ, enhanced wall function	Ay001re	Ay010re	Ay100re
COMSOL k-ϵ, wall function	Cy001	Cy010	Cy100

Table 12.9: Simulation design for y^+ investigation

In the first evaluation the data sets on the fourth and fifth row of the table are selected to estimate the differences between the results of the cases using the *realizable k-ϵ* model and *enhanced wall function* (for FLUENT), which are plotted in Fig. 12.15. This evaluation focuses only on the cases with the most accurate models, thus reduce their influence, so that the effect of different values of y^+ is significant enough to be identified.

The results show that, far a give turbulence model used, among the FLUENT results, those with y^+=10 and $y^+ = 100$ are much closer to the results of y^+=1 for most of the investigated flow properties for both fuel sat and lead coolant. Among these properties the turbulent kinetic energy and the flow velocities appear to have strong dependence on the y^+ value, which is reasonable based on the definition of the y^+. The relative difference between y^+=10 and y^+=100 is small enough to be neglected while the relative difference with y^+=1 is quite noticeable, as for the turbulent kinetic energy d_r reaches -5.0% in the fuel salt and -32% in the coolant lead, while for the velocity the relative differences are around 1.0% for both fluids. The results calculated with COMSOL show the a similar patters, which confirms the validity of the calculation. However, the COMSOL results demonstrate fewer differences between the different y^+ cases, a can be observed directly in the diagram.

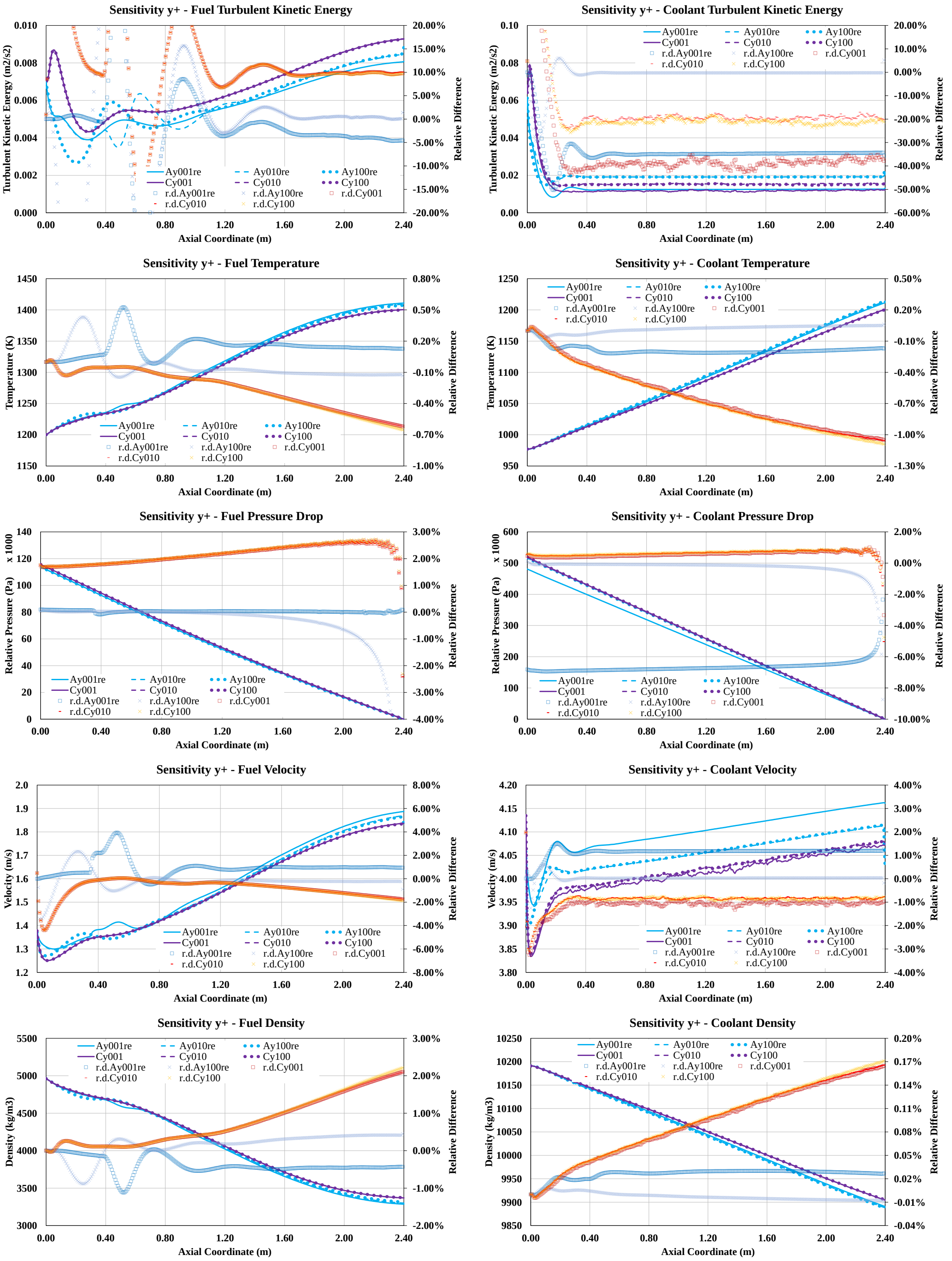

Figure 12.15: Selected y^+ results on axial distribution of flow properties

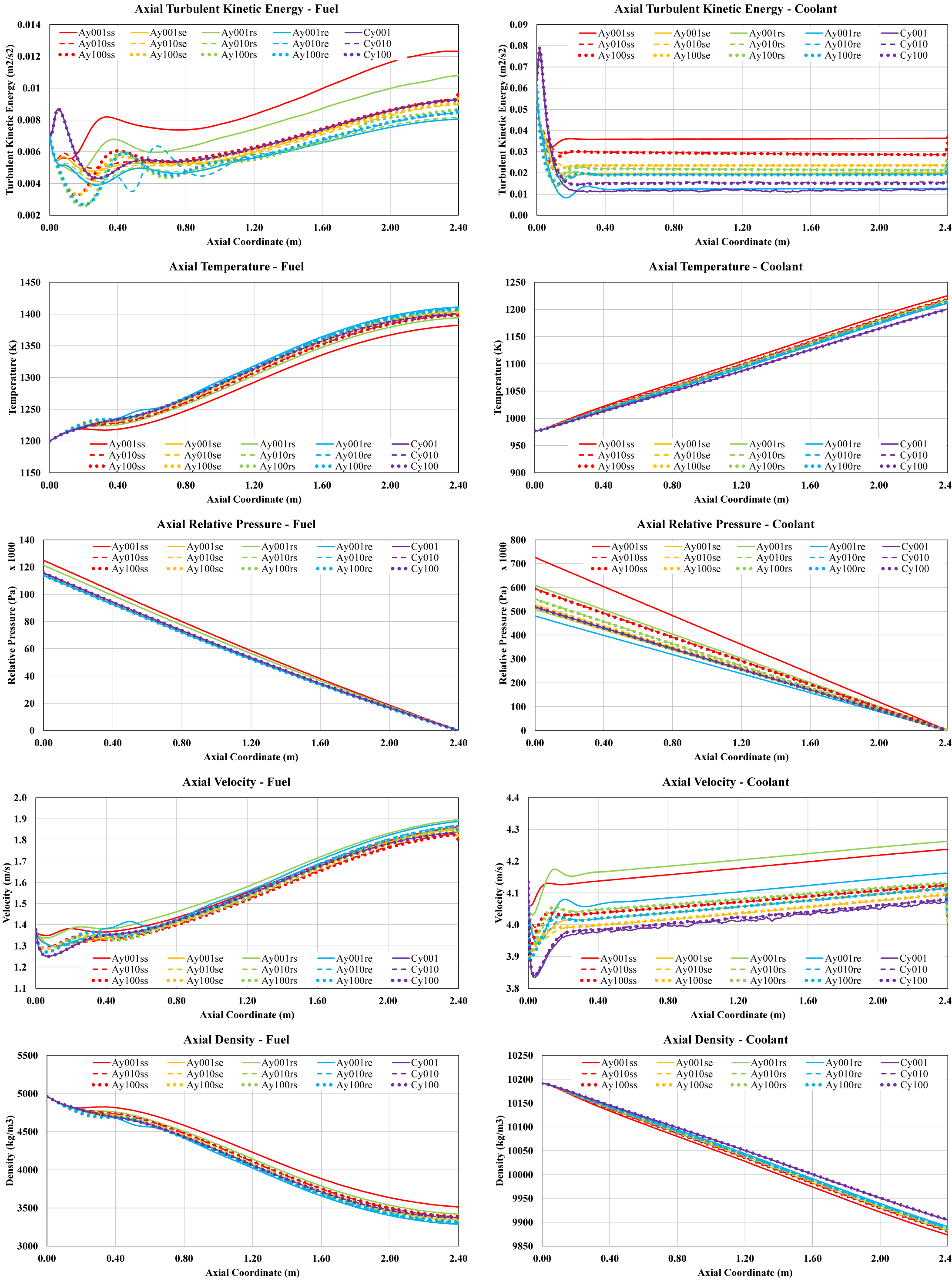

Figure 12.16: Completed y^+ results on axial properties

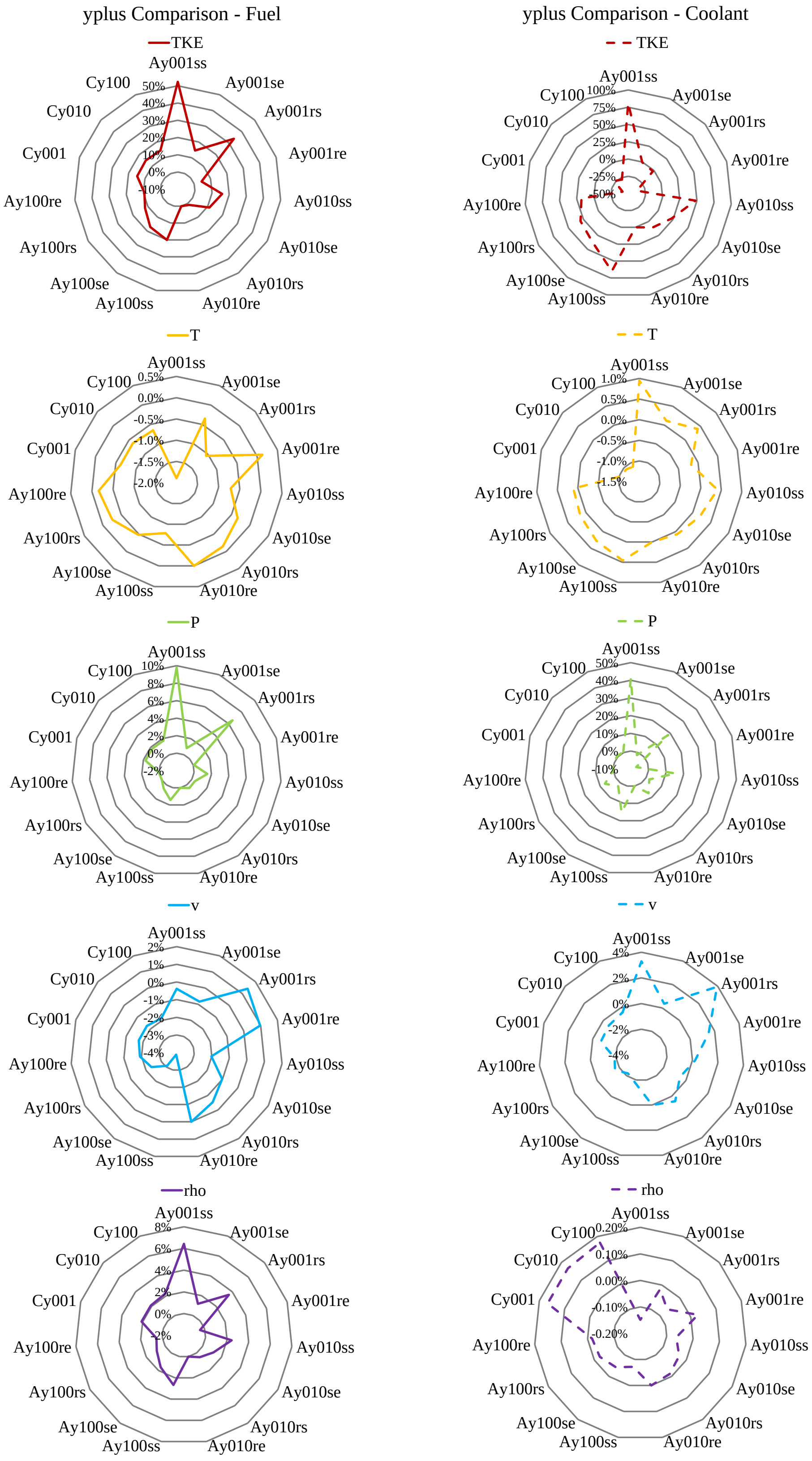

yplus Comparison - Fuel

yplus Comparison - Coolant

Figure 12.17: Relative differences of y^+ results in axial distribution of properties

The complete comparison for all the cases listed in the table for both fluids is shown in Fig. 12.16. Different combinations of turbulence model and wall function configurations have been marked with colors, while y^+ cases are distinguished by changing the line styles from solid line to dotted line. From the direct observation of the figure, without the detailed numerical comparison, it is revealed that first, from the point of view of the two codes tools FLUENT and COMSOL, based on the investigated cases and given settings, the results given by the two codes are closer in the fuel salt than in the lead coolant. The curves join together the fuel salt, while in the lead coolant, the curves calculated by COMSOL stay apart from those of FLUENT. Second, from the point of view of y^+, the phenomena observed in the last section proves to be applicable to all the turbulence and wall-function combinations and the results with y^+=1 deviate from the results with y^+=10 or y^+=100.

The relative differences in the results are plotted in the form of radar chart in Fig. 12.17. The charts on the left side indicate the relative differences in the fuel salt flow properties, while the charts on the right side are for the lead coolant flow. The charts on each row present one property.[2] From these charts, the phenomena observed in Fig. 12.16 can be clearly explained. The most significant characteristic in all the charts is the peak pointed to Ay001ss, which means that the value of Ay001ss deviates the most from the reference value of Ay010re. This can be easily understood as these two cases are too different regarding the turbulence model and the wall-function, and even the y^+ value. The second noticeable point is the saw-tooth formed curve on the right side of each chart, which covers the data points from Ay001ss to Ay010re. The periodic fluctuations tell that the cases with the same wall-function configurations have closer results than the cases with the same turbulence models, or, that is to say, the wall function has more impact on the flow system than the form of the turbulence models or the value of y^+. On the left side of each chart, the CyXXX series and Ay100xx series form two plateaus inside of which the values of a given property are relative close to each other. It means that for Ay100xx series the value of y^+ has overcome the difference introduced by the turbulence model and the wall function, while for the CyXXX series, it is just the opposite.

After the comparisons discussed above, it can be concluded that for the fuel salt flow the various turbulence models do not introduce significant differences in the results. Contrarily, the wall function, as well as, the value of y^+ yields discrepancies, which can be seen in Fig. 12.7. When y^+=1 the difference of the u^+ value obtained with the *Standard Wall Function* and the *Enhanced Wall Function* can be up to ca. 5, and when y^+=10 the difference is reduced to 2∼3. When y^+=100 the two functions overlap. However, for the lead coolant the wall function is decisive. The figures have shown clearly that for some flow properties the results can be distributed across a wide range. Surprisingly, when considering the results from different codes, the results from COMSOL are generally close to the results calculated with FLUENT *Realizable* k-ϵ turbulence model and *Enhanced Wall Function*, though the configuration in COMSOL itself is labeled as *Standard* k-ϵ turbulence model and *Standard Wall Function*. If the expression of the COMSOL models is recalled, the formulation of this model can be found just between the FLUENT *Standard* k-ϵ and *Realizable* k-ϵ turbulence model.

---

[2] TKE is short for “Turbulence Kinetic Energy”

Calculation tool	FLUENT		
Dimension	2D		
Series Nr.	(M1)	(M0)	(M2)
Geometry	equivalent axis-symmetric		
Turbulence model	*realizable* k-ϵ		
Wall function	*enhanced*		
Mesh type	prismatic		
Mesh elements	105 602	240 037	1 439 192
Mesh ave. quality	0.36	0.58	0.89
Velocity Profile	parabolic		

Table 12.10: Cases in the mesh sensitivity study

12.3.2.3 Mesh Sensitivity

The refinement of the mesh plays an important role in CFD simulations. In order to find out the effect of different meshes on the simulation of the DFR fuel cell, a study including three calculations with different mesh refinements was performed and its results are analyzed in this section. The information of the study is shown in Table. 12.10. The layout of the three mesh settings is displayed in Fig. 12.18, which is generated by FLUENT. The plots from left to the right are M0, M1 and M2, respectively. It needs to be noticed that M0 is the reference data set and equals Cases V4 and S2.

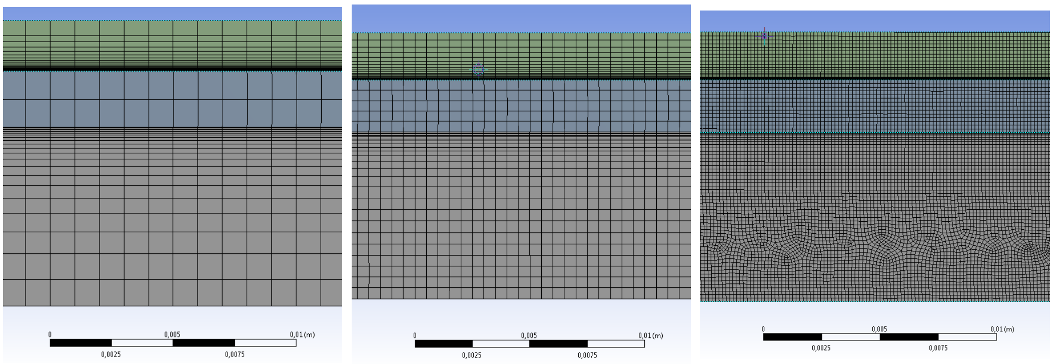

Figure 12.18: Layout of mesh size

The results of the simulations are displayed in Fig. 12.19 separately according to the flow properties. The blue curves are a result of the calculations, while the red curves with circles are the relative differences. Generally speaking, except for the turbulent kinetic energy, of which the relative difference exceeds ±1%, the comparison of other properties of both flows shows a good consistency, even when the mesh number of M2 is more than 10 times of that of M1. It means that in this case, which is a relative simple one, the size of the mesh does not have so much impact on the simulation results as other factors such as the value of y^+.

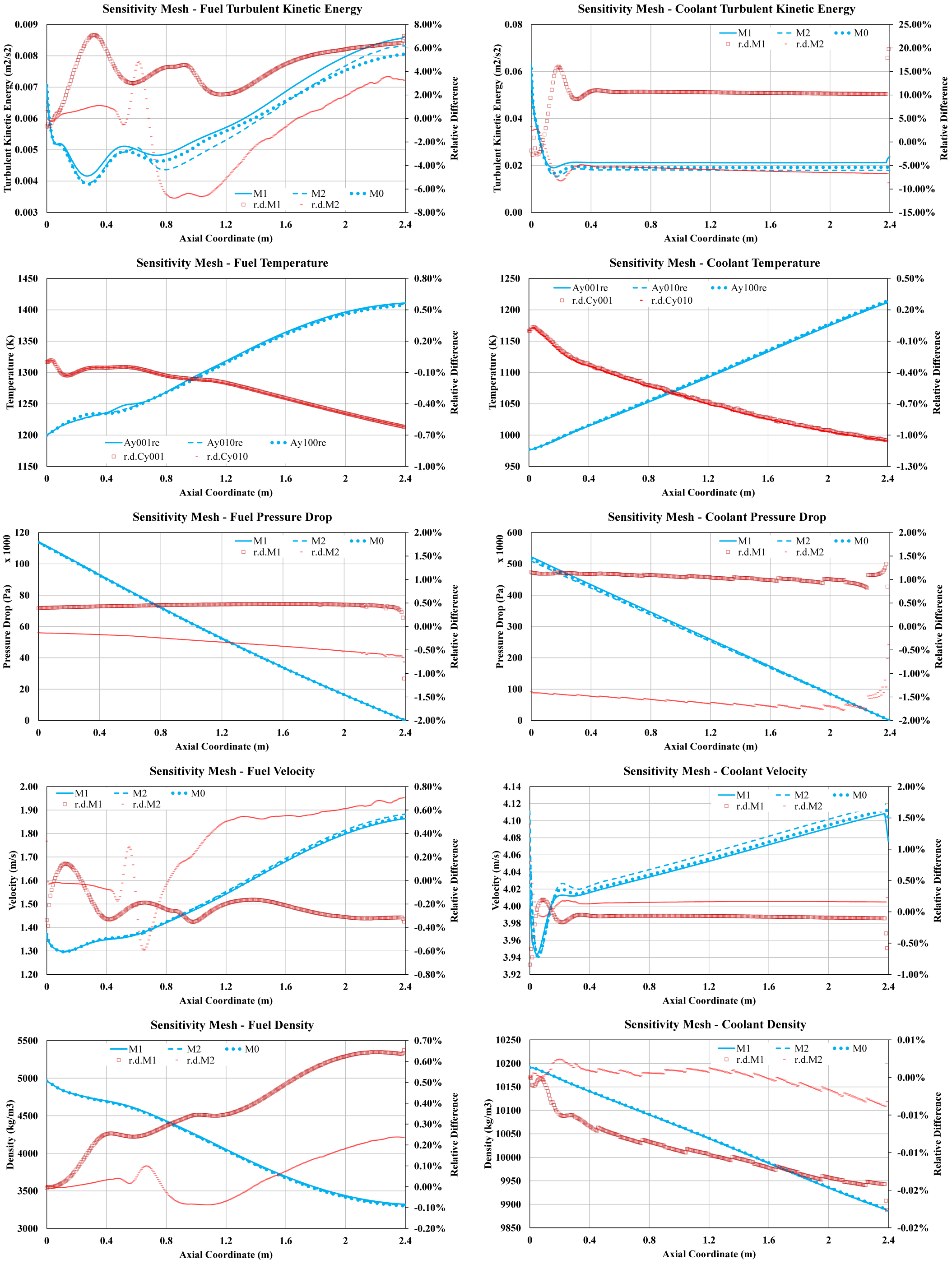

Figure 12.19: Mesh Sensitivity. Comparison (axial)

Dimension	2D				
Calculation tool	FLUENT				
Geometry	equivalen axissymmetric				
Turbulence model	*realizable* k-ϵ				
Wall function	*enhanced*				
Mesh type	quadrangle				
Mesh elements	240 037				
Mesh ave. quality	0.58				
Velocity Profile	parabolic				
Series Nr.	(FC1)	(FC2)	(FC0)	(FC3)	(FC4)
$C_p(J/(kg \cdot K))$	300	350	400	450	500
Series Nr.	(FT1)	(FT2)	(FT0)	(FT3)	(FT4)
$\kappa((W/(m \cdot K))$	0.5	1	2	5	10

Table 12.11: Cases in the sensitivity of the fuel salt properties

12.3.2.4 Sensitivity to Fuel Salt Properties

As mentioned in the introduction, because of the lack of reliable and acccurate experimental data for the properties of the fuel salt, the properties used for the calculations are based assumptions and approximated values. Therefore, it is necessary to perform a sensitivity study for the selected fuel salt properties. These are the heat capacity and the thermal conductivity of the fuel salt, which are set as constant during the calculation in this work. These two properties have a direct influence on the heat transfer between the fuel salt and the coolant, according to the theoretical analysis in the previous sections.

In this study the values of the selected properties are illustrated in Table. 12.11. The other basic settings and models are maintained the same. Among the five data sets, FC0 and FT0 are the reference data sets, which, in the previous sections, where labelled with names such as M0, etc.

The comparison for the heat capacity variation is plotted in Fig. 12.20. The solid curves in rainbow color show the results, which are presented on the left vertical axis, while the curves with circles of the same color represent the relative differences of each data set with respect to the reference data set FC0, shown on the right vertical axis. Since the density is closely related to the temperature, Fig. 12.21 omits the plot of the density for both fluid flows.

Since the changed variable is the heat capacity of the fuel salt, it is obvious that the influence on the fuel salt is much larger than that on the coolant, which confirms the conclusion made in the previous section that the heat transfer between the fuel salt and the coolant is saturated. The plot of the temperature shows clearly that, with a smaller heat capacity, the fuel salt operating temperature increases. On the whole, the results show a almost linear change for all the selected flow properties. Around the reference value, the relative differences of the results of the other four data sets are symmetric with respect to the 0% line. For the given range of the

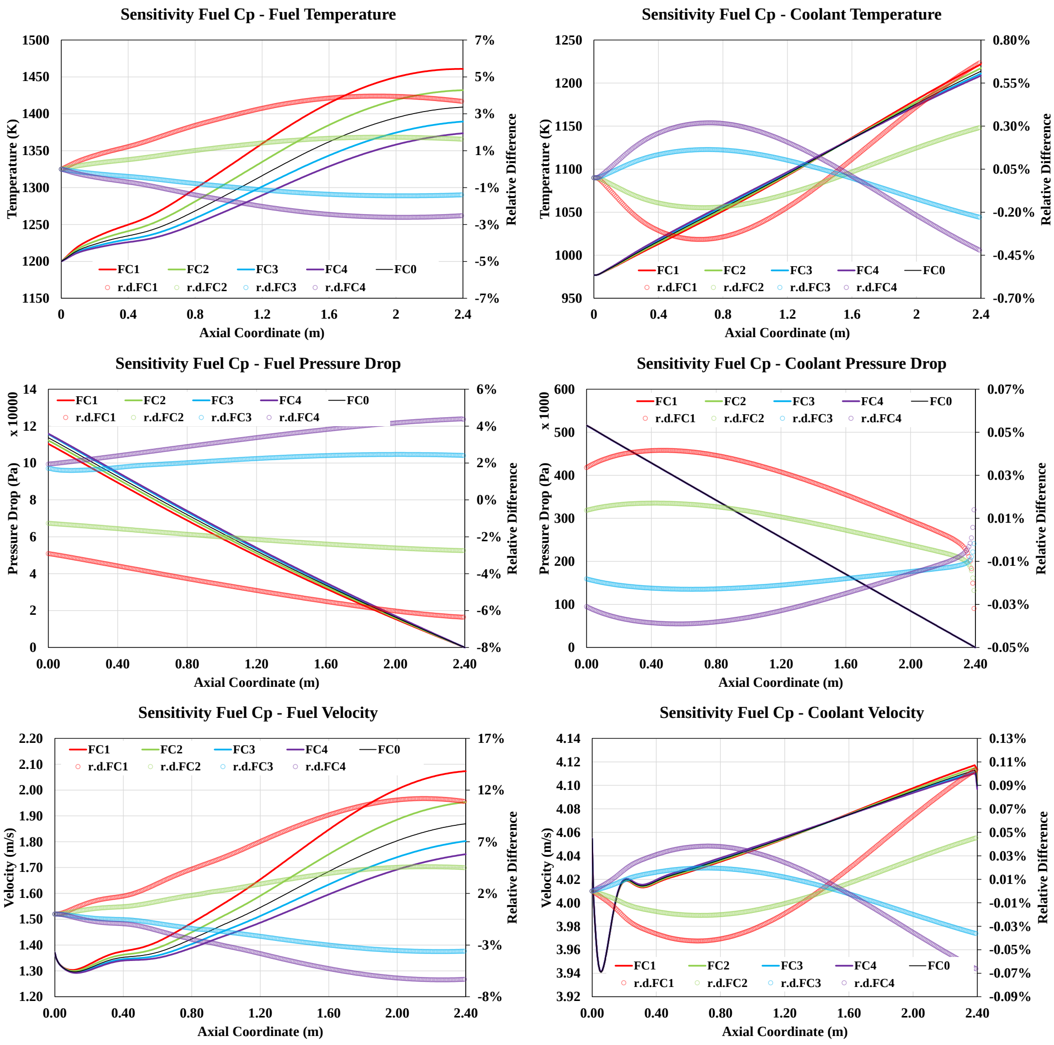

Figure 12.20: Sensitivity to the heat capacity of the fuel salt. Comparison (axial)

C_p, the amplitude of the change of the temperature stays within -2.7%∼3.7%, the pressure drop varies from -6.5% to 4.5%, while the velocity shows a maximum change from -6% to 10%. Changes in the coolant properties are generally smaller than ±1%.

The comparison of the sensitivity to thermal conductivity is plotted in Fig. 12.21. The type and the color of the curves have the same setting as the comparison of the heat capacity.

Because the thermal conductivity is an important parameter in the heat transfer coefficient, the change of the thermal conductivity has also an impact on the properties of the coolant flow. The reference value FT0 used in the comparison lays in the middle among the five data sets, the curves representing the results stay therefore on the both sides of the reference value. However, the relationship between the amplitude of the results and the thermal conductivity is not the same as the in the case of the heat capacity. The increase of the thermal conductivity of the fuel salt from the default value 2 to 10 in FT4 causes a temperature shift of -3% in the fuel

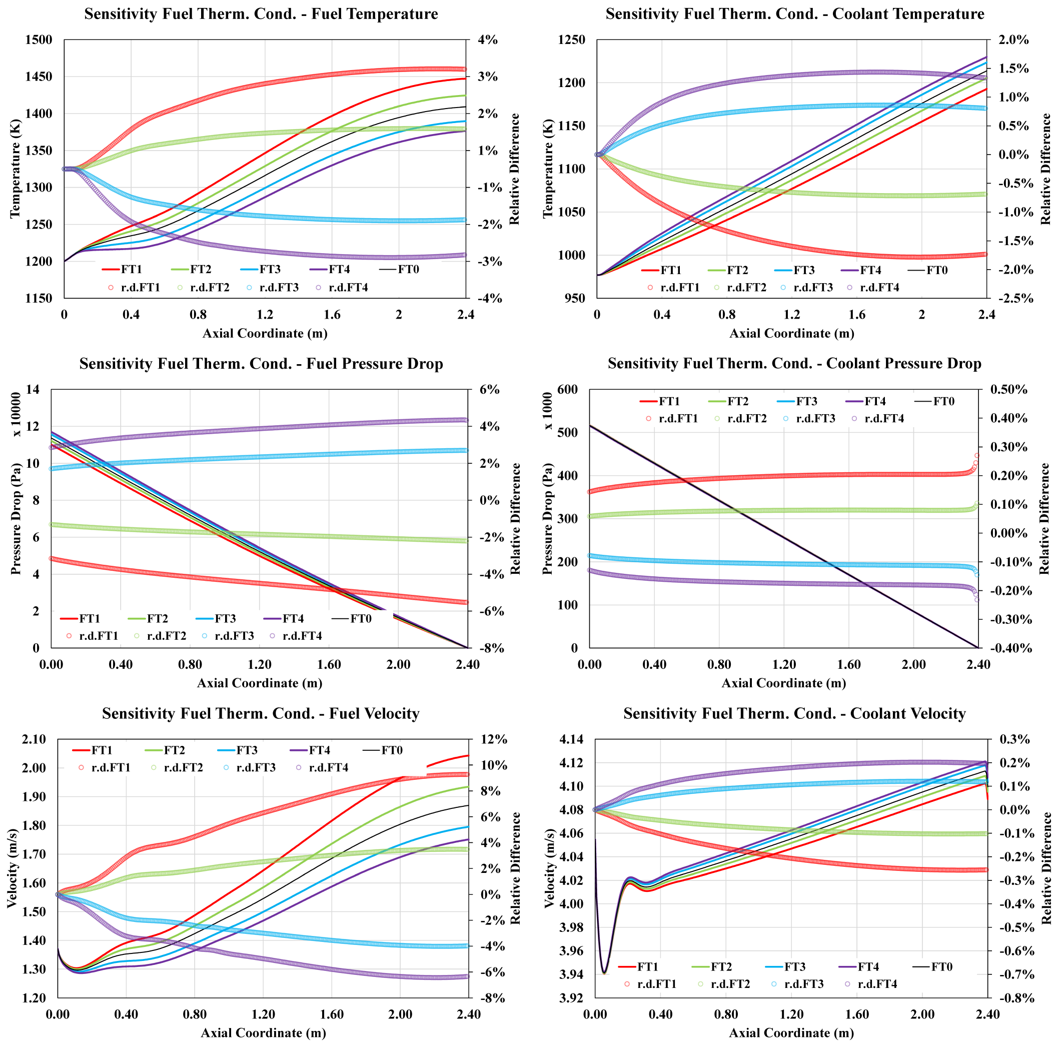

Figure 12.21: Sensitivity to the fuel salt thermal conductivity. Comparison (axial)

salt and -1.7% in the coolant, a pressure drop of ca. -6% in the fuel salt and -0.2% in the coolant, as well as, a velocity change of -6% in the fuel salt and -0.25% in the coolant, the absolute value of which is not so different from the consequence of a decrease of the fuel salt from 2 to 0.5 in FT1.

12.3.2.5 Sensitivity to Wall Properties

The study of the sensitivity to the wall properties is thought a supplement to the study of sensitivity to the fuel salt properties. In this way, all the parameters, which are set as constant in the simulations, have undergone a sensitivity analysis in order to ensure the validity of the results within a reasonable range. The heat capacity of the fuel tube wall has proven to have no influence on the results when it varies from $600J/(kg \cdot K)$ to $800J/(kg \cdot K)$. The relative differences are so small to be recognized. Therefore, only the results produced with various thermal conductivities of the fuel

Dimension	2D				
Calculation tool	FLUENT				
Geometry	equivalen axissymmetric				
Turbulence model	*realizable* k-ϵ				
Wall function	*enhanced*				
Mesh type	quadrangle				
Mesh elements	240 037				
Mesh ave. quality	0.58				
Velocity Profile	parabolic				
Series Nr.	(WT1)	(WT2)	(WT0)	(WT3)	(WT4)
$\kappa((W/(m \cdot K))$	45	50	52.9	55	60

Table 12.12: Cases in the sensitivity of the wall property

tube wall are presented here. The selected values are listed in Table. 12.12.

The comparison of the results of various values of thermal conductivity of the fuel tube wall is displayed in Fig. 12.22. No significant changes due to the different values of thermal conductivity can be found in all the plots. The maximum relative difference is observed for the fuel salt velocity, which is around ±1%.

12.4 Conclusion

This chapter has focused on the thermal-hydraulic analysis of the DFR system from the total system to a single fuel cell.

The analysis has verified the design flow condition and the expected operational situation. Because the neutronics and the thermal-hydraulic description is not yet coupled, a cosine axial power profile has been used as calculated in the Part of neutronic analysis. By using this power profile, the most important assumption is that the temperature feed-back has not been considered in the simulation.

The steady-state calculation has provided a means or the assessment of the influence in the results of different CFD codes, turbulence models, mesh types, as well as, mesh sizes and model dimensionality. The results are consistent, at least for a the preliminary phase of the research. The question still remains of how consistent the results in this chapter are, especially without temperature feed-back, with the results in the last Chapter, in which a simplified neutronics was coupled to a thermal-hydraulic model in one-dimensional geometry. The answer to this question is shown in Fig. 12.23

The results in two- and three-dimensions have been calculated for steady-state (Sec. 12.3.1)for cases S2 and S4, respectively. The relative differences between the results are smaller than 1.5%, no matter which one is taken as the reference value, because here the results can only be verified by comparison between themselves. The consistency reveals that, although in two- and three-dimensional models the temperature feedback has not been taken into account, the consistency of the steady-state results can be

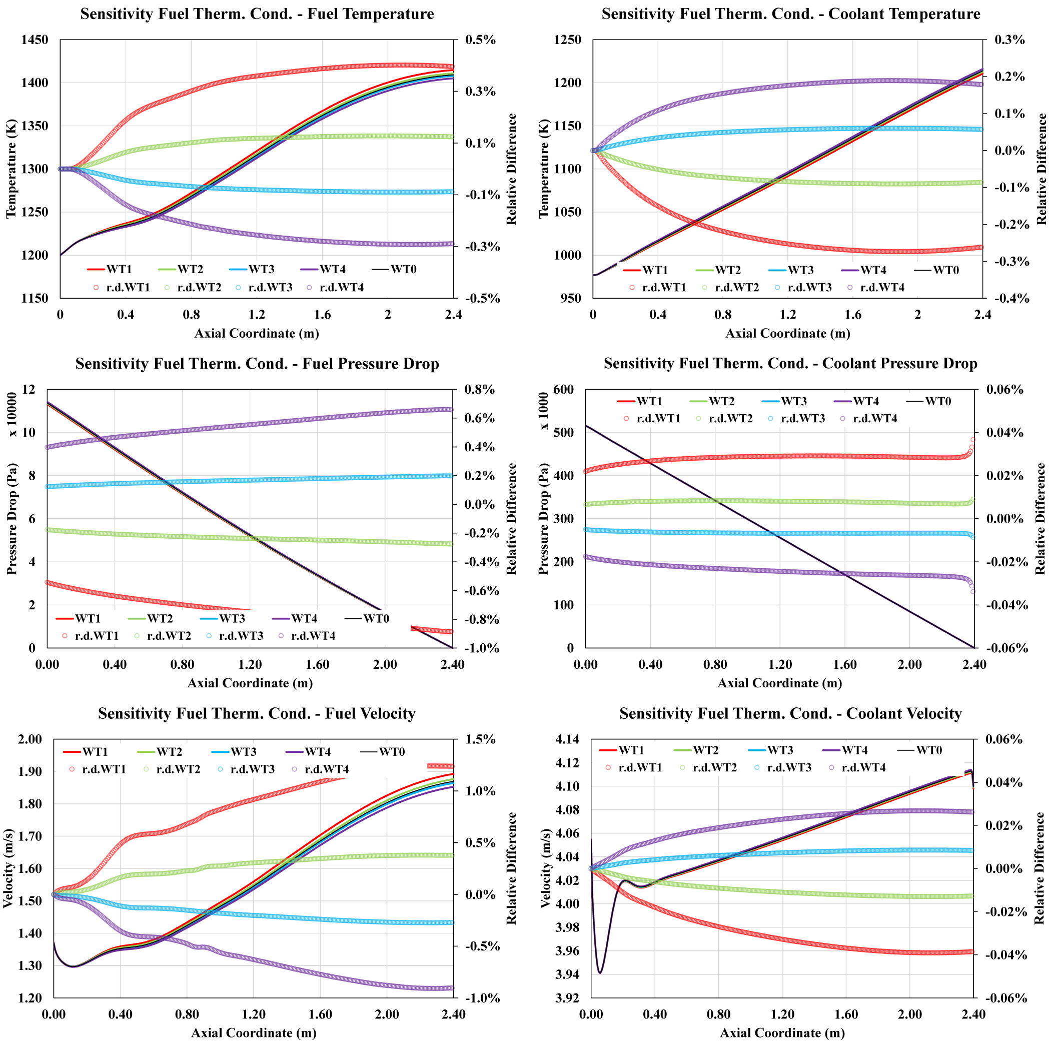

Figure 12.22: Sensitivity to wall thermal conductivity. Comparison (axial)

accepted.

It has to be mentioned that the analysis has involved the fission zone (zero- and one-dimensional models) and a single fuel cell (two- and three dimensional models). The entire reactor has not yet been simulated thermal-hydraulically, since it is quite complex in its configuration, as explained in Sec. 11.4.

After the steady state conclusion, the next question refers to the reliability of the results. To answer this question, the sensitivity calculations were performed. Limited by time and the computational resources, the sensitivity analyses were carried out only for some selected issues such as the influence of the velocity profiles, the value of y^+, the mesh size, and the physico-chemical properties of the fuel salt and of the fuel tube wall. For the velocity profile, the uniform velocity profile of the fuel salt and the coolant were shown to develop into the a fully developed turbulent profile in the first one fourth length of the flow channel, so the shape of the flow velocity profile is parabolic along the rest of the flow channel. However, the values of the

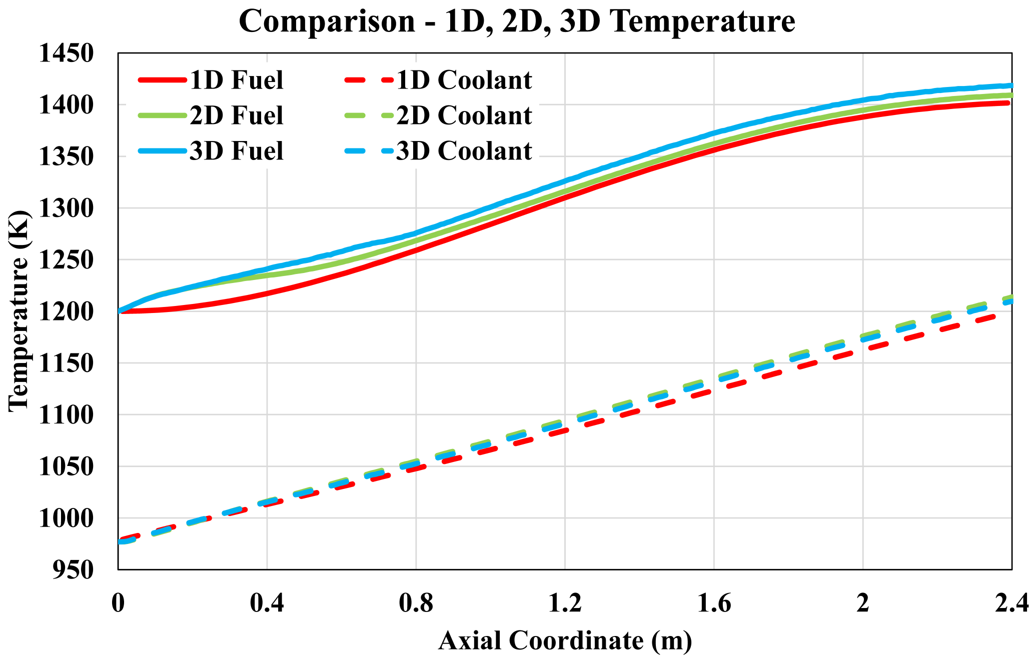

Figure 12.23: Comparison of axial temperature profile from 1D, 2D and 3D

velocities are different to those obtained when the parabolic velocity profile is used from the beginning of the flow channel. The maximum relative difference amongst the flow variables is found in the velocity, of course, with a value of over 10%, which is significant compared to other variables. This indicates that the uniform velocity profile should be avoided during the simulation and the parabolic velocity profile should be the preferred option.

The sensitivity analysis to the value of y^+ reveals that a higher y^+ should be adopted, but the y^+ value between 10 and 100 should be sufficient. The y^+ value has noticeable impact on the simulation results. Nevertheless, this impact is comparable to the impact caused by other factors such as the choice of the turbulence models or that of the wall function. The comparison points out that the selection of the turbulence models has less influence on the properties of the fuel salt flow, but is quite decisive for the coolant flow. Yet, the wall function has shown to have the most significant impact on the characteristics of both flows.

The mesh size, the fuel salt properties, as well as, the fuel tube wall properties have been proven less influential in the simulation, at least for the given range of the variables and for the operating conditions of the DFR. However these comparisons are quite simplified. More interpolated points should be given to these sensitivity analysis, so that a continuous trend of the variation of the properties could be produced and more definitive statements about the influence of the properties could be given.

This chapter has assessed important thermal-hydraulic aspects of the initial DFR design, and has identified a series of still open technical issues that need to be solved. Some issues such as material properties for the salt, optimal and safe flow configurations and heat transfer, etc. are still challenges for research and development of molten salt reactors in the world [SAB$^+$14, pp.315].

Part V

Discussions

Chapter 13

Summary

Since the very beginning, plenty time and energy have been investigated in the DFR project by setting up models and performing preliminary calculations. Till now it is however hard to evaluate the social or practical value of the DFR concept, after so many years, which is also not the primary study of this work.

This work focuses on the basic characteristics and properties of the neutronics and thermal-hydraulics of the DFR system and tries to provide a foundation of the research on the DFR system for the possible future.

After the introduction of the DFR the neutronics calculations are carried out. The detailed model of the whole reactor was established in both SERPENT and SCALE calculation codes. With these models the static characteristic and some selected sensitivity analysis are performed. From the results and the comparison it can be concluded that with the designed structure and the given fuel salt as well as the coolant, the reactor is able to achieve critical with the U-Pu fuel salt composition. Thanks to the delayed neutron during the fission reactions, the chain reaction is continuous and sustainable, providing a total thermal power generation of $3GW_{th}$.

If the inlet temperature ($1200K$) and outlet temperature ($1400K$) of the fuel salt as well as its axial profile are recalled, it can be found that the fuel salt leaves the core with its highest temperature. The consequence of this design is that about 30% of the generated heat is taken away by the fuel salt, or that is to say, the reactor with a designed thermal output of $3GW_{th}$ gives only around $2.1GW_{th}$ to the coolant and further loops for the steam generation, without consideration of the inertial energy consume like the pump power. The consequence is, the efficiency will be lower than conventional nuclear reactors unless the heat taken away by the fuel salt is well utilized.

It is so designed that the fuel salt will use some of the power as the initial temperature to take part in the online-processing. The online-processing unit, where removes the fission products away and feed new fuel salt or desired nuclides into the fuel salt. The online-processing in this work is simulated with two scenarios, which, as has been analyzed in the conclusion in Sec. 10.3, are simple and crude. However they can still serve as the preliminary approach to the online-processing of the DFR and provides a view to the change of the inventory during the depletion.

The final part of the thermal-hydraulic calculation is also simplified. From different dimension, it is expected to get close to the real thermal-hydraulic behavior of the DFR. By comparison the results of different approaches are consistent, which validates the calculation itself and verifies the design of the DFR.

Chapter 14

Outlook

In the DFR project, or more specifically on the DFR itself, there are still a lot of unknown issues to be discovered and solved. As a new conceptional nuclear reactor design, almost every detailed description of the DFR itself needs to be validated and verified. Though there are already common or general analysis on the other molten salt reactors, which are indeed excellent works, for the DFR with a unique structure and new parameters, the application of the results should be handled individually.

So far the simple neutronics and thermal-hydraulics and even the couple of those two parts have been done in this work and in the work finished by others at the same time. However from the technical point of view, there are still and all some interesting issues that are worthy to be investigated with more time and energy. Limited by the time these issues do not show up in this work, but it would be glad to see them solved or clarified in the future.

14.1 Longitudinal Study

14.1.1 Coupling

The coupling on a deeper level between the neutronics and the thermal-hydraulic calculations is the next goal. The current zero-dimensional point kinetics model homogenized the reactor core as a unity, which is not exactly the case. Inside of the core power generation and velocity of the fuel salt both have distributions, and these will affect the neutron distribution and the precursor concentrations. Especially the one-dimensional point kinetics model that to be implemented in the system.

14.1.2 Other Fuel Types

In order to expand the applicability of the DFR, it should be studied the if other types of fuel salts are also appropriate for the DFR core. The composition and the inventory can be interested.

14.2 Cross-Sectional Study

14.2.1 On Reactor Control

The control rods in the nuclear energy system are components to absorb neutrons and suppress neutron reactions inside of the reactor and therefore adjust the reactivity and regulate the temperature of the fuel salt. The consequence of these manners can be change of the power output or the operation state of the reactor. Therefore the control rods are considered very important for the safety control of the reactor and its position and total worth are needed to be investigated.

The original DFR concept doesn't include the existence of the control rods, which is considered a highlight of the reactor design [HRW$^+$15]. The reactor is then supposed to be self-regulated by its strong negative temperature feedback, mainly because of the fuel salt, the analysis of which is in Sec. 7.3. However, not only from the regulation point of the view but also from the academical point of view it is necessary to investigate the existence of the control rod seriously. This chapter bases on the concept of the DFR system and try to discuss the possibility of the appearance of the control rods.

14.2.2 On Drain Tank

Unlike conventional nuclear reactors, the DFR doesn't have control rods. In order to shut down the reactor without introducing a cold slug, a large positive reactivity change due to the sudden reduction of the fuel temperature, the DFR uses the experience in the MSRE project [Rob65, pp.17] for reference. The drain tank system as the auxiliary system to shut down the reactor is one of the most important control and safety measurement of the DFR energy system. [HRW$^+$15, pp.5]

The drain tank system is supposed to locate in a large room underneath the reactor, so that the gravity instead of any external power source drains the liquid fuel passively from the reactor into the storage tanks in the tank room, which is also known as the subcritical storage tanks for the liquid fuel.

This system and the core is blocked off by melting fuse plugs, which were already proved effective in the early MSRE project. [BHLT64, pp.28] The melting fuse plugs are maintained in a lower temperature by external cooling system and for this reason the melting fuse plugs keeps in the solid form. This mechanism ensures that in the emergency like high core temperature or power outage, or even the break down of the cooling system of the melting fuse plugs, the plugs melt and the core is then connected to the storage tanks. With help of the gravity the liquid fuel can be drained out of the reactor into the storage tanks, and consequently the potential risk is prevented.

14.2.3 On Flow Direction

The design of core in the DFR energy system describes the flow direction of both fluids, which are both upwards through the core. In the previous calculations the flow features of the fuel salt and the coolant lead are present. However whether this is the optimized design or not still needs to be investigated. The different flow direction of the fluids will cause changes in the heat transfer as well as the relative pressure drop.

14.2.4 On Inlet/Outlet Distribution Zone

Based on the design of the DFR, the relationship between the position of the in-/outlet nozzles on the in-/outlet plenum served for the fuel salt and the fluid properties should be further studied. It can be imagined that in the current structure of the in-/outlet distribution zone whirlpools will appear in the corner or other possible places. The temperature in this region might be also higher than the normal temperature. The effect of such higher temperature is still till now unknown. It can be worse that since the fuel salt is already radioactive before it flows into the inlet distribution zone, the delay of the fluid flowing into the fission zone due to the whirlpools in the distribution zone can result in the uncontrolled change of the fuel compositions inside of the fission zone.

14.2.5 On Further Heating

As mentioned in Sec. 11.2.1.2 that the heat generated in the reactor core has two destinations: one is like usual that the energy is transferred to the coolant lead and brought to the next circulation loop; the other one is that the fuel salt itself will take a large amount of energy out of the core with a high temperature. The steady state and transient analysis have shown that the once-through style heat transfer in the DFR concept is not sufficient to remove most of the generated heat with the coolant lead, which results a lower thermal/electricity output of the whole reactor.) Under this circumstance, a further discussion on the reactor design that how to improve the rate of the utilization of the generated heat is necessary.

Bibliography

[ABC$^+$08] T. Auger, G. Barreau, J.P. Chevalier, X. Doligez, S. Delpech, H. Flocard, B. Haas, D. Heuer, and E. Merle-Lucotte. The CNRS Research Program on the Thorium Cycle and the Molten Salt Reactor. Technical report, CNRS/IN2P3, June 2008.

[AH02] A.E. Aboanber and Y.M. Hamada. PWS: an efficient code system for solving space-independent nuclear reactor dynamics. *Annals of Nuclear Energy*, 29:2159–2172, 2002.

[ANS13] ANSYS Inc. *ANSYS Fluent Theory Guide*, version: 15.0 edition, 2013.

[BCM$^+$57] E.S. Bettis, W.B. Cottrell, E.R. Mann, J.L. Meem, and G.D. Whitman. The Aircraft Reactor Experiment-Operation. *Nuclear Science and Engineering*, 2, 1957.

[BHLT64] S.E. Beall, P.N. Haubenreich, R.B. Lindauer, and J.R. Tallackson. MSRE Design And Operations Report: Part V - Reactor Safety Analysis Report. Technical report: ORNL-TM-0732, Oak Ridge National Laboratory (ORNL), 1964.

[Bla13] P. R. H. Blasius. Das Aehnlichkeitsgesetz bei Reibungsvorgangen in Flüssigkeiten. *Forschungsheft*, 131, 1913.

[BMLR$^+$13] M. Brovchenko, E. Merle-Lucotte, H. Rouch, F. Alcaro, M. Aufiero, A. Cammi, S. Dulla, O. Feynberg, L. Frima, O. Geoffroy, D. Heuer, V. Ignatiev, J.L. Kloosterman, D. Lathouwers, A. Laureau, L. Luzzi, B. Merk, P. Ravetto, A. Rineiski, P. Rubbiolo, R. Li, M. Szieberth, S.S. Wang, and B. Yamaji. Optimization of the pre-conceptual design of the MSFR - Evaluation and Viability of Liquid Fuel Fast Reactor System EVOL. Technical report, CNRS/IN2P3/LPSC et al, September 2013.

[BNG$^+$01] A.H. Bond, K.L. Nash, A.V. Gels, J.C. Sullivan, M.P. Jensen, and L. Rao. Plutonium mobilization and matrix dissolution during experimental sludge washing of bismuth phosphate, redox and pure waste simulates. *Separation Science and Technology*, 36, 2001.

[Bor69] V. M. Borishanskii. Heat Transfer to Liquid Metal Flowing Longitudinally in Wetted Bundles of Rods. *Atomic Energy*, 27:549, 1969.

[Bow11] S. M. Bowman. SCALE 6: Comprehensive Nuclear Safety Analysis Code System. *Nuclear Technology*, 174(2):126, 2011.

[CA85] Y. Chao and A. Attard. A Resolution of the Stiffness Problem of Reactor Kinetics. *Nuclear Science and Engineering*, 90:40–46, 1985.

[CC59] D.O. Campbell and G.I. Cathers. Processing of Molten Salt Power Reactor Fuel. Technical report: ORNL-CF-59-2-61, Oak Ridge National Laboratory (ORNL), 1959.

[CC81] C. J. Chen and J. S. Chiou. Laminar and Turbulent Heat Transfer in the Pipe Entrance Region for Liquid Metal. *Int. J. Heat Mass Transfer*, 24:1179–1189, 1981.

[CFS10] A. Cammi, C. Fiorina, and B. Spinelli. Preliminary Analysis of The MSRE Dynamic Behaviour. Technical report, Corso di Laurea Specialistica in Ingegneria Nucleare, Facolta di Ingegneria dei Processi Industriali, Politechnico Milano, 2010.

[CN72] W.L. Carter and E.L. Nicholson. Design and Cost Study of A Fluorination Reductive Extraction Metal Transfer Processing Plant for the MSBR. Technical report: ORNL-TM-3579, Oak Ridge National Laboratory (ORNL), 1972.

[COM15] COMSOL AB. *CFD Module User's Guide*, version: 5.2 edition, 2015.

[CT06] X. Cheng and N.I. Tak. CFD analysis of thermal-hydraulic behavior of heavy liquid metals in sub-channels. *Nuclear Engineering and Design*, 236:1874–1885, 2006.

[DH75] James J. Duderstadt and Louis J. Hamilton. *Nuclear Reactor Analysis.* John Wiley & Sons Inc., 1975.

[DIBL05] David P. DeWitt, Frank P. Incropera, Theodore L. Bergman, and Adrienne S. Lavine. *Fundamentals of Heat and Mass Transfer.* John Wiley & Sons, New York, 6th. edition, 2005.

[DKSL13] J. Dufek, D. Kotlyar, E. Shwageraus, and J. Leppaenen. Numerical stability of the predictor-corrector method in Monte Carlo burnup calculations of critical reactors. *Ann. Nucl. Energy*, 56:34–38, 2013.

[DT60] O. E. Dwyer and P. S. Tu. Analytical Study of Heat Transfer Rates for Parallel Flow of Liquid Metals Through Tube Bundles, Part I. *Chemical Engineering Progress Symposium Series*, 56(30):183–193, 1960.

[Dwy63] O. E. Dwyer. Eddy Transport in Liquid Metal Heat Transfer. *AIChE J.*, 9:261–268, 1963.

[EGB+80] J. R. Engel, W. R. Grmes, H. F. Bauman, E. H. McCoy, J. F. Dearing, and W. A. Rhoades. Conceptual Design Characteristics of a Denatured Molten-Salt Reactor with Once-Through Fueling. Technical report: ORNL-TM-7207, Oak Ridge National Laboratory (ORNL), 1980.

[Els13] Badawy M. Elsheikh. Safety assessment of mlten salt reactors in comparison with light water reactors. *Journal of Radiation Research and Applied Sciences*, 6:63–70, 2013.

[FAC$^+$13] C. Fiorina, M. Aufiero, A. Cammi, F. Franceschini, J. Krepel, L. Luzzi, K. Mikityuk, and M.E. Ricotti. Investigation of the MSFR core physics and fuel cycle characteristics. *Progress in Nuclear Energy*, 68:153–168, 2013.

[FAE$^+$08] K. Furukawa, K. Arakawa, L. B. Erbay, Y. Ito, Y. Kato, H. Kiyavitskaya, A. Lecocq, K. Mitachi, R. Moir, H. Numata, J. P. Pleasant, Y. Sato, Y. Shimazu, V. A. Simonenco, D. D. Sood, C. Urban, and R. Yoshioka. A road map for the realization of global-scale thorium breeding fuel cycle by single molten-fluoride flow. *Energy Conv. Manag.*, 49:1832–1848, 2008.

[Fan07] Thomas H. Fanning. Topical Seminar Series on Sodium Fast Reactors - Sodium as a Fast Reactor Coolant. Technical report, Nuclear Engineering Division, U.S. Nuclear Regulatory Commission, U.S. Department of Energy, 2007.

[FBA$^+$11] J. D. Freels, I. T. Bodey, R. V. Arimilli, F. G. Curtis, K. Ekici, and P. K. Jain. Priliminary Multiphysics Analyses of HFIR LEU Fuel Conversion using COMSOL. Technical report: ORNL/TM-2011/007, Oak Ridge National Laboratory (ORNL), 2011.

[Fea61] A. Friedland and et al. Heat Transfer to Mercury in Parallel Flow through Bundles of Circular Rods. In *Proceedings*. International Heat Transfer Conference, 1961.

[FEA12] K. Furukawa, L. B. Erbay, and A. Aykol. A study on a symbiotic thorium breeding fuel-cycle: THORIMS-NES through FUJI. *Energy Conv. Manag.*, 63:51–54, 2012.

[FHRa] FHR Reports. https://www.ornl.gov/content/national-laboratory-reports-fhrs.

[FHRb] Fluoride Salt-Cooled High Temperature Reactor. https://www.iaea.org/NuclearPower/Downloadable/Meetings/2014/2014-06-10-06-13-TM-NPTD/6_Sridharan_USA__IAEA_Presentation_June_2014.pdf.

[FLC$^+$89] R.J. Forrester, M.J. Lineberry, I. Charak, J.H. Tessier, C.W. Solbrig, and J.D. Gabor. Safety Aspects of the IFR Pyroprocess Fuel Cycle. Technical Report: CONF-890841-4, Department of Energy, USA, January 1989.

[FMO$^+$87] K. Furukawa, H. Minami, T. Oosawa, M. Ohta, N. Nakamura, and K. Mitachi et.al. Design stdy of small MS fission power station suitable for coupling with accelerator MS breeders. In *Proceedings*. Emerg nucl energy system (Proc 4th ICENES), 1987.

[For04] C. W. Forsberg. A Large Low-Pressure Advanced High-Temperature Reactor(AHTR). In *Proceedings*, Honolulu, Hawaii, USA, 2004. 14th. Pacific Basin Nuclear Conference, American Nuclear Society.

[For06] C. W. Forsberg. Developments in molten salt and liquid salt cooled reactors. In *Proceedings*. International Congress on Advances in Nuclear Power Plants(ICAPP), 2006.

[For07] C. W. Forsberg. Liquid Salt Applications and Molten Salt Reactors. *Revue Générale du Nucléaire*, 63(4), 2007.

[Fur90] K. Furukawa. Summary report: thorium molten-salt nuclear energy synergetics. *J. Nucl. Sci. Technol.*, 27:1155–1178, 1990.

[GCL13] Claudia Guerrieri, Antonio Cammi, and Lelio Luzzi. An approach to the MSR dynamics and stability analysis. *Progress in Nuclear Energy*, 67:56–73, 2013.

[Gea92] U. Gat and et at. Molten Salt Reactors for Burning Dismantled Weapons Fuel. *Nuc. Tech.*, 100(3):390–394, 1992.

[Gea97] U. Gat and et at. Molten Salt Reactors - Safety options galore. In *Proceedings*. International ANS Topical Meeting on Advanced Reactor Safety, 1997.

[gen02] A Technology Roadmap for Generation IV Nuclear Energy Systems. Technical report: GIF-002-00, U.S. DOE Nuclear Energy Research Advisory Committee and the Generation IV International Forum, 2002.

[gen14] Technology Roadmap Update for Generation IV Nuclear Energy Systems. Technical report, U.S. DOE Nuclear Energy Research Advisory Committee and the Generation IV International Forum, 2014.

[GGH$^+$10] S. R. Greene, J. C. Gehin, D. E. Holcomb, J. J. Carbajo, D. Ilas, A. T. Cisneros, V. K. Varma, W. R. Corwin, D. F. Wilson, G. L. Yoder Jr., A. L. Qualls, F. J. Peretz, G. F. Flanagan, D. A. Clayton, E. C. Bradley, G. L. Bell, J. D. Hunn, P. J. Pappano, and M. S. Cetiner. Pre-Conceptual Design of a Fluoride-Salt-Cooled Small Modular Advanced High-Temperature Reactor (SmAHTR). Technical report: ORNL/TM-2010/199, Oak Ridge National Laboratory (ORNL), 2010.

[GR72] H. Gräber and M. Rieger. Experimentelle Untersuchung des Wärmeübergangs an Flüssigmetalle (NaK) in parallel durchströmten Rohrbündeln bei konstanter und exponentieller Wärmeflußdichteverteilung. *Atomkernenergie*, 19(1):23–40, 1972.

[Gre10a] S. R. Greene. SmAHTR - The Small Modular Advanced High Temperature Reactor. Presentation, Oak Ridge National Laboratory (ORNL), Berkeley, CA, USA, June 2010. 4th. Annual Asia-Pasific Nuclear Energy Forum.

[Gre10b] S. R. Greene. SmAHTR - The Small Modular Advanced High Temperature Reactor. Presentation, Oak Ridge National Laboratory (ORNL), September 2010. DOE FHR Workshop.

[HE62] P. N. Haubenreich and J. R. Engel. Safety Calculations For MSRE. Technical Report: ORNL-TM-251, Oak Ridge National Laboratory, May 1962.

[heu06] Concept de r*é*acteurs *á* sels fondus en cycle thorium sans mod*é*rateur. *Revue Générale du Nucléaire*, 5/2006:92–99, 2006.

[Hol14] J. P. Holman. *Heat Transfer*. McGraw Hill Education, 10th. edition, 2014.

[Hro06] M. Hron. Molten Salt Reactor: Current Status and Future Prospects Within European Activities. Technical report: EUR 21231, FISA 2006 EU Research and Training in Reactor Systems, 2006.

[HRW$^+$15] A. Huke, G. Ruprecht, D. Weissbach, S. Gottlieb, A. Hussein, and Konrad Czerski. The Dual Fluid Reactor - A new reactor and safety concept. In *Proceedings*, volume Track 3 - 15176, Nice, France, 2015. International Congress on Advances in Nuclear Power Plants(ICAPP).

[Hur49] H.Jr. Hurwitz. Derivation and Integration of the pile-kinetic equations. *Nucleonics*, 5:61, 1949.

[iae13] Challenges Related to the Use of Liquid Metal and Molten Salt Coolants in Advanced Reactors. Technical report: IAEA-TECDOC-1696, International Atomic Energy Agency (IAEA), 2013.

[Iea05] V. Ignatiev and et al. Characteristics of Molten Salt Actinide Recycler and Transmuter System. In *Proceedings*, Brussels, Belgium, 2005. International Conference on Emerging Nuclear Energy System.

[IF12] V. Ignatiev and O. Feynberg. *Actinide And Fission Product Partitioning and Transmutation*. OECD, 2012.

[IFO$^+$04] D. T. Ingersoll, C. W. Forsberg, L. J. Ott, D. F. Williams, J. P. Renier, D. F. Wilson, S. J. Ball, L. Reid, W. R. Corwin, and G. D. Del Cul. Status of Preconceptual Design of the Advanced High-Temperature Reactor (AHTR). Technical Report: ORNL/TM-2004/104, Oak Ridge National Laboratory (ORNL), 2004.

[IFR] Integral Fast Reactor. http://www.ne.anl.gov/About/reactors/integral-fast-reactor.shtml.

[Iiz01] Masatoshi Iizuka. Development of plutonium recovery process by molten salt electrorefining with liquid cadmium cathode. In *Proceedings*, Madrid, Spain, 2001. 6th Information Exchange Meeting on Actinide and Fission Product Partitioning and Transmutation.

[IMS] Integral Molten Salt Reactor. http://terrestrialenergy.com/media/downloads.

[IN70] M. Izumi and T. Noda. An Implicit Method for Solving the Lumped Parameter Reactor-Kinetics Equations by Repeated Extrapolation. *Nuclear Science and Engineering*, 41:299–303, 1970.

[Iso13] Asrno Isotalo. *Computational Methods for Burnup Calculations with Monte Carlo Neutronics.* PhD thesis, Aalto University, 2013.

[Jan75] G. J. Janz. Molten Salts âĂŞ Chlorides and Mixtures. *J. Phys. Chem. Ref. Data*, 4(4), 1975.

[JXD12] Mianheng Jiang, Hongjie Xu, and Zhimin Dai. Advanced Fission Energy Program-TMSR Nuclear Energy System. *Bulletin of Chinese Academy of Sciences*, 27(3), 2012.

[KA04] M. Kinard and E. Allen. Efficient numerical solution of the point kinetics equations in nuclear reactor dynamics. *Annals of Nuclear Energy*, 31:1039–1051, 2004.

[KB66] T. W. Kerlin and S. J. Ball. Experimental Dynamic Analysis Of The Molten-Salt Reactor Experiment. Technical Report: ORNL/TM-1647, Oak Ridge National Laboratory (ORNL), 1966.

[KBNF58] S. S. Kutalteladze, V. M. Borishanskii, I. I. Novikov, and O. S. Fedynskii. *Liquid Metal Heat Transfer Media.* 1958.

[KC76] M.S. Kazimi and M.D. Carelli. Heat Transfer Correlation For Analysis Of CRBRP Assemblies. Technical Report: CRBRP-ARE-0034, Westinghouse Inc., 1976.

[Kee64] G. Robert Keepin. *Physics of Nuclear Kinetics.* Addison-Wesley Publishing Company, INC, 1st. edition, 1964.

[Kog72] J.W. Koger. Evaluation of Hastelloy N Alloys After Nine Years Exposure To Both A Molten Fluoride Salt And Air At Temperature From $700\,^{\circ}C$To $560\,^{\circ}C$. Technical Report: ORNL-TM-4189, Oak Ridge National Laboratory (ORNL), 1972.

[KU01] P. L. Kirillov and P. A. Ushakov. Heat transfer to liquid metals: specific features, methods of investigation, and main relationships. *Therm. Eng.*, 48(1):50–59, 2001.

[Kuc11] Bernhard Kuczera. Das schwere Tohuku-Seebeben in Japan und die Auswirkungen auf das Kernkraftwerk Fukushima-Daiichi. *atw - Internationale Zeitschrift für Kernenergie*, 56(4/5), April/Mai 2011. Sonderdruck.

[kwe08] Key World Energy Statistics 2008. Technical Report, International Energy Agency (IEA), 2008.

[kwe09] Key World Energy Statistics 2009. Technical Report, International Energy Agency (IEA), 2009.

[kwe10] Key World Energy Statistics 2010. Technical Report, International Energy Agency (IEA), 2010.

[kwe11] Key World Energy Statistics 2011. Technical Report, International Energy Agency (IEA), 2011.

[kwe12] Key World Energy Statistics 2012. Technical Report, International Energy Agency (IEA), 2012.

[kwe13] Key World Energy Statistics 2013. Technical Report, International Energy Agency (IEA), 2013.

[kwe14] Key World Energy Statistics 2014. Technical Report, International Energy Agency (IEA), 2014.

[kwe15] Key World Energy Statistics 2015. Technical Report, International Energy Agency (IEA), 2015.

[KWF07] Y. Katoh, D.F. Wilson, and C.W. Forsberg. Assessment of Silicon Carbide Composites for Advanced Salt-Cooled Reactors. Technical Report: ORNL/TM-2007/168, Oak Ridge National Laboratory (ORNL), 2007.

[LAF$^+$14] J. Lepp*ä*nen, M. Aufiero, E. Fridman, R. Rachamin, and S. van der Marck. Calculation of effective point kinetics parameters in the Serpent 2 Monte Carlo code. *Ann. Nucl. Energy*, 65:272–279, 2014.

[LB01] John R. Lamarsh and Anthony J. Baratta. *Introduction to Nuclear Engineering*. Prentice Hall, 3rd. edition, 2001.

[LCLZ09] Haofeng Li, Wenzhen Chen, Lei Luo, and Qian Zhu. A new integral method for solving the point reactor neutron kinetics equations. *Annals of Nuclear Energy*, 36:427–432, 2009.

[LeB10a] D. LeBlanc. Denatured nolten salt reactors (DMSR): an idea whose time has finally come? In *Vol. 2 of 2*, Montreal, Canada, May 2010. 31st Annual Conference of the Canadian Nuclear Safety & 34th CNS/CNA Student Conference 2010.

[LeB10b] David LeBlanc. Molten Salt Reactors: A new beginning for an old idea. *Nuclear Engineering and Design*, 240:1644–1656, 2010.

[Lee83] S. L. Lee. Liquid Metal Heat Transfer in Turbulent Pipe Flow with Uniform Wall Flux. *Int. J. Heat Mass Transfer*, 26:349–356, 1983.

[Lep12] J. Leppaenen. SERPENT - a Continuous-energy Monte Carlo Reactor Physics Burnup Calculation Code. Presentation, Technical Research Centre of Finland (VTT), March 2012.

[Lep13] J. Leppaenen. *SERPENT - a Continuous-energy Monte Carlo Reactor Physics Burnup Calculation Code*. VTT Technical Research Centre of Finland, 2013.

[Lew60] Jeffery Lewins. The Use of the Generation Time in Reactor Kinetics. *Nuclear Science and Engineering*, 7(2):122–126, February 1960.

[Lew81] Jeffery Lewins. Neutron Lifetime, Generation Time and Reproduction Time. *Nuclear Science Engineering*, 78:105, 1981.

[LI12] J. Leppaenen and A. Isotalo. Burnup calculation methodology in the Serpent 2 Monte Carlo code. In *Proceedings*, Knoxville, USA, April 2012. American Nuclear Society.

[LI14] David LeBlanc and Simon Irish. The Integral Molten Salt Reactor. *Nuclear News*, 57(13):54–57, December 2014.

[Lin69] R.B. Lindauer. Processing of the MSRE Flush and Fuel Salts. Technical report: ORNL-TM-2578, Oak Ridge National Laboratory (ORNL), 1969.

[LK55] B. Lubarski and S. J. Kaufman. Review of Experimental Investigations of Liquid Metal Heat Transfer. Naca technical note: Tn-3336, 1955.

[LMR01] G. Lapenta, F. Mattioda, and P. Ravetto. Point Kinetic Model for Fluid Fuel Systems. *Annals of Nuclear Energy*, 28:1759–1772, 2001.

[LS72] B. E. Launder and D. B. Spalding. *Lectures in Mathematical Models of Turbulence.* Academic Press, London, England, 1972.

[LS74] B. E. Launder and D. B. Spalding. The Numerical Computation of Turbulent Flows. *Computer Methods In Applied Mechanics And Engineering*, 3:269–289, 1974.

[Lyo51] R.N. Lyon. Liquid Metal Heat Transfer Coefficients. *Chem. Eng. Prog.*, 47:75, 1951.

[Mad82] David G. Madland. New Calculation of Prompt Fission Neutron Spectra and Average Promt Neutron Multiplicities. *Nuclear Science And Engineering*, 81:213–271, 1982.

[Mad90] David G. Madland. Theoretical Descriptions of Neutron Emission in Fission. In *Proceedings*, pages 201–231, Vienna, Austria, Oct. 1990. The International Atomic Energy Agency.

[Mad06] David G. Madland. Total Prompt Energy Release in the Neutron-Induced Fission of ^{235}U , ^{238}U , and ^{239}Pu . *Nuclear Physics A*, 772:113–137, 2006.

[mar14] The UK's Forgotten Molten Salt Reactor Programme. http://www.the-weinberg-foundation.org/2014/11/13/the-uks-forgotten-molten-salt-reactor-programme/, November 2014.

[McW70] J.R. McWherter. Molten Salt Breeder Experiment Design Basis. Technical report: ORNL-TM-3177, Oak Ridge National Laboratory (ORNL), 1970.

[MD64] M. W. Maresca and O. E. Dwyer. Heat Transfer to Mercury Flowing in-line through a Bundle of Circular Rods. *Journal of Heat Transfer*, 86(2):180–186, 1964.

[mek11] MEK4450 - Offshore Technology. https://www.uio.no/studier/emner/matnat/math/MEK4450/h11/undervisningsmateriale/modul-5/Pipeflow_intro.pdf, October 2011.

[MHea06] L. Mathieu, D. Heuer, and et al. The Thorium Molten Salt Reactor: Moving on from the MSBR. *Prog. in. Nucl. Eng.*, 48:664–679, 2006.

[Mik09] K. Mikityuk. Heat Transfer to Liquid Metal: Review of Data and Correlations for Tube Bundles. *Nuclear Engineering and Design*, 239(4):680–687, 2009.

[MLH08] E. Merle-Lucotte and D. Heuer. *NATO Science for Peace and Security Series - B*. Springer, 2008.

[MLHA+07] E. Merle-Lucotte, D. Heuer, M. Allibert, V. Ghetta, C. Le Brun, L. Mathieu, R. Brissot, and E. Liatard. Optimized Transition from the Reactors of Second and Third Generations to the Thorium Molten Salt Reactor. In *Proceedings*, Nice, France, 2007. International Congress on Advances in Nuclear Power Plants (ICAPP).

[MLHB+06] E. Merle-Lucotte, D. Heuer, C. Le Brun, L. Mathieu, R. Brissot, E. Liatard, O. Meplan, and A. Nuttin. Fast Thorium Molten Salt Reactors started with Plutonium. In *Proceedings*, Reno, USA, 2006. International Congress on Advances in Nuclear Power Plants (ICAPP).

[MLHB+07] E. Merle-Lucotte, D. Heuer, C. Le Brun, M. Allibert, V. Ghetta, L. Mathieu, R. Brissot, and E. Liatard. The Non-Moderated TMSR, an Efficient Actinide Burner and a Very Promising Thorium Breeder. In *Proceedings*, La Boise, USA, 2007. Global 2007 International Conference.

[MLHea09] E. Merle-Lucotte, D. Heuer, and et al. Minimizing the Fissile Inventory of the Molten Salt Fast Reactor. In *Proceedings*, Hilton Head Island, USA, 2009. Advances in Nuclear Fuel Management IV (ANFM 2009).

[MMLea09] L. Mathieu, E. Merle-Lucotte, and et al. Possible Configurations for the Thorium Molten Salt Reactor and Advantages of the Fast Non-Moderated Version. *Nucl. Sci. and Eng.*, 161:78–89, 2009.

[moi15] A Primer on Nuclear Safety: 2.6 Defense in Depth. http://energyfromthorium.com/2008/10/18/a-primer-on-nuclear-safety-2-6-defense-in-depth/, November 2015.

[Mot70] J. Moteff. Neutron Fluence Measurements. Technical report: Sti/doc/10/107, International Atomic Energy Agency (IAEA), 1970.

[MPDS15] J. Magill, G. Pfennig, R. Dreher, and Z. Soti. *Karlsruher Nuklidkarte*. nucleonica GmbH, 9th. edition, 2015.

[MS76] W. C. May and W. E. Simmons. Conceptual Design and Assessment of a 2500MWe Molten Salt Fast Reactor with Integrated Gas Turbine Plant. Technical report: Aeew r1059, Atomic Energy Research Establishment (AERE), 1976.

[Mun97] R. G. Munro. Material Properties of a Sintered α-SiC. *J. Phys. Chem. Ref. Data*, 26(5):1195–1201, 1997.

[MYY05] K. Mitachi, T. Yamamoto, and R. Yoshioka. Three-region core design for 200MWe molten-salt reactor with Th-U fuel. In *Proceedings*, Tukuba, 2005. GLOBAL2005.

[nas12] Correlation of Friction Coefficients for Laminar and Turbulent Flow with Ratios of Surface to Bulk Temperature from 0.35 to 7.35. Technical Report: NASA TR R-267, National Aeronautics And Space Administration (NASA), June 2012.

[NEA67] Spent Nuclear Fuel Reprocessing Flowsheet. Technical Report: NSC/WPFC/DOC(2012)15, Nuclear Energy Agency (NEA), September 1967.

[nea15] Handbook on Lead-bismuth Eutectic Alloy and Lead Properties, Materials Compatibility, Thermalhydraulics and Technologies. Technical Report: NEA-7268, Nuclear Energy Agency (NEA), 2015.

[Nee71] L.E. Neese. Engineering Development Studies for Molten-Salt Breeder Reactor Processing No. 2. Technical report: ORNL-TM-3137, Oak Ridge National Laboratory (ORNL), 1971.

[NH05] A. Nuttin and D. Heuer. Potential of Thorium Molten Salt Reactors. *Prog. in Nucl. En.*, 46:77–99, 2005.

[NK05] Yasushi Nauchi and Takanori Kameyama. Proposal of Direct Calculation of Kinetic Parameters β_{eff} and Λ Based on Continuous Energy Monte Carlo Method. *Journal of Nuclear Science and Technology*, 42(6):503–514, June 2005.

[NK06] Yasushi Nauchi and Takanori Kameyama. Estimation of 6 Groups of Effective Delayed Neutron Fraction Based on Continuous Energy Monte Carlo Method. In *Proceedings*, Vancouver, Canada, 2006. American Nuclear Society.

[NKLvdH10] K. Nagy, J.L. Kloosterman, D. Lathouwers, and T.H.J.J. van der Hagen. Definition of Breeding Gain for Molten Salt Reactors. In *on CD-ROM*, Pittsburgh, USA, Apr. 2010. American Nuclear Society.

[NMH$^+$97] O. Nilsson, H. Mehling, R. Horn, J. Fricke, R. Hofmann, S.G. Müller, R. Eckstein, and D. Hofmann. Determination of the thermal diffusivity and conductivity of monocrystalline silicon carbide (300 - 2300 K). *High Temperature-High Pressure*, 29:73–79, 1997.

[Nob71] J. A. W. Da Nobrega. A new solution of the point kinetics equations. *Nuclear Science and Engineering*, 46(3):366–375, 1971.

[Nov94] Vladimir M. Novikov. The results of the investigations of Russian Research Center - “Kurchatov Institute” on molten salt applications to problems of nuclear energy systems. In *Proceedings*, Las Vegas, USA, 1994. AIP Conference.

[nrc13] Backgrounder on the Three Mile Island Accident. Technical Report, United States Nuclear Regulation Commission (NRC), February 2013.

[NS72] R. H. Notter and C. A. Sleicher. A Solution to the Turbulent Graetz Problem III. Fully Developed and Entry Region Heat Transfer Rates. *Chem. Eng. Sci.*, 27:2073–2093, 1972.

[nts07] Nuclear Technology Review 2007. Technical Report, International Atomic Energy Agency (IAEA), 2007.

[nts08] Nuclear Technology Review 2008. Technical Report, International Atomic Energy Agency (IAEA), 2008.

[nts09] Nuclear Technology Review 2009. Technical Report, International Atomic Energy Agency (IAEA), 2009.

[nts10] Nuclear Technology Review 2010. Technical Report, International Atomic Energy Agency (IAEA), 2010.

[nts11] Nuclear Technology Review 2011. Technical Report, International Atomic Energy Agency (IAEA), 2011.

[nts12] Nuclear Technology Review 2012. Technical Report, International Atomic Energy Agency (IAEA), 2012.

[nts13] Nuclear Technology Review 2013. Technical Report, International Atomic Energy Agency (IAEA), 2013.

[nts14] Nuclear Technology Review 2014. Technical Report, International Atomic Energy Agency (IAEA), 2014.

[Oak11] Oak Ridge National Laboratory. *SCALE: A Comprehensive Modeling and Simulation Suite for Nuclear Safety Analysis and Design*, version 6.1 edition, Jan. 2011. ORNL-TM-2005-39. Available from Radiation Safety Information Computational Center at Oak Ridge National Laboratory as CCC-785.

[omp15] The OpenMP API specification for parallel programmingh. http://openmp.org/wp/, November 2015.

[Pfa77] Jaroslav Pfann. A New Description Of Liquid Metal Heat Transfer In Closed Conduits. *Nuclear Engineering and Design*, 41:149–163, 1977.

[PL12] M. Pusa and J. Leppaenen. An efficient implementation of the Chebyshev rational approximation method (CRAM) for solving the burnup equations. In *Proceedings*, Knoxville, USA, Apr. 2012. American Nuclear Society.

[PMT05] B. A. Pint, J. L. Moser, and P. F. Tortorelli. INVESTIGATION OF Pb-Li COMPATIBILITY FOR THE DUAL COOLANT TEST BLANKET MODULE. Technical Report, Oak Ridge National Laboratory (ORNL), 2005.

[Reu08] Paul Reuss. *Neutron Physics.* EDP Science, 2008.

[RHE$^+$03] Bradley T. Rearden, Calvin M. Hopper, Karla R. Elam, Sedat Goluoglu, and Cecil V. Parks. Application of the TSUNAMI Sensitivity and Uncertainty Analysis Methodology. In *Submitted to*, Tokai-mura, Japan, Oct. 2003. Japan Atomic Energy Research Institute.

[Rob65] R.C. Robertson. MSRE Design and Operations Report Part I - Description of Reactor Design. Technical report: ORNL-TM-0728, Oak Ridge National Laboratory (ORNL), 1965.

[Ros72] M. W. Rosenthal. Molten Salt Reactor Program Semiannual Progress Report. Technical report: ORNL-4812, Oak Ridge National Laboratory (ORNL), 1972.

[RPJW11] B. T. Rearden, L. M. Petrie, M. A. Jessee, and M. L. Williams. SAMS: Sensitivity Analysis Module For SCALE. Technical report: ORNL/TM-2005/39, Oak Ridge National Laboratory (ORNL), 2011.

[RSBB70] R.C. Robertson, O.L. Smith, R.B. Briggs, and E.S. Bettis. Two-fluid molten-salt breeder reactor design study. Technical report: ORNL-4528, Oak Ridge National Laboratory (ORNL), 1970.

[Rus79] James H. Rust. *Nuclear Power Plant Engineering.* Haralson Publishing Company, P.O. Box 20366, Atlanta, Georgia 30325, 1st. edition, 1979.

[SAB$^+$14] J. Serp, M. Allibert, O. Benes, S. Delpech, O. Feynberg, V. Ghetta, D. Heuer, D. Holcomb, V. Ignatiev, J. L. Kloosterman, L. Luzzi, E. Merle-Lucotte, J. Uhlii, R. Yoshioka, and Z. M. Dai. The molten salt reactor (MSR) in generation IV: Overview and perspectives. *Progress in Nuclear Energy*, 77:308–319, 2014.

[San89] J. Sanchez. On the Numerical Solution of the Point Kinetics Equations by Generalized Runge-Kutta Methods. *Nuclear Science and Engineering*, 24(3):94–99, 1989.

[SB87a] R. K. Shah and M. S. Bhatti. *Handbook of Single-Phase Convective Heat Transfer.* John Wiley & Sons Inc., 1987.

[SB87b] R.K. Shah and M.S. Bhatti. *Handbook of Single-Phase Convective Heat Transfer.* Willy, New York, 1987.

[SBD14] N. Soppera, M. Bossant, and E. Dupont. JANIS 4: An Improved Version of the NEA Java-based Nuclear Data Information System. *Nuclear Data Sheets*, 120:294–296, June 2014.

[Sco66] C. D. Scott. Preliminary design study of continuous fluorination-vacuum-destillation system for regenerating fuel and fertile streams in a molten salt breeder reactor. Technical report: ORNL-3791, Oak Ridge National Laboratory (ORNL), January 1966.

[SLS$^+$95] T.-H. Shih, W. W. Liou, A. Shabbir, Z. Yang, and J. Zhu. A New $k-\epsilon$ Eddy-Viscosity Model for High Reynolds Number Turbulent Flows - Model Development and Validation. *Computers Fluids*, 103(3):227–238, 1995.

[Sob11] Vitaly Sobolev. Database of thermophysical properties of liquid metal coolants for GEN-IV. Technical report: SCK·CEN-BLG-1069, Studiencentrum voor Kernenergie (SCK·CEN), November 2011.

[SSA$^+$74] J. Smith, W. E. Simmons, Dr. R. C. Asher, Dr. G. Long, Dr. H. A. C. Mckay, and Dr. D. L. Reed. An Assessment of a 2500MWe Molten Chloride Salt Fast Reactor. Technical report: Aeew r956, Atomic Energy Research Establishment (AERE), 1974.

[ST57] C. A. Sleicher and M. Tribus. Heat Transfer in a Pipe with Turbulent Flow and Arbitrary Wall-Temperature Distribution. *Trans. ASME*, 79:789–797, 1957.

[STV65] E. Skupinski, J. Tortel, and L. Vautrey. Determination des coefficients de convection d'un allage sodium-potassium dans un tube circulaire. *Int. J. Heat Mass Transfer*, 9:937–951, 1965.

[SUK$^+$65] V.I. Subbotin, P.A. Ushakov, P.L. Kirillov, M.H. Ibragimov, M.N. Ivanovski, E.M. Nomofilov, D.M. Ovechkin, L.N. Sorokin, and V.P. Sorokin. Heat transfer in elements of reactors with a liquid metal coolant. In *Proceedings*, pages 192–200, New York, USA, 1965.

[SVD$^+$13] A. Shadrin, S. Veselov, K. Dvoeglazov, V. Volk, O. Schmidt, M. Kormilitszn, and A. Osipenko. Combined (Pyro+Hydro) technology for FR SNF reprocessing. Presentation, Bochvar Institute (VNIINM), Moscow and RIAR, Dimitrovgrad, March 2013.

[TD76] Yemada Taitel and A. E. Dukler. A model for predicting flow regime transitions in horizontal and near horizontal gas-liquid flow. *AlChE Journal*, 22, January 1976.

[TJ79] L. S. Tong and Weismann Joel. *Thermal Analysis of Pressurized Water Reactors.* LaGrange Park, 1st. edition, 1979.

[TK90a] Neil E. Todreas and Mujid S. Kazimi. *Nuclear System I Thermal Hydraulic.* Taylor and Francis, 1st. edition, 1990.

[TK90b] Neil E. Todreas and Mujid S. Kazimi. *Nuclear System II Elements of Thermal Hydraulic Design*. Taylor and Francis, 1st. edition, 1990.

[TL74] M. Taube and J. Ligou. Molten plutonium chloride fast breeder reactor cooled by molten uranium chloride. *Annual Nuclear Science and Engineering*, 1, 1974.

[TMS14] Construction of Prototype Reactor of TMSR. http://news.ifeng.com/a/20140620/40822730_0.shtml, June 2014.

[UZM77] P. A. Ushakov, A. V. Zhukov, and M. M. Matyukhin. Heat transfer to liquid metals in regular arrays of fuel elements. *High Temperature*, 15:868–873, 1977.

[VHP$^+$12] V. K. Varma, D. E. Holcomb, F. J. Peretz, E. C. Bradley, D. Ilas, A. L. Qualls, and N. M/ Zaharia. AHTR Mechanical Structural and Neutronic Preconceptural Design. Technical report: ORNL-TM-2012/320, Oak Ridge National Laboratory (ORNL), September 2012.

[Vig67] John Vigil. Solution of the Reactor Kinetics Equations by Analytical Continuation. *Nuclear Science and Engineering*, 29(3):292–401, 1967.

[Von76] D.R. Vondy. On Nuclear Fuel, Mass Balances, Conversion Ratio, Doubling Time and Uncertainty. Technical report: ORNL-TM-5050, Oak Ridge National Laboratory (ORNL), November 1976.

[Wil93] David C. Wilcox. *Turbulence Modeling for CFD*. DCW Industries Inc., 1st. edition, 1993.

[wim16] WIMS Library Update Project - Actinides burnup chain. http://www-nds.iaea.org/wimsd/achain.htm, Janurary 2016.

[wna08] World Nuclear Power Reactors & Uranium Requirements. http://www.world-nuclear.org/info/Facts-and-Figures/World-Nuclear-Power-Reactors-and-Uranium-Requirements/, October 2008.

[WSM15] X. Wang, M. Seidl, and R. Macian. Preliminary Analysis of Basic Reactor Physics of the Dual Fluid Reactor Concept. In *Proceedings*, volume Track 6 - 15270, Nice, France, 2015. International Congress on Advances in Nuclear Power Plants(ICAPP).

[WW06] M.A. Williamson and J.L. Willit. Pyroprocessing Flowsheets for Recycling Used Nuclear Fuel. *Nuclear Engineering and Technology*, 43(4):329–334, August 2006.

[Xu15] Hongjie Xu. China's TMSR Programme. https://public.ornl.gov/conferences/MSR2015/pdf/10-China's TMSR programm_HongjieXu.pptx.pdf, October 2015.

[ZQS09] Dalin Zhang, Suizheng Qiu, and Guanghui Su. Development of a safety analysis code for molten salt reactors. *Nuclear Engineering and Design*, 239:2778–2785, 2009.